Conference Proceedings of the Society for Experimental Mechanics Series

Dario Di Maio · Paolo Castellini *Editors*

Rotating Machinery, Hybrid Test Methods, Vibro-Acoustics & Laser Vibrometry, Volume 8

Proceedings of the 35th IMAC, A Conference and Exposition on Structural Dynamics 2017

Springer

Conference Proceedings of the Society for Experimental Mechanics Series

Series Editor

Kristin B. Zimmerman, Ph.D.
Society for Experimental Mechanics, Inc.,
Bethel, CT, USA

More information about this series at http://www.springer.com/series/8922

Dario Di Maio • Paolo Castellini
Editors

Rotating Machinery, Hybrid Test Methods, Vibro-Acoustics & Laser Vibrometry, Volume 8

Proceedings of the 35th IMAC, A Conference and Exposition on Structural Dynamics 2017

Springer

Editors
Dario Di Maio
Mechanical Engineering
University of Bristol
Bristol, UK

Paolo Castellini
DIISM
Università Politecnica delle Marche
Ancona, Italy

ISSN 2191-5644 ISSN 2191-5652 (electronic)
Conference Proceedings of the Society for Experimental Mechanics Series
ISBN 978-3-319-54647-6 ISBN 978-3-319-54648-3 (eBook)
DOI 10.1007/978-3-319-54648-3

Library of Congress Control Number: 2017935572

Printed on acid-free paper

This Springer imprint is published by Springer Nature
The registered company is Springer International Publishing AG
The registered company address is: Gewerbestrasse 11, 6330 Cham, Switzerland

Preface

Rotating Machinery, *Hybrid Test Methods*, *Vibro-Acoustics & Laser Vibrometry* represent one of ten volumes of technical papers presented at the 35th IMAC, A Conference and Exposition on Structural Dynamics, organized by the Society for Experimental Mechanics, and held in Garden Grove, California, January 30–February 2, 2017. The full proceedings also include volumes on Nonlinear Dynamics; Dynamics of Civil Structures; Model Validation and Uncertainty Quantification; Dynamics of Coupled Structures; Sensors and Instrumentation; Special Topics in Structural Dynamics; Structural Health Monitoring & Damage Detection; Shock & Vibration, Aircraft/Aerospace and Energy Harvesting, and Topics in Modal Analysis & Testing.

Each collection presents early findings from experimental and computational investigations on an important area within Structural Dynamics. Topics represent papers on enabling technologies such as: rotating machinery, vibro-acoustics and laser Vibrometry, advances in wind energy and hybrid testing methods.

The organizers would like to thank the authors, presenters, session organizers, and session chairs for their participation in this track.

Bristol, UK — Dario Di Maio
Ancona, Italy — Paolo Castellini

Contents

Chapter 1
Strategies for Testing Large Aerospace Structures with 3D SLDV

Daniel P. Rohe

Abstract The 3D Scanning Laser Doppler Vibrometer (3D SLDV) has the ability to scan a large number of points with high accuracy compared to traditional roving hammer or accelerometer tests. The 3D SLDV has disadvantages, however, in that it requires line-of-sight from three scanning laser heads to the point being measured. This means that multiple scans can become necessary to measure large or complex parts, and internal components cannot typically be measured. In the past, large aerospace structures tested at Sandia National Laboratories typically have used a handful of accelerometer stations and instrumented internal components to characterize these test articles. This work describes two case studies that explore the advantages and difficulties in using a 3D SLDV to measure the same test articles with a much higher resolution scan of the exterior. This work proposes strategies for combining a large number of accelerometer channels with a high resolution laser scan. It explores the use of mirrors and laser head mounts to enable efficient re-alignment of the lasers with the test article when many scans are necessary, and it discusses the difficulties and pitfalls inherent with performing such a test.

Keywords 3D • SLDV • Aerospace • Modal

1.1 Introduction

Scanning Laser Doppler Vibrometry has been shown to have advantages over traditional mounted sensors [1]. For example, it allows for non-contact measurements which do not mass-load the test article. Additionally, a finer measurement point resolution can often be achieved through the use of scanning mirrors in the laser heads which are much more precise than a roving hammer or roving accelerometer test. It can also be quicker to set up a scan of, for example, 100 measurement points than to mount 100 accelerometers on the test article or perform 100 roving hammer impacts. This last result suggests that the 3D SLDV may be well-suited for performing tests with large numbers of measurement points, for example a large aerospace structure.

There are, however, some disadvantages to SLDV that might impede such a test. 3D SLDV requires line-of-sight from each of the three laser heads to the measurement point of interest. This often precludes the measurement of the motions of internal components of the test article, which can often times be the measurements that designers are most interested in. Additionally, scans may need to be performed from multiple directions to measure all sides of the test article, and these extra alignment steps may significantly increase the time required to perform a test.

This work investigates the effectiveness of using the 3D SLDV system to perform a high-resolution scan of the exterior of a large aerospace structure using two case studies. It discusses strategies for incorporating a large number of accelerometer channels, as well as using mirrors and laser head mounts to enable efficient re-alignment of the lasers with the test article when many scans are necessary.

Sandia National Laboratories is a multi-program laboratory managed and operated by Sandia Corporation, a wholly owned subsidiary of Lockheed Martin Corporation, for the U.S. Department of Energy's National Nuclear Security Administration under contract DE-AC04-94AL85000.

D.P. Rohe (✉)
Structural Dynamics Department, Sandia National Laboratories, P.O. Box 5800 - MS0557, Albuquerque, NM, 87185, USA
e-mail: dprohe@sandia.gov

D. Di Maio, P. Castellini (eds.), *Rotating Machinery, Hybrid Test Methods, Vibro-Acoustics & Laser Vibrometry, Volume 8*,
Conference Proceedings of the Society for Experimental Mechanics Series, DOI 10.1007/978-3-319-54648-3_1

1.2 Challenges Associated with Large Aerospace Test Articles

Aerospace test articles are generally large, complex structures that have high programmatic value. As a result of their size, a large number of measurement points may be necessary to achieve a fine resolution scan of the exterior of the structure. Due to the sequential nature of the SLDV measurement, this can result in long test times, especially considering that the laser may need to be repeatedly aligned with the structure to scan different sections of the test article. Therefore, time saving strategies should be implemented whenever possible. For example, performing a multiple-input test with three shakers attached would reduce the amount of measurement time by a factor of three compared to performing three single-input tests sequentially. Also, because of the potentially large number of alignments, it is important to develop an efficient way of repositioning the laser heads, because the alignment procedure is the most labor intensive portion of the SLDV test. Additionally, the SLDV measurement may need to be supplemented with a large number of accelerometer channels measuring the internal components of the aerospace structure.

Because large aerospace structures are often very valuable and costly to replace, it is standard procedure to minimize damage to the test article in the event that the test boundary conditions (e.g. bungee cords) should fail. This typically involves not lifting the test article higher than necessary from its supported position at rest. A requirement such as this can significantly limit the placement of the laser heads as they try to scan the bottom of the test article; there may not be enough room underneath the test article, so an alternative strategy must be devised, potentially using a different safety catch.

Even for a top or side scan of a test article, there may not be adequate space to place the laser heads when considering the placement of shakers and the footprints of the shaker stands or laser tripods. Setting up for such a scan may not be trivial. Bungee cords, shakers, and accelerometer cabling may all occlude the path of the laser beams resulting in portions of the test article that are unmeasurable.

1.3 Case Study Tests

Two test articles were used as case studies for performing tests on large aerospace structures. The first test article, shown schematically in Fig. 1.1, was conical with fewer external features and contained 58 channels of internal accelerometers. This test article was used to refine the approach before moving to the second, larger test article. The second test article is shown schematically in Fig. 1.2.

1.3.1 Conical Structure Modal Test

Because shaker testing is more often used on large aerospace structures, shaker testing was investigated in this work. To excite all of the modes in the bandwidth of interest, three shakers were attached simultaneously to the aft end of the test article in the three principal directions. Initially MB-50 shakers were used, but they occluded much of the aft end of the test article, and the stands required to support these shakers had a very large footprint which would interfere significantly with the laser head tripods. Instead smaller, lighter Labworks MT-161 shakers were used, and these could be supported by

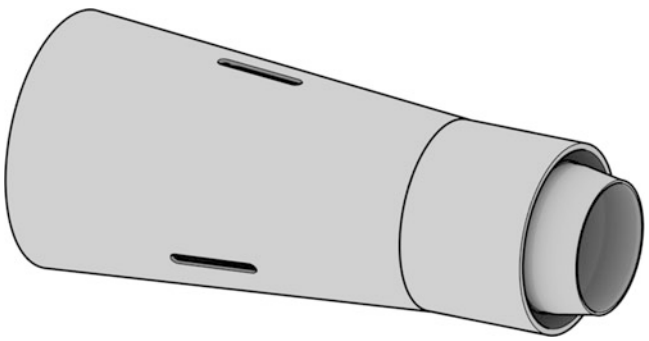

Fig. 1.1 Conical test article

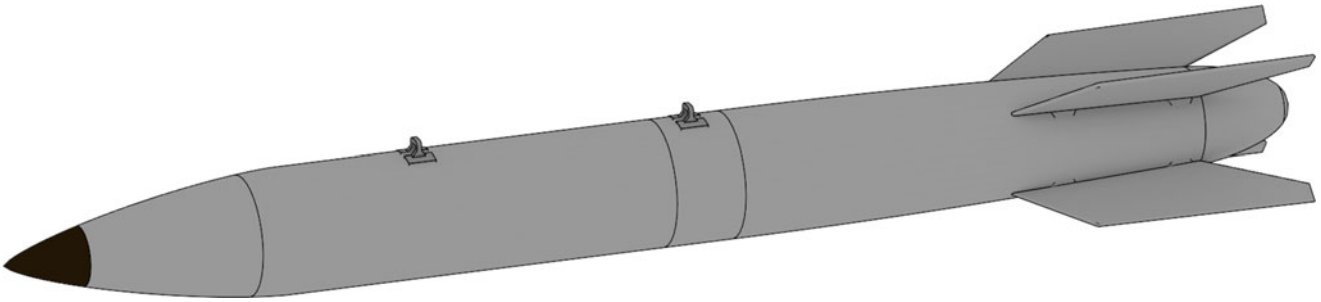

Fig. 1.2 Empty bomb case test article

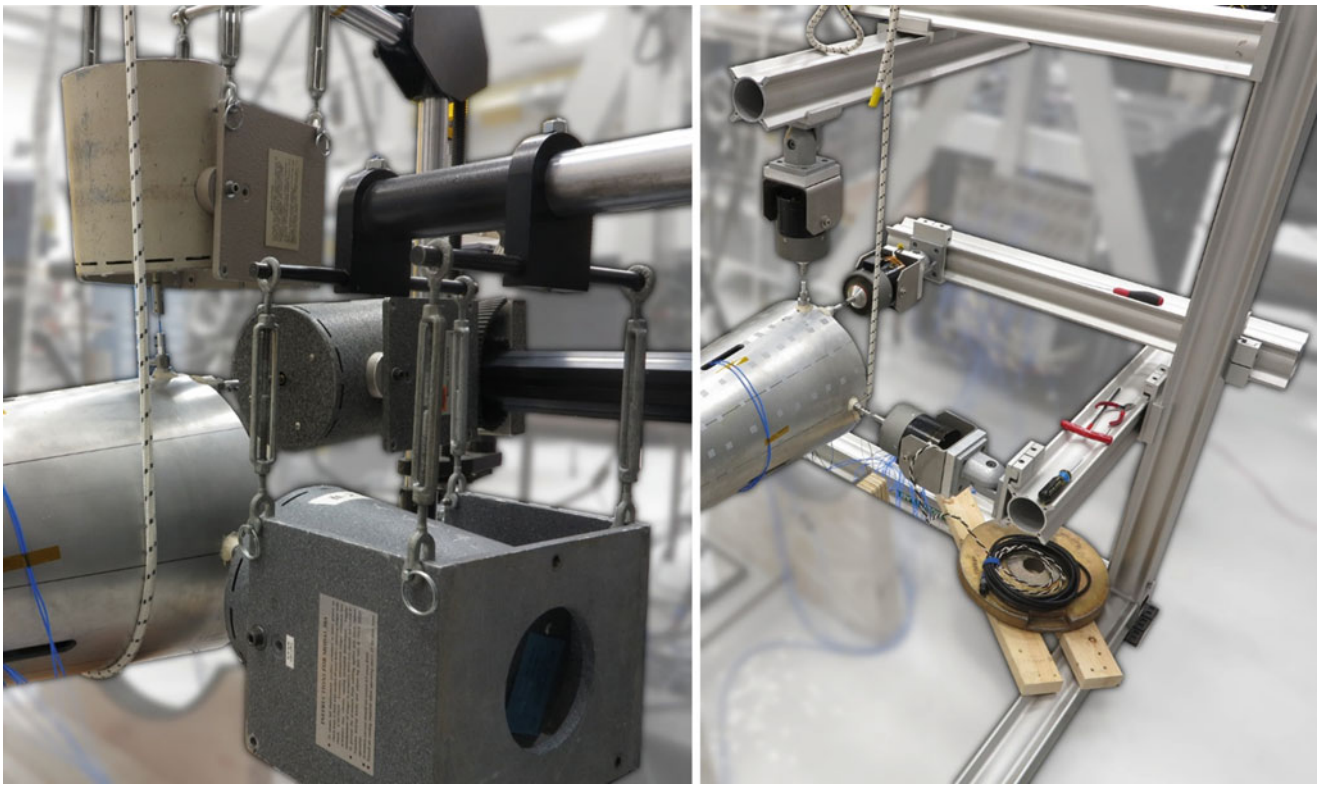

Fig. 1.3 Shaker support strategies using MB-50 (*left*) and MT-161 (*right*) shakers

a single frame made from 95 mm optical rail. As one can observe in Fig. 1.3, the smaller shakers supported on the optical rail system provided much better line-of-sight for the SLDV system. Bungee cords were used to support the test article, and retro-reflective tape was applied to the surface at each measurement point.

1.3.1.1 Data Acquisition Setup

Because the 3D SLDV data acquisition system (DAS) only supported eight additional measurement channels, the 58 channels of internal accelerometer measurements had to be measured by a separate DAS. A 64-channel VXI DAS was used for this purpose. The signals from the three drive point accelerometers and three force gauges were split to both systems so each could compute frequency response functions (FRFs). Similar data acquisition parameters were used between the two DASs. Current to power all of the integrated electronic piezoelectric (IEPE) accelerometers was supplied by the VXI DAS, so this output was disabled in the SLDV DAS.

Random white noise was applied to the shakers from the 3D SLDV sources. This eased the triggering and synchronization requirements between the two data acquisition systems. The SLDV system was set to measure 30 averages, but due to the

sequential nature of that measurement, the accelerometer DAS could be set to measure many times that number of averages. 200 averages were selected for the accelerometer data acquisition system, which corresponded to measuring approximately seven points using the 3D SLDV. To acquire data, the VXI was first started in preview mode so the gauges would be powered. Then, the SLDV data acquisition process was initiated, which started the shakers. During the SLDV measurement, the VXI would be set to acquire so those data would be measured. After 200 averages, the VXI would stop recording, and some time later (depending on the number of measurement points being scanned) the SLDV system would stop.

1.3.1.2 Laser Alignment

Perhaps the most difficult aspect of the test was the laser alignment. Though the conical test article was not an incredibly costly or programmatically important piece of hardware, throughout this work it was treated as such. It was therefore kept fairly close (about 15 cm) to the chocks from which it was lifted. The chocks were approximately 30 cm (1 ft) tall, which left approximately 45 cm (1.5 ft) between the ground and the test article. To scan the bottom of the test article, it would be necessary to position each of the laser heads such that it could see the bottom of the test article and still maintain the physical separation necessary to get a good 3D measurement. Initially it was thought that the conical test article could be scanned in four quadrants; however, it soon became apparent that six scans would be necessary due to the limited distance between the ground and the test article and the limited field of view of the laser heads. Similarly, it was found that the bungee cords blocked a portion of the test article, which required splitting the top scan into two portions.

Since the bottom scan was judged to be the most difficult, it was attempted first. It became obvious that mirrors would be necessary, so a variety of laser head configurations were attempted (see Fig. 1.4). By using mirrors, one can effectively increase the distance between the test article and the laser head. This is advantageous because it can increase the field of view of the lasers. One limitation was that the mirrors provided in the mirror kit marketed by the SLDV vendor were quite small. This required the laser heads to be very close to the mirrors in order to maintain their field of view, which required the laser heads to be very close to the ground and prohibited the use of the standard tripods to support the laser heads. Laser heads were instead mounted on optical rails which could be set directly on the ground.

Aligning the lasers to the test article required a two-step procedure for each scan. Due to the conical nature of the part, there were not any sharp features on the test article that could be used for alignment. Instead, when space was available, the laser heads were aligned using a separate reference object with known 3D coordinate locations. If there was no space for the reference object, an automatic 3D alignment procedure was used where the operator positions all three laser spots at points defining an origin, an axis, and a plane and the laser system computes the coordinate system from the mirror deflections at each point and the distance to each point from the top laser. This second approach was not as accurate as using the reference object, but it was necessary for some of the tighter setups.

Both alignment procedures aligned the lasers to an arbitrary coordinate system, so some coordinate transformation was required to bring the laser heads into the part coordinate system and allow the measurements to be stitched together. Sixteen alignment points were drawn on the test article in two axial stations. The first station was approximately 4 cm (1.6 in) aft of the joint in the body, and the second station at the aft end of the test article. These points were drawn before the test article was set up, and therefore some oversight was made in their positioning. The aft alignment points were blocked by the shakers and the chocks, and were therefore only visible from one of the scan directions. The forward alignment points were sufficient for the alignment, but because they were all positioned in the same plane, small errors in their positioning would result in relatively large rotational alignment errors. This can be seen in a plot of the computed measurement points, shown in

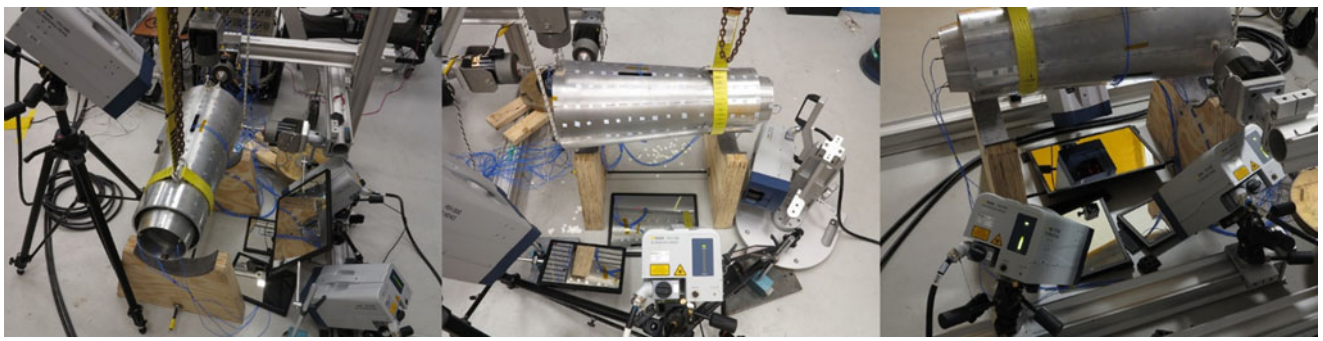

Fig. 1.4 Various attempts to measure the bottom quadrant of the conical test article

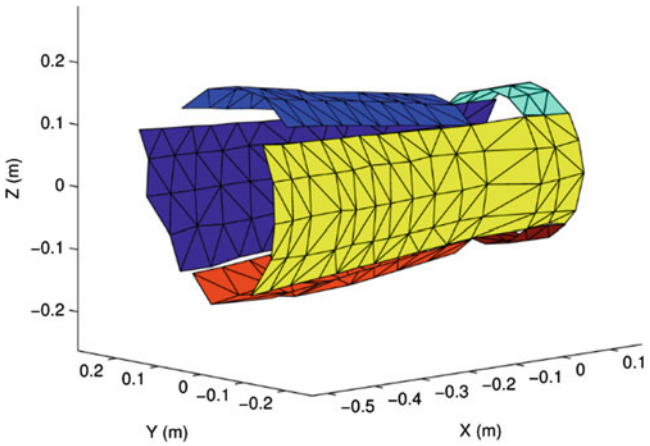

Fig. 1.5 Measurement point positions computed by the SLDV software. Points on the scan boundaries should be nominally coincident, but are seen to be rotated due to sensitivity of the geometry to alignment errors

Fig. 1.5. Points on the boundaries of each of the scan areas (differentiated by color in Fig. 1.5) should nominally be coincident, but because only the front alignment points were used for the majority of the scan positions, the gap between the nominally coincident points grows larger towards the aft end of the structure. After the coordinate transformation, the effective positions of the laser heads (i.e. the positions of the laser heads reflected through the mirrors) could then be extracted from the SLDV software for each scan, and these are shown in Fig. 1.6.

1.3.1.3 Data Analysis

In this test, data came from two separate DASs: SLDV and VXI. Additionally, the laser data consisted of six separate scans. All of this data had to be combined into a suitable format for modal analysis using the chosen Synthesize Modes and Correlate (SMAC) [2] algorithm. The laser data were combined using the SLDV software. A combined file was created from all of the separate scan files and exported to MATLAB for analysis.

The data from all internal gauges were measured each time a laser scan took place. Since the same channels were measured each time, the data should be nominally identical. This observation was used to gauge data consistency between laser scans; because a large amount of time might elapse between laser scans due to alignment difficulties, the bungee cord boundary conditions could sag and the shaker stingers could potentially be cross-loaded causing shifts in the natural frequencies. This was seen early in the testing before the bungee cords had significantly relaxed, and is shown in Fig. 1.7.

After the bungee sag issue was discovered, the stingers were re-aligned after each scan to ensure consistent data. The internal data from each of the separate scans were then averaged into one set of FRFs and combined with the laser data to perform mode fitting. Fifty-three modes were extracted below 4000 Hz, many of which were ovaling modes of the case. However, these could be easily identified due to the relatively high resolution of measurement points on the case. The MAC matrix for this test was very good, with only two off-diagonal entries greater than 0.3, and the vast majority of the off-diagonals below 0.1.

1.3.1.4 Lessons Learned from the Conical Test Article

The empty bomb case is significantly longer than the conical structure, so portions of the test that were tedious or labor-intensive would be even more so when applied to that structure. The testing strategies applied to the conical article were therefore evaluated before the empty bomb case was tested.

The optical rail shaker supports provided a very small footprint and did not significantly block line-of-sight to the test article, so this strategy was thought to be adequate for the empty bomb case.

In the conical test, the 3D SLDV system was able to scan about 90° of the test article at a time. This will be the goal of the empty bomb case test as well. However, there were some issues with the choice of quadrants used for the conical test article. For that test, the quadrants were chosen primarily due to the difficulty in setting up the bottom scan as described in Sect. 1.3.1.2. This required the alignment of three mirrors, one for each laser head, to enable each laser to scan as much

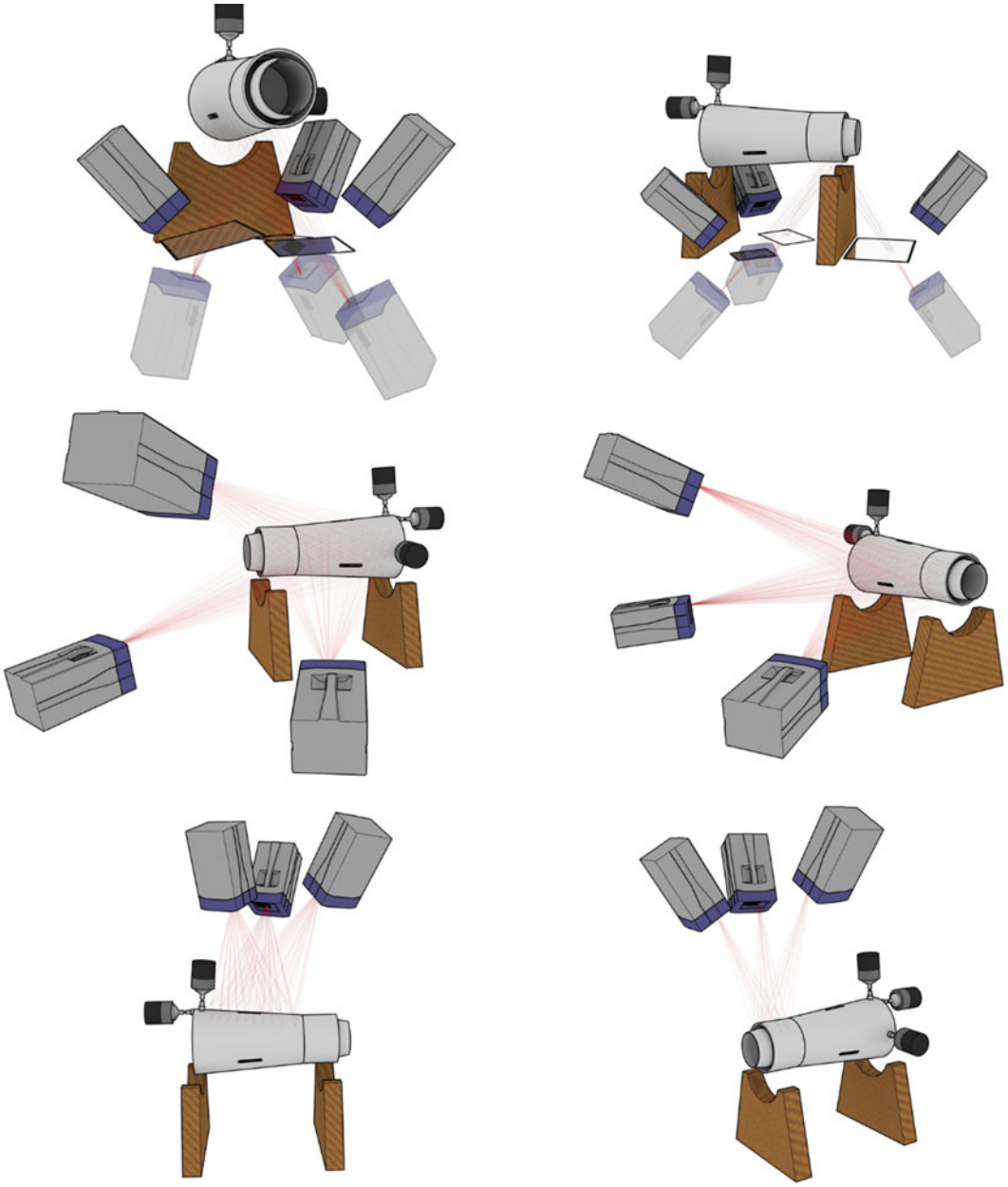

Fig. 1.6 Laser head positions for the various scans of the conical test article. The transparent laser heads in the figure show the effective position after being reflected across the mirror

of the bottom side of the test article as possible. It was originally thought for the conical test article that performing just one "bottom" scan would be the best approach. However, it was found as testing proceeded that bungee cords, dangling accelerometer cables, and shakers were located directly in the middle of the quadrants, and it was difficult to scan around these obstructions.

An alternative approach would be to shift the measured quadrants by 45°, positioning the bungee cords, dangling accelerometer cables, and shakers at the boundaries of the quadrants rather than in the middle. These approaches were investigated during the conical test (the first two frames of Fig. 1.4 show two such setups). The disadvantage to this approach (and the reason it was not used during the conical structure test) is that the test setup still required aligning three mirrors, one for each laser head, only now there were twice as many "bottom" quadrants to scan, so the effort for this approach is effectively doubled. Therefore, a strategy for efficiently orienting the laser heads and mirrors would be necessary in order to make this approach worthwhile.

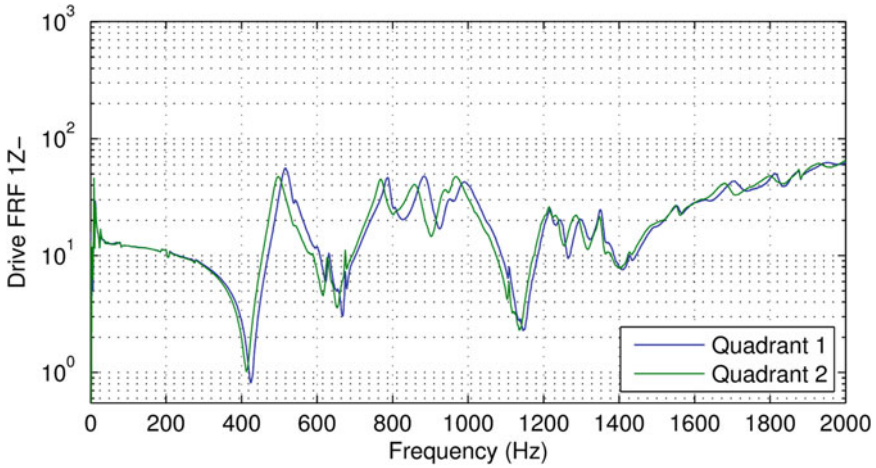

Fig. 1.7 Shifting peaks in the drive point FRFs between two scans

Fig. 1.8 Photograph (*left*) and schematic (*right*) of the laser cart used to scan the bottom quadrants of the empty bomb case. The schematic shows the effective position of the mirrored laser head

Performing the alignment, especially through mirrors, can be a labor-intensive part of any 3D SLDV measurement. However, if the test article moves with respect to the laser heads and the effective positions of the laser heads remain constant with respect to one another, then the laser head positions can be updated in the software using a simple coordinate transformation. This can save a significant amount of time when a large number of scans are needed. The goal then is to devise a system where the laser heads and any mirrors can be moved and positioned as one rigid body. The SLDV vendor markets a wheeled stand that holds all three laser heads just for this purpose, but this stand is quite large and does not incorporate mirrors. Instead, a cart was made from 95 mm optical rails. Several design iterations were evaluated: the key flaws discovered in early designs were a cart that was too big so it interfered with shaker supports as well as a cart with four "feet" so an uneven floor would warp the cart and misalign the lasers. The final design is shown in Fig. 1.8.

The laser cart was immensely useful for measuring the bottom of the empty bomb case; a single 3D alignment could be performed, then all the bottom sections could be measured. Only a coordinate system transformation was required between each scan. The coordinate system transformation requires alignment points at which the (x,y,z) coordinates were known, and since the conical structure test revealed that an insufficient number of these alignment points could lead to significant errors in geometry, a grid of alignment points was drawn every 15 cm (6 in) and 45°. This ensured that approximately 20 alignment points would be visible for each scan.

Finally, it was recognized that there was not an efficient way to produce documentation for large laser scans. This documentation should provide information about the alignment accuracy, measurement point locations, and other data acquisition parameters that would be useful in evaluating a test, and collecting all of this data manually would be very tedious, especially for a large number of scans. Thankfully, the SLDV software provides a programming interface from

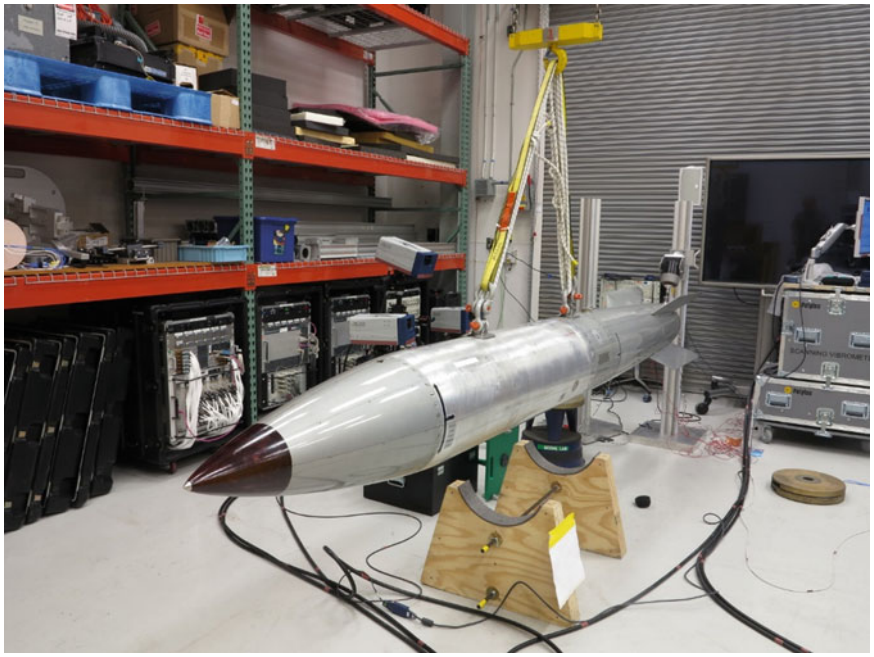

Fig. 1.9 Empty bomb case

which much of this information can be extracted, so a script was written to traverse the output from the laser scan and produce a report that contained data, images, and test information.

1.3.2 Empty Bomb Case Modal Test

With the improvements from the conical structure test implemented, the empty bomb case testing was initiated. The test article was suspended from an overhead crane using bungee cords to provide a soft support approximating a free boundary condition. The test article is shown in Fig. 1.9. Because the laser cart required more space below the test article, the existing chocks could not be used as a safety catch, though they were kept below the test article regardless. Instead, two slings were attached loosely to the test article to serve as a safety catch in case the bungee cords were to fail. Due to the large number of measurement points anticipated in this test, no surface preparation was applied to the test article.

1.3.2.1 Data Acquisition Setup

The setup for the SLDV DAS was similar to that of the conical structure modal test. One important distinction is that the frequency content of the white noise signal that was applied to the shakers was cut off below 10 Hz. The low frequency content below 10 Hz induced rigid body motion in the structure, and while this motion was small it significantly increased the amount of noise in the laser measurements.

1.3.2.2 Laser Alignment

For this test, 17 scans were used to measure the entire test article. Each scan was able to view approximately 60 cm (2 ft) axially and 90° circumferentially of the surface of the test article. The surface of the structure visible to the laser vibrometer in each of the scans is shown in Fig. 1.10. The effective laser head positions for all of the scans are shown in Fig. 1.11.

For the bottom scans, the lasers were mounted in the cart shown in Fig. 1.8, and an alignment was performed using a reference object. The laser cart was then moved into position beside the test article, and measurement points were placed at

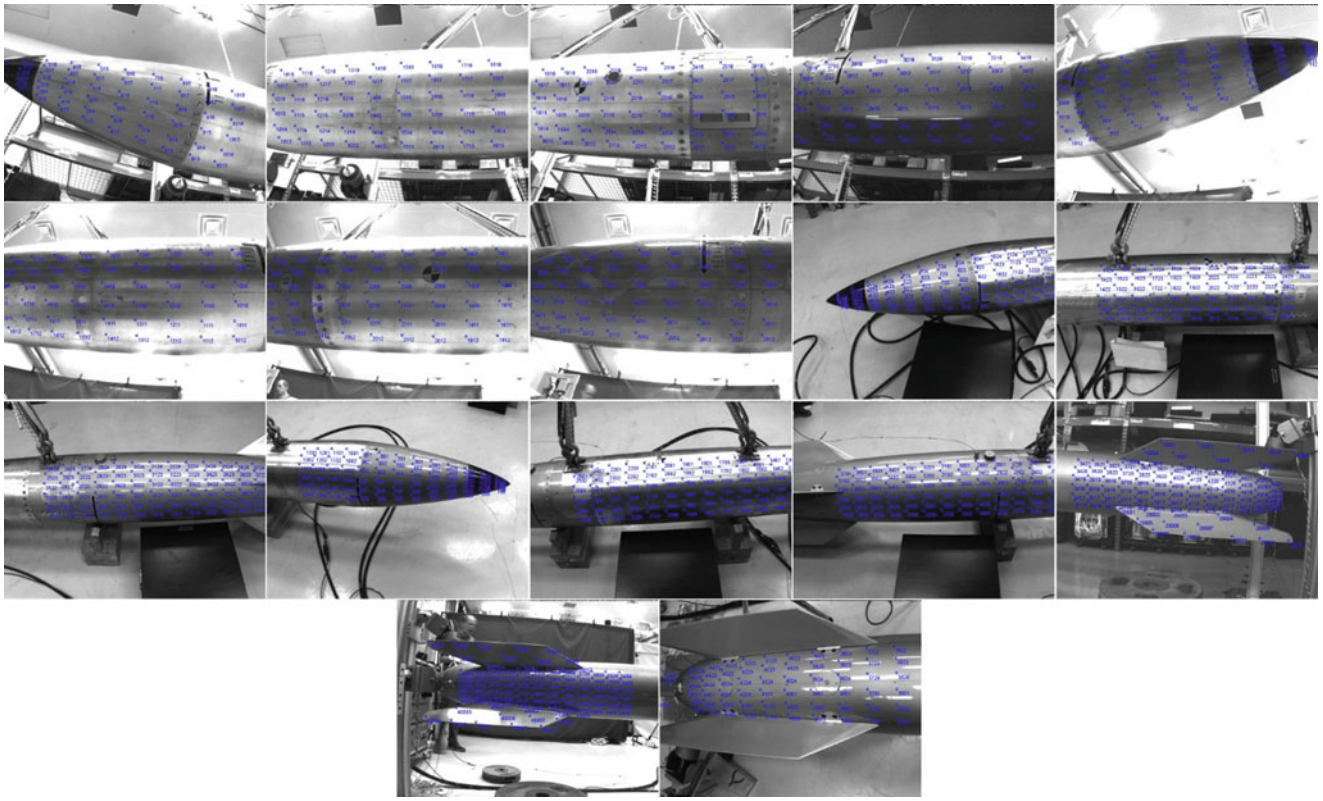

Fig. 1.10 Portion of the test article visible for each scan

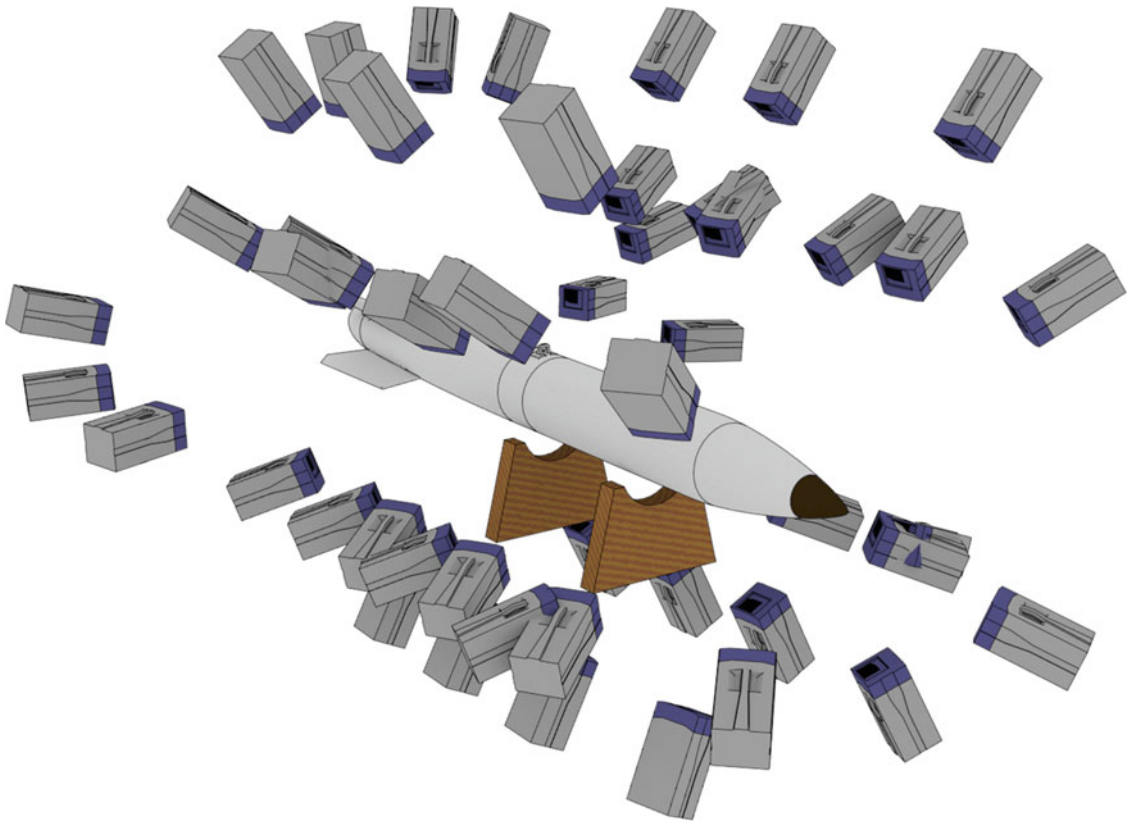

Fig. 1.11 All effective laser head positions for measuring the empty bomb case

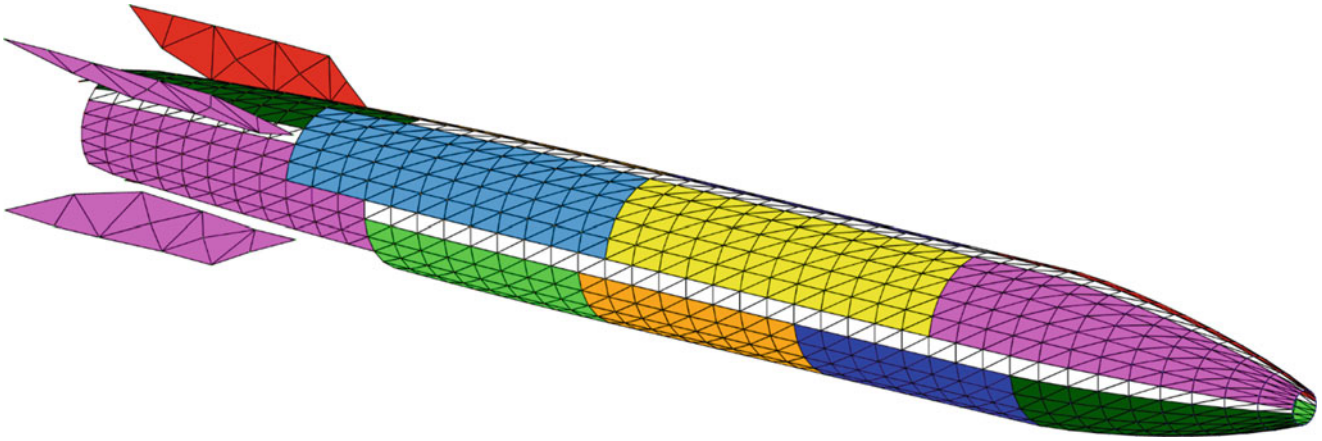

Fig. 1.12 Geometry showing the 1075 measurement point locations colored per scan. *White* elements denote the space between scan patches

5–10 alignment points. A coordinate system transformation was then computed by the SLDV software using the locations of the alignment points in the current coordinate system and the locations in the part coordinate system. This process allowed efficient re-alignment of the laser heads and mirrors with the test article for each scan.

For the top scans, the lasers were arranged on tripods; therefore, the two step alignment-and-transform procedure described in Sect. 1.3.1.2 was followed for those scans. In hindsight it would have been prudent to build a second stand from the 95-mm optical rails in order to bypass the alignment portion as was done for the bottom scans.

A large number of measurement points were to be scanned for this test, so the most efficient way to define them in the laser software was to import the measurement points from an external geometry file. These points then needed to be reduced for each scan to those points within the lasers' field of view and on the side facing the laser heads. Points were also removed if the angle of incidence between any of the laser beams and the surface were too high. Figure 1.12 shows the measurement geometry color-coded by scan.

Even with the efficient bottom alignment strategy, this test was long running due to the sequential scanning of over 1000 points as well as labor-intensive setting up and aligning the lasers for all of the scans. Testing was performed over 5 days, so it would be very difficult to go back and retake data if some data acquisition parameter needed to be changed (e.g. forgetting to apply a window, bandwidth too low, etc.). This is contrary to testing with a large number of accelerometers where once the gauges are adhered to the surface data can be taken and retaken rather easily if there are enough channels available.

1.3.2.3 Data Analysis

Similarly to the conical structure test, the laser data was collected into a single scan file and exported to analyze in MATLAB. Over 6000 FRFs were measured by the laser system, accounting for the over 1000 scan points, two shaker inputs, and three measurement directions per point. It became clear when performing this analysis that the SMAC algorithm began to struggle with a data set of this size. When all 6000+ FRFs were included in the SMAC analysis, the correlation coefficient—a key parameter indicating the presence of a mode in the SMAC algorithm—was approximately unity for the entire bandwidth. Essentially, SMAC was identifying a mode at every frequency line. When the set of FRFs was reduced by only keeping one of every 5 or 25 measurement points, the correlation coefficient began to look more reasonable, as shown in Fig. 1.13. The frequency and damping parameters extracted from the reduced analysis could then be imported into a full analysis to extract the full mode shapes. Extracted mode shapes were somewhat noisy which is attributed to the large angle of incidence and relatively poor surface properties of the test article, especially on the darker surface near the tip of the nose. Two example mode shapes are shown in Fig. 1.14.

1.4 Lessons Learned and Lingering Deficiencies

A number of lessons were learned from the testing of the two test articles described in this report. Large, complex test articles will often require multiple scans to measure all parts of the test article, so developing an efficient method of repositioning the laser head is likely the most important step to making SLDV measurements of large structures practical. Because multiple

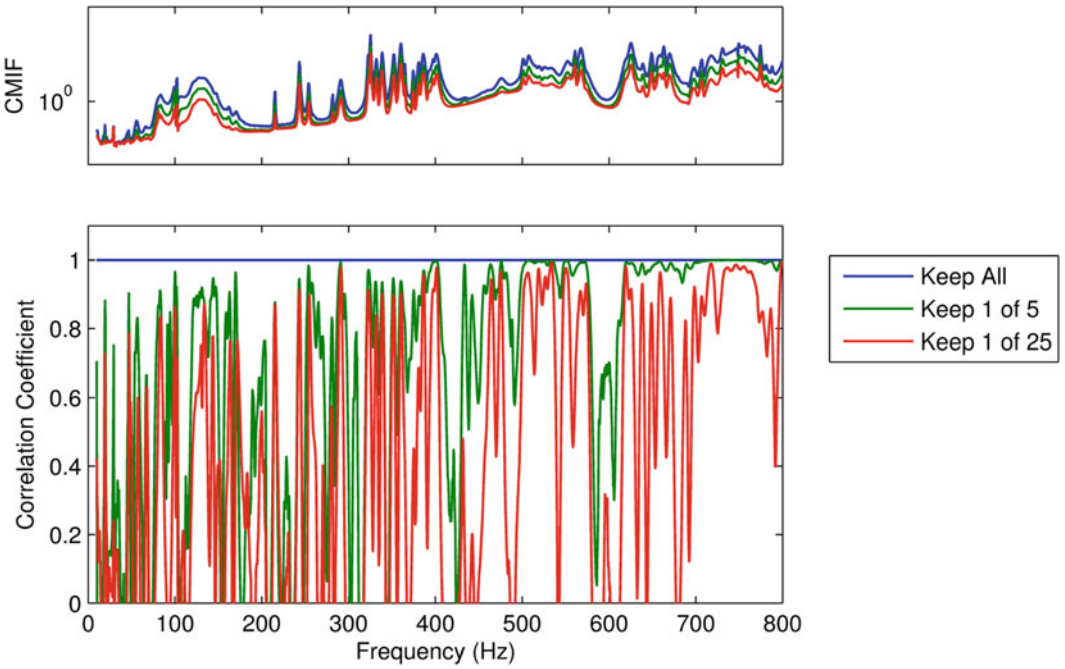

Fig. 1.13 Complex Mode Indicator Function (CMIF) and the SMAC correlation coefficient based on number of points kept in the analysis

scans will need to be stitched together into one coherent model, a sufficient number of alignment points need to be available; in many cases it may be advisable to define and mark these as a preliminary step in test setup. Simultaneous excitation from multiple input locations is also an excellent way to decrease the amount of time spent scanning a test article.

Utilizing mirrors proved to be an excellent way to allow the laser heads to be positioned farther from the test article. However, because the test articles in this effort were quite large, the mirrors marketed by the SLDV vendor were found to be too small to gain the full benefit; the field of view is artificially limited unless the laser heads were quite close to the mirrors. This reduced the measurable surface to approximately 60 cm (2 ft) along the length of the test article and drove the number of scans required. Since this work was performed, two larger first-surface mirrors have been acquired which should allow larger scan areas.

The laser cart allowed the laser heads and mirrors to be moved as one rigid body, and this greatly simplified the alignment procedure for this test. However, even with the refined alignment procedure, this test still required a large amount of time to perform. Because of the sequential nature of the SLDV it is imperative when performing such a test that all test setup and data acquisition parameters be correct the first time, because repeating such a test due to some simple oversight in test setup (for example if the shaker stinger were misaligned) would be particularly painful. Accelerometer testing can be labor intensive when a large number of gauges must be adhered to the test article, but that labor is not wasted if the test needs to be repeated for any reason. With SLDV testing, the labor of aligning the laser heads multiple times would need to be repeated if the test needed to be redone.

Surface preparation using retroreflective tape can be used to increase the signal returning to the laser head, which can reduce the measurement noise. For the conical structure, retroreflective tape was applied at all measurement points. However, for the 1000+ measurement points on the empty bomb case, it was thought that the application of that much retroreflective tape would require a prohibitive amount of time. Spray-on retroreflective beads were attempted as an easier-to-apply alternative to tape, but this technique was not met with much success. The beads would drip down the test article before the solution could dry, leaving clumps of beads in some locations with very few beads over the majority of the area.

Many curve fitters and modal software were designed to handle a "reasonable" number of FRFs. As techniques such as DIC and SLDV become more standard in the modal testing community, it may be necessary to revisit these tools to make sure they are sufficiently capable in dealing with the large amount of data that can arise from these techniques. The SMAC algorithm, for example, struggled to identify modes when too many FRFs were used. This was easy enough to work around by reducing the number of functions supplied to the curve fitter, extracting the natural frequencies and damping ratios extracted from that analysis, and importing those modal parameters into an analysis of all of the FRFs.

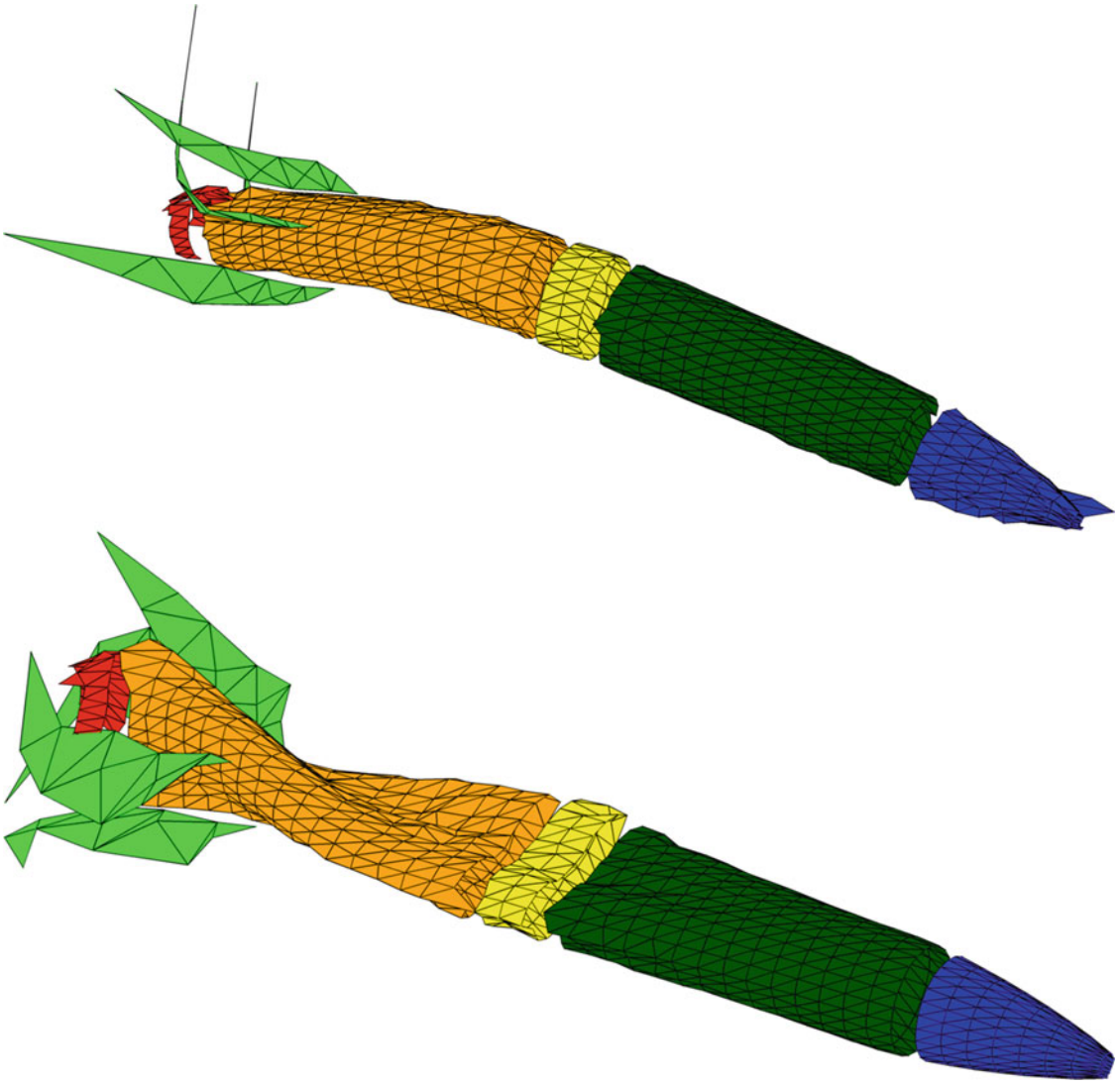

Fig. 1.14 Example mode shapes of the empty bomb case. Some points are noisy, particularly near the tip of the nose where the angles of incidence of the laser beams to the part were the highest and where the surface was darkest

1.5 Conclusions

Two case studies were performed to determine the feasibility of using a 3D SDLV to measure a large aerospace structure with fine measurement point resolution. The alignment procedure to measure a large number of points on a long cylindrical test article was very labor-intensive. If there is no explicit reason to measure a large number of measurement points for the test, it is feasible that more traditional methods using accelerometers could be more appropriate. However, if a large number of data points are required, it may be difficult to acquire a data acquisition system that could measure that many accelerometer channels simultaneously. In such scenarios, SLDV may be an attractive option. Compared to roving hammer testing, the 3D SLDV system is quicker, more precise, and perhaps most importantly it can additionally measure directions tangent to the surface rather than just perpendicular.

References

1. Castellini, P., Martarelli, M., Tomasini, E.P.: Laser Doppler vibrometry: development of advanced solutions answering to technology's needs. Mech. Syst. Sig. Process. **20**(6), 1265–1285 (2006)
2. Hensley, D.P., Mayes, R.L.: Extending SMAC to Multiple References. In: Proceedings of the 24th International Modal Analysis Conference, pp. 220–230 (February 2006)

Chapter 2
Modal Model Validation Using 3D SLDV, Geometry Scanning and FEM of a Multi-Purpose Drone Propeller Blade

Daniel J. Alarcón, Karthik Raja Sampathkumar, Kamenzky Paeschke, Tarun Teja Mallareddy, Sven Angermann, Andreas Frahm, Wolfgang Rüther-Kindel, and Peter Blaschke

Abstract The ATISS (Autonomous Flying Testbed for Integrated Sensor Systems) is a measurement unmanned aircraft vehicle—commonly known simply as "drone". The ATISS is a multi-purpose sensor carrier drone used for professional aerial photography, aerial surveying, air pollution measurements, etc., propelled by two carbon fiber propellers.

The kinetic energy of these propellers can excite undesired vibration modes on these blades and excite the drone structure unless a careful design is chosen. Generally, a detailed modelling of the vibrational characteristics is needed for any aerospace component; for the successful correlation and validation of these models through experimental vibration testing. However, lightweight, innovative composite components such as carbon fiber propellers pose challenges on this validation cycle. Material non-linearities and non-proportional damping responses are inherent to composite materials and therefore, a further degree of precision on the testing and simulation is necessary for the successful validation of these components.

The experimental modal analysis is performed by the combination of a 3D Scanning Laser Doppler Vibrometer and a scalable automatic modal hammer. The geometry used for the FE simulation is obtained by means of a 3D geometry scanner, a high resolution-digitalization is carried out on the tested rotor blade surface. The obtained points are reverse-engineered in a CAD model and imported into the FEA software. A further validation of the FE modal model would prove the successful implementation of these techniques on the study of the vibrational modes of composite lightweight structures.

Keywords Experimental modal analysis • 3D SLDV • Composite material • FEA validation • Reverse engineering

Abbreviations

ATISS Autonomous Flying Testbed for Integrated Sensor Systems
CAD Computed-Aided Design
DOF Degree(s) of Freedom
EMA Experimental Modal Analysis
FEA Finite Elements Analysis
FRF Frequency Response Function
IGES Initial Graphics Exchange Specification
LDV Laser Doppler Vibrometry
NVH Noise, Vibration, Harshness
SAM Scalable Automatic Modal Hammer

2.1 Introduction and Motivation

The ATISS (Autonomous Flying Testbed for Integrated Sensor Systems) is an unmanned aircraft vehicle, also known as drone, based on a modular concept; designed, engineered, manufactured and tested at the Technical University for Applied Sciences Wildau (Fig. 2.1). The ATISS is designed as a motor glider and intended as a multi-purpose sensor carrier, which

D.J. Alarcón (✉) • K.R. Sampathkumar • K. Paeschke • T.T. Mallareddy • P. Blaschke
Laboratory for Machine Dynamics and NVH, Technical University of Applied Sciences Wildau, Hochschulring 1, 15745, Wildau, Germany
e-mail: daniel.alarcon@th-wildau.de

S. Angermann • A. Frahm • W. Rüther-Kindel
Institute for Aeronautical Engineering, Technical University of Applied Sciences Wildau, Hochschulring 1, 15745, Wildau, Germany

D. Di Maio, P. Castellini (eds.), *Rotating Machinery, Hybrid Test Methods, Vibro-Acoustics & Laser Vibrometry, Volume 8*,
Conference Proceedings of the Society for Experimental Mechanics Series, DOI 10.1007/978-3-319-54648-3_2

Fig. 2.1 The ATISS drone with the *red* painted payload container between the rotors. It has a wingspan of about 5 m and an empty weight of 15 kg

Fig. 2.2 Manufacturing process of the propeller blade used on this study

allows its deployment in a variety of cases: professional aerial photography, aerial surveying, the generation of 3D terrain models and air pollution measurements. In the current project SAPODS (Smart Airborne Pollutants Detection System) the ATISS is intended to fly through volcanic ash clouds in order to measure the concentration and composition of air pollutants [1]. With a wingspan of about 5 m and a basic or empty weight of 15 kg, the ATISS drone is capable of carrying payloads of more than 10 kg. Driven by two brushless electric motors with 2.5 kW power each, two especially designed folding carbon propellers and two Lithium-Polymer batteries, the ATISS can fly for more than 60 min without gliding.

The propeller analyzed on this paper is part of a bi-propeller rotor. The other propeller and the joint in between are not analyzed on this study for simplicity reasons. The ATISS propellers were designed to be folded if necessary, improving the gliding properties of the drone. Only one twin-shell negative mold was used for the manufacturing of both propellers. These were manufactured in the negative mold shown in Fig. 2.2 using carbon-fiber and epoxy resin.

The propeller blades of the ATISS work therefore at very high rotational speeds for long periods of time. The kinetic energy of this rotation can excite undesired vibration modes on these blades and excite in turn the drone structure unless a careful design is chosen. Consequently, the data gathered by the integrated sensors could be distorted by excessive resonance on the drone structure. One clear example of resonance-induced problems is the wobbling in aerial videography recordings, also known as “jello effect”, a well-known problem among hobbyists and aerial videography aficionados. The resonance of the propellers at certain rotation regimes is transferred to the drone body and to the camera as a result, rendering the recordings unusable [2]. Several home-made techniques have been developed in order to balance the drone propellers. Nevertheless these procedures are not as immediate or as straightforward in a fast-growing large-scale drone industry and in applications where excessive vibration at undesired regimes/frequencies can impact the data recorded by very sensitive transducers and the integrity of the propeller blades.

Generally, these vibrational problems, both at small scale (for drones) and large scale (i.e. for gas turbine blades) require for their analysis a detailed Finite Element Analysis (FEA) modelling of their vibrational characteristics. The aerospace and automotive NVH industries have developed and improved cycles of correlation and validation during the last years by updating the parameters of the FEA models with experimental vibrational data usually derived from experimental modal analysis (EMA). This procedure is widely known as “modal updating”, and it is still hindered by several challenges nowadays. For example, the use of lightweight innovative composite materials is constantly growing in the aerospace industry [3] but components made of this kind of materials present difficulties on this correlation and validation cycle [4]. Material non-linearities, anisotropy, non-proportional force/response curves, etc., are inherent to composite materials—such as the composite of carbon fiber and epoxy resin used on the propeller analyzed on this study.

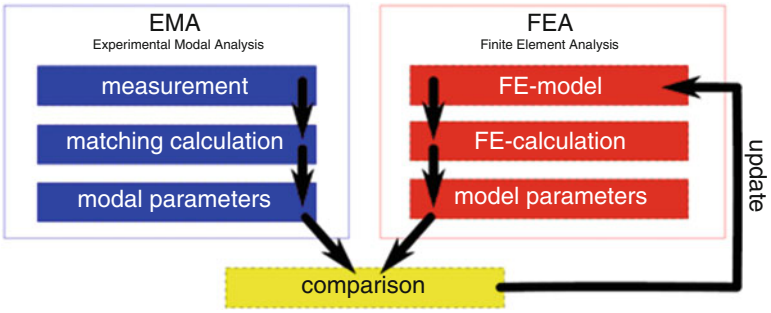

Fig. 2.3 Continuous correlation cycle for the validation of modal models proposed in [5]

A solution for this problem is a continuous correlation cycle between FEA modal models and experimental modal data, proposed already by [5–7] among others (Fig. 2.3). Experimental data can be collected in a variety of means, being experimental modal analysis of wide application in the industry. During the recent years, the world of vibration testing has undergone many changes that allow nowadays a proper data collection that makes this continuous validation process feasible.

Non-contacting response measurement techniques, such as Laser Doppler Vibrometry (LDV) are of common use on its single-point or scanning variants. LDV is nowadays the standard method for the acquisition of output signals on EMA due to its versatility, accuracy, reduction of the testing time, and the fact that the tested system is free of mass loading effects. The advantages of this method have been widely described in [8, 9] to name a few. In the case of this paper, this system offers an extra advantage: while only flap (out-of-plane) modes can be investigated with 1-point and SLDV techniques, the edgewise (in-plane), simultaneous vibrational components of these modes can be investigated only through the application of 3D SLDV. These edgewise modes need to be evaluated for a good correlation, as they appear on the FEA modal models.

A high degree of adjustability and repeatability on the excitation is needed on the modal testing of non-linear materials, as their mechanical properties depend on non-proportional force/response ratios [10]. Several excitation techniques are applied in the industry, each one with its advantages and drawbacks: semi-automatic modal hammers, electrodynamic/piezoelectric shakers and shaker-based, non-contact magnetic exciters. The automatic alternatives currently available in the market fail to allow a fine-tuned and truly repeatable impacting force adjustment while making no changes in the tested structure. In most cases, the experimental repeatability will be an issue due to the fact that the human factor is not fully eliminated during the hammer positioning and force adjustment or re-adjustment throughout the measurement. Other techniques such as electrodynamic and piezoelectric shakers have a series of drawbacks described in [10], they not specified on this paper for brevity. For this reason, the Scalable Automatic Modal Hammer (SAM) is later introduced.

Leaving the experimental techniques aside, computational models can be also a source of error. Models used for the correlation are typically exported from the CAD software used on the design phase of that component. These CAD models, if available, are ideal; and tend to not faithfully represent the real component in terms of surface and dimensional tolerances, or due to limitations on their manufacturing process. There might be cases where the CAD model is not available for the studied part, i.e., when reverse-engineering a product from a competitor. This paper proposes generating these FE models via 3D geometry scanning. The 3D geometry scanner used for this study, property of the Laboratory for Machine Dynamics and NVH at the TUAS Wildau, is capable of digitalizing any kind of surface with a tolerance of around ± 10 µm. In theory, small manufacturing defects, holes, or wear marks can be incorporated to a faithful model, which can be later imported in the FEA software for its further processing, as described in [11].

The aim of this work is threefold: (1) demonstrating that a precise modal test, at a single point of the non-linear force/response curve can be achieved in complex structures, such a drone propeller blade, through the full automatization of a modal test by combining automatic modal excitation with a 3D SLDV system; (2) showing that, in the studied case, a FE surface model obtained by means of 3D geometry scanning can replace an unavailable CAD model on a FE simulation, and (3) proving that an acceptable degree of correlation on the modal model generated in FEA is possible by means of the joint work of the devices described in the next chapters.

2.2 Materials and Methods: Experimental Modal Analysis

The experimental leg of this correlation cycle consisted on performing a modal test on the propeller blade. The experimental setup is shown in Fig. 2.4, built inside the hemi-anechoic chamber at the TUAS Wildau. A workbench clamp was used to constrain the propeller at its pinhole in order to imitate real constraints (Fig. 2.4, left). This fixture was, at its time, rigidly

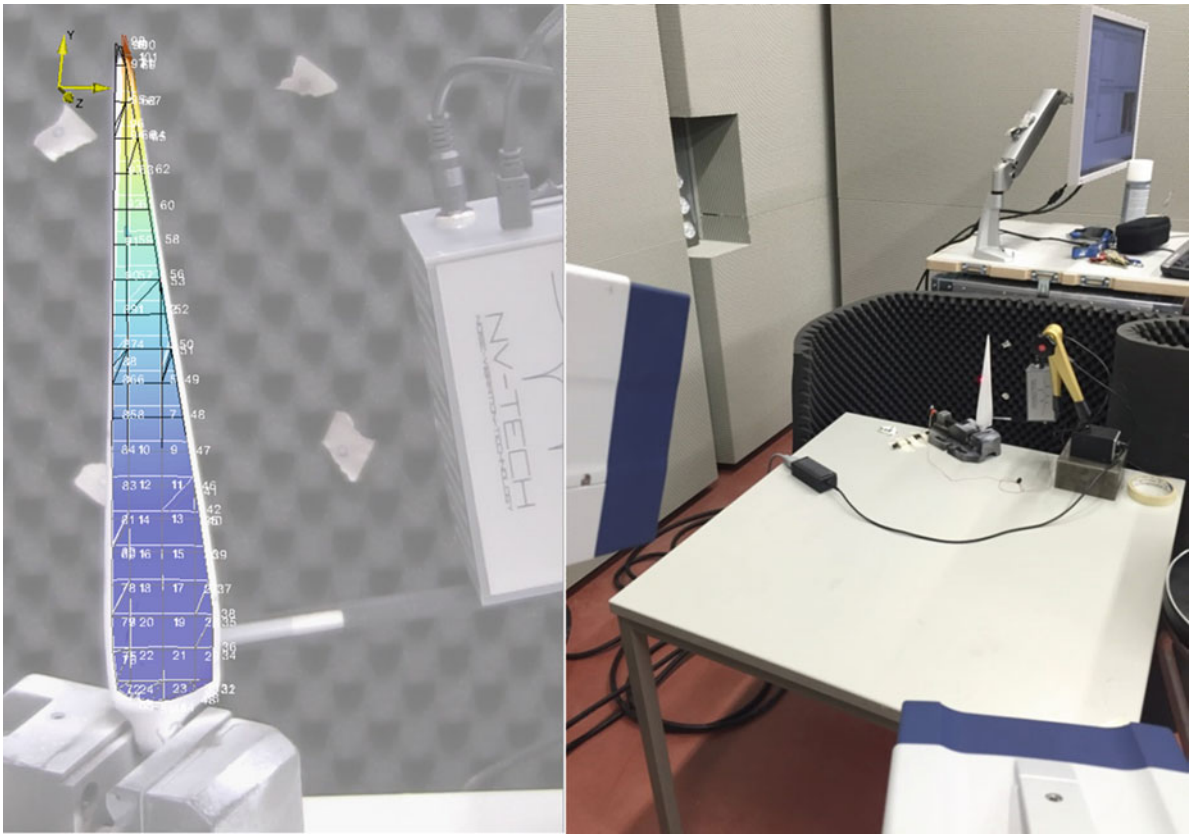

Fig. 2.4 *Left*—Clamping of the propeller blade and SAM impact position. 101 DOFs were used for this modal analysis. *Right*—Experimental setup for this test. A large angle between scanning laser heads was needed in order to better acquire the in-plane vibration components

fixed to the testing surface with help of a set of parallel clamps. The propeller blade was excited at its pressure surface [12], at the height of the degree of freedom (DOF) number 21 (Fig. 2.4, left) with a Scalable Automatic Modal Hammer (SAM) (NV-TECH, Steinheim a.d. Murr, Germany), presented in [13]. The response signal was measured by means of a 3D SLDV system model PSV-500-3D-H (Polytec GmbH, Waldbronn, Germany), property of the Laboratory for Machine Dynamics and NVH at the TUAS Wildau. The tested propeller was uniformly sprayed before the measurement with a non-aqueous white color developer (ARDROX 9D1B, Chemetall GmbH, Frankfurt a.M., Germany) to improve the laser beams reflectivity. A mesh with 101 DOFs (Fig. 2.4, left) was chosen to better display the mode shapes at higher frequency ranges and thus better to observe the local in-plane phenomena occurring in some out-of-plane modes; while keeping a relatively low testing time. A large number of these DOFs were placed directly at the trailing edge of the propeller, where a large amount of local motion occurs.

The excitation force was provided in this modal test by the aforementioned SAM, as seen on Fig. 2.4. The sensor tip applied on this case was a model 086E80 (PCB Piezotronics, Inc., Depew, NY, USA), assembled on a small stepper motor. The rotation movement and its velocity are digitally controlled via the stepper motor software and transmitted to the motor via USB. This fact allows a very fine rotation tuning. For this experiment, a resolution of $\pm 0.45°$ per step proved to be precise enough. Without the SAM, the testing time for a large number of DOFs would be of several hours and difficulties related with operator fatigue would arise.

By using the PSV Scanning Vibrometer Software form Polytec GmbH for the data acquisition, the sampling frequency was set at 24.6 kHz, which resulted in an effective bandwidth of 10 kHz. With 12,800 FFT lines, the measurement resolution is of 0.78 Hz and thus, each measurement block was 1.28 s long. No function windows or signal overlap were applied to avoid distorting the time input and output signals in any way. The laser velocity range was fixed at 100 mm/s/V with a fast tracking filter. It was already known beforehand that some DOFs close to the propeller tip are very compliant, and they would present velocity peaks higher than 100 mm/s/V. For this reason, the software options regarding laser auto-ranging and the re-measurement of DOFs out of velocity range were set to on.

For this experimental setup, the SAM was set with an inward acceleration of 1000 microsteps/s^2 and 90 microsteps rotation (this is, approximately, 5° between the hammer tip at its starting position and the impact point at the propeller). This

resulted in an impact force of 10 N in this case. The waiting time in-between impacts is set at 2 s, which is more than enough time to let the propeller freely vibrate until its motion completely fades out, and a higher value than the measurement time block. A positive slope pre-trigger of 1% of the input power threshold and starting at 5% of the measurement time are set on the input signal. Three averages were demonstrated enough to achieve satisfactory results with the SAM with an acceptable degree of coherence.

FFT data has been analyzed with the program PSV after the measurements data and a generally damped SDOF curve-fitting was performed on the obtained Frequency Response Functions (FRFs) in order to extract the modal parameters with vModal (Maul-Theet GmbH, Berlin, Germany).

2.3 Materials and Methods: Geometry Scanning, Reverse Engineering and FE Simulation

The analytical part of this correlation cycle consisted on several different operations, carried out by combining different software packages.

The first step was scanning the entire propeller surface, up to the pinhole, with an ATOS Triple Scan II (GOM mbh; Braunschweig, Germany) 3D geometry scanner. The propeller was constrained with the same clamp shown in Fig. 2.3 and fixed to a turntable. The working principle of this kind of geometry scanner is not described here for brevity, but can be consulted in [11] among other works. The software ATOS Professional, by the same manufacturer, was used to collect 39 geometry scans from different angles and process them together to generate a triangulated point cloud (Fig. 2.5). Further operations were carried out by the program to repair small holes and seams in the triangulated grid, typical of scans in complex geometries with hard edges.

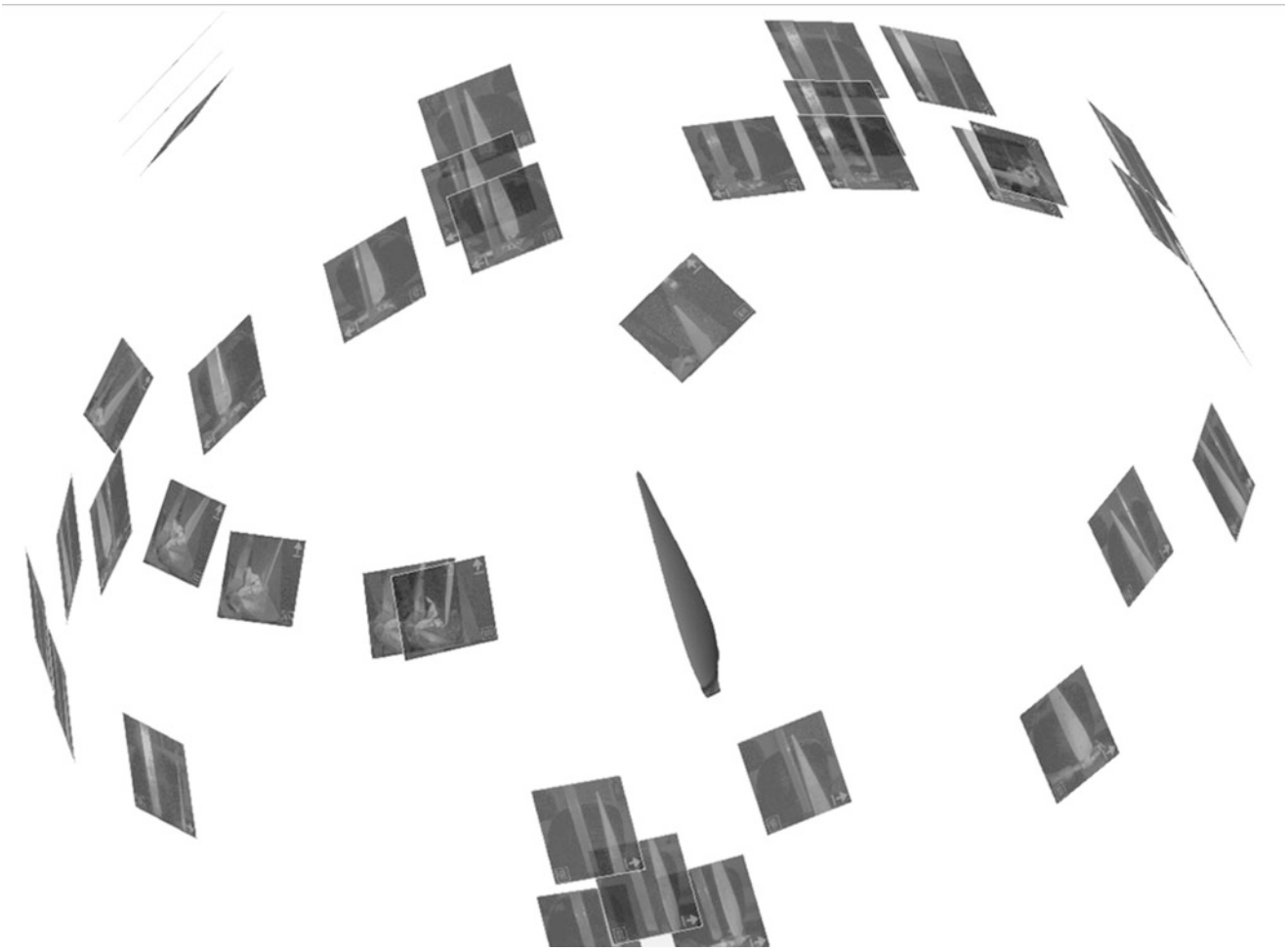

Fig. 2.5 Idealized display of the 39 geometry scans used for the generation of the triangulated points cloud. The blade was clamped to a turntable, which allowed the rotation of the propeller blade for its scan

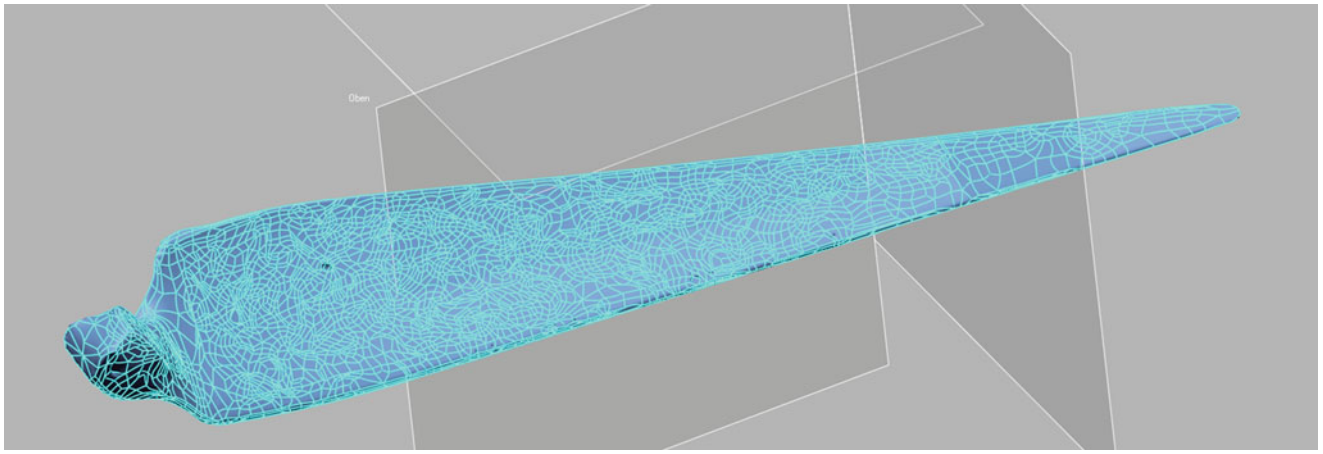

Fig. 2.6 Segmented points cloud after the automatic surface estimation with Geomagic Design X. Note that some of the propeller blade defects are segmented, increasing in exchange the computing time for this procedure

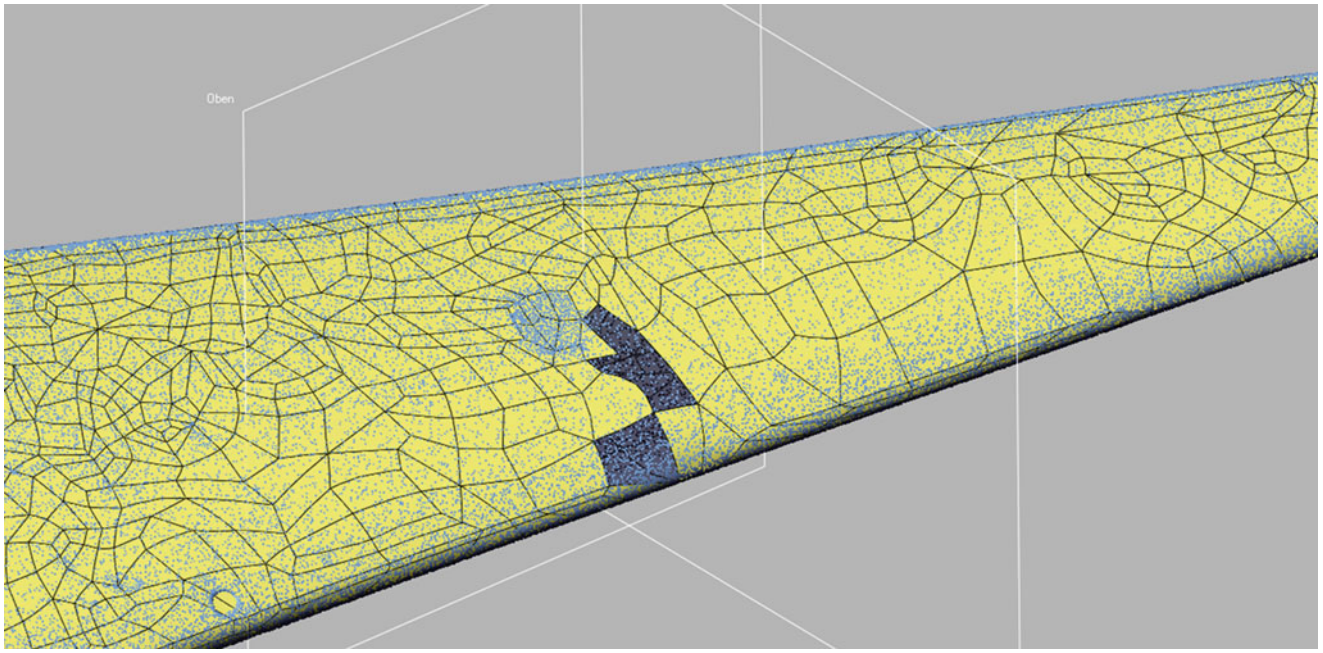

Fig. 2.7 Example of failed surfacing at Geomagic Design X. This defect is later successfully repaired in ANSYS DesignModeler

The triangulated points cloud was subsequently imported as a STL file in Geomagic Design X software (3D Systems, Rock Hill, SC, USA) and further processed to repair failed triangles or incoherent geometries. The repair process yielded a points cloud of about 1.5 million points, resulting in 3 million triangles. According to the software workflow, contour curves were generated on the geometry, with a curvature sensibility of 100% and a minimum surfacing of 2 mm^2. The software was allowed to automatically estimate the number of segments in which to divide the points cloud to obtain a faithful surfacing (Fig. 2.6). A compromise was to be found between accuracy on the segmentation and computing time, which was on this case of about 20 min.

After the segmentation, surfaces are generated. An adaptive adjusting method was used with a 75% precision on the adjustment, a tolerance of 0.1141 mm, and an allowable deviation of 1 (internal program parameter). These are not optimum parameters, but they are compromise solutions, which lead to a further computing time of about 1 h. Higher levels of accuracy increase the computing time and the data size dramatically, and most of the times, lead to system crashes. The surfacing procedure failed at a few regions of the blade. Tweaking the surfacing parameters never led to a perfect surfacing (Fig. 2.7), therefore, a defected surface model was obtained and exported as an IGES surface CAD model, for the further repair of these defects in ANSYS DesignModeler.

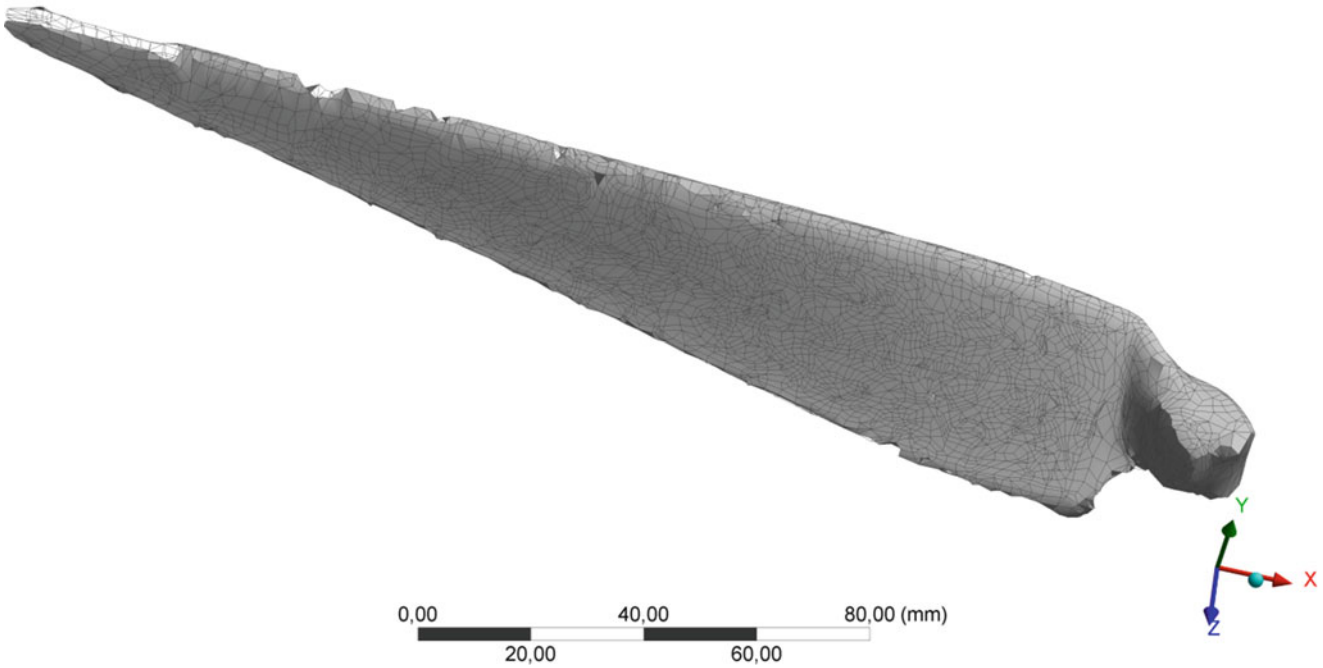

Fig. 2.8 FE mesh used in this simulation. Note how the mesh does not adjust to the geometry properly at the blade edges due to the coarseness of the element sizing

The obtained IGES surface model was imported in ANSYS DesignModeler (ANSYS Inc., Canonsburg, PA, USA) to prepare it for its FE modeling. Hard edges, seams, hard angles, slivers and holes were repaired on the surface model to the best of the author's knowledge.

The repaired surface model was later used in ANSYS Mechanical for its simulation. As the model is composed of surfaces, a FE modeling based on SHELL181 elements was chosen for simplicity and assigned a thickness of 1 mm. The model was meshed with a face sizing with moderately large, maximum 3 mm elements. This lead to a coarse but rather time-consuming meshing, about 1 h long; although accurate enough to display the desired mode shapes. The generated FE mesh was composed of 7553 nodes resulting in 8443 SHELL181 finite elements (Fig. 2.8). The boundary conditions recreate those on the experimental setup, only constraining the propeller pinhole area with two fixed support contacts.

Finally, the FE modal model was solved for all eigenfrequencies lower than 10 kHz as a target. Several solver iterations, by testing different material parameters, were needed to reach satisfactory results on the correlation. The results are discussed on the next section.

2.4 Results and Discussion

Validating the FE model of this paper was not possible in this work due to a variety of issues. This is due to the limitations of the propeller model in this work, such as:

1. The FE simulation shown in this paper dealt with a hollow surface model, which is not faithful to the reality in this aspect; as the propeller blade is actually not hollow. The SHELL181 elements are assigned a thickness value, but the effects of mass and stiffness inside the material are not taken into account in the model; thus distorting the results.
2. The material parameters are unknown. Several iterative simulations have been carried out by adjusting the material parameters from the basis of "Epoxy Carbon UD (230 GPa) Prepreg" ANSYS default material, but it is difficult to achieve convergence due to the material anisotropy.
3. Limitations in the available computation power and program licensing had also an influence on the accuracy of the surfacing and the FE meshing.

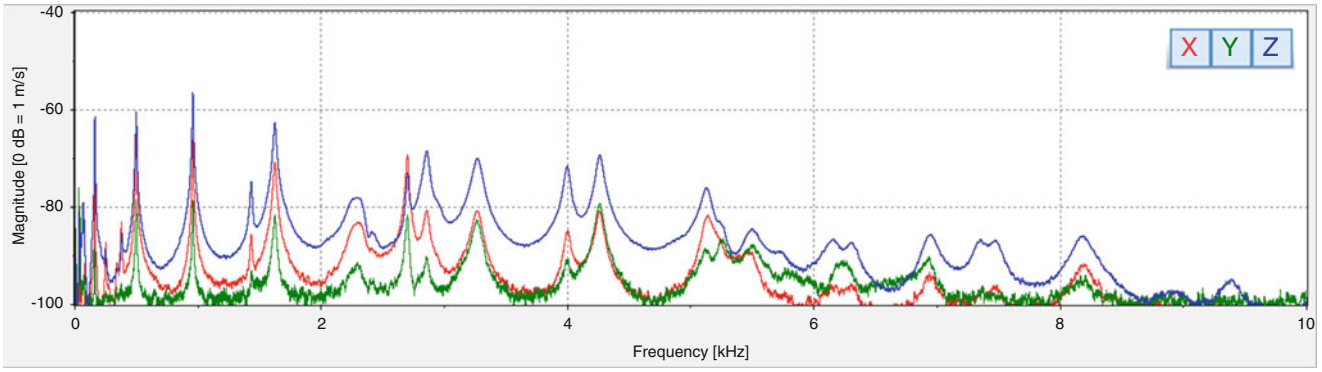

Fig. 2.9 Averaged FRFs plot (dB scaling) for this experiment. Note the strong in-plane components (those on the XY plane) of some modes, impossible to determine with other kinds of LDV systems

Bypassing these limitations meant finally not taking into account the small defects the propeller blade presents. The solution to these issues is left for discussion as further work.

Two datasets have been obtained for this paper, EMA modal parameters (eigenfrequencies, damping ratios and mode shapes) and FEA modal parameters (only eigenfrequencies and mode shapes in this case). An averaged FRF plot is shown on Fig. 2.9 displaying the modes obtained experimentally on this work. This plot serves as a first "sanity check" for the simulation results, and to know the limits of the correlation. The experiment was performed up to 10 kHz, but the complexity of the shapes increases sharply after 5 kHz. More spatial resolution on the DOFs would be needed, together with a stronger energy input in that region to better display the mode shapes beyond 5 kHz. In exchange, testing time would sharply increase, and impact modal testing should be replaced by a more mass-loading excitation method. Consequently, only modal parameters up to 5 kHz are shown in Fig. 2.11.

Figures 2.10 and 2.11 show a comparison between EMA and FEA eigenfrequencies and mode shapes. The obtained FEA mode shapes have however a clear correlation with their experimental counterparts.

2.5 Conclusions and Further Work

The scope of this paper is proving that establishing a correlation and validation cycle is possible by using the previously described procedures. Modal testing by means of 3D SLDV or 3D geometry scanning have multiple applications separately in several industries. This work serves as a proof, although not a full study case, that these techniques can be also applied and combined on the research and the reverse-engineering of the dynamic properties of composite aerospace structures.

Modal testing via 3D SLDV has been proven to be a robust and reliable technique, capable of delivering results that can be simply compared back-to-back with those derived from FEA.

Nonetheless, a full validation cycle could not be described in this paper, and remains as the most immediate future work. As it has been widely described, the simulation leg of this cycle has suffered of several drawbacks that have been solved to the best of the authors' knowledge. However, these drawbacks are of a technical nature—they can be solved with increased training and higher computing power. Further work will be devoted to solve these technical issues while keeping computing times low. Low computing times are a priority, as the described methodology is intended to serve an industry with constantly decreasing delivery times and shorter development cycles.

The presented work has been carried out outside a project framework. The authors are open to establish national and/or international research cooperation projects in order to further develop the proposals presented in this paper.

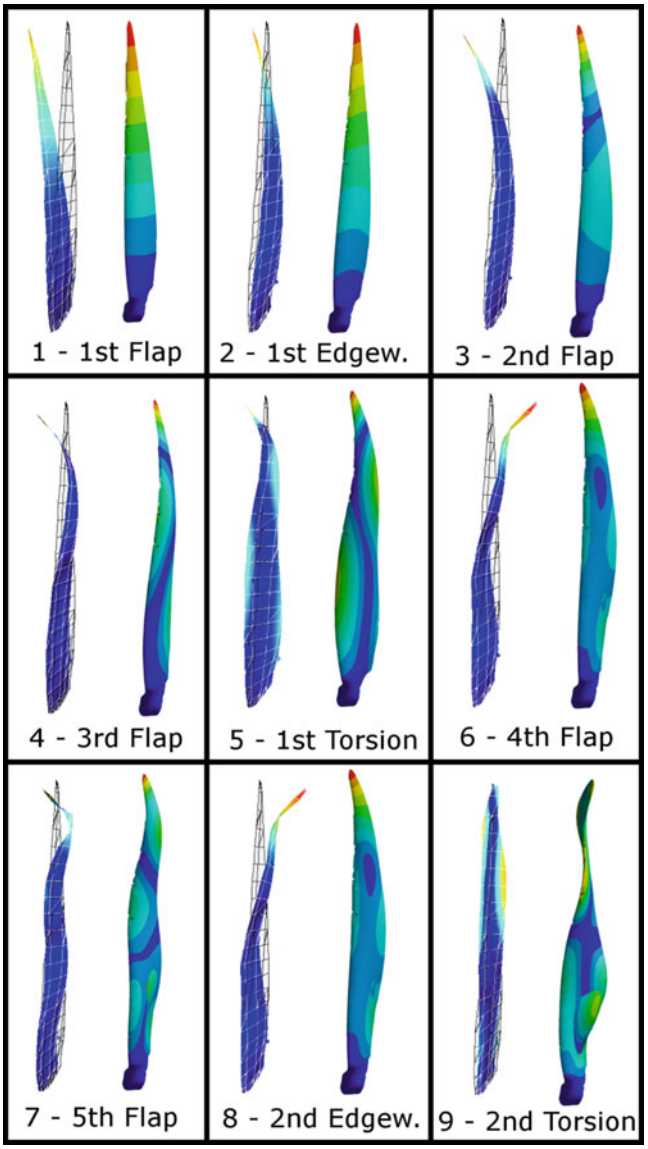

Fig. 2.10 Comparison between experimental and simulated mode shapes. Note how the edgewise mode shapes (2 and 8) can be analyzed and correlated by the use of the 3D SLDV. There is good correlation between mode shapes

	EMA		FEA			EMA		FEA	
Mode	Freq. [Hz]	Mode shape	Freq. [Hz]	Mode shape	Mode	Freq. [Hz]	Mode shape	Freq. [Hz]	Mode shape
1	164	1st Flap	110	1st Flap	8	2700	2nd Edgewise	2546	2nd Edgewise
2	379	1st Edgewise	327	1st Edgewise	9	2859	2nd Torsion	2981	6th Flap
3	499	2nd Flap	510	2nd Flap	10	3271	6th Flap	3394	2nd Torsion
4	959	3rd Flap	1030	3rd Flap	11	4001	3rd Torsion	3720	7th Flap
5	1432	1st Torsion	1424	1st Torsion	12	4264	4th Torsion	4169	3rd Torsion
6	1624	4th Flap	1902	4th Flap	13	5131	3rd Edgewise	4387	8th Flap
7	2299	5th Flap	2466	5th Flap	14	-	-	4740	4th Torsion

Fig. 2.11 Comparison between experimental and simulated eigenvalues and mode shapes. There is poor correlation between the obtained eigenfrequencies due to the aforementioned limitations in the FE model

References

1. Federal Ministry of Education and Research: Drohnen für den Katastrophenschutz – Entwicklung einer Drohne zur Messung wissenschaftlicher Daten bei Vulkanausbrüchen, *Program "Forschung an Fachhochschulen"* – Research project of the month, April 2014
2. Diaz, T.J.: Lights, drone . . . action! North American Spectrum IEEE.org, pp. 36–41, July 2015
3. Body, J.: Airbus future composite wing. SE Composites Seminar, p. 8, December 2014
4. Berman, A.: Inherently incomplete finite element model and its effects on model updating. AIAA J. **38**(11), 2142–2146 (2000)
5. Blaschke, P., Schneider, T.: Reactioneless test to identify dynamic Young's modulus and damping of isotropic plastic materials. In: Topics in Modal Analysis, vol. 7: Proceedings of the XXXI International Modal Analysis Conference, pp. 511–516, February 2014
6. Baumann, K. et al.: Bottom-up-strategie zur Validierung des FE-Modells einer Abgasanlage unter besonderer Berücksichtigung der Systemdämpfung. In: Proceedings of the 4th VDI Conference "Vibrations and Identification", VDI-Berichte 2259, p. 149, March 2016
7. Di Maio, D. et al.: Experimental non-linear modal testing of an aircraft engine casing assembly. In: Topics in Nonlinear Dynamics, vol. 1: Proceedings of the XXXI International Modal Analysis Conference, pp. 15–36 (2013)
8. Schell, J. et al.: Three dimensional vibration testing in automotive applications utilizing a new non-contact scanning method. SAE Technical Paper #2006-01-1095 (2006)
9. Oliver, D.E., Schüssler, M.: Automated robot-based 3D vibration measurement system. J. Sound Vib. **2006**, 12–15 (2006)
10. Blaschke, P., Mallareddy, T.T., Alarcón, D.J.: Application of a scalable automatic modal hammer and a 3D scanning laser doppler vibrometer on turbine blades. In: Proceedings of the 4th VDI Conference "Vibrations and Identification", VDI-Berichte 2259, p. 87, March 2016
11. Schneider, M., Friebe, H., Galanulis, K.: Validation and optimization of numerical simulations by optical measurements of tools and parts. In: International Deep Drawing Research Group (IDDRG) International Conference, June 2008
12. Hurt, H.H. Jr.: Aerodynamics for Naval Aviators, pp. 21–22 (1965)
13. Blaschke, P. et al.: Non-linearity identification of composite materials by scalable impact modal testing. In: Topics in Nonlinear Dynamics. Proceedings of the XXXI International Modal Analysis Conference (2017)

Chapter 3
Effect of Dry Friction Damping on the Dynamic Response of Helicopter Tail Shaft

Onur Ozaydin and Ender Cigeroglu

Abstract Tail Drive Shaft of a helicopter transmits torque from the main gear box to the tail rotor and in most of the helicopter designs, tail shafts are designed to work in supercritical speeds. In order to limit resonance vibrations of the tail drive shaft, dry friction dampers can be used. Therefore, in order to study the effect of dry friction damping on the response of tail drive shaft, a mathematical model is developed. The tail drive shaft is modeled as a beam by using Euler-Bernoulli beam theory. Bearings supporting the shaft structure and couplings used are represented by linear and torsional springs, respectively. The dry friction damper is located at the middle section of the shaft which is modeled by using a one-dimensional macroslip friction model with constant normal load. The partial differential equation of motion obtained is discretized by using Galerkin's Method with multiple trial functions. The resulting nonlinear ordinary differential equations are converted into a set of nonlinear algebraic equations by using harmonic balance method utilizing single harmonic. Finally, the solution of the resulting set of nonlinear algebraic equations are obtained by using Newton's method. Using the model developed effects of parameters of the friction damper on the response of the tail drive shaft are studied.

Keywords Helicopter tail drive shaft • Dry friction damper • Macroslip friction • Nonlinear vibrations • Harmonic balance method • Euler-Bernoulli beam theory

3.1 Introduction

Dynamics of the tail drive shaft of a helicopter is an important problem since excessive vibrations may result in a catastrophic failure. In the literature, there exits two different designs for tail drive shafts: subcritical design (operating below the first natural frequency) and supercritical design (operating above the first natural frequency). Using minimum number of long shafts working at supercritical speed is more advantageous than using many short shafts working at subcritical speed. On the other hand, in the supercritical design, in order to reach to the operating speed, shafts should pass through the resonance region where excessive vibrations can be observed which can be avoided by using proper dampers [1].

Dry friction dampers are widely used in different applications such as turbomachinery [2], turbine or compressor blades [3, 4], buildings under seismic excitation [5, 6], and railway bogies [7] to reduce resonant vibrations. In this paper, a continuous dynamic model of a tail drive shaft of a helicopter with dry friction damper is developed. In order to discretize the partial differential equation of motion, Galerkin's Method with multiple trial functions is used. Due to the nonlinear behavior of dry friction, it is complicated to model and analyze systems including dry friction. In the literature, Harmonic Balance Method (HBM), a frequency domain solution method, is widely used instead of direct time integration, which requires high computational effort and computation time [8]. Therefore, in this study, HBM is used to convert the resulting nonlinear ordinary differential equations into a set of nonlinear algebraic equations. The resulting equations are solved by using Newton's method. Several case studies are performed in order to investigate the effects of dry friction damper on the response of tail drive shaft system.

O. Ozaydin
Department of Mechanical Engineering, Middle East Technical University, Universiteler Mahallesi, Dumlupinar Bulvari No:1, 06800, Cankaya-Ankara, Turkey

Turkish Aerospace Industries, Inc. (TAI), Fethiye Mahallesi Havacilik Bulvari No: 17, 06980, Kazan-Ankara, Turkey

E. Cigeroglu (✉)
Department of Mechanical Engineering, Middle East Technical University, Universiteler Mahallesi, Dumlupinar Bulvari No:1, 06800, Cankaya-Ankara, Turkey
e-mail: ender@metu.edu.tr

D. Di Maio, P. Castellini (eds.), *Rotating Machinery, Hybrid Test Methods, Vibro-Acoustics & Laser Vibrometry, Volume 8*,
Conference Proceedings of the Society for Experimental Mechanics Series, DOI 10.1007/978-3-319-54648-3_3

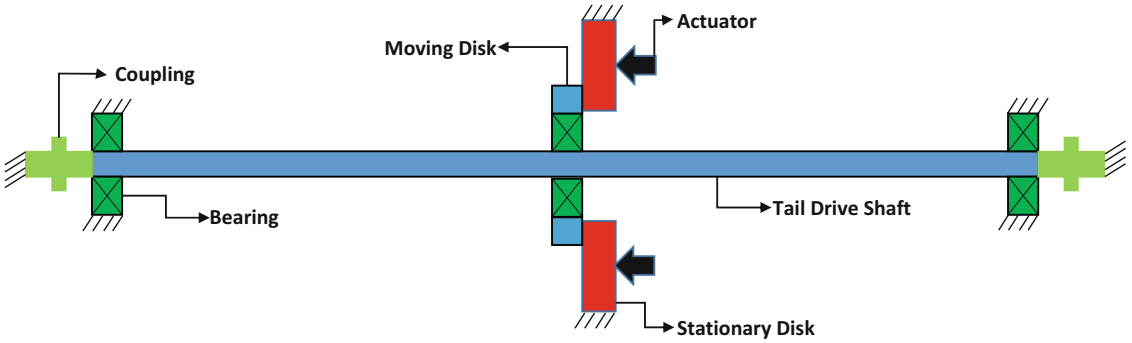

Fig. 3.1 Tail drive line

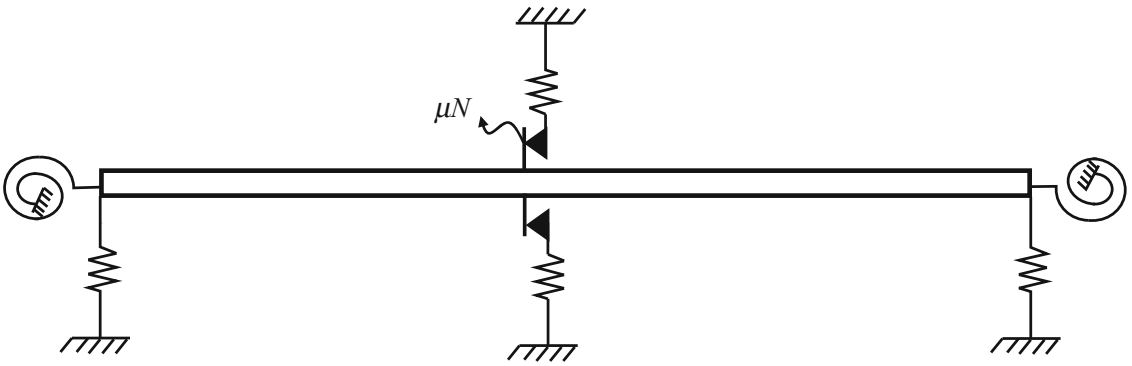

Fig. 3.2 Dynamic model of tail drive line

3.2 Mathematical Model of the System

The tail drive shaft system shown in Fig. 3.1 consists of a shaft supported by two bearings at both ends and connected to two couplings. A dry friction damper is used in the middle of the shaft in order to decrease vibration amplitudes. The tail drive shaft is modeled by Euler-Bernoulli Beam theory and spring elements are used to represent the bearings and couplings as shown in Fig. 3.2. Equation of motion of an Euler Bernoulli beam can be written as follows

$$\rho A \frac{\partial^2 w(x,t)}{\partial t^2} + EI \frac{\partial^4 w(x,t)}{\partial y^4} + c \frac{\partial w(x,t)}{\partial t} = f(\mathrm{t})\,\delta(x - L_2) - f_n(w(x,t))\,\delta(x - L_1)\,, \tag{3.1}$$

where $w(x,t)$ is transverse displacement, ρ is density, A is cross sectional area, E is Young's Modulus, I is moment of inertia, c is viscous damping coefficient, $f_n(w(x,t))$ is the nonlinear friction force, $f(t)$ is external forcing, L_1 is the location of dry friction damper and L_2 is location of external forcing.

3.3 Solution Methodology

For the solution of the partial differential equation of motion given in Eq. (3.1) Galerkin's method is used. Utilizing expansion theorem, transverse displacement of the shaft can be expressed as given below;

$$w(x,t) = \sum_j a_j(t)\phi_j(x), \tag{3.2}$$

where $a_j(t)$ and $\phi_j(\mathrm{x})$ are the j^{th} generalized coordinate and mass normalized eigenfunction of a beam with springs at the supports are included. Substituting Eq. (3.2) into Eq. (3.1) the following result is obtained.

$$\rho A \sum_j \frac{d^2 a_j(t)}{dt^2}\phi_j(x) + EI \sum_j a_j(t)\frac{d^4\phi_j(x)}{dx^4} + c\sum_j \frac{da_j(t)}{dt}\phi_j(x) + f_n(t)\delta\left(x - L_1\right) = f(t)\delta\left(x - L_2\right), \tag{3.3}$$

Multiplying both side of Eq. (3.3) by ϕ_i(x) and integrating over the spatial domain, the following result is obtained

$$[I]\{\ddot{a}\} + [C_r]\{\dot{a}\} + [\Omega]\{a\} + \{F_n(\{a\})\} = \{F(t)\}. \tag{3.4}$$

Since mass normalized eigenfunctions are used in the expansion, $[I]$, $[C_r]$, $[\Omega]$, $\{F_n\}$ and $\{F\}$ are identity matrix, diagonal damping matrix, diagonal matrix of squares of natural frequencies, nonlinear modal forcing vector and external modal forcing vector, respectively. Elements of these matrices and vectors can be calculated as follows

$$\Omega_{ii} = {\omega_i}^2 = \int_0^L EI\frac{d^4\phi_i(x)}{dx^4}\phi_i(x)dx, \tag{3.5}$$

$$C_{r_{ii}} = \int_0^L c\phi_i(x)^2 dx = 2\zeta_i\omega_i, \tag{3.6}$$

$$F_{n_i}(t) = f_n(t)\phi_i\left(L_1\right), \tag{3.7}$$

$$F_i(t) = f(t)\phi_i\left(L_2\right), \tag{3.8}$$

where ω_i and ζ_i are the natural frequency and damping ratio of the i^{th} mode.

3.4 Harmonic Balance Method

The nonlinear ordinary differential equation set defined by Eq. (3.4) is converted into a set of nonlinear algebraic equations by using Harmonic Balance Method. For this purpose, by using a single harmonic representation, generalized coordinate can be expressed as follows

$$\{a\} = \{a_s\}\sin(\omega t) + \{a_c\}\cos(\omega t), \tag{3.9}$$

where $\{a_s\}$ and $\{a_c\}$ are the sine and cosine components of the vector of generalized coordinates. Similarly, utilizing Fourier series, nonlinear forcing and external excitation force vectors can be written as

$$\{F_n(t)\} = \{F_{ns}\}\sin(\omega t) + \{F_{nc}\}\cos(\omega t), \tag{3.10}$$

$$\{F(t)\} = \{F_s\}\sin(\omega t) + \{F_c\}\cos(\omega t) \tag{3.11}$$

where $\{F_{ns}\}$ and $\{F_{nc}\}$ are the sine and cosine components of the nonlinear internal forcing vector and $\{F_s\}$ and $\{F_c\}$ are the sine and cosine components of external forcing vector. After inserting Eqs. (3.9)–(3.11) into Eq. (3.4) and separating sine and cosine components, the following nonlinear algebraic equations are obtained

$$\begin{bmatrix} [\Omega] - \omega^2[I] & 0 \\ 0 & [\Omega] - \omega^2[I] \end{bmatrix}\begin{Bmatrix} a_s \\ a_c \end{Bmatrix} + \begin{bmatrix} 0 & -\omega[C_r] \\ \omega[C_r] & 0 \end{bmatrix}\begin{Bmatrix} a_s \\ a_c \end{Bmatrix} + \begin{Bmatrix} F_{ns} \\ F_{nc} \end{Bmatrix} = \begin{Bmatrix} F_s \\ F_c \end{Bmatrix}, \tag{3.12}$$

Equation (3.12) is a set of nonlinear algebraic equations, which can be solved by a nonlinear equation solver such as Newton's method.

Dry friction can be modeled in several different ways in dynamic analysis of systems. In this study, one dimensional macroslip friction model [3, 9], shown in Fig. 3.3, is used. Here,k_d is the tangential contact stiffness, N is the normal load, μ is coefficient of friction, $u(t)$ is the tangential input motion and $v(t)$ is the slip motion. Figure 3.4 shows the hysteresis curve for the friction element given in Fig. 3.3 for single harmonic motion.

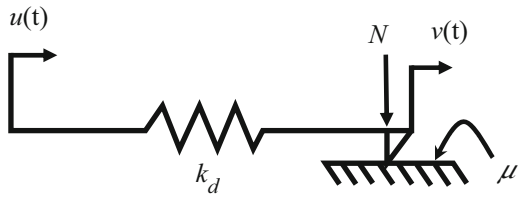

Fig. 3.3 Dry friction element

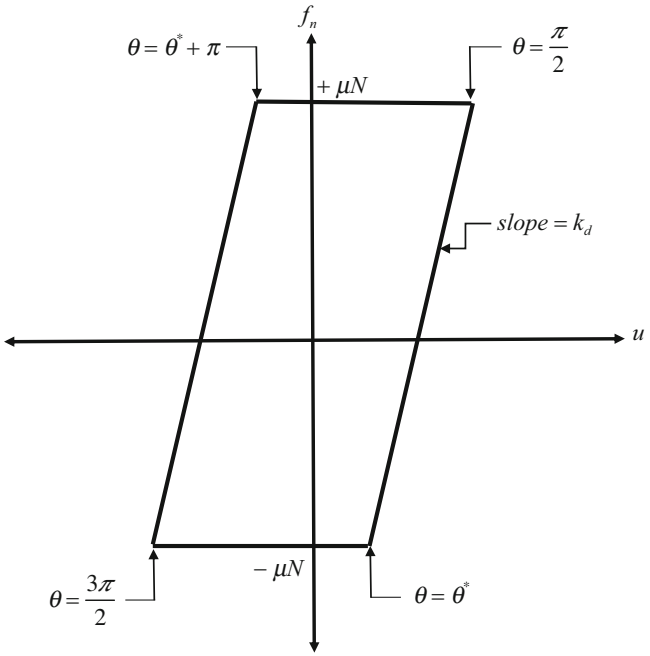

Fig. 3.4 Hysteresis curve for single harmonic motion

Hysteresis curve given in Fig. 3.4 can be defined as follows

$$f_n = \begin{cases} k_d\,(A\sin(\theta) - A) + \mu N \text{ when } \dfrac{\pi}{2} \le \theta \le \theta^* \\ -\mu N \text{ when } \theta^* \le \theta \le \dfrac{3\pi}{2} \\ k_d\,(A\sin(\theta) + A) - \mu N \text{ when } \dfrac{3\pi}{2} \le \theta \le \theta^* + \pi \\ \mu N \text{ when } \theta^* + \pi \le \theta \le \dfrac{5\pi}{2} \end{cases}, \tag{3.13}$$

$$\theta^* = \pi - a\sin\left(1 - \frac{2\mu N}{k_d A}\right) \tag{3.14}$$

where A is the amplitude of harmonic tangential motion and $\theta = \omega t$. The nonlinear dry friction force can be represented by using a single harmonic as

$$f_n(t) = f_{ns}\sin(\theta) + f_{nc}\cos(\theta), \tag{3.15}$$

$$f_{ns} = \frac{2}{\pi}\int_{\frac{\pi}{2}}^{\frac{3\pi}{2}} f_n(t)\sin(\theta)\,d\theta, \tag{3.16}$$

$$f_{nc} = \frac{2}{\pi}\int_{\frac{\pi}{2}}^{\frac{3\pi}{2}} f_n(t)\cos(\theta)\,d\theta, \tag{3.17}$$

where the sine and cosine components are given in [5] as follows

$$f_{ns} = \left(-\frac{4\mu N}{\pi} + \frac{2Ak_d}{\pi}\right)\cos\left(\theta^*\right) - \frac{Ak_d}{2\pi}\sin\left(2\theta^*\right) + \frac{Ak_d}{\pi}\theta^* - \frac{Ak_d}{2}, \tag{3.18}$$

$$f_{nc} = \left(\frac{4\mu N - 2Ak_d}{\pi}\right)\sin\left(\theta^*\right) + \frac{Ak_d}{\pi}\sin\left(\theta^*\right)^2 + \frac{Ak_d}{\pi}. \tag{3.19}$$

3.5 Case Studies

The parameters of an example helicopter tail shaft assembly with a dry friction damper are given in Table 3.1. Dry friction damper is characterized by two factors namely; slip force μN, contact stiffness k_d where L, D_o and D_i are length, outer diameter and inner diameter of the tail drive shaft, respectively.

In the first case study given, dry friction damper is located at the midpoint of the shaft and effect of slip force, μN, on the maximum vibration amplitude of the shaft around its first critical speed is investigated. Displacement amplitude of the tail drive shaft obtained at the midpoint is given in Fig. 3.5 for an external forcing applied at the same point. It is observed from the results that increasing slip load decreases the vibration amplitude until a certain point where further increase in the slip force results in an increase in the maximum vibration amplitude. Moreover, as the slip load increases, resonance frequency of the tail drive shaft system also increases which is due to the increased stiffness effect of the dry friction damper. For a slip

Table 3.1 Parameters of the example system

Parameter	Numerical value
L [m]	3
D_o [m]	0.09
D_i [m]	0.07
E [GPa]	68.9
ρ [kg/m^3]	2700
k [N/m]	10^6
k_t [Nm/rad]	10^8
k_d [N/m]	10^6
ζ	0.02
F [N]	$60\sin(\omega t)$

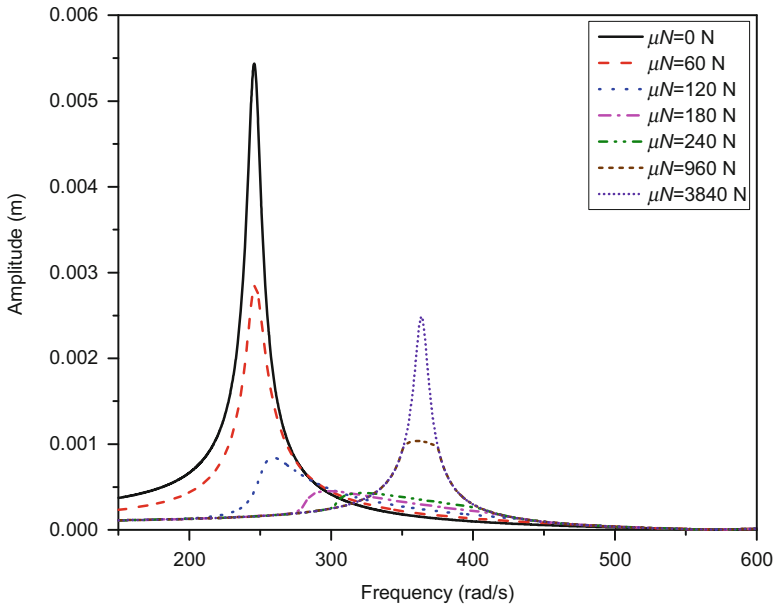

Fig. 3.5 Effect of slip force (μN) on the peak amplitude ($L_1 = 0.5L$ and $L_2 = 0.5L$)

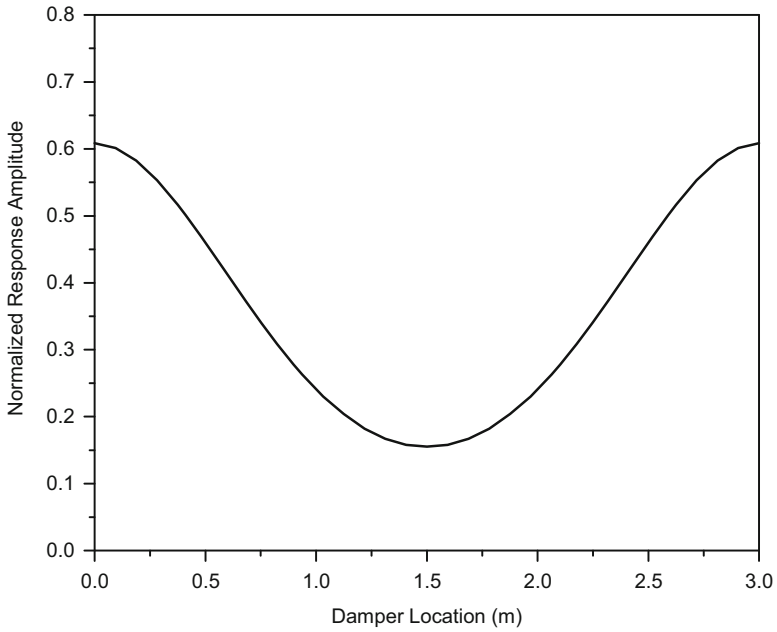

Fig. 3.6 Effect of damper location on the maximum vibration amplitude ($\mu N = 120$, $L_2 = 0.5L$)

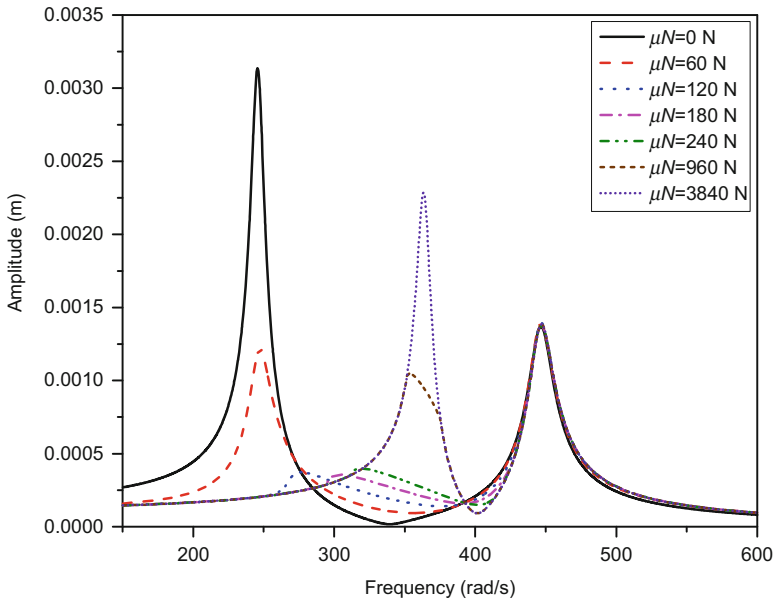

Fig. 3.7 Effect of slip force (μN) on the peak amplitude ($L_1 = 0.5L$ and $L_2 = 0.25L$)

load of 3840 N, friction damper becomes fully stuck and behaves like a linear spring element. From these results, it can be concluded that there is an optimum slip load which minimizes the vibration amplitude. In the next study given, in order to see the effect of damper location on the system response, system given in previous case study with different damper locations is studied. Maximum vibration amplitude normalized with respect to the maximum vibration amplitude of the no damper case is given in Fig. 3.6. It is clearly seen that the optimum damper location for the first vibration mode is the midpoint of the shaft where the highest amplitude is seen.

In the next two case studies, external force is applied at $0.25L$ and the results are taken from that point. In the first case study presented in Fig. 3.7, damper is located at the midpoint and it is seen that although the damper is able to damp vibrations around the first mode, it is ineffective around the second mode. This is due to the fact that the damper is located on the nodal point for the second mode. In the second case study, damper location is moved to $0.25L$ and the results obtained are given in Fig. 3.8. It is observed from these results that in this case, in addition to the first mode, vibrations around the second mode

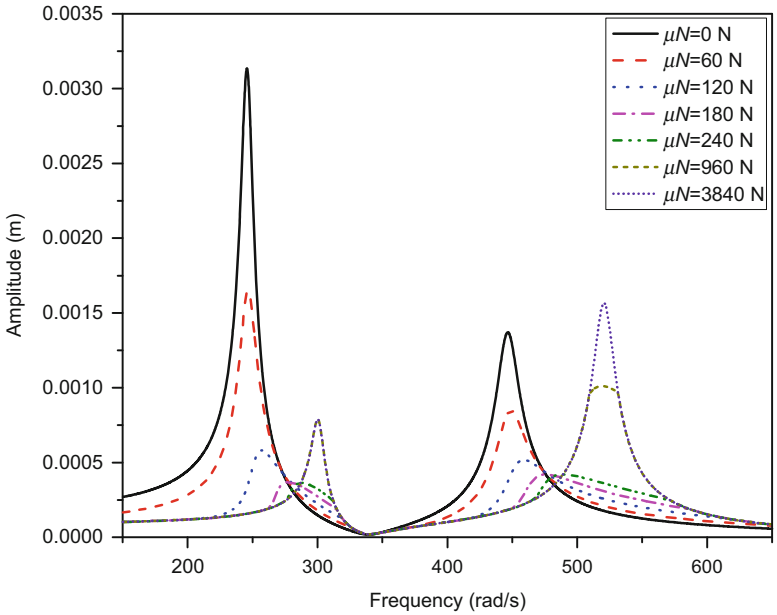

Fig. 3.8 Effect of slip force (μN) on the peak amplitude ($L_1 = 0.25L$ and $L_2 = 0.25L$)

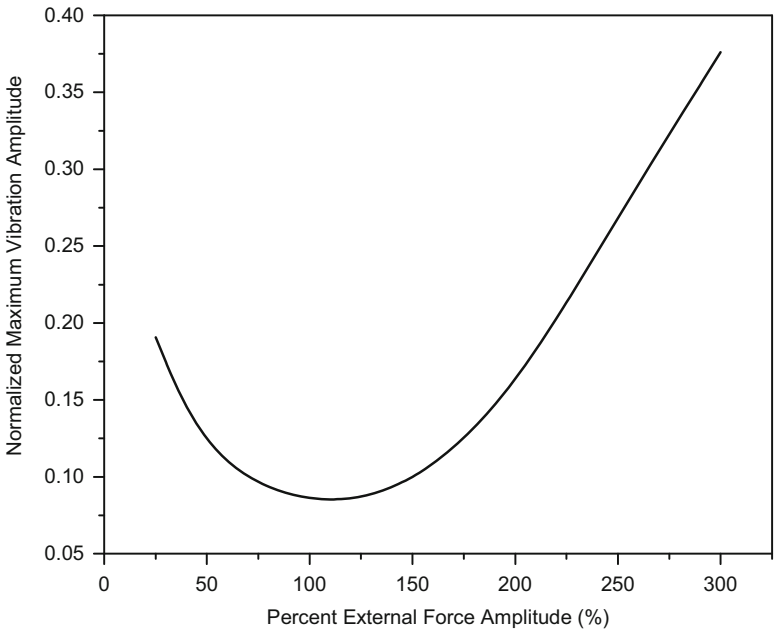

Fig. 3.9 Effect of amplitude variation of external forcing ($\mu N = 240$N, $L_1 = 0.5L$, $L_2 = 0.5L$)

are as well damped out. It can be concluded that if more than one mode is required to be damped, optimum damper location should be sought and nodal points should be avoided.

In the final case study, while holding the slip force as constant at the optimal value, amplitude of the external force is varied. External forcing is applied at the midpoint and displacement amplitude of the shaft at the same point is considered. For this case, optimum slip force is determined to be 240N for 60N external force. Maximum vibration amplitude normalized with respect to the maximum vibration amplitude of the corresponding linear case is plotted in Fig. 3.9 as a function of percent external forcing amplitude. It can observed that, effectiveness of the damper depends on the accurate estimation of the amplitude of external forcing.

3.6 Conclusion

In this study, effect of dry friction damping on vibration attenuation of helicopter tail shaft is studied. The tail drive shaft is modeled by Euler-Bernoulli theory supported by springs which represent the bearings and couplings used. The partial differential equation of motion obtained is discretized by using Galerkin's Method and the resulting nonlinear ordinary differential equations are converted into a set of nonlinear algebraic equations by using Harmonic Balance Method. In order to model the dry friction damper, one dimensional macroslip friction model with constant normal load is used. It is observed from the results obtained that dry friction dampers can be used to suppress excessive vibrations when the shaft is rotating around its critical speed. The amount of the slip load and the location of the friction damper are the two important parameters affecting the performance of the friction damper. Depending on the number of critical speeds to be considered in the vibration reduction, an optimum damper location needs to be determined in addition to the slip force. In case of a single critical speed, location of the maximum vibration amplitude is the best place for the friction damper. Moreover, since the performance of the friction damper decreases as the excitation amplitude varies, it is also important to accurately estimate the amplitude of the external forcing.

References

1. Prause, R.H., Meacham, H.C., Voorhees, J.E.: The design and evaluation of a supercritical-speed helicopter power-transmission shaft. J. Eng. Ind. **89**, 719–727 (1967)
2. Childs, D.W., Bhattacharya, A.: Prediction of dry-friction whirl and whip between a rotor and a stator. J. Vib. Acoust. **129**, 355–362 (2007)
3. Wang, J.H., Chen, W.K.: Investigation of the vibration of a blade with friction damper by HBM. J. Eng. Gas Turbines Power. **115**, 294–299 (1993)
4. Pust, L., Pesek, L., Radolfova, A.: Blade couple with dry friction connection. Appl. Comput. Mech. **9**, 31–40 (2015)
5. Erisen, Z.E., Cigeroglu, E.: Frequency domain optimization of dry friction dampers on buildings under harmonic excitation. In: IMAC XXX: Conference & Exposition on Structural Dynamics, Jacksonville, FL, USA, January 30–February 02, 2012
6. Belash, T.: Dry friction dampers in quake-proof structures of buildings. Procedia Eng. **117**, 397–403 (2015)
7. True, H., Asmund, R.: The dynamics of a railway freight wagon wheelset with dry friction damping. Veh. Syst. Dyn. **38**, 149–113 (2003)
8. Mingfu, L., Mingbo, S., Wang, S.: Active elastic support/dry friction damper with piezoelectric ceramic actuator. Shock. Vib. **2014**, 1–10 (2014)
9. Ciğeroğlu, E., Özgüven, N.: Nonlinear vibration analysis of bladed disks with dry friction dampers. J. Sound Vib. **295**, 1028–1043 (2006)

Chapter 4
Nonlinear Dynamic Analysis of a Spiral Bevel Geared System

Siar Deniz Yavuz, Zihni Burcay Saribay, and Ender Cigeroglu

Abstract A nonlinear dynamic model of a spiral bevel gear train mounted on flexible shafts and bearings is proposed in this study. The finite element model of shafts is combined with a three-dimensional discrete mesh model of a spiral bevel gear pair. Bearing flexibilities are as well included in the model. Gear backlash is incorporated into the model in the form of clearance-type displacement functions and clearance nonlinearity and stiffness fluctuations of the bearings are neglected. A time-invariant mesh stiffness is assumed for the gear pair to simplify the dynamic model. Eigenvalue solution is used to predict the natural modes of the system. A multi-term Harmonic Balance Method (HBM) is employed for the solution of resulting equations of motion for periodic steady-state response. The results of HBM are validated by comparing them to the solutions obtained by direct numerical integration. Forced response of the system in the form of dynamic mesh force is studied to demonstrate the effects of static mesh force and backlash amount.

Keywords Nonlinear gear dynamics • Spiral bevel gear train • Gear backlash nonlinearity • Time-invariant mesh stiffness • Multi-term Harmonic Balance Method

Nomenclature

b	Half of gear backlash
c_m	Mesh damping coefficient
$\mathbf{C}$	Damping matrix
e_m	Static transmission error
f_n	Nonlinear displacement function
$\mathbf{F}$	External force vector
F_m	Dynamic mesh force
$\mathbf{F}_N$	Nonlinear restoring force vector
$\mathbf{h}$	Transformation vector
i	Unit imaginary number
$\mathbf{J}$	Jacobian matrix
$\mathbf{K}$	Stiffness matrix
k_m	Mesh stiffness
$\mathbf{M}$	Mass matrix
$\mathbf{n}$	Line of action (LOA) directional cosine vector
n	Directional cosine
$\mathbf{p}$	Extended coordinate transformation vectors

S.D. Yavuz
Department of Mechanical Engineering, Middle East Technical University, Universiteler Mahallesi, Dumlupinar Bulvari No:1, 06800, Cankaya-Ankara, Turkey

Turkish Aerospace Industries, Inc. (TAI), Fethiye Mahallesi Havacilik Bulvari No:17, 06980, Kazan-Ankara, Turkey

Z.B. Saribay
Turkish Aerospace Industries, Inc. (TAI), Fethiye Mahallesi Havacilik Bulvari No:17, 06980, Kazan-Ankara, Turkey

E. Cigeroglu (✉)
Department of Mechanical Engineering, Middle East Technical University, Universiteler Mahallesi, Dumlupinar Bulvari No:1, 06800, Cankaya-Ankara, Turkey
e-mail: ender@metu.edu.tr

D. Di Maio, P. Castellini (eds.), *Rotating Machinery, Hybrid Test Methods, Vibro-Acoustics & Laser Vibrometry, Volume 8*,
Conference Proceedings of the Society for Experimental Mechanics Series, DOI 10.1007/978-3-319-54648-3_4

$\mathbf{r}$	Position vector of the effective mesh point
r	Harmonic index
S	Pinion/gear coordinate system
$\mathbf{S}$	Nonlinear algebraic equations in vector form
T	Torque
t	Time
$\mathbf{U}$	Solution vector
$\mathbf{u}$	Harmonic amplitudes of displacement vector
$\mathbf{x}$	Displacement vector
β	Rayleigh damping coefficient
δ_d	Dynamic transmission error
λ	Directional rotational radius
ρ	Discrete time interval
θ	Rotational displacement
ω	Frequency

Subscripts

b	Bearing
i	Pinion ($i = p$) and gear ($i = g$)
l	Linear DOFs
n	Nonlinear DOFs
s	Shaft

Superscripts

rms	Root-mean-square value
$\cdot$	Derivative with respect to time

4.1 Introduction

Dynamic analysis of gear systems has been one of the main topics in power transmission research. Under dynamic conditions, gear systems exhibit much higher gear mesh forces than static forces transmitted. These high frequency dynamic forces are transmitted to the housing and other structures, resulting in excessive noise levels. Moreover, dynamic mesh loads cause increased tooth root and contact stresses and reduce fatigue lives of the driveline components. Therefore, a better understanding of the gear system dynamics is crucial in order to design products with acceptable noise levels and fatigue lives.

There are a large number of studies regarding dynamics of parallel axis gears in the literature. Numerous mathematical models and solution methods are developed in those studies. However, studies related to dynamics of non-parallel axis gears such as hypoid gears and spiral bevel gears are limited due to the complexity of tooth geometry, kinematics and meshing process of these types of gears. A single-point gear mesh-coupling model using the exact spiral bevel gear geometry is developed in [1]. Based on this mesh model, a nonlinear model of a spiral bevel gear pair including time varying mesh stiffness and time-varying directional rotation radius is formulated and solved by using direct numerical integration [2] and HBM [3]. Moreover, the same mesh model is used to develop multiple degrees of freedom (DOFs), lumped parameter model of a spiral bevel geared system and the effects of various gear system parameters on the dynamics of this system are investigated in [4]. Due to the deficiency of this lumped parameter model in representing the shaft-bearing structural characteristics, two different modeling methods, i.e., the finite element model and an enhanced equivalent lumped parameter synthesis, are introduced in [5] for a linear time-invariant (LTI) spiral bevel geared system.

In this study, a nonlinear dynamic model of a spiral bevel gear pair mounted on flexible shafts and bearings is considered. The dynamic model combines the finite element model of shaft-bearing structures with a three-dimensional discrete mesh

model of a spiral bevel gear pair. The resulting differential equations of motion are converted into a set of nonlinear algebraic equations for periodic steady-state response by using multi-term HBM coupled with discrete Fourier transform (DFT). The resulting set of nonlinear algebraic equations is solved by Newton's method with arc-length continuation. The accuracy of the solutions obtained by HBM is demonstrated by comparing them with the solutions obtained by direct numerical integration, which are computationally very expensive. The effects of static mesh force and backlash amount on the dynamic response are studied.

4.2 Dynamic Model Formulation

4.2.1 Physical System and Dynamic Model

The geared system considered in this study consists of a spiral bevel gear pair mounted on flexible shafts and bearings. The shafts including the gear blanks are modeled by using Timoshenko beam formulation, since rotary inertia and shear deformations are expected to be significant. The bearings supporting the gear shafts are represented by linear and torsional springs. Clearance nonlinearity and stiffness fluctuations of bearings due to the alternating number of rolling elements in the loaded zone are neglected.

The stiffness matrix, $\mathbf{K}_{sn}$, and mass matrix, $\mathbf{M}_{sn}$, of each individual shaft $n\,(n=1,2)$ are formed by assembling the stiffness and mass matrices of each beam element. Overall shaft stiffness and mass matrices of the system are then assembled as $\mathbf{K}_s = Diag[\mathbf{K}_{s1}, \mathbf{K}_{s2}]$ and $\mathbf{M}_s = Diag[\mathbf{M}_{s1}, \mathbf{M}_{s2}]$. Both matrices are square matrices of dimension q where $q = 6\sum_{n=1}^{2}(m_n+1)$ is the total number of degrees of freedom of the system (m_n is the number of beam elements used to model shaft n and each node has 6 DOFs).

In practical applications, each shaft is usually supported by at least two bearings of varying type and size. For a system having a total of n_b bearings, the overall bearing stiffness matrix of the complete system can be obtained by assembling the individual bearing stiffness matrices $\mathbf{K}_{bi} = Diag\left[k_{bxi}, k_{byi}, k_{bzi}, k_{b\theta_x i}, k_{b\theta_y i}, k_{b\theta_z i}\right]$ $(i = 1 \text{ to } n_b)$ as $\mathbf{K}_b = Diag\left[\cdots \mathbf{K}_{b1} \cdots \mathbf{K}_{b1} \cdots \mathbf{K}_{bn_b} \cdots\right]$. Then, the stiffness matrix of the whole shaft-bearing assembly can be written as $\mathbf{K} = \mathbf{K}_s + \mathbf{K}_b$. Assuming Rayleigh damping for the shafts and bearings for simplicity, the damping matrix of the shaft-bearing assembly is obtained as $\mathbf{C} = \beta\,\mathbf{K}$ where β is the Rayleigh damping coefficient.

Figure 4.1 shows the mesh coupling between the gears including gear backlash, mesh stiffness, mesh damping and static transmission error, which is along the line of action (LOA), i.e., in the direction of tooth normal. The parameters used to characterize a gear mesh such as gear mesh stiffness, damping, acting point and direction of effective spring-damper element vary substantially for spiral bevel gears due to the tooth geometry as the gear pair rolls. However, they are assumed to remain unchanged under dynamic conditions. A single point mesh model consisting of an effective mesh point and a constant line of action vector for a single spring-damper element is used in this study. Moreover, a time-invariant mesh stiffness is assumed for the gear pair, and gear mesh damping element is assumed not to be subjected to gear backlash nonlinearity in order to simplify the study.

Utilizing six degrees of freedom for each gear, the gear pair has a total of 12 degrees of freedom that defines the coupling between the two shafts holding the gears. The generalized coordinates of the gears are expressed as $\mathbf{x}_i = \{x_i, y_i, z_i, \theta_{xi}, \theta_{yi}, \theta_{zi}\}^T\,(i = p, g)$, which are relative to each local coordinate system $S_i\,(i = p, g)$ whose origin is at the pinion or gear centroid.

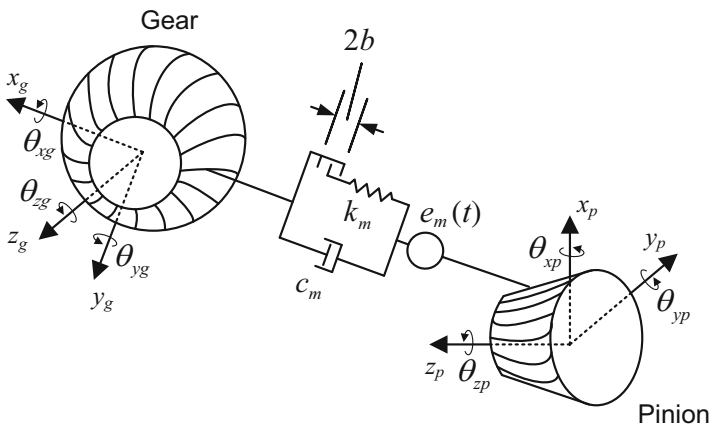

Fig. 4.1 Spiral bevel gear pair dynamic model

The dynamic transmission error along the LOA can be written as follows

$$\delta_d = \mathbf{h}_p \mathbf{x}_p - \mathbf{h}_g \mathbf{x}_g, \tag{4.1}$$

where $\mathbf{x}_i$ $(i = p, g)$ is the displacement vector and $\mathbf{h}_i$ $(i = p, g)$ is the transformation vector, consisting of the directional cosines and directional rotation radii between the LOA and the respective coordinates of pinion or gear. Transformation vectors can be expressed as

$$\mathbf{h}_i = \left\{ n_{ix}, n_{iy}, n_{iz}, \lambda_{ix}, \lambda_{iy}, \lambda_{iz} \right\} \quad (i = p, g)\,. \tag{4.2}$$

The directional rotation radii, λ, is defined as

$$\lambda_{ix} = \mathbf{n}_i \cdot (\mathbf{u}_{xi} \times \mathbf{r}_i) \quad (i = p, g)\,, \tag{4.3a}$$

$$\lambda_{iy} = \mathbf{n}_i \cdot \left(\mathbf{u}_{yi} \times \mathbf{r}_i\right) \quad (i = p, g)\,, \tag{4.3b}$$

$$\lambda_{iz} = \mathbf{n}_i \cdot (\mathbf{u}_{zi} \times \mathbf{r}_i) \quad (i = p, g)\,, \tag{4.3c}$$

where $\mathbf{r}_i = \{x_{im}, y_{im}, z_{im}\}^T$ is the position vector of the effective mesh point, $\mathbf{n}_i = \{n_{ix}, n_{iy}, n_{iz}\}^T$ is the directional cosine vector of LOA and $\mathbf{u}_{xi} = \{1\ 0\ 0\}^T$, $\mathbf{u}_{yi} = \left\{0\ 1\ 0\right\}^T$ and $\mathbf{u}_{zi} = \left\{0\ 0\ 1\right\}^T$ are the triad of unit vectors for coordinate system S_i. Subscript $i = p\,, g$ indicates that the quantity is defined in the local reference frame of the pinion or gear, respectively, in all the above equations.

The dynamic mesh force, F_m, along the LOA can be expressed as

$$F_m(t) = k_m f_n\left(\delta_d(t) - e_m(t)\right) + c_m\left(\dot{\delta}_d(t) - \dot{e}_m(t)\right), \tag{4.4}$$

where the nonlinear displacement function $f_n(\delta_d(t) - e_m(t))$ is defined as given in the following equation by considering backlash nonlinearity:

$$f_n\left(\delta_d(t) - e_m(t)\right) = \begin{cases} \delta_d(t) - e_m(t) - b, & \delta_d(t) - e_m(t) > b \\ 0, & |\delta_d(t) - e_m(t)| \le b \\ \delta_d(t) - e_m(t) + b, & \delta_d(t) - e_m(t) < -b \end{cases}. \tag{4.5}$$

Here, b denotes the half of the gear backlash.

Rearranging the order of nodes such that mesh nodes are located below the other nodes in the displacement vector, the equation of motion of the whole spiral bevel geared system can be written as

$$\mathbf{M}\ddot{\mathbf{x}}(t) + \mathbf{C}\dot{\mathbf{x}}(t) + \mathbf{K}\mathbf{x}(t) + \mathbf{F}_N(t) = \mathbf{F}(t), \tag{4.6}$$

where $\mathbf{F}(t)$ is the external force vector including the external torques T_i $(i = p, g)$ acting on the gears:

$$\mathbf{F}(t) = \mathbf{F} = \left\{ \{0\}\,,\ \left\{0\ 0\ 0\ 0\ 0\ T_p\right\},\ \left\{0\ 0\ 0\ 0\ 0\ -T_g\right\} \right\}^T. \tag{4.7}$$

In this study, only internal vibratory excitation, i.e., static transmission error, is considered by assuming constant torque values. The only nonzero elements of the forcing vector, $\mathbf{F}$, are the ones related to rotation of gears about z axis. Due to nonlinearity, the mesh stiffness k_m and the mesh damping c_m are incorporated into the equation of motion through the dynamic mesh force, which forms the nonlinear restoring force $\mathbf{F}_N(t)$ as given in the following equation:

$$\mathbf{F}_N(t) = F_m(t)\ \ \mathbf{p}, \tag{4.8}$$

where $\mathbf{p}$ denotes the extended form of the coordinate transformation vectors $\mathbf{h}_i$ $(i = p, g)$

$$\mathbf{p} = \left\{0,\ \ \mathbf{h}_p,\ \ -\mathbf{h}_g\right\}^T. \tag{4.9}$$

4.2.2 Solution Method

4.2.2.1 Multi-Term Harmonic Balance Method with DFT

In order to solve the nonlinear equations of motion for **x**, multi-term Harmonic Balance Method coupled with discrete Fourier Transform, which has been successfully applied in [3, 6–10], is used. Since static transmission error excitation is periodic, the solution and the nonlinear displacement function $f_n(\delta_d(t) - e_m(t))$ can also be described periodically [8]. The harmonic expressions for the static transmission error and its derivative with respect to time can be expressed as

$$e_m(t) = \sum_{j=1}^{J} \left[\varepsilon_{cj} \cos(j\omega t) + \varepsilon_{sj} \sin(j\omega t) \right], \tag{4.10a}$$

$$\dot{e}_m(t) = \sum_{j=1}^{J} \left[-(j\omega)\, \varepsilon_{cj} \sin(j\omega t) + (j\omega)\, \varepsilon_{sj} \cos(j\omega t) \right]. \tag{4.10b}$$

Given the periodic excitation defined by Eq. (4.10a), the steady-state solution can as well be assumed periodic as

$$\mathbf{x}(t) = \mathbf{u}_0 + \sum_{r=1}^{R} \left[\mathbf{u}_{cr} \cos(r\omega t) + \mathbf{u}_{sr} \sin(r\omega t) \right], \tag{4.11}$$

which can be differentiated to yield

$$\dot{\mathbf{x}}(t) = \sum_{r=1}^{R} \left[-(r\omega)\, \mathbf{u}_{cr} \sin(r\omega t) + (r\omega)\, \mathbf{u}_{sr} \cos(r\omega t) \right]. \tag{4.12}$$

Sampling N points within one fundamental mesh period, the time series of the dynamic mesh force can be obtained as

$$F_m(t_n) = k_m f_n \left(\mathbf{h}_p \mathbf{x}_p(t_n) - \mathbf{h}_g \mathbf{x}_g(t_n) - e_m(t_n) \right) + c_m \left(\mathbf{h}_p \dot{\mathbf{x}}_p(t_n) - \mathbf{h}_g \dot{\mathbf{x}}_g(t_n) - \dot{e}_m(t_n) \right), \tag{4.13}$$

where $t_n = n\rho$ $(n = 0, 1, 2, \cdots, N-1)$. Here, $\rho = 2\pi/(N\omega)$ and N must be larger than $2R$ where R is the highest harmonic number used in the solution in order to avoid aliasing errors.

Similarly, the dynamic mesh force can be represented by Fourier series as follows

$$F_m(t) = F_{m0} + \sum_{r=1}^{R} \left[F_{m(cr)} \cos(r\omega t) + F_{m(sr)} \sin(r\omega t) \right], \tag{4.14}$$

where, utilizing discrete Fourier Transform,

$$F_{m0} = \frac{1}{N} \sum_{n=0}^{N-1} F_m, \tag{4.15a}$$

$$F_{m(cr)} = \frac{2}{N} \sum_{n=0}^{N-1} F_m \cos\left(\frac{2\pi rn}{N} \right), \tag{4.15b}$$

$$F_{m(sr)} = \frac{2}{N} \sum_{n=0}^{N-1} F_m \sin\left(\frac{2\pi rn}{N} \right). \tag{4.15c}$$

Fourier coefficients of the nonlinear forcing vector $\mathbf{F}_N(t)$ can be obtained by using the extended form of the coordinate transformation vectors, **p**, given in Eq. (4.9) as

$$\mathbf{F}_N(t) = \mathbf{F}_{N(0)} + \sum_{r=1}^{R} \left[\mathbf{F}_{N(cr)} \cos(r\omega t) + \mathbf{F}_{N(cr)} \sin(r\omega t) \right], \tag{4.16a}$$

$$\mathbf{F}_{N(0)} = F_{m0}\,\mathbf{p}, \tag{4.16b}$$

$$\mathbf{F}_{N(cr)} = F_{m(cr)}\,\mathbf{p}, \tag{4.16c}$$

$$\mathbf{F}_{N(sr)} = F_{m(sr)}\,\mathbf{p}. \tag{4.16d}$$

Substituting Eqs. (4.11) and (4.16a) into Eq. (4.6) and equating the coefficients of the like harmonic terms, the following nonlinear equations are obtained for $r = 1, 2, \ldots R$

$$\mathbf{S}_0 = \mathbf{K}\cdot\mathbf{u}_0 + \left(\mathbf{F}_{N(0)} - \mathbf{F}_{(0)}\right) = 0, \tag{4.17a}$$

$$\mathbf{S}_r = \left(\mathbf{K} - (r\omega)^2\mathbf{M} + ir\omega\mathbf{C}\right)(\mathbf{u}_{sr} + i\,\mathbf{u}_{cr}) + \left(\mathbf{F}_{N(sr)} + i\,\mathbf{F}_{N(cr)}\right) - (\mathbf{F}_{sr} + i\,\mathbf{F}_{cr}) = 0. \tag{4.17b}$$

Equation (4.17a) is a real equation related to the bias terms while Eq. (4.17b) is a complex equation including the sine and cosine terms of the rth harmonic. Therefore, a total of $q\cdot(2R+1)$ nonlinear real equations are solved in order to obtain the dynamic response of the spiral bevel geared system considered in this study. The solution of this nonlinear equations set, i.e. displacement vector $\mathbf{U} = \{\mathbf{u}_0, \mathbf{u}_{c1}, \mathbf{u}_{s1}, \mathbf{u}_{c2}, \mathbf{u}_{s2}, \ldots, \mathbf{u}_{cR}, \mathbf{u}_{sR}\}^T$, is obtained by using Newton's Method with arc length continuation. Application of Newton's method results in the following iterative scheme

$$\mathbf{U}^{(k)} = \mathbf{U}^{(k-1)} - \left(\mathbf{J}^{-1}\right)^{(k-1)}\mathbf{S}^{(k-1)}, \tag{4.18}$$

where $\mathbf{U}^{(k)}$ denotes the k^{th} iterative solution based on the $(k-1)^{th}$ solution and $(\mathbf{J}^{-1})^{(k-1)}$ is the inverse of the Jacobian matrix of the nonlinear vector function, $\mathbf{S}$, estimated at the previous point $(k-1)$. The iteration procedure described by Eq. (4.18) is repeated until the vector norm of $\mathbf{S}^{(k)}$ is below a predefined error limit. Moreover, arc-length continuation method is used in the solution procedure and a new parameter, arc-length, which is the radius of a hypothetical sphere in which the next solution point is searched, is chosen as the continuation parameter instead of frequency in order to follow the solution path even at the turning points. Details of Newton's method with arc-length continuation can be found in [11–13].

4.3 Results and Discussion

A spiral bevel geared system with the parameters listed in Table 4.1 is considered as the example case. In order to simplify the study, a time-invariant mesh stiffness k_m is assumed for the gear pair and only the first harmonic of the static transmission error $e_m(t)$ is considered.

Firstly, the period-1 motion solutions obtained by HBM are compared to the results of the direct numerical integration (NI). Figure 4.2 shows the comparison of the root-mean-square (rms) values of the dynamic mesh force. The response of the corresponding linear system is also shown in Fig. 4.2. The resonance peaks in the linear response observed at $\omega = 1134$Hz, $\omega = 1744$Hz, $\omega = 3059$Hz, $\omega = 3984$Hz, $\omega = 4911$Hz and $\omega = 6608$Hz are the 2nd, 4th, 7th, 10th, 11th and 16th natural frequencies of the corresponding linear system. These entire modes exhibit coupled transverse-axial-rotational motions with non-zero relative gear mesh displacements. Three harmonics ($R = 3$ in Eq. (4.11)) are assumed in the HBM solution. The rms values are calculated as

$$F_m^{(rms)} = \left\{\frac{1}{2}\sum_{r=1}^{R}(A_r)^2\right\}^{1/2}, \tag{4.19}$$

where A_r is the amplitude of the r^{th} harmonic of $F_m(t)$ that can be expressed as

$$A_r = \sqrt{\left(F_{m(cr)}\right)^2 + \left(F_{m(sr)}\right)^2}. \tag{4.20}$$

It can be observed from Fig. 4.2 that both HBM and NI solutions agree well with each other except around the resonance peak observed at $\omega = 3952$Hz. This is due to the existence of subharmonic motions dictating this frequency range, which

Table 4.1 Parameters of the example system

	Pinion	Gear
Shaft parameters		
Outer diameter (mm)	55	70
Inner diameter (mm)	40	50
Length (mm)	202	234
β	$3(10^{-6})$	$3(10^{-6})$
Gear parameters		
Number of teeth	31	39
Spiral angle (°)	30	30
Normal pressure angle (°)	20	20
Pitch angle (°)	38.48	51.52
Pitch radius (mm)	65.1	81.9
Face width (mm)	34	34
Hand	Left	Right
Locations (mm)	172	209
T (Nm)	200	251.61
Bearing parameters		
Locations (mm)	42	74
	127	144
$\mathbf{k}_b$ (N/m, Nm/rad)	$Diag[2(10^9), 2(10^9), 1(10^9), 1(10^6), 1(10^6), 0]$	
Gear mesh parameters		
k_m (N/m)	$3(10^8)$	
c_m (Ns/m)	1500	
ε_{s1} (μm)	10	
b (μm)	20	

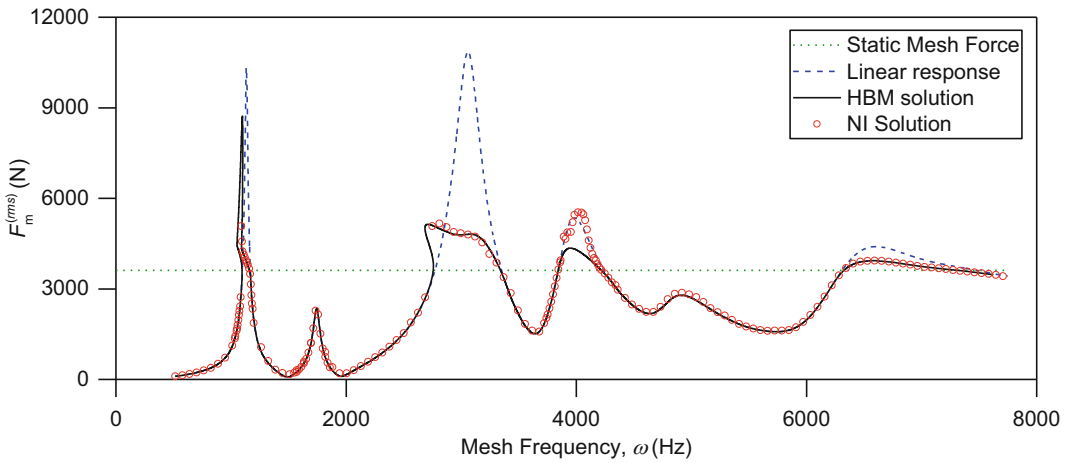

Fig. 4.2 Comparison of rms values of the dynamic mesh force $F_m(t)$ predicted by HBM and NI for $T = 200$Nm and $b = 20\,\mu$m

is illustrated in Fig. 4.3 showing the time trace and Fourier spectrum of the response at $\omega = 3952$Hz obtained by NI. The response is dominated by the subharmonics with the frequencies of 1/4 and 3/4 of the excitation frequency, i.e., the mesh frequency, as well as the fundamental harmonic. While the NI can capture these behaviors depending on the initial condition used, HBM cannot capture since the subharmonics are not included in the solutions assumed.

Past studies [1–4] show that spiral bevel gears can exhibit both single-sided and double-sided tooth impacts depending on the system parameters. Similar behaviors are also seen here in the results of both HBM and NI. It is seen from Fig. 4.4 that gear pair behaves quite linearly with no tooth impact in the low frequency range. When the frequency increases to $\omega = 1095$Hz, $F_m^{(\mathrm{rms})}$ forced response curve begins to exhibit single-sided tooth impact. Since this is a softening-type nonlinear behavior due to tooth separation, the response curve veers left towards the lower frequency range and continues along the same trajectory as the frequency decreases from $\omega = 1095$Hz to $\omega = 1052$Hz. At $\omega = 1052$Hz, double-sided tooth impact,

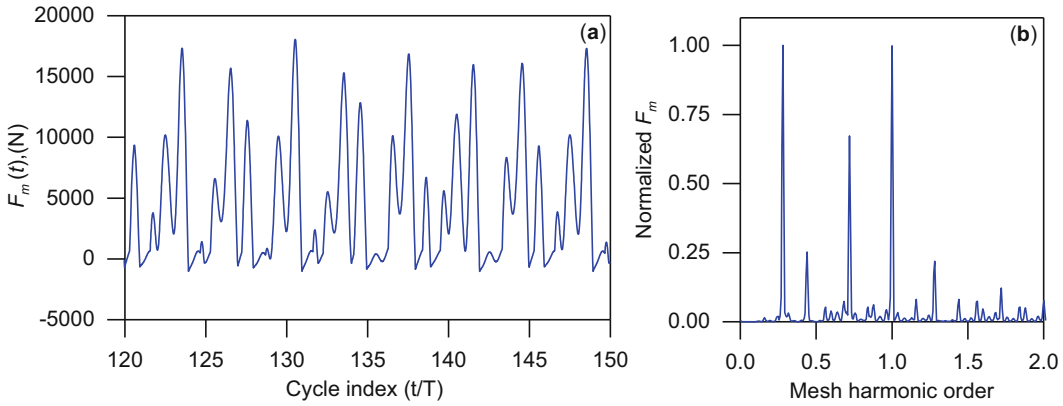

Fig. 4.3 (**a**) Time trace and (**b**) corresponding Fourier spectrum of $F_m(t)$ at $\omega = 3952$Hz obtained by NI

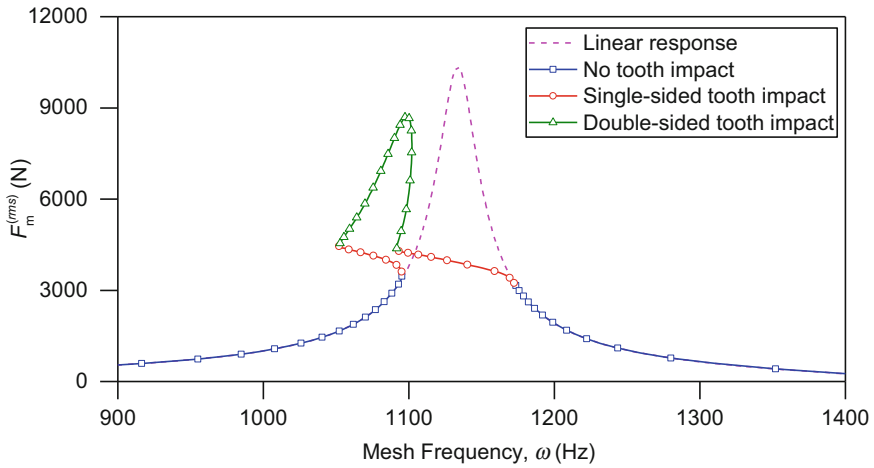

Fig. 4.4 Nonlinear behavior of the spiral bevel geared system

which includes both tooth separation and additional impact with the preceding tooth, begins to emerge. Due to the hardening with respect to single-sided tooth impact, the response curve takes a sharp turn towards the right and begins to climb in both amplitude and frequency. After reaching the peak amplitude at $\omega = 1098$Hz, the response curve begins to decrease in amplitude as the double-sided tooth impact behavior continues. When the frequency decreases to $\omega = 1092$Hz, the response changes back to single-sided tooth impact and becomes linear as the frequency increases further.

Returning back to Fig. 4.2, the effect of backlash nonlinearity shows itself as single-sided tooth impact around the 3rd, the 4th and the 6th resonance peaks observed at $\omega \cong 3060$Hz, $\omega \cong 3950$Hz and $\omega \cong 6590$Hz, respectively. Since the vibration amplitudes at these frequencies are small compared to the backlash amount, double-sided tooth impacts are not observed around these peaks. Another observation from Fig. 4.2 is that the amplitudes of the 2nd and the 5th resonance peaks observed at $\omega = 1744$Hz and $\omega = 4911$Hz, respectively, are smaller than the static mesh force. Therefore, the gear pair behaves linearly around these peaks.

The influence of the static mesh force on the dynamic response of the system due to different external torques is shown in Fig. 4.5 for $b = 20\,\mu$m. When the pinion torque is increased to $T = 400$Nm, tooth separation and tooth impact again occur, i.e., backlash nonlinearity is effective, around the 1st and the 3rd resonance peaks while the dynamic behavior of the gear pair around the other peaks is linear. It is also clear from Fig. 4.5 that tooth separation begins to show up at a higher response level compared to the case with $T = 200$Nm. As the pinion torque is increased further to $T = 800$Nm, the maximum amplitude of the dynamic mesh force remains below the amplitude of the static mesh force, i.e., dynamic factor is lower than 1, no loss of contact or tooth impact occurs. Therefore, the response of the nonlinear system is exactly the same as the corresponding linear system.

Figure 4.6 shows the influence of backlash amount, which is a significant parameter especially for lightly loaded gear systems. Only the frequency range around the 1st resonance peak is shown in Fig. 4.6, since doubled-sided tooth impacts are only observed in this range when $T = 200$Nm. When the backlash amount is increased to $b = 40\,\mu$m, double-sided tooth

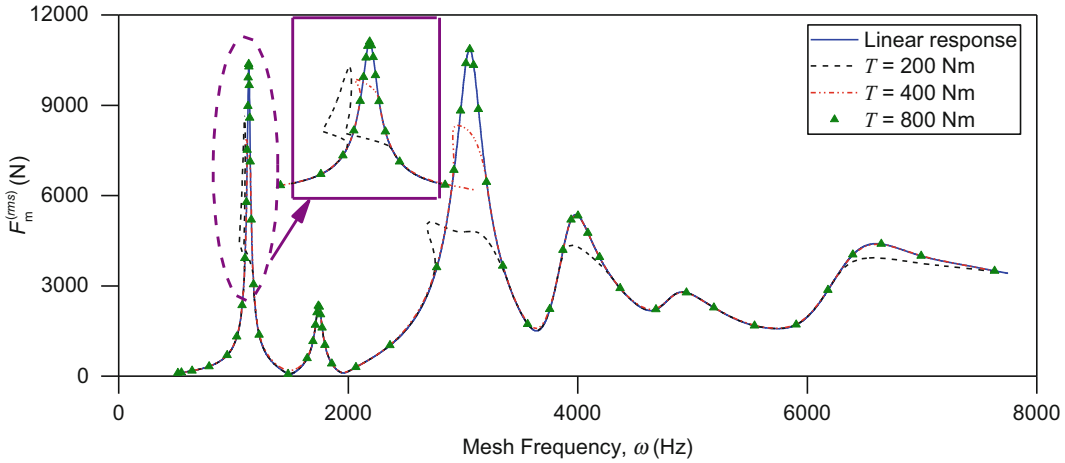

Fig. 4.5 Effect of static mesh force, i.e., external torque, on the dynamic response for $b = 20\,\mu$m

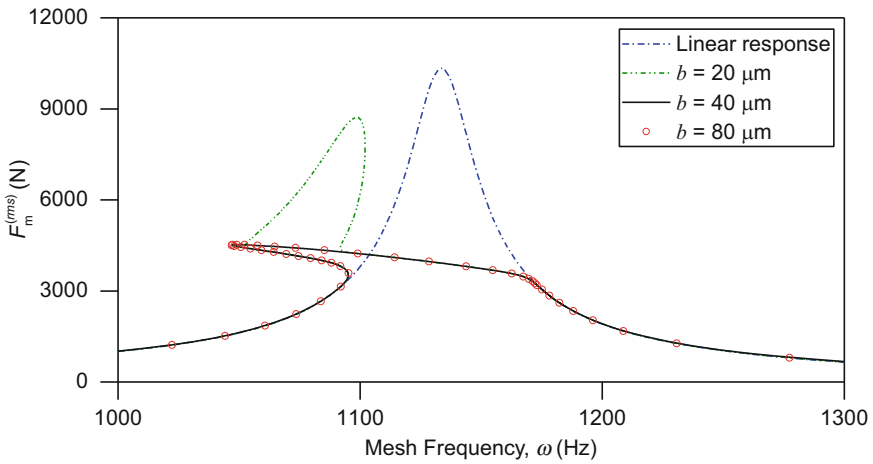

Fig. 4.6 Effect of backlash amount on the dynamic response for $T = 200$Nm

impact disappears, since the amplitude of the relative mesh displacement is smaller than the total amount of static deflection and backlash. Thus, single-sided tooth impacts dominate the nonlinear response range. As the backlash amount is increased further, since double-sided tooth impacts cannot occur, the nonlinear response of the system is not affected any more.

4.4 Conclusion

A nonlinear dynamic model of a spiral bevel gear train consisting of a finite element model of shaft-bearing assembly combined with a three-dimensional mesh model of a spiral bevel gear pair is formulated in this study. A multi-term Harmonic Balance Method in conjunction with discrete Fourier Transform is used to solve the resultant equations of motion for steady-state period-1 response. The solutions obtained by HBM are validated by comparing them to the solutions obtained by direct numerical integration. The results show that the spiral bevel gear pair exhibits nonlinear behavior as single-sided and double-sided tooth impacts with the given system parameters. Subharmonic motions are also observed in the results of direct numerical integration.

Forced vibration characteristics of the system are studied to demonstrate the influence of static mesh force and backlash amount. There is potential for loss of contact and tooth impact for lightly loaded cases, where the gear backlash is the critical factor for the range and appearance of nonlinear responses. In contrast, for heavily loaded cases, dynamic factor tends to be lower; hence, backlash nonlinearity becomes ineffective.

References

1. Cheng, Y., Lim, T.C.: Vibration analysis of hypoid transmissions applying an exact geometry-based gear mesh theory. J. Sound Vib. **240**(3), 519–543 (2001)
2. Wang, J., Lim, T.C., Li, M.: Dynamics of a hypoid gear pair considering the effects of time-varying mesh parameters and backlash nonlinearity. J. Sound Vib. **308**, 302–329 (2007)
3. Yang, J., Peng, T., Lim, T.C.: An enhanced multi-term harmonic balance solution for nonlinear period-one dynamic motions in right-angle gear pairs. Nonlinear Dyn. **67**(2), 1053–1065 (2011)
4. Peng, T., Lim, T.C.: Coupled multi-body dynamic and vibration analysis of high-speed spiral bevel geared rotor system. In: Proceedings of the SAE Noise and Vibration Conference and Exposition, St. Charles, IL, USA, 2007
5. Hua, X., Lim, T.C., Peng, T., Wali, W.E.: Dynamic analysis of spiral bevel geared rotor systems applying finite elements and enhanced lumped parameters. Int. J. Automot. Technol. **13**(1), 97–107 (2012)
6. Kahraman, A., Blankenship, G.W.: Steady state forced response of a mechanical oscillator with combined parametric excitation and clearance type non-linearity. J. Sound Vib. **185**(5), 743–765 (1995)
7. Kahraman, A., Blankenship, G.W.: Interactions between commensurate parametric and forcing excitations in a system with clearance. J. Sound Vib. **194**(3), 317–336 (1996)
8. Al-shyyab, A., Kahraman, A.: Non-linear dynamic analysis of a multi-mesh gear train using multi-term harmonic balance method: period-one motions. J. Sound Vib. **284**, 151–172 (2005)
9. Al-shyyab, A., Kahraman, A.: Non-linear dynamic analysis of a multi-mesh gear train using multi-term harmonic balance method: sub-harmonic motions. J. Sound Vib. **279**, 417–451 (2005)
10. Yavuz, S.D., Saribay, Z.B., Cigeroglu, E.: Nonlinear time-varying dynamic analysis of a multi-mesh spur gear train. In: Proceedings of the 34th IMAC, A Conference and Exposition on Structural Dynamics, Orlando, FL, USA, 2016
11. Cigeroglu, E., Samandari, H.: Nonlinear free vibration of double walled carbon nanotubes by using describing function method with multiple trial functions. Physica E. **46**, 160–173 (2012)
12. Yümer, M.E., Ciğeroglu, E., Özgüven, H.N.: Non-linear forced response analysis of mistuned bladed disk assemblies. In: Proceedings of the ASME Turbo Expo 2010: Power for Land, Sea and Air, Glascow, UK, 2010
13. Von Groll, G., Ewins, D.J.: The harmonic balance method with arc-length continuation in rotor/stator contact problems. J. Sound Vib. **241**(2), 223–233 (2001)

Chapter 5
Estimating Material Wavespeed Using the Wavenumber Transform of Rectangular Plate Mode Shapes

Micah R. Shepherd

Abstract Experimental modal analysis is often used to estimate the natural frequencies and damping of a material sample. While the geometry of the sample is often arbitrary, thin rectangular samples are easy to manufacture, model and test and therefore are commonly-used for these measurements. The roving hammer approach can be used to collect frequency response functions at a rectangular grid of points located on plate. Once the mode shapes have been estimated for the rectangular sample, the discrete wavenumber transform can be used to find the wavenumber spectrum of each mode. For simply-supported boundary conditions, the relationship between the mode shape and the modal wavenumber can be determined analytically using the length of the plate and the distance between zeros in the wavenumber spectrum. For the more realistic free-free boundary, no simple relationship holds. However, it will be shown that the wavenumber verse frequency curve can still be accurately estimated using thin-plate theory to minimize the error of the modal wavenumber at each of the modes. The wavenumber curve can then be used to obtain the material wavespeed.

Keywords Vibration • Modal analysis • Wavenumber transform • Wavespeed • Acoustics

5.1 Introduction

The bending wavespeed of a material is an important characteristic in defining the vibration and sound radiation of a structure and depends on fundamental material properties such as density, ρ, and Young's modulus, E. If E of a material is not known, it is difficult to model or predict the vibration. This paper shows that the material wavespeed can be accurately estimated using experimental modal analysis of rectangular plate of that material and the discrete Fourier transform (DFT) of its mode shapes. The combination of modal wavenumbers and natural frequencies can then be used to estimate the bending wavespeed. Results are presented for an aluminum, rectangular plate, whose natural frequencies and mode shapes were obtained in free conditions using experimental modal analysis.

5.2 Methodologies

5.2.1 Wavenumber Transform Theory

In order to represent the spatial energy distribution of mode shape, the wavenumber transform can be used. For a thin, rectangular plate with dimensions L_x x L_y and simply-supported boundaries, the flexural mode shapes are described by

$$\Psi_{mn}(x,y) = \sin\left(\frac{m\pi x}{L_x}\right)\sin\left(\frac{n\pi y}{L_y}\right), \tag{5.1}$$

where m and n are positive, non-zero integers representing the mode order in the x and y directions respectively. The wavenumber representation of the normal modes is a result of a two-dimensional Fourier transform in the spatial coordinates x and y:

M.R. Shepherd (✉)
Applied Research Laboratory, The Pennsylvania State University, PO Box 30, State College, PA 16801, USA
e-mail: mrs30@psu.edu

D. Di Maio, P. Castellini (eds.), *Rotating Machinery, Hybrid Test Methods, Vibro-Acoustics & Laser Vibrometry, Volume 8*,
Conference Proceedings of the Society for Experimental Mechanics Series, DOI 10.1007/978-3-319-54648-3_5

$$S_{mn}(k_x, k_y) = \int_{-\infty}^{\infty} \int_{-\infty}^{\infty} \Psi_{mn}(x, y) e^{-jk_x x} e^{-jk_y y} dxdy, \tag{5.2}$$

where k_x, k_y are the wavenumbers in the x and y directions.

The integral in Eq. (5.2) is separable in x and y, and for the x-direction alone reduces to

$$S_m(k_x) = \frac{k_m[(-1)^m e^{-jk_x L_x} - 1]}{k_x^2 - k_m^2}, \tag{5.3}$$

where $k_m = m\pi/L_x$ is the modal wavenumber [1]. The energy spectrum or wavenumber sensitivity function can be found by squaring the magnitude of Eq. (5.3):

$$|S_m(k_x)|^2 = \frac{2(k_m)^2\big(1 - (-1)^m \cos(k_x L_x)\big)}{(k_x^2 - k_m^2)^2}. \tag{5.4}$$

Using a series of trigonometric identities, an alternative formulation of Eq. (5.4) is given as

$$|S_m(k_x)|^2 = \left[\frac{2k_m}{k_x^2 - k_m^2}\right]^2 \sin^2\left(\frac{k_x L_x - k_m L_x}{2}\right). \tag{5.5}$$

Recent work by Shepherd and Hambric show that k_m of a mode shape can be identified from a modal wavenumber spectrum using

$$k_m = k_{z1} - 2\pi/L_x, \tag{5.6}$$

where k_{z1} is the wavenumber of the first zero after the peak value [2]. A graphical version of Eq. (5.6) is shown in Fig. 5.1. This result was also verified experimentally using a special rig to create simply-supported boundaries on a rectangular plate [3].

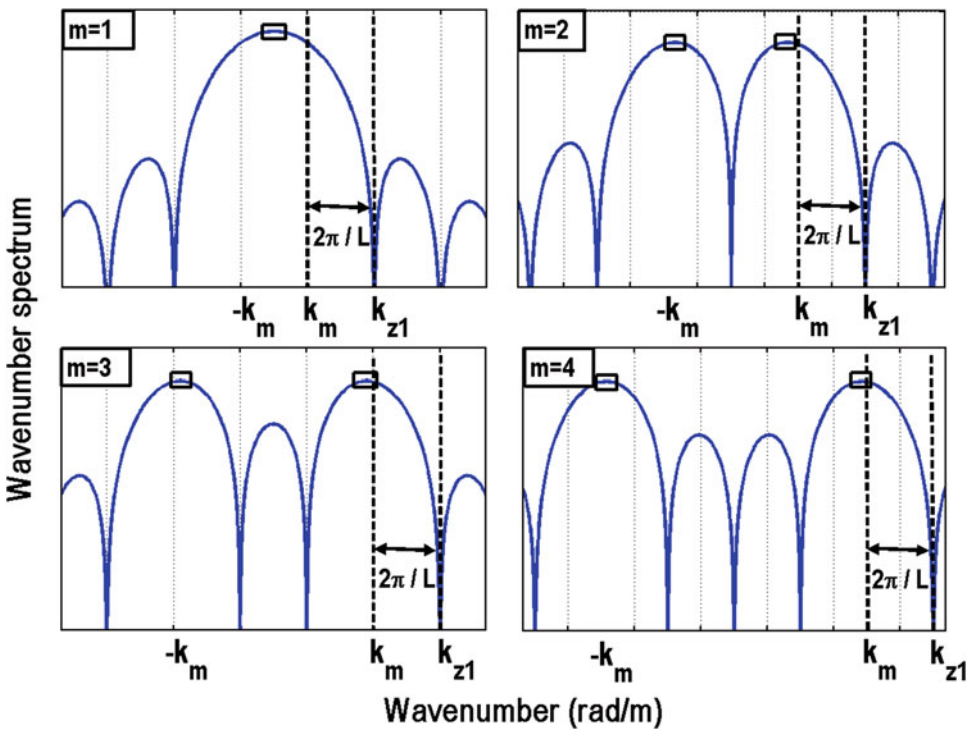

Fig. 5.1 Using the wavenumber transform of a rectangular plate mode shape with simply-supported mode shapes, the modal wavenumber can be found from the zeros in the spectrum. The results for four simply-supported mode shapes are shown

In practice, it is simpler and more common to measure the modes of structures with free boundary conditions than simply-supported. However, for a thin, rectangular plate, the mode shapes are defined by hyperbolic sine and cosine functions which prohibit the analytical determination of their wavenumber spectrum and subsequent computation of the modal wavenumber.

5.2.2 Discrete Wavenumber Transform

It is often convenient to estimate a plate's mode shape at regularly-spaced intervals in x and y. For implementation of the 2-D wavenumber transform with this discrete data, the discrete Fourier transform (DFT) must be used. The infinite bounds are reduced to a finite number defined by the inverse of the spatial step size multiplied by 2π. This is analogous to the sampling frequency equaling the inverse of the sampling period for discrete time data, with the 2π factor necessary since we are using the cyclic frequency (i.e. $\omega = 2\pi/T \rightarrow k = 2\pi/\lambda$ so that $f \rightarrow k/2\pi$ and $dt \rightarrow dx/2\pi$). In order to resolve high wavenumbers, a small spatial step must be used. The wavenumber resolution is defined by the inverse of the spatial length multiplied by 2π (since $T \rightarrow L/2\pi$). The plate can be thought of as being in an infinite baffle as there exists no motion outside the boundaries of the plate. Therefore, any desired wavenumber resolution can be achieved by placing the mode shape data in a matrix of zeros, a procedure often referred to as "zeropadding." In summary, the x component of the wavenumber vector is defined as

$$k_x = -\frac{\pi}{dx} : \frac{2\pi}{\bar{L}} : \frac{\pi}{dx}, \tag{5.7}$$

where $\bar{L}$ is the effective length of plate with zero-padding.

In practice, the discrete Fourier transform can be efficiently computed using the two-dimensional fast Fourier transform (fft) algorithm. Using only the plate length (L) without zeropadding will almost always result in very low wavenumber resolution and significant wavenumber leakage. Therefore, the modeshape data should always be zeropadded prior to taking the DFT. While a zero-pad factor (Z_p) of 10 or 20 is usually sufficient, Z_p can be set arbitrarily to achieve any desired wavenumber resolution. Figure 5.2 compares the wavenumber energy spectrum of a rectangular plate mode shape using the DFT to the analytical form of the wavenumber energy spectrum. The error is very small at and near the peak wavenumber and is only 1–2 dB as you get to higher wavenumbers. The zeros in the spectrum are matched very well due to zeropadding.

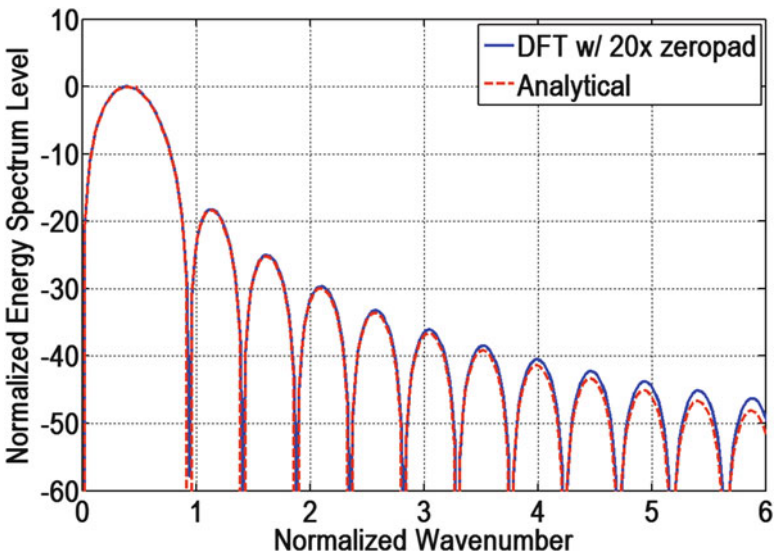

Fig. 5.2 The wavenumber transform of a plate mode shape can be well estimated using the discrete Fourier transform

5.2.3 Determination of Mode Shapes

To determine the natural frequencies and mode shapes of the rectangular plate, experimental modal analysis was used. A regular grid of eqi-spaced points are laid out on the plate and a roving hammer is used to excite the plate with an impulse. Fixed reference accelerometers are attached to the plate and the force-to-acceleration transfer functions are simultaneously acquired.

The matrix of acceleration to force transfer functions were processed using the singular value decomposition, one frequency at a time. The data were arranged in matrix form with each column representing the response to a different drive point and each row representing a different response point. The resulting matrix was input to the singular value decomposition algorithm, which decomposes the matrix into three matrices as

$$\boldsymbol{H}(\omega_0) = \boldsymbol{U}(\omega_0)\boldsymbol{S}(\omega_0)\boldsymbol{V}^H(\omega_0), \tag{5.8}$$

where ω_0 is the analysis frequency. The matrix $\boldsymbol{U}$ represents the vibration patterns associated with each of the singular values, and thus are interpreted as unscaled mode shapes. The matrix $\boldsymbol{V}$ represents the required input forces at the drive points to excite the left-singular vectors and is therefore discarded in this analysis. In general, the $\boldsymbol{U}$ and $\boldsymbol{V}$ matrices do not change significantly from one frequency to the next, and thus most of the frequency dependence in the transfer function data is contained in the singular values. In this implementation, 128 frequency bins were used for each modal transfer function.

The SVD algorithm relegates noise to the lowest singular values, thus reducing the noise levels in the top few curves that typically contain most of the modal information. Unfortunately, the singular values are output from the decomposition in order of magnitude, so that they switch the modes they are tracking whenever two singular values cross. This problem is avoided by computing modal transfer functions, which force the singular values to track a single mode. These functions are computed by using the singular value decomposition at an initial frequency to decompose the transfer function matrix at nearby frequencies as

$$\bar{\boldsymbol{S}} = \boldsymbol{U}^H(\omega)\boldsymbol{H}(\omega)\boldsymbol{V}(\omega_0). \tag{5.9}$$

The overbar on the matrix S indicates that it is no longer real-valued or diagonal. Savitz-Golay filters are applied to the data to reduce noise and the modal assurance criteria (MAC) is used to detect duplicate modes. Once a peak is found, the modal parameters are then estimated using a linear least squares circle fit of the modal transfer function equation for a single mode.

To refine the SVD estimates for the resonance frequencies and loss factors, the modal parameters are then updated using rational fraction polynomial (RFP) curve-fitting. Residual contributions of nearby modes are accounted for using higher-order polynomial fits. The displacement data can then be synthesized once the resonance frequencies, loss factors, and mass normalized mode shapes have been determined. More details on experimental modal analysis can be found in [4].

5.2.4 Computation of Wavespeed

Once the mode shapes are estimated for the plate, the wavenumber spectrum is computed using the DFT. The modal wavenumber for each mode can then be estimated by finding the zeros in the spectrum and applying Eq. (5.6). Once this procedure is performed for each mode, the set of modal wavenumbers and their accompanying natural frequencies can be used to compute the bending wavespeed using $c_b(\omega) = \omega_m/k_m$.

The wavespeed can only be estimated at the natural frequencies of the plate and therefore will not be defined below the first modal frequency. However, the zero m/s wavespeed at zero Hz can be appended to the set to fill in an estimate of the wavespeed in the low frequency range. To minimize any errors in the wavespeed estimation, a least-squares fit can be used to smooth out the curve. Given the thickness and density of the plate, the Young's modulus can be found which minimizes the error between the experimentally-obtained wavespeeds and those predicted using bending theory for thin plates.

5.3 Results: Thin, Aluminum Plate

A thin, aluminum plate was used validate the wavespeed approach. The dimensions of the plate are listed in Table 5.1. A rectangular grid of 221 hit points were laid out on the plate and five accels were adhered to the surface. Bungee cords were

Table 5.1 Properties of the rectangular, aluminum plate

Property	Value
L_x	0.305 m
L_y	0.422 m
Δ_x	2.54 cm
Δ_y	2.64 cm
Thickness	9.54 mm
Mass	3.32 kg

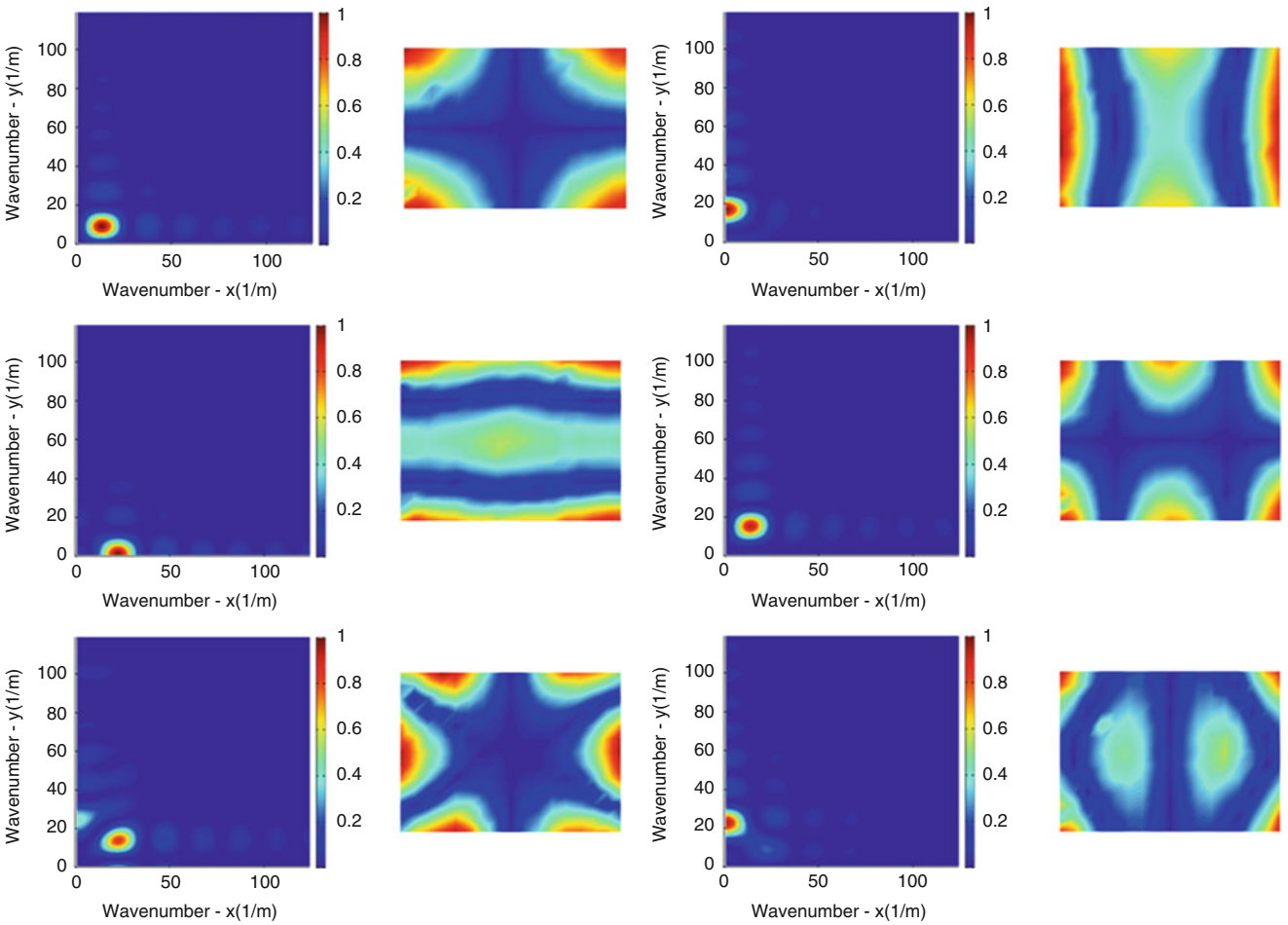

Fig. 5.3 The mode shape and wavenumber spectrum for the first six plate modes

used to suspend the plate to simulate free boundary conditions. The modes and natural frequencies were estimated using the previously-described procedure.

The wavenumber spectrum was then computed for each mode using a zeropad factor of 20. Several representatives mode shapes are shown in Fig. 5.3 with their respective wavenumber transform. The negative portions of the spectra are omitted.

The modal wavenumber was estimated in both the x and y directions and combined using $k_m^2 = k_x^2 + k_y^2$. The wavespeed at each natural frequency was then computed, as shown in Fig. 5.4. The analytical wavespeed is also shown to verify the general accuracy of the procedure. While some of the error in the wavespeed estimate is due to inaccuracies in the estimated mode shapes, it is speculated that additional error occurs due to the effect of Poisson's ratio on the mode shapes.

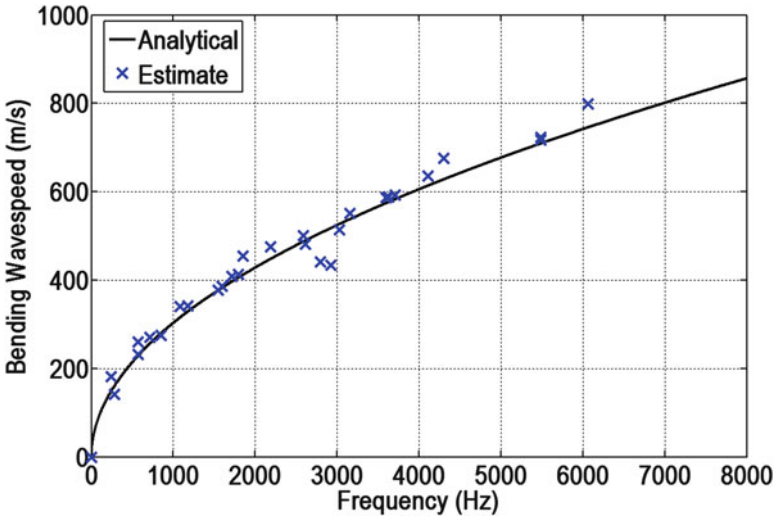

Fig. 5.4 The wavespeed estimates match the analytical wavespeed well

5.4 Conclusions

The wavenumber transform has been used to estimate the material wavespeed of a thin, rectangular isotropic plate with free boundary conditions. Previous theory regarding the modal wavenumber of simply-supported plate mode shapes was used and found to produce accurate estimates. This procedure can be used to estimate the wavespeed for any rectangular plate and would be especially useful if material properties are not known.

References

1. Fahy, F., Gardonio, P.: Sound and Structural Vibration, 2nd edn. Academic, Oxford (2007)
2. Shepherd, M.R., Hambric, S.A.: Comment on plate modal wavenumber transforms. In: Sound and Structural Vibration. Academic, New York (1987, 2007). J. Acoust. Am. **132**(4), 2155–2157 (2012)
3. Robin, O., Berry, A., Atalla, N., Hambric, S.A., Shepherd, M.R.: Experimental evidence of the modal wavenumber relation to zeros in the wavenumber spectrum of a rectangular simply supported isotropic thin plate. J. Acoust. Am. **137**(5), 2978–2981 (2015)
4. Ewins, D.J.: Modal Testing, Theory, Practice, and Application, 2nd edn. Wiley, New York (2009)

Chapter 6
In-Operation Wind Turbine Modal Analysis via LPV-VAR Modeling

L.D. Avendaño-Valencia, E.N. Chatzi, and S.D. Fassois

Abstract This work deals with the identification of non-stationary/time-dependent dynamics based on vector measurements by means of postulated Linear Parameter Varying Vector AutoRegressive models, applied to the identification of the vibration response of an operating wind turbine blade. The focus here lies in estimation of the model parameters and their corresponding covariances, as well as the calculation of "frozen" modal quantities from identified models. The proposed methodology is verified on a simulated case study, consisting of an operational wind turbine blade.

Keywords Linear parameter varying models • Operational modal analysis • Non-stationary vibration • Wind turbine vibration

6.1 Introduction

The main topic of this work is the monitoring-based identification of modal parameters (modal frequencies and shapes) of wind turbine blades in regular operating conditions. This is a challenging problem necessitating adoption of specialized methods able to account for the time-dependent dynamics in the vibration response of operational wind turbines [1, 2]. Currently available methods comprise, for the most part, extensions or modifications of conventional Operational Modal Analysis (OMA) techniques, which are based on non-parametric spectral analysis techniques [1, 3, 4]. These methods are formulated on the basis of the following assumptions: (1) the spectral density of the excitation forces is flat; (2) the rotational speed of the wind turbine is "almost" constant. Furthermore, sufficiently long records are required to attain acceptable resolution in the frequency domain. Clearly, these requirements hardly ever satisfied in a real-life environment.

In recent works of the authoring team [5, 6], Linear Parameter Varying AutoRegressive (LPV-AR) models have been postulated for the representation of the vibration response of wind turbines, where the (instantaneous) rotor azimuth acts as a (short-term) scheduling variable. Incorporation of this feature facilitates the tracking of time-dependent dynamics due to variable rotor configurations while accounting for changing rotor speeds. Given their parametric nature, LPV-AR models offer improved tracking accuracy and resolution compared to the non-parametric counterpart. Following up from our previous works, the present contribution aims at providing an identification methodology based on LPV Vector AR (LPV-VAR) models for the representation of the vibration response of operating wind turbines at different locations on the blade.

The following methodological issues are tackled in this paper: (1) *Estimation of the parameters of the LPV-VAR model*: In earlier studies [7], the estimation was based on the vectorization of the parameter matrix, leading to a very large regression matrix ($O(n^2)$, with n denoting the dimension of the measurement vector) which is later involved in an inversion operation to evaluate the estimates of the model coefficients. In the framework presented here, the parameter matrices are estimated directly (avoiding the vectorization operation), leading to reduced-size regression matrix ($O(n)$) and an alleviation of the computational burden on estimation. (2) *Computation of the covariance matrix of the estimated parameters:* The results of asymptotic analysis presented in [8, Chap. 9] are adapted to the case of the postulated LPV-VAR model. (3) *Modal analysis based on identified LPV-VAR models:* A modal analysis procedure is postulated based on the concept of "frozen" modal

L.D. Avendaño-Valencia (✉) • E.N. Chatzi
Department of Civil, Environmental and Geomatic Engineering, Institute of Structural Engineering, ETH Zürich, Stefano-Franscini-Platz 5, 8093 Zürich, Switzerland
e-mail: avendano@ibk.baug.ethz.ch

S.D. Fassois
Stochastic Mechanical Systems and Automation Laboratory, Department of Mechanical and Aeronautical Engineering, University of Patras, University Campus, Rio, Patras, Greece

D. Di Maio, P. Castellini (eds.), *Rotating Machinery, Hybrid Test Methods, Vibro-Acoustics & Laser Vibrometry, Volume 8*,
Conference Proceedings of the Society for Experimental Mechanics Series, DOI 10.1007/978-3-319-54648-3_6

quantities [9], from which "frozen" natural frequencies and damping ratios may be obtained. Within this context, a method for the extraction of mode shapes associated with a particular "frozen" natural frequency is formulated.

The methods discussed in this work are evaluated on a simulated case study, produced via the use of the FAST aeroelastic simulation code [10]. Acceleration time series are assumed as available measurements from different sensor locations along the blade, with the wind turbine operating normally and under typical wind conditions.

6.2 Methods

6.2.1 The Linear Parameter Varying Vector AR model

A Linear Parameter Varying Vector AR (LPV-VAR) model, of a multivariate time-series $\boldsymbol{y}[t] \in \mathbb{R}^n$, is defined as follows [5]:

$$\boldsymbol{y}[t] = \sum_{i=1}^{n_a} \boldsymbol{A}_i(\beta[t]) \cdot \boldsymbol{y}[t-i] + \boldsymbol{w}[t] \qquad \boldsymbol{w}[t] \sim \texttt{NID}\,(0, \boldsymbol{\Sigma}_{\boldsymbol{w}}) \tag{6.1}$$

where n_a is AR order, $\boldsymbol{A}_i(\cdot) \in \mathbb{R}^{n\times n}$, for all $i = 1, \ldots, n_a$ are the LPV parameter matrices, $\beta[t] \in [0, 1]$ is a scheduling variable, and $\boldsymbol{w}[t] \in \mathbb{R}^n$ is a multivariate NID innovations with zero mean and covariance matrix $\boldsymbol{\Sigma}_{\boldsymbol{w}} \in \mathbb{R}^{n\times n}$.

An important component of the model is the scheduling variable, which is a variable determining the instantaneous dynamics of the system, and consequently the instantaneous values of the model parameters. For example, in the case of wind turbines and other rotating systems, the scheduling variable may be the instantaneous rotor angle. Also, in the case of time-dependent systems, the scheduling variable may be directly time, in which case the model simplifies into a Time-dependent VAR model [7, 9]. For convenience, in the present formulation the scheduling variable is constrained to lie in the [0, 1] interval. In actual implementations, where this assumption may be violated, a normalization procedure may be simply put in place.

According to the previous discussion, the parameter matrices comprise functions of the scheduling variable, and their evolution is determined by the following functional series expansion [5]:

$$\boldsymbol{A}_i(\beta) \triangleq \sum_{j=1}^{p_a} \boldsymbol{A}_{i,j} \cdot g_{b_{a(j)}}(\beta) \tag{6.2}$$

where p_a is the order of the functional series expansion, $\boldsymbol{A}_{i,j} \in \mathbb{R}^{n\times n}$, $\forall j = 1, \ldots, p_a$ are the projection matrices, $g_\ell(\cdot) \in \mathbb{R}$ is a real valued function belonging to the functional subspace F, which contains the (infinite) set of ordered set of indexed real valued functions, defined as follows:

$$F = \{g_\ell(\cdot) | \forall \ell \in \mathbb{N}_0\} \tag{6.3}$$

and $b_{a(j)}, \forall j = 1, \ldots, p_a$ are the coefficients of the functions used in the functional series expansion, which may be grouped in the vector $\boldsymbol{b_a} = \left[b_{a(1)}\ b_{a(2)} \cdots b_{a(p_a)}\right]^T$. In the simplest case, the index vector may be constructed from consecutive basis indices up to the a certain value, as in $\boldsymbol{b_a} = \left[0\ 1\ 2 \cdots 10\right]^T$, while some of these indices may be omitted, as in $\boldsymbol{b_a} = \left[0\ 2\ 4 \cdots 10\right]^T$, which may allow for a more compact representation when certain functions are deemed unnecessary.

After introducing Eq. (6.2) into Eq. (6.1), it is easy to see that the LPV-VAR model is linear in the parameters. Moreover, after collecting terms and reorganizing the equation, it is possible to obtain the alternative formulation of the LPV-VAR model as a single matrix product, as follows:

$$\boldsymbol{y}[t] = \boldsymbol{\Theta} \cdot \boldsymbol{\Phi}(\beta[t], \boldsymbol{y}_{t-n_a}^{t-1}) + \boldsymbol{w}[t] \tag{6.4}$$

where $\boldsymbol{\Theta}$ is the parameter matrix and $\boldsymbol{\Phi}(\beta[t], \boldsymbol{y}_{t-n_a}^{t-1})$ is the regression matrix, both defined as:

$$\boldsymbol{\Phi}(\beta[t], \boldsymbol{y}_{t-n_a}^{t-1}) = \begin{bmatrix} \boldsymbol{g}(\beta[t]) \otimes \boldsymbol{y}[t-1] \\ \boldsymbol{g}(\beta[t]) \otimes \boldsymbol{y}[t-2] \\ \vdots \\ \boldsymbol{g}(\beta[t]) \otimes \boldsymbol{y}[t-n_a] \end{bmatrix}_{n \cdot n_a \cdot p_a \times 1} \tag{6.5a}$$

$$\boldsymbol{g}(\beta[t]) = \begin{bmatrix} g_{b_{a(1)}}(\beta[t]) \\ g_{b_{a(2)}}(\beta[t]) \\ \vdots \\ g_{b_{a(p_a)}}(\beta[t]) \end{bmatrix} \tag{6.5b}$$

$$\boldsymbol{\Theta} = \begin{bmatrix} \boldsymbol{A}_{1,1} \cdots \boldsymbol{A}_{1,p_a} \mid \cdots \mid \boldsymbol{A}_{n_a,1} \cdots \boldsymbol{A}_{n_a,p_a} \end{bmatrix}_{n \times n \cdot n_a \cdot p_a} \tag{6.5c}$$

which is referred to as the *regression form* of the LPV-VAR model.

6.2.1.1 Estimation of the Parameter Matrix and Innovations Covariance Matrix

An important issue regarding the application of the postulated LPV-VAR model is the estimation of the parameter matrix $\boldsymbol{\Theta}$ and the innovations covariance matrix $\boldsymbol{\Sigma}_{\boldsymbol{w}}$. The present discussion is limited to the parameter estimation by means of least squares methods, which aims at minimizing the sum of squared errors defined as [8, Chap. 7]:

$$\hat{\boldsymbol{\Theta}}_{OLS} := \underset{\boldsymbol{\Theta} \in \mathbb{R}^{n \times n \cdot n_a \cdot p_a}}{\arg\min} \ \operatorname{tr}\left(\boldsymbol{E}^T(\boldsymbol{\Theta}) \cdot \boldsymbol{E}(\boldsymbol{\Theta})\right) \tag{6.6}$$

$$\boldsymbol{E}(\boldsymbol{\Theta}) = \begin{bmatrix} \boldsymbol{e}[n_a+1|\boldsymbol{\Theta}] \ \boldsymbol{e}[n_a+2|\boldsymbol{\Theta}] \cdots \boldsymbol{e}[N|\boldsymbol{\Theta}] \end{bmatrix}_{n \times (N-n_a)}$$

where $\operatorname{tr}(\cdot)$ represents the trace operation and $\boldsymbol{e}[t|\boldsymbol{\Theta}]$ is the one-step-ahead prediction error of the LPV-VAR model, defined in terms of the regression form of the LPV-VAR model as follows:

$$\boldsymbol{e}[t|\boldsymbol{\Theta}] := \boldsymbol{y}[t] - \boldsymbol{\Theta} \cdot \boldsymbol{\Phi}(\beta[t], \boldsymbol{y}_{t-n_a}^{t-1}) \tag{6.7}$$

and is referred to as the *Ordinary Least Squares* (OLS) estimate of the parameter matrix.

Based on the optimization criterion shown in Eq. (6.6), and after computing the gradient with respect to the parameters and solving for $\boldsymbol{\Theta}$, it may be shown that the OLS estimate can be computed as:

$$\hat{\boldsymbol{\Theta}}_{OLS} = \boldsymbol{Y} \cdot \boldsymbol{\Phi}^T \cdot (\boldsymbol{\Phi} \cdot \boldsymbol{\Phi}^T)^{-1} \tag{6.8}$$

where $\boldsymbol{Y} \in \mathbb{R}^{n \times N - n_a}$ is the response super-matrix and $\boldsymbol{\Phi} \in \mathbb{R}^{n \cdot n_a \cdot p_a \times N - n_a}$ the regression super-matrix, defined as:

$$\boldsymbol{Y} = \begin{bmatrix} \boldsymbol{y}[n_a+1] \ \boldsymbol{y}[n_a+2] \cdots \boldsymbol{y}[N] \end{bmatrix}_{n \times N - n_a}$$

$$\boldsymbol{\Phi} = \left[\boldsymbol{\Phi}(\beta[n_a+1], \boldsymbol{y}_1^{n_a}) \ \boldsymbol{\Phi}(\beta[n_a+2], \boldsymbol{y}_2^{n_a+1}) \cdots \boldsymbol{\Phi}(\beta[N], \boldsymbol{y}_{N-n_a}^{N-1}) \right]_{n \cdot n_a \cdot p_a \times (N-n_a)}$$

Moreover, the innovations covariance matrix may be estimated from the one-step-ahead prediction error as:

$$\hat{\boldsymbol{\Sigma}}_{\boldsymbol{w}} = \frac{1}{N-n_a}\left(\boldsymbol{E}(\hat{\boldsymbol{\Theta}}_{OLS}) \cdot \boldsymbol{E}^T(\hat{\boldsymbol{\Theta}}_{OLS})\right) \tag{6.9}$$

Remark 1. The OLS estimator provided in Eq. (6.8) is of a different structure than the one derived in [7], which is based on the vectorization of the parameter matrix. A consequence of this difference is that the regression matrix in the present case is of dimension $n \cdot n_a \cdot p_a$ rows by $N - n_a$ columns, while the regression matrix in the vectorized framework is of dimension $n^2 \cdot n_a \cdot p_a$ rows by $N - n_a$ columns. Therefore, although the results are rendered identical, the computational savings are significant, particularly with respect to the computation of the inverse.

Remark 2. It is possible to consider a time-dependent innovations covariance, in which case, a functional series expansion may be considered for the representation of the time-dependent covariance matrix, following the approach already demonstrated for the parameters of the LPV-VAR model. This possibility is further elaborated upon in [7].

6.2.2 Covariance Matrix of the Parameter Estimates

An estimate of the covariance matrix of the parameter estimates may also be inferred. To this end, it is necessary to transform the parameter matrix into a vector using the vectorization operation [11, p. 244], which stacks the columns of an $n \times p$ matrix into a column vector of size $n \cdot p \times 1$. Then, the regression form of the LPV-VAR model in Eq. (6.4) can be alternatively written as follows [11, p. 254]:

$$\text{vec}\{\boldsymbol{y}[t]\} = \left(\boldsymbol{\Phi}^T(\beta[t], \boldsymbol{y}_{t-n_a}^{t-1}) \otimes \boldsymbol{I}_n\right) \cdot \text{vec}\{\boldsymbol{\Theta}\} + \text{vec}\{\boldsymbol{w}[t]\} \tag{6.10}$$

Besides,

$$\text{vec}\{\boldsymbol{E}(\boldsymbol{\Theta})\} = \text{vec}\{\boldsymbol{Y}\} - \left(\boldsymbol{\Phi}^T \otimes \boldsymbol{I}_n\right) \cdot \text{vec}\{\boldsymbol{\Theta}\} \tag{6.11}$$

Then, according to the asymptotic analysis provided in [8, Chap. 9], the covariance matrix of the vectorized parameter estimates is:

$$\boldsymbol{\Sigma}_{\text{vec}\{\boldsymbol{\Theta}\}} := \left[\mathrm{E}\left\{ (\boldsymbol{\Phi}^T(\beta[t], \boldsymbol{y}_{t-n_a}^{t-1}) \otimes \boldsymbol{I}_n) \cdot \boldsymbol{\Sigma}_{\boldsymbol{w}}^{-1} \cdot (\boldsymbol{\Phi}(\beta[t], \boldsymbol{y}_{t-n_a}^{t-1}) \otimes \boldsymbol{I}_n) \right\} \right]^{-1} \tag{6.12}$$

where $\mathrm{E}\{\cdot\}$ denotes the statistical expectation operator. For the present case, an estimate of this covariance matrix is obtained by replacing the unknown innovations covariance matrix by its estimate—given in Eq. (6.9)—, and by computing the expectation through a sample average, which leads to the following expression:

$$\hat{\boldsymbol{\Sigma}}_{\text{vec}\{\boldsymbol{\Theta}\}} := \left[\frac{1}{N - n_a} \sum_{t=n_a+1}^{N} (\boldsymbol{\Phi}^T(\beta[t], \boldsymbol{y}_{t-n_a}^{t-1}) \otimes \boldsymbol{I}_n) \cdot \boldsymbol{\Sigma}_{\boldsymbol{w}}^{-1} \cdot (\boldsymbol{\Phi}(\beta[t], \boldsymbol{y}_{t-n_a}^{t-1}) \otimes \boldsymbol{I}_n) \right]^{-1} \tag{6.13}$$

6.2.3 Model Based Analysis

Once an LPV-VAR model is available, it is possible to determine the "frozen" FRF and PSD matrices of the vibration response at any frequency $\omega \in [-\pi, \pi]/T_s$ (in radians per second) for a given instantaneous value of β, using the following equations [7]:

$$\boldsymbol{H}_F(\omega, \beta) = \frac{1}{2\pi} \cdot \boldsymbol{A}^{-1}(\mathrm{e}^{-j\omega T_s}, \beta) \qquad \boldsymbol{H}_F(\omega, \beta) \in \mathbb{C}^{n \times n} \tag{6.14a}$$

$$\boldsymbol{S}_F(\omega, \beta) = \frac{1}{2\pi} \cdot \boldsymbol{A}^{-1}(\mathrm{e}^{-j\omega T_s}, \beta) \cdot \boldsymbol{\Sigma}_{\boldsymbol{w}} \cdot \boldsymbol{A}^{-T}(\mathrm{e}^{-j\omega T_s}, \beta), \qquad \boldsymbol{S}_F(\omega, \beta) \in \mathbb{R}^{n \times n} \tag{6.14b}$$

where $\boldsymbol{A}(z, \beta)$ is the instantaneous polynomial matrix of the LPV-VAR model for a specific instantaneous value of β, defined as:

$$\boldsymbol{A}(z, \beta) = \boldsymbol{I}_n + \sum_{i=1}^{n_a} \boldsymbol{A}_i(\beta) \cdot z^i, \qquad \boldsymbol{A}(z, \beta) \in \mathbb{C}^{n \times n} \tag{6.15}$$

Moreover, consider an eigenvalue decomposition of the polynomial matrix, aiming to find the *eigenvectors* $\boldsymbol{v}_i(\beta)$ and *eigenvalues* $\lambda_i(\beta)$ satisfying:

$$\boldsymbol{A}(z,\beta)\cdot\boldsymbol{v}(\beta)=\lambda(\beta)\cdot\boldsymbol{v}(\beta) \tag{6.16}$$

for a given value of β. Thus, "frozen" natural frequencies and damping ratios may be derived from the "frozen" eigenvalues (or "frozen" poles) $\lambda_i(\beta)$, as:

$$\omega_{ni}(\beta)=\frac{|\ln\lambda_i(\beta)|}{T_s}\ [\text{rad/s}] \qquad\qquad \zeta_i(\beta)=-\cos(\arg(\ln\lambda_i(\beta))) \tag{6.17}$$

for $i=1,\ldots,n\cdot n_a$.

Likewise, "frozen" mode shapes may be derived from the "frozen" eigenvectors, as follows:

$$\boldsymbol{\mu}_i(\beta)=2\cdot\Re\{\boldsymbol{v}_i(\beta)\} \tag{6.18}$$

where $\Re\{\cdot\}$ denotes the real part of the complex argument. "Averaged" mode shapes may be extracted as well, by averaging a given mode shape on a given trajectory of $\beta[t]$, $t=1,\ldots,N$, as:

$$\bar{\boldsymbol{\mu}}_i=\frac{1}{N}\sum_{t=1}^{N}\boldsymbol{\mu}_i(\beta[t]) \tag{6.19}$$

which may serve for comparison with stationary mode shape estimates.

The evaluation of the eigenvalues of the polynomial matrix for varying values of β may yield unsorted "frozen" natural frequencies and damping ratios. It is therefore necessary to sort the eigenvalues in accordance to the values of β. In this sense, the procedure shown in Table 6.1 can be followed in order to sort and match the "frozen" modal quantities derived from the parameter matrices of the LPV-VAR model, evaluated for a certain trajectory $\beta[t]$, with $t=1,\ldots,N$.

Table 6.1 Algorithm for sorting the "frozen" modes of a LPV-VAR model

1. For $t=1$:
   a. Compute the "frozen" modal quantities $\lambda_i(\beta[1])$, $\omega_{ni}(\beta[1])$ and $\zeta_i(\beta[1])$ from the characteristic polynomial $\boldsymbol{A}(z,\beta[1])$,
   b. Sort them according to the "frozen" natural frequencies.
2. For $t=2,3,\ldots,N$:
   a. Compute the "frozen" modal quantities $\tilde{\lambda}_i$, $\tilde{\omega}_{ni}$ and $\tilde{\zeta}_i$ from the characteristic polynomial $\boldsymbol{A}(z,\beta[t])$,
   b. Make $j=1$ and $\boldsymbol{\ell}=\begin{bmatrix}1\ 2\ \cdots\ n\cdot n_a\end{bmatrix}^T$,
   c. Evaluate the Euclidean distances:

$$d\Big(\tilde{\lambda}_{\ell_i},\lambda_j(\beta[t-1])\Big)=\Big\|\tilde{\lambda}_{\ell_i}-\lambda_j(\beta[t-1])\Big\|_2$$

   for all $i=1,\ldots,(n\cdot n_a)-j+1$,
   d. Find ℓ^* as:

$$\ell^*=\underset{\ell_i\in\boldsymbol{\ell}}{\arg\min}\,d\Big(\tilde{\lambda}_{\ell_i},\lambda_j(\beta[t-1])\Big)$$

   e. Assign $\lambda_j(\beta[t])=\tilde{\lambda}_{\ell^*}$, $\omega_{nj}(\beta[t])=\omega_{n\ell^*}$ and $\zeta_j(\beta[t])=\zeta_{\ell^*}$,
   f. Make $j=j+1$ and remove ℓ^* from $\boldsymbol{\ell}$,
   g. If $j\leq n\cdot n_a$ return to (c), otherwise, continue.

6.2.4 Extraction of Linear Parameter Varying Mode Shapes

By extending the observations from the LTI case to the present LPV case, it may be shown that the response of the LPV-VAR model may be represented (in a frozen sense) as the superposition of several time-dependent modal components, as follows:

$$\boldsymbol{y}[t] = \sum_{i=1}^{N_i} \boldsymbol{\mu}_i \cdot \rho_i(\beta[t]) \cdot \mathrm{e}^{j\omega_{ni}(\beta[t])\cdot T_s \cdot t} \tag{6.20}$$

where $N_i = n \cdot n_a$ is the number of modes, $\boldsymbol{\mu}_k \in \mathbb{R}^n$ is the kth mode shape, $\omega_{ni}(\beta[t])$ is the "frozen" natural frequency in Eq. (6.17), and $\rho_k(\beta[t])$ is the "frozen" modal amplitude. Note that the modal decomposition determined by Eq. (6.20) is valid as long as the rate of variation of the modal amplitude $\rho_k(\beta[t])$ is lower than the rate of variation of the oscillatory component $\mathrm{e}^{j\omega_{ni}(\beta[t])\cdot t/T_s}$ [12]. According to the modal decomposition in Eq. (6.20), the amplitude of the vibration response is determined by the coefficient $\rho_k(\beta[t])$, which is an amplitude modulating function depending on the scheduling variable. In addition, the mode shape $\boldsymbol{\mu}_k$ determines the relation of the amplitudes at different locations in the structure.

The instantaneous amplitudes of the modal components may be related to the diagonal components of the "frozen" FRF matrix evaluated at the respective "frozen" natural frequencies. More specifically, consider the vector:

$$\boldsymbol{\alpha}_i(\beta[t]) = \begin{bmatrix} \alpha_{i1}(\beta[t]) \\ \alpha_{i2}(\beta[t]) \\ \vdots \\ \alpha_{in}(\beta[t]) \end{bmatrix} = \begin{bmatrix} \Re\{H_{F_{11}}(\omega_{ni}(\beta[t]), \beta[t])\} \\ \Re\{H_{F_{22}}(\omega_{ni}(\beta[t]), \beta[t])\} \\ \vdots \\ \Re\{H_{F_{nn}}(\omega_{ni}(\beta[t]), \beta[t])\} \end{bmatrix} \tag{6.21}$$

which contains the real part of the diagonal components of the "frozen" FRF matrix evaluated at the ith "frozen" natural frequency. The idea is that the vector $\boldsymbol{\alpha}_i(\beta[t])$ is proportional to the product $\boldsymbol{\mu}_i \cdot \rho_i(\beta[t])$. Then, an approximate value of the mode shape, denoted as $\tilde{\boldsymbol{\mu}}_i$, may be obtained by averaging $\boldsymbol{\alpha}_i(\beta[t])$ over time in order to eliminate the time dependency, as follows:

$$\tilde{\boldsymbol{\mu}}_i = \frac{1}{N} \sum_{t=1}^{N} \boldsymbol{\alpha}_i(\beta[t]) \tag{6.22}$$

An important aspect of this method is the accurate extraction of the "frozen" natural frequencies further enabled via the sorting and matching procedure presented earlier.

6.3 Application Example

6.3.1 Simulated Operating Wind Turbine Vibration

This application focuses on the identification and analysis of the vibration acceleration signals obtained via simulations of a fully operational wind turbine. The analyzed wind turbine is the NREL 5MW reference offshore wind turbine, fully described in [13]. The simulation is performed by means of the FAST wind turbine aeroelastic code, which uses a turbulent wind excitation generated by means of the TurbSim code [10]. Acceleration signals are measured at different locations along the span of on one of the blades of the wind turbine on the flapwise direction, as depicted in Fig. 6.1.

Simulations of both turbulent wind and vibration response are computed for a period of 10 min (600 s) with a sampling rate of 200 Hz. Moreover, the rotor azimuth is also extracted, which will further serve as the scheduling variable in the LPV-VAR model. The obtained acceleration signals are subsequently downsampled at 25 Hz for further analysis and processing. In order to avoid aliasing, the simulated signals are low-pass filtered with a 100 order FIR filter with cut-off frequency of 5 Hz.[1]

[1]The cut-off frequency has been selected in order to preserve the structural modes which are under 4 Hz. The filter has been applied in a forward-backward fashion to compensate the phase delay by using the Matlab command `filtfilt`.

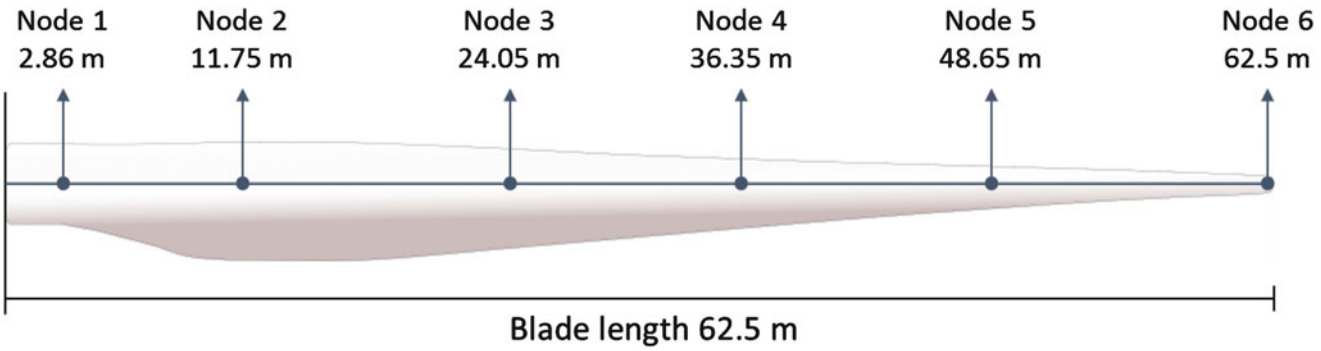

Fig. 6.1 Location of the sensors in the blade of the wind turbine. Acceleration signals are measured on the flapwise direction of the blade (normal to the surface of the page)

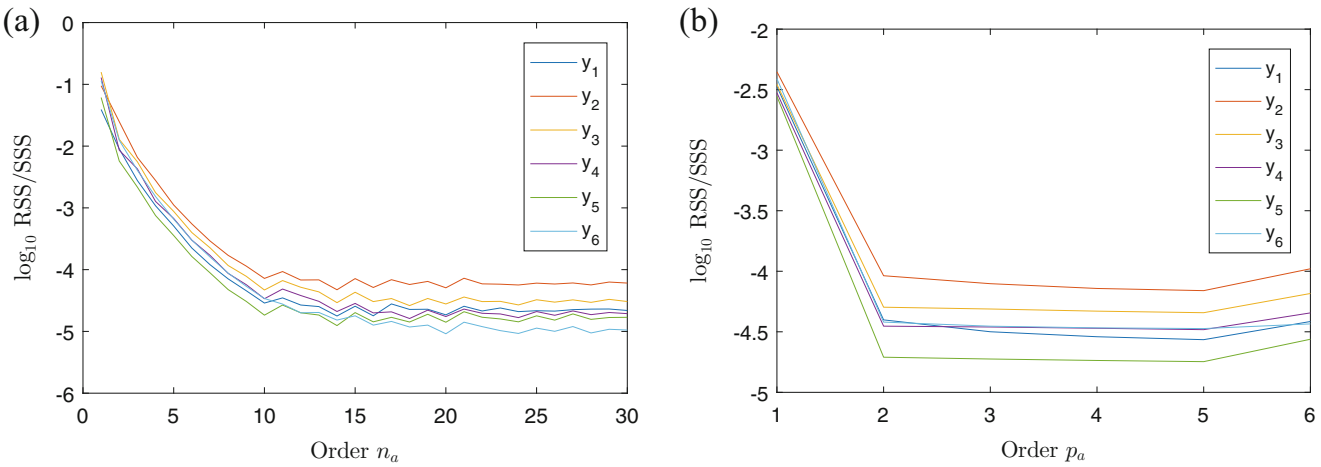

Fig. 6.2 Selection of the structure of the LPV-VAR model: (**a**) RSS/SSS of the LPV-VAR model as a function of the AR order for $p_a = 4$; (**b**) RSS/SSS of the LPV-VAR model as a function of the basis order for $n_a = 10$

6.3.2 Identification of the LPV-VAR Model

LPV-VAR models are identified on the basis of the six acceleration time histories measured from the blade at the locations indicated in Fig. 6.1. As mentioned before, the (instantaneous) rotor azimuth, assumed available via SCADA, is used as a scheduling variable for the LPV-VAR model. The rotor azimuth is normalized into the range $[0, 1]$, where 0 indicates a 0° angle, while 1 is equivalent to a 360° angle. The selected basis for the representation of the parameter trajectories is a third order B-spline basis with constant node separation [14, pp. 186–189]. Due to the periodic motion of the rotor, the azimuth values 1 (360°) and 0 (0°) are the same. Thus, in order to avoid discontinuities in the boundary between both values, a periodic structure is imposed by superposition of the conventional B-spline whose values are shifted a single unit to the left and to the right, as follows:

$$g_\ell(\beta[t]) = B_{\ell,m}(\beta[t]) + B_{\ell,m}(\beta[t]+1) + B_{\ell,m}(\beta[t]-1) \tag{6.23}$$

where $B_{\ell,m}(\beta[t])$ is the ℓth conventional m order B-spline.

Initially, LPV-VAR models are estimated with $n_a = 2, \ldots, 30$ and $p_a = 4$. The obtained RSS/SSS on each one of the measurement points as a function of the model order is illustrated in Fig. 6.2a. The obtained curves clearly indicate an order of $n_a = 10$ as optimal, while higher values do not yield noticeable improvement in the performance. A waved pattern is also evident in the RSS/SSS for orders over $n_a = 10$, which turns to be related reduced numerical accuracy as evident by large values of the condition number of the matrix $\mathbf{\Phi} \cdot \mathbf{\Phi}^T$ used on the calculation of the OLS estimates (see Equation (6.8)). On the other hand, Fig. 6.2b displays the RSS/SSS of LPV-VAR models with $n_a = 10$ and basis order $p_a = 1, 2, \ldots, 6$. A polynomial order $p_a = 2$ proves sufficient to effectively represent the acceleration response.

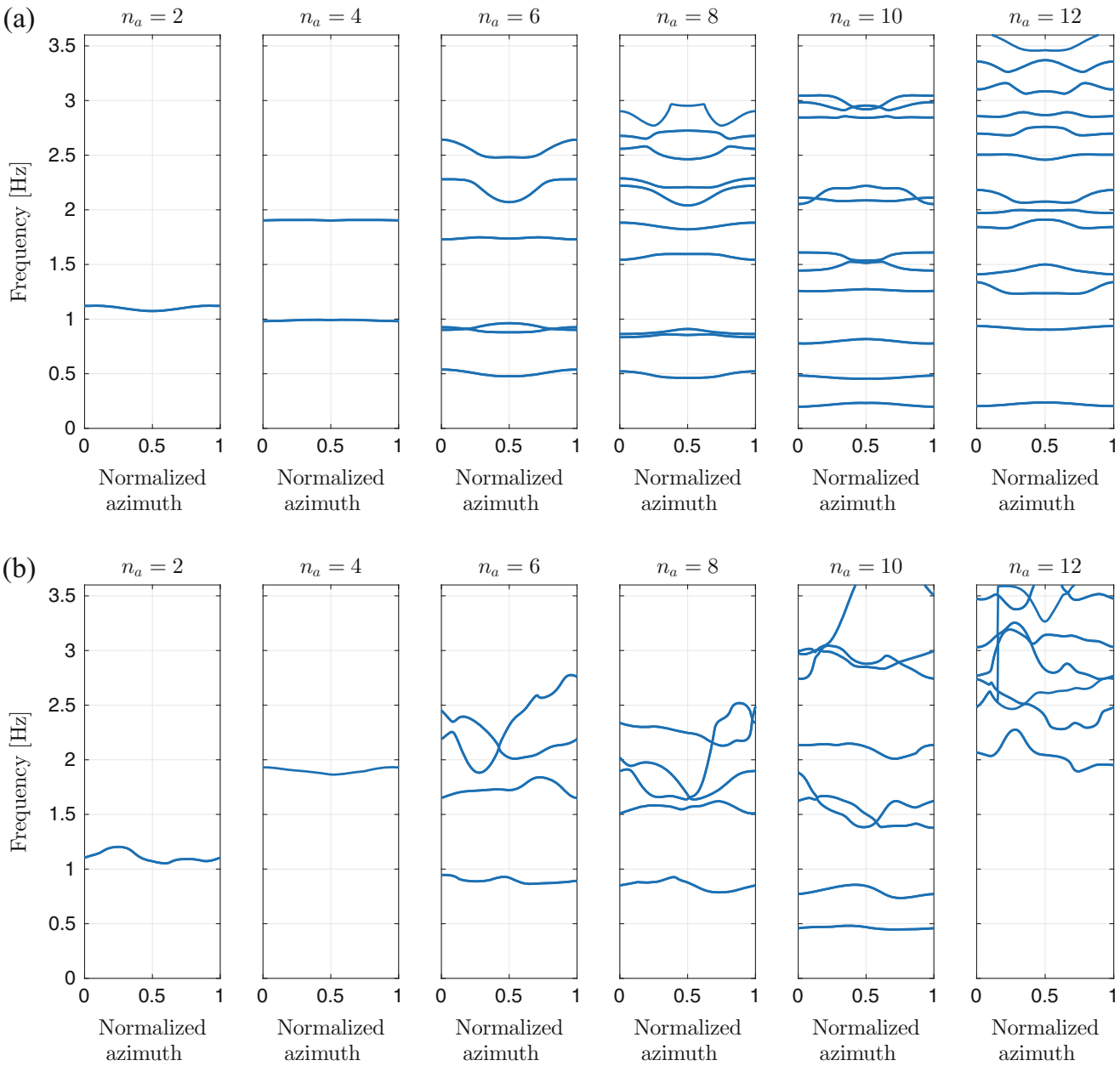

Fig. 6.3 "Frozen" natural frequencies of the LPV-VAR model with AR order $n_a = \{2, 4, \ldots, 12\}$ and basis order (**a**) $p_a = 2$; (**b**) $p_a = 4$. Only the "frozen" natural frequencies with "frozen" damping ratio lower than 25% are shown

The "frozen" natural frequencies derived from LPV-VAR models of varying AR and polynomial orders $n_a = \{2, 4, \ldots, 12\}$ and $p_a = \{2, 4\}$ are indicated in Fig. 6.3. The stabilization plot helps to confirm the results obtained in the model structure selection procedure. In particular it is observed that the number of identified modes increases with an increasing AR order. It is moreover obvious that higher basis order ($p_a = 4$) appears to disproportionally elevate the complexity, rendering the "frozen" natural frequencies difficult to discern. In compromising these issues, the lowest admissible model structure is selected, corresponding to $n_a = 10$ and $p_a = 2$.

Further assessment of the identified model aims at determining if there is sparsity in the estimated parameter matrices, which in turn may be used to decide if some coefficients may be dropped from the representation. Towards this end, consider the Mahalanobis distance:

$$d((\boldsymbol{A}_{i,j})_{p,q}) = (\hat{\boldsymbol{A}}_{i,j})^2_{p,q} / (\hat{\boldsymbol{\Sigma}}_{\mathrm{vec}\{\boldsymbol{\Theta}\}})_{k,k}; \qquad k = n^2 \cdot n_a \cdot (j-1) + n^2 \cdot (i-1) + n \cdot (q-1) + p \tag{6.24}$$

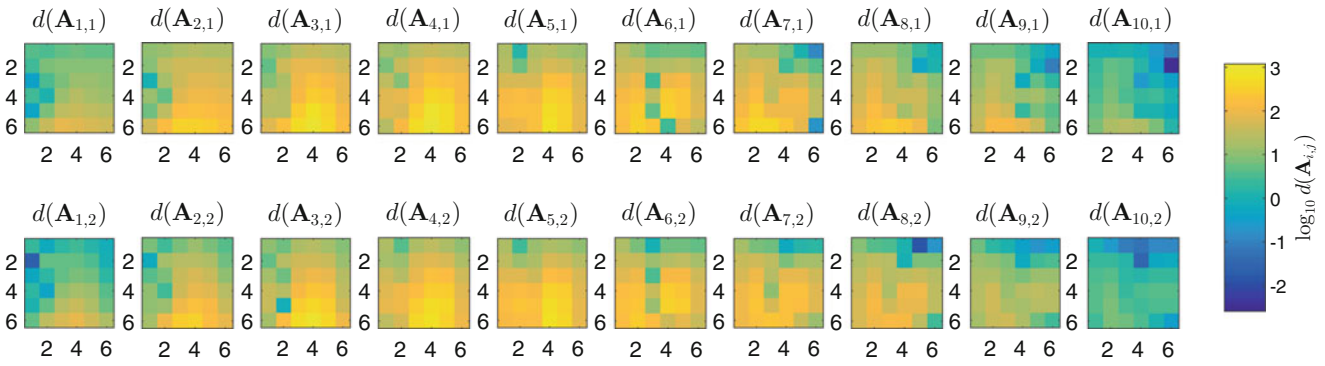

Fig. 6.4 Mahalanobis distance of each one of the model parameters to zero

where $(\boldsymbol{M})_{p,q}$ denotes the (p,q)th entry of the matrix $\boldsymbol{M}$, while $\hat{\boldsymbol{\Sigma}}_{\text{vec}\{\boldsymbol{\Theta}\}}$ is the estimated covariance matrix of the vectorized parameter matrices. This distance function attempts to determine the proximity of each parameter of the LPV-VAR model to zero. Thus, one could consider removing a parameter matrix if its entries are sufficiently close to zero. Figure 6.4 shows the results of this analysis in the estimated parameters of the LPV-VAR$(10)_2$ model of the blade's vibrational response. The resulting distances indicate that despite few individual entries reaching values close to zero, all matrices feature sufficiently large distance components, thus demonstrating the necessity of a complete representation.

6.3.3 Model Based Analysis

In this section, the dynamic characteristics of the vibration response of the wind turbine blade are analyzed with respect to the identified LPV-VAR$(10)_2$ model. The "frozen" PSDs of the wind turbine blade vibration at each one of the sensor locations are shown in Fig. 6.5. Notice that only the elements in the diagonal of the "frozen" PSD matrix are shown in the plot. The plot demonstrates the presence of different modal components, some of them with clear evidence of amplitude and frequency modulation. Additionally, it is evident that the power of the vibration is much higher at farther positions on the blade, while the relative power of some modes is also dependent on the sensor location. This latter characteristic may be associated with the mode shapes as shall be analyzed next.

Figure 6.6a demonstrates the "frozen" natural frequencies obtained from the LPV-VAR model. From the complete set of "frozen" natural frequencies, only those with associated "frozen" damping lower than 25% are selected for calculation of their respective mode shapes, as shown in Fig. 6.6b. According to the results obtained from eigenanalysis based on a physical model of the wind turbine shown in [13], the first two flapwise bending modes should lie in the vicinity of 0.7 and 2 Hz spectral lines. Both modes may be correlated with modes M3 and M8 obtained from the LPV-VAR model. As can be seen in both the "frozen" PSDs and in the "frozen" natural frequencies, these modes demonstrate visible amplitude modulations and less evident (but still important) frequency modulations. These results confirm earlier findings obtained from single-channel simulations, which have been reported in previous contributions [5]. A significant added benefit of the proposed formulation is the inference of the mode shapes, which result in agreement with those calculated from the physical model, as reported in [13] and also displayed with the mode shapes of modes M3 and M8 in Fig. 6.6b.

6.4 Conclusion

This work proposes a method for the identification of non-stationary/time-dependent dynamics based on multiple acceleration response measurements by means of the postulated Linear Parameter Varying Vector AR model. Key elements of this formulation are the estimation of the parameter matrices and the covariance matrix of the parameter estimates, as well as the calculation of "frozen" modal quantities from identified models. The method is exemplified on a simulated case study of a wind turbine blade under regular operating conditions.

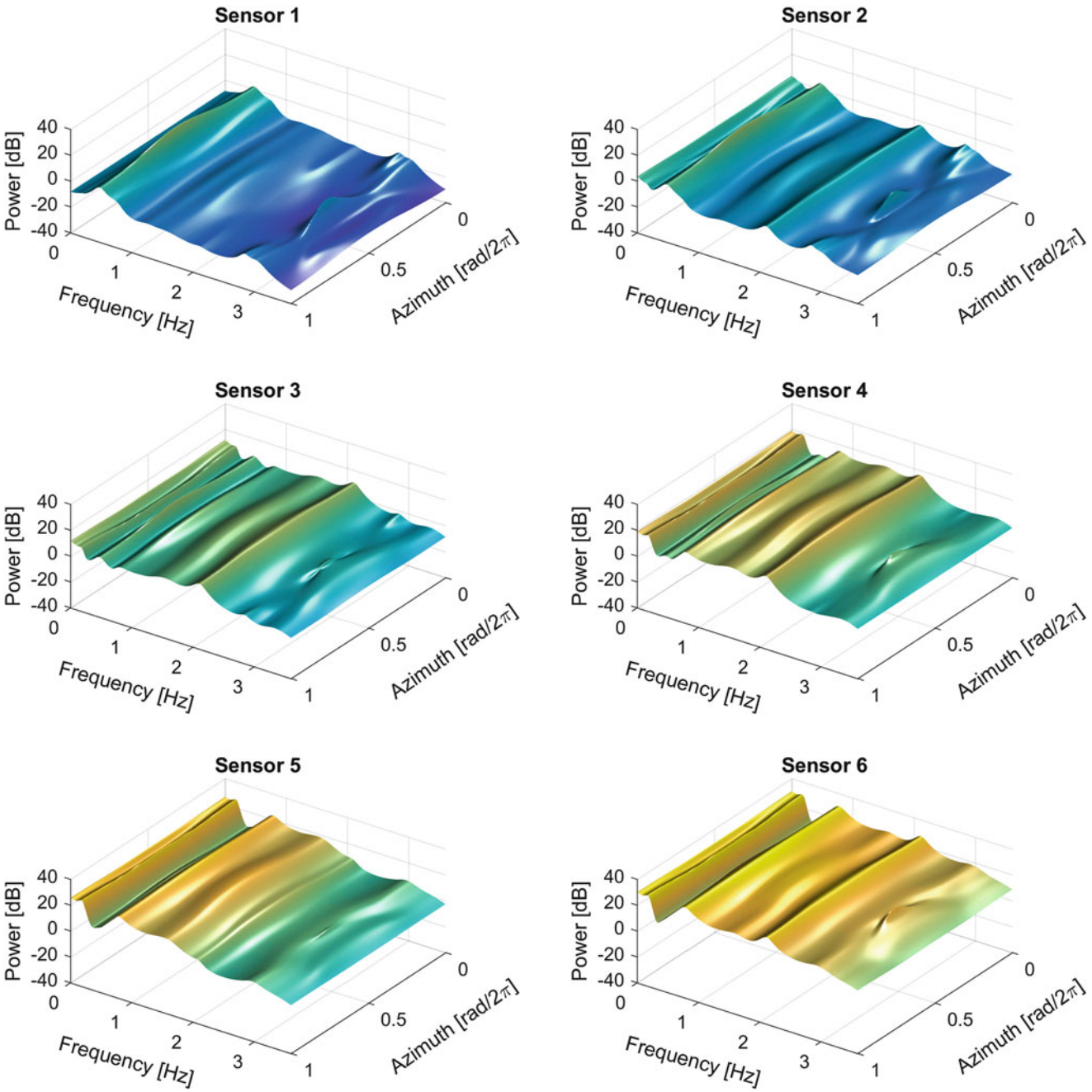

Fig. 6.5 LPV-VAR$(10)_2$ model based "frozen" Power Spectral Density evaluated at each sensor location as a function of the (normalized) rotor azimuth. Only the elements of the diagonal of the "frozen" PSD matrix are shown

The derivation of mode-shapes follows at this stage a primitive, yet promising, formulation, rendering satisfactory results. The current findings motivate further research into the topic of modal analysis on time-dependent models, where alternative modeling or model-based analysis methods may be pursued, aiming at providing more effective identification methods for both natural frequencies and mode shapes of time-dependent systems.

Acknowledgements L.D. Avendaño-Valencia, E.N. Chatzi, and S.D. Fassois gratefully acknowledge the support of the ETH Zurich Postdoctoral Fellowship FEL-45 14-2 *"A data-driven computational framework for damage identification and life-cycle management of wind turbine facilities"*.

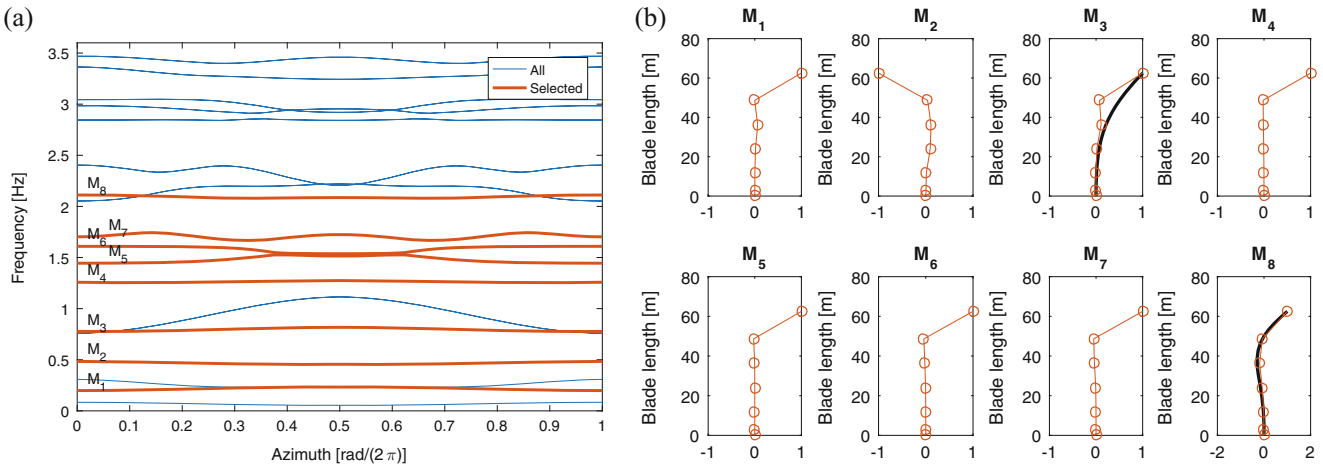

Fig. 6.6 LPV-VAR model based modal analysis of the vibration response of the wind turbine in the blade: (**a**) "Frozen" natural frequencies derived from the identified LPV-VAR$(10)_2$ model. Selected "frozen" natural frequencies plotted with *thick red lines*. (**b**) Averaged mode shapes associated with the selected "frozen" natural frequencies. *Thick black lines* in modes M3 and M8 indicate the actual mode shapes used by FAST

References

1. Allen, M.S., Sracic, M.W., Chauhan, S., Hansen, M.H.: Output-only modal analysis of linear time-periodic systems with application to wind turbine simulation data. Mech. Syst. Signal Process. **25**(4), 1174–1191 (2011)
2. Avendaño-Valencia, L.D., Fassois, S.D.: Stationary and non-stationary random vibration modelling and analysis for an operating wind turbine. Mech. Syst. Signal Process. **47**(1–2), 263–285 (2014)
3. Hu, W.-H., Thöns, S., Rohrmann, R., Said, S., Rücker, W.: Vibration-based structural health monitoring of a wind turbine system. Part II: environmental/operational effects on dynamic properties. Eng. Struct. **89**, 273–290 (2015)
4. Tcherniak, D.: Rotor anisotropy as a blade damage indicator for wind turbine structural health monitoring systems. Mech. Syst. Signal Process. **74**, 183–198 (2016)
5. Avendaño-Valencia, L.D., Fassois, S.D.: On multiple-model linear-parameter-varying based SHM for time-dependent structures under uncertainty. In: International Conference Surveillance 8, Roanne Institute of Technology, France (2015)
6. Avendaño-Valencia, L.D., Chatzi, E.N., Spiridonakos, M.D.: Surrogate modeling of nonstationary systems with uncertain properties. In: Proceedings of the European Safety and Reliability Conference ESREL 2015, Zürich (2015)
7. Spiridonakos, M.D., Fassois, S.D.: Parametric identification of a time-varying structure based on vector vibration response measurements. Mech. Syst. Signal Process. **23**, 2029–2048 (2009)
8. Ljung, L.: System Identification: Theory for the User, 2nd edn. Prentice Hall PTR, Upper Saddle River, NJ (1999)
9. Poulimenos, A., Fassois, S.D.: Parametric time-domain methods for non-stationary random vibration modeling and analysis: a critical survey and comparison. Mech. Syst. Signal Process. **20**(4), 63–816 (2006)
10. Jonkman, J.M., Buhl, M.L.: FAST user's guide. Technical Report, National Renewable Energy Laboratory, U.S. Department of Energy, Office of Energy Efficiency and Renewable Energy, Battelle, CO (2005)
11. Horn, R.A., Johnson, C.R.: Topics in Matrix Analysis. Cambridge University Press, Cambridge (1991)
12. Boashash, B.: Estimating and interpreting the instantaneous frequency of a signal – part 1: fundamentals. Proc. IEEE **80**(4), 520–538 (1992)
13. Jonkman, J.M., Butterfield, S., Musial, W., Scott, G.: Definition of a 5-MW reference wind turbine for offshore system development. Technical Report, National Renewable Energy Laboratory, U.S. Department of Energy, Office of Energy Efficiency and Renewable Energy, Battelle, CO (2009)
14. Hastie, T., Tibshirani, R., Friedman, J.: The Elements of Statistical Learning, Data Mining, Inference, and Prediction. Springer Series in Statistics. Springer, Berlin (2009)

Chapter 7
Structural Damage Identification Using Free Response Measured by a Continuously Scanning Laser Doppler Vibrometer System

Y.F. Xu, Da-Ming Chen, and W.D. Zhu

Abstract Spatially dense operating deflection shapes and mode shapes can be rapidly obtained by use of a continuously scanning laser Doppler vibrometer (CSLDV) system, which sweeps its laser spot over a vibrating structure surface. This paper introduces a new type of vibration shapes called a free response shape (FRS) that can be obtained by use of a CSLDV system, and a new damage identification methodology using FRSs is developed for beam structures. An analytical expression of FRSs of a damped beam structure is derived, and FRSs from the analytical expression compare well with those from a finite element model. In the damage identification methodology, a free-response damage index (FRDI) is proposed, and damage regions can be identified near neighborhoods with consistently high values of FRDIs associated with different modes. The proposed methodology was numerically applied to identify damage in a beam structure.

Keywords Damage identification • Beam structure • Continuously scanning laser Doppler vibrometer system • Free response shape • Free-response damage index

7.1 Introduction

Vibration-based damage detection has become a major research topic of structural dynamics in the past few decades [1]. Changes of physical properties of a structure, such as mass, stiffness and damping, are directly related to those of modal properties of the structure, i.e., natural frequencies, mode shapes (MSs) and modal damping ratios [2]. Damage that exist in a structure can be detected, located and characterized by use of modal properties. Methods that use changes of natural frequencies due to damage have been investigated by many researchers. They require a minimum amount of vibration measurement and can accurately detect locations and extent of damage, since natural frequencies are global properties of a structure and relatively easy to measure [3–8]. However, spatial information of structural property changes due to occurrence of damage cannot be directly obtained by use of natural frequencies, and one needs to construct accurate, physics-based models in order to apply the methods [3–8], which can be difficult to achieve in practice, especially for complex large-scale structures. Since occurrence of damage can introduce local abnormalities in MSs near damage regions [9], unlike use of natural frequencies, the damage can be identified by inspecting smoothness of MSs without necessity of constructing models of structures. Being more sensitive to damage of small extent than MSs, curvatures of MSs (CMSs) are more often used to locate damage [10]. Effects of damage in a beam structure can be observed as severer local abnormalities in its CMSs than in MSs, and one can isolate the effects by comparing a CMS of the damaged beam structure with that of an undamaged one. It was shown that relatively large differences between a CMS of a damaged beam structure and that of an undamaged one mainly occur near a region of damage and the differences increase as severity of damage increases [10]. CMS-based and wavelet-transform-based methods were proposed in [11] to identify embedded horizontal cracks in beam structures, where global trends of CMSs and wavelet transforms of MSs were eliminated by use of MSs from polynomials that fit MSs of cracked beam structures with properly determined orders in a global manner.

A laser Doppler vibrometer (LDV) is capable of accurate, non-contact surface vibration measurement; its mechanism is based on Doppler shifts between the incident light from and scattered light to the system [12]. The concept of a continuously scanning LDV (CSLDV) system was first proposed in [13, 14]. A CSLDV system continuously sweeps its laser over a surface of a structure under sinusoidal excitation to obtain its ODSs, which can be approximated by Chebyshev series with coefficients determined by processing velocities measured by the system. Two CSLDV measurement methods were later proposed to obtain ODSs of a structure under sinusoidal excitation: demodulation and polynomial methods [15, 16]. A

Y.F. Xu • D.-M. Chen • W.D. Zhu (✉)
Department of Mechanical Engineering, University of Maryland, Baltimore County, 1000 Hilltop Circle, Baltimore, MD 21250, USA
e-mail: yxu2@umbc.edu; damingc1@umbc.edu; wzhu@umbc.edu

D. Di Maio, P. Castellini (eds.), *Rotating Machinery, Hybrid Test Methods, Vibro-Acoustics & Laser Vibrometry, Volume 8*,
Conference Proceedings of the Society for Experimental Mechanics Series, DOI 10.1007/978-3-319-54648-3_7

"lifting" method was proposed to obtain MSs from measured free response of a structure, where velocities measured by a CSLDV system are treated as output of linear time-periodic systems [17]. Use of a CSLDV system for damage identification was first proposed in [18], where the demodulation method was used to obtain ODSs of various structures by scanning their cracked surfaces, and effects of cracks could be observed as local abnormalities in obtained ODSs. The demodulation and polynomial methods were synthesized to identify damage in beams, where damage can be identified by use of a CSLDV system that scans intact surfaces of damaged beam structures [19].

In this work, a new type of vibration shapes called a free response shape (FRS) that can be obtained by use of a CSLDV system is introduced. An analytical expression of FRSs of a damped beam structure is derived. It is shown in the analytical expression that amplitudes of FRSs exponentially decay to zero with time. A finite element model of a damped beam structure is constructed, and a CSLDV system is simulated to measure its free response. FRSs associated with the structure are obtained from the response measured by the simulated CSLDV system from the demodulation method, and they are compared with those from the analytical expression. A new damage identification methodology that uses FRSs is proposed for beam structures. A free-response damage index (FRDI) is defined, which consists of differences between curvatures of FRSs obtained by use of a CSLDV system and those from polynomials that fit the FRSs, and damage regions can be identified near neighborhoods with consistently high values of FRDIs associated with different modes. Effectiveness of the methodology for identifying damage in a beam structure is numerically investigated.

7.2 Methodology

7.2.1 Free Response of a Damped Beam Structure

A linear time-invariant Euler-Bernoulli beam structure with a uniform cross-section is considered. The structure has a length L, a bending stiffness EI and a linear mass density m. It is viscously damped, and damping effects are modeled using the Kelvin-Voigt viscoelastic model with a damping coefficient c [20, 21]. Excitation in the form of a single impulse with an intensity G_0 is applied to the structure at position $x = L_0$ at time $t = 0$. Response of the structure can be obtained by solving its governing partial differential equation

$$EI\left[\frac{\partial^4 y(x,t)}{\partial x^4} + c\frac{\partial}{\partial t}\left(\frac{\partial^4 y(x,t)}{\partial x^4}\right)\right] + m\frac{\partial^2 y(x,t)}{\partial t^2} = G_0\delta(x - L_0)\,\delta(t) \tag{7.1}$$

with given boundary and initial conditions, where $y(x,t)$ is the displacement of the structure at position x at time t. Based on the expansion theorem [20], a solution to Eq. (7.1) can be expressed by

$$y(x,t) = \sum_{h=1}^{\infty} Y_h(x)\,F_h(t) \tag{7.2}$$

where $Y_h(x)$ is the mass-normalized eigenfunction of the hth mode of the corresponding undamped structure and $\eta_h(t)$ is the corresponding time function. The eigenfunction $Y_h(x)$ can be expressed by

$$Y_h(x) = C_1 \sin\beta_h x + C_2 \cos\beta_h x + C_3 \sinh\beta_h x + C_4 \cosh\beta_h x \tag{7.3}$$

where C_1, C_2, C_3, C_4 and β_h are determined by the boundary conditions and the orthonormality condition of eigenfunctions

$$\int_0^L mY_h(x)\,Y_j(x)\,\mathrm{d}x = \delta_{h,j} \tag{7.4}$$

in which $\delta_{h,j}$ is the Kronecker delta. The time function $F_h(t)$ can be obtained by solving an ordinary differential equation

$$\ddot{F}_h(t) + c(2\pi f_h)^2\dot{F}_h(t) + (2\pi f_h)^2 F_h(t) = G_0 Y_h(L_0)\,\delta(t) \tag{7.5}$$

with initial conditions $F_h(0)$ and $\dot{F}_h(0)$ determined by those of Eq. (7.1), where f_h is the natural frequency of the undamped structure in Hz associated with its hth mode. A relation between β_h and f_h can be expressed by

$$\beta_h^4 = \frac{(2\pi f_h)^2 m}{EI} \tag{7.6}$$

The solution to Eq. (7.5) can be expressed by Rao [22]

$$\begin{aligned} F_h(t) &= \mathrm{e}^{-2\pi\zeta_h f_h t}\left[F_h(0)\cos(2\pi f_{h,d}t) + \left(\frac{\dot{F}_h(0) + 2\pi\zeta_h f_h F(0)}{2\pi f_{h,d}} + \frac{G_0 Y_h(L_0)}{2\pi f_{h,d}}\right)\sin(2\pi f_{h,d}t)\right] \\ &= A_h \mathrm{e}^{-2\pi\zeta_h f_h t}\cos(2\pi f_{h,d}t - \gamma_h) \end{aligned} \tag{7.7}$$

where

$$A_h = \sqrt{(F_h(0))^2 + \left[\frac{\dot{F}_h(0) + 2\pi\zeta_h f_h F(0)}{2\pi f_{h,d}} + \frac{G_0 Y_h(L_0)}{2\pi f_{h,d}}\right]^2} \tag{7.8}$$

is an amplitude constant and

$$\gamma_h = \operatorname{actan2}\left(\frac{\dot{F}_h(0) + 2\pi\zeta_h f_h F(0)}{2\pi f_{h,d}} + \frac{G_0 Y_h(L_0)}{2\pi f_{h,d}}, F_h(0)\right) \tag{7.9}$$

is a phase angle;

$$\zeta_h = c\pi f_h \tag{7.10}$$

and

$$f_{h,d} = f_h\sqrt{1-\zeta_h^2} \tag{7.11}$$

are the damping ratio and damped natural frequency of the structure associated with its hth mode, respectively. Based on Eqs. (7.2) and (7.7), $y(x,t)$ can be expressed by

$$y(x,t) = \sum_{h=1}^{\infty} A_h Y_h(x)\,\mathrm{e}^{-2\pi\zeta_h f_h t}\cos(2\pi f_{h,d}t - \gamma_h) \tag{7.12}$$

7.2.2 FRS

A FRS associated with the hth mode of the beam structure can be defined by

$$\phi_h(x,t) = A_h Y_h(x)\,\mathrm{e}^{-2\pi\zeta_h f_h t} \tag{7.13}$$

and Eq. (7.12) becomes

$$y(x,t) = \sum_{h=1}^{\infty}\phi_h(x,t)\cos(2\pi f_{h,d}t - \gamma_h) \tag{7.14}$$

It can be seen that Y_h, which can be considered as a MS associated with the hth mode, exists in the definition of a FRS in Eq. (7.13). A similarity between Y_h and ϕ_h is that they both correspond to the same mode of the structure. Since a MS describes amplitude ratios of displacement, velocity or acceleration at different positions on the structure while it vibrates, the multiplication factor of the MS can be an arbitrarily chosen non-zero constant, and the MS can be considered time-invariant. However, ϕ_h differs from Y_h due to two extra terms in Eq. (7.13), i.e., A_h and $\mathrm{e}^{-2\pi f_h\xi_h t}$. The coefficient A_h is determined by the initial conditions of and impulse to the structure, and $\mathrm{e}^{-2\pi f_h\xi_h t}$ indicates that amplitudes of ϕ_h at different positions exponentially decay to zero with time. Hence, A_h cannot be arbitrarily chosen, and ϕ_h is time-varying.

A CSLDV system continuously sweeps its laser spot over a vibrating structure surface with a specific scan pattern. It can measure response of a measurement point, where its laser spot is located during a scan, and a finite number of modes of a structure are included in free response measured by a CSLDV system. Let $\tilde{x}(t)$ be the position of a laser spot on a beam structure at time t; free response of the structure measured by the CSLDV system with a straight scan line along its length can be expressed by

$$\tilde{y}(t) = \sum_{h=1}^{n} \tilde{\phi}_h(\tilde{x}(t))\, \tilde{\eta}_h(t) \tag{7.15}$$

where n is the number of measured modes, and $\tilde{\phi}_h$ and $\tilde{\eta}_h$ are the FRS and time function associated with the hth mode measured by the system, respectively. The FRS $\tilde{\phi}_h$ in Eq. (7.15) can be defined in a way similar to ϕ_h in Eq. (7.13):

$$\tilde{\phi}_h(t) = A_h Y_h(\tilde{x}(t))\, \mathrm{e}^{-2\pi f_h \zeta_h t} \tag{7.16}$$

A major difference between ϕ_h in Eq. (7.13) and $\tilde{\phi}_h$ is that x in the former becomes $\tilde{x}$ in the latter, which is a function of t and is unique in a scan of the system. Similar to ϕ_h, $\tilde{\phi}_h$ contains both A_h and $\mathrm{e}^{-2\pi f_h \zeta_h t}$, and it is time-varying. The time function $\tilde{\eta}_h$ can be expressed by

$$\tilde{\eta}_h(t) = \cos(2\pi f_h t - \alpha_h - \theta_h) \tag{7.17}$$

where α_h is the difference between a phase determined by the initial conditions and impulse associated with the hth mode and that by a mirror feedback signal, and θ_h is a phase variable that controls amplitudes of in-phase and quadrature components of $\tilde{\phi}_h$, which can be expressed by

$$\tilde{\phi}_{I,h} = \tilde{\phi}_h \cos(\alpha_h + \theta_h) \tag{7.18}$$

and

$$\tilde{\phi}_{Q,h} = \tilde{\phi}_h \sin(\alpha_h + \theta_h) \tag{7.19}$$

respectively [19].

7.2.3 Demodulation Method for FRSs

The demodulation method has been proposed to obtain MSs and ODSs of a structure under sinusoidal excitation [16], where its steady-state response measured by a CSLDV system are analyzed. FRSs of a linear damped beam structure measured by a CSLDV system, as described by $\tilde{\phi}_h$ in Eq. (7.16), can also be obtained from the demodulation method by analyzing its free response of half-scan periods measured by the system, and each obtained $\tilde{\phi}_h$ corresponds to a mode in a half-scan period. A half-scan period starts when the laser spot of the system arrives at one end of a scan line, and it ends when the laser spot arrives at the other end. Hence, multiple $\tilde{\phi}_h$ can be obtained from free response of the structure measured by the system in one scan. To identify the start and end of a half-scan period, one can refer to mirror feedback signals of a CSLDV system and determine instants when its laser spot arrives at ends of a scan line.

Application of the demodulation method for obtaining $\tilde{\phi}_k$ associated with the hth mode in a half-scan period of a CSLDV system is described below. Based on Eqs. (7.15) through (7.19), a half-scan period of free response of the structure that is measured by a CSLDV system can be expressed by

$$\begin{aligned} \tilde{y}(t) &= \sum_{h=1}^{n} \tilde{\phi}_h(\tilde{x}(t)) \cos(2\pi f_h t - \alpha_h - \theta_h) \\ &= \sum_{h=1}^{n} \left[\tilde{\phi}_{I,h}(\tilde{x}(t)) \cos(2\pi f_h t) + \tilde{\phi}_{Q,h}(\tilde{x}(t)) \sin(2\pi f_h t) \right] \end{aligned} \tag{7.20}$$

The response $\tilde{y}(t)$ is then multiplied by $\cos(2\pi f_k t)$ and $\sin(2\pi f_k t)$, which gives

$$\begin{aligned}\tilde{y}(t)\cos(2\pi f_k t) &= \tilde{\phi}_{I,k}(\tilde{x}(t))\cos(2\pi f_k t)\cos(2\pi f_k t) + \tilde{\phi}_{Q,k}(\tilde{x}(t))\sin(2\pi f_k t)\cos(2\pi f_k t) + \\ &\quad \sum_{h=1,h\neq k}^{n}\tilde{\phi}_h(\tilde{x}(t))\,\tilde{\eta}_h(t)\cos(2\pi f_k t) \\ &= \frac{1}{2}\tilde{\phi}_{I,k}(\tilde{x}(t)) + \frac{1}{2}\tilde{\phi}_{I,k}(\tilde{x}(t))\cos(4\pi f_k t) + \frac{1}{2}\tilde{\phi}_{Q,k}(\tilde{x}(t))\sin(4\pi f_k t) + \\ &\quad \sum_{h=1,h\neq k}^{n}\tilde{\phi}_h(\tilde{x}(t))\,\tilde{\eta}_h(t)\cos(2\pi f_k t) \end{aligned} \tag{7.21}$$

and

$$\begin{aligned}\tilde{y}(t)\sin(2\pi f_k t) &= \tilde{\phi}_{I,k}(\tilde{x}(t))\cos(2\pi f_k t)\sin(2\pi f_k t) + \tilde{\phi}_{Q,k}(\tilde{x}(t))\sin(2\pi f_k t)\sin(2\pi f_k t) + \\ &\quad \sum_{h=1,h\neq k}^{n}\tilde{\phi}_h(\tilde{x}(t))\,\tilde{\eta}_h(t)\sin(2\pi f_k t) \\ &= \frac{1}{2}\tilde{\phi}_{Q,k}(\tilde{x}(t)) - \frac{1}{2}\tilde{\phi}_{Q,k}(\tilde{x}(t))\cos(4\pi f_k t) + \frac{1}{2}\tilde{\phi}_{I,k}(\tilde{x}(t))\sin(4\pi f_k t) + \\ &\quad \sum_{h=1,h\neq k}^{n}\tilde{\phi}_h(\tilde{x}(t))\,\tilde{\eta}_h(t)\sin(2\pi f_k t) \end{aligned} \tag{7.22}$$

respectively. A low-pass filter is then applied to $\tilde{y}(t)\cos(2\pi f_k t)$ and $\tilde{y}(t)\sin(2\pi f_k t)$ in Eqs. (7.21) and (7.22) to obtain $\frac{1}{2}\tilde{\phi}_{I,k}$ and $\frac{1}{2}\tilde{\phi}_{Q,k}$, respectively, and the second and third terms on the third lines and terms on the fourth lines of Eqs. (7.21) and (7.22) are removed. Further, $\tilde{\phi}_{I,k}$ and $\tilde{\phi}_{Q,k}$ can be obtained by multiplying the corresponding filtered signals by two. The value of θ_h in Eq. (7.20) can be optimized so that $\tilde{\phi}_{I,h}$ and $\tilde{\phi}_{Q,h}$ attain their maximum and minimum amplitudes, respectively. In what follows, all FRSs are represented by their in-phase components with maximum amplitudes.

7.2.4 FRDI

A CMS Y_h'' is the second-order spatial derivative of Y_h, where a prime denotes first-order differentiation with respect to x. A curvature FRS $\tilde{\phi}_h''$ can be defined as

$$\tilde{\phi}_h''(\tilde{x}(t)) = \frac{\partial^2\tilde{\phi}_h}{\partial\tilde{x}^2} = A_h Y_h''(\tilde{x}(t))\,\mathrm{e}^{-2\pi f_h\zeta_h t} \tag{7.23}$$

Since Y_h'' is related to the bending stiffness of a beam structure that can decrease due to occurrence of damage and regions of the decrease correspond to damage regions, it can be used for damage identification [10], and so can $\tilde{\phi}_h''$, since it explicitly contains Y_h'', as shown in Eq. (7.23).

Since a MS of an undamaged beam structure can be well approximated by that from a polynomial that fits a MS of a damaged beam structure [11], it can be inferred that a FRS of an undamaged structure can also be well approximated by that from a polynomial that fits a FRS of a damaged structure. A damage index similar to that in [11] can be defined by comparing $\tilde{\phi}_h''$ of a damaged beam structure and that from a polynomial that fits $\tilde{\phi}_h$ with a properly determined order, which can be expressed by

$$\delta_h(\tilde{x}) = \sum_{i=1}^{N_d}\left[\tilde{\phi}_{h,i}''(\tilde{x}) - \tilde{\phi}_{h,i}^{p\prime\prime}(\tilde{x})\right]^2 \tag{7.24}$$

where N_d is the number of FRSs to be included in the index, $\tilde{\phi}_{h,i}$ is a FRS associated with the hth mode in the ith half-scan period, and $\tilde{\phi}_{h,i}^{p}$ is a FRS from a polynomial that fits $\tilde{\phi}_{h,i}$ with a properly determined order. The index $\delta_h(\tilde{x})$ in Eq. (7.24) is termed as a free-response damage index (FRDI) at $\tilde{x}$. Since there can be FRSs associated with multiple modes corresponding to $\tilde{y}$ measured by a CSLDV system in one scan, FRDIs associated with multiple modes can be obtained using measurement

by a CSLDV system in one scan, and damage regions can be identified near neighborhoods with consistently high values of FRDIs associated with different modes. Note that use of δ_h associated with rigid-body modes should be excluded in damage identification as curvatures of their FRSs are zero, and one should use δ_h associated with elastic modes in damage identification.

7.3 Numerical Investigation

7.3.1 FRSs from Analytical and FE Models

Based on Eq. (7.1), the analytical model of an undamaged aluminum cantilever beam structure with $L = 0.8\,\text{m}$, $E = 68.9\,\text{GPa}$, $m = 0.1950\,\text{kg/m}$ and $c = 8 \times 10^{-7}\,\text{s}$ is formulated; the structure has a uniform square cross-section with a side length of 0.01 m. The structure has fixed and free ends at $x = 0$ and $x = L$, respectively, and it has zero initial conditions. A single impulse with an intensity of 0.01 N s is applied to the free end of the structure. A corresponding FE model of the structure under the same initial conditions and excitation is constructed using ABAQUS with 16,384 linear beam elements for comparison purposes, where the damping in the analytical model can be equivalently modeled using Rayleigh damping [20]. The formulation of the FE model can be expressed by

$$\mathbf{M}\ddot{\mathbf{z}}(t) + \mathbf{C}\dot{\mathbf{z}}(t) + \mathbf{K}\mathbf{z}(t) = \mathbf{f}(t) \tag{7.25}$$

with initial conditions $\mathbf{z}(0) = \mathbf{0}$ and $\dot{\mathbf{z}}(0) = \mathbf{0}$, where $\mathbf{M}$, $\mathbf{C}$ and $\mathbf{K}$ are mass, damping and stiffness matrices, respectively, in which $\mathbf{C} = \alpha\mathbf{M} + \beta\mathbf{K}$ with Rayleigh damping coefficients $\alpha = 0$ and $\beta = c$, i.e., $\mathbf{C} = c\mathbf{K}$, and $\mathbf{z}$ and $\mathbf{f}$ are displacement and force vectors, respectively. Mass-normalized MSs of the first four modes from the analytical and FE models compare well, as shown in Fig. 7.1.

Response of the beam structure is then measured by a simulated CSLDV system with a scan period of $T = 2\,\text{s}$ and a sampling frequency of 16,384 Hz; the simulated CSLDV system is capable of measuring response in the form of displacement. The position of its laser spot is shown in Fig. 7.2a; the first half-scan period starts at $t = 0.0625\,\text{s}$, and measured response of the structure from the analytical and FE models in the first 8 s is shown in Fig. 7.2b.

Based on Eq. (7.16), FRSs from the analytical model associated with the first four modes of the beam structure in the first three half-scan periods of the simulated CSLDV system are shown in Fig. 7.3a–d, respectively. FRSs from the FE model obtained by use of the simulated CSLDV system, which are obtained from the demodulation method, are shown in Fig. 7.4. It can be seen from Figs. 7.3 and 7.4 that the FRSs from the analytical and FE models are in good agreement. Amplitudes of the FRSs associated with the fourth mode of the structure in the second and third half-scan periods drastically decrease to almost zero due to the damping; the FRS in the first half-scan period is included in $\delta_h(\tilde{x})$ associated with the fourth mode for damage identification that follows.

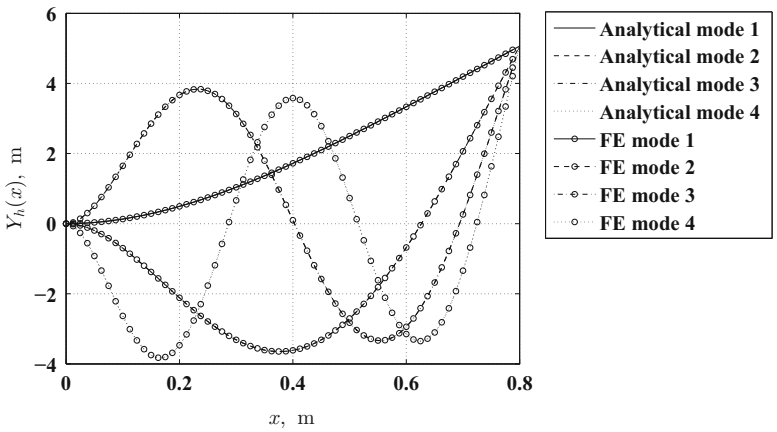

Fig. 7.1 Mass-normalized MSs of the cantilever beam structure associated with its first four modes from its analytical and FE models

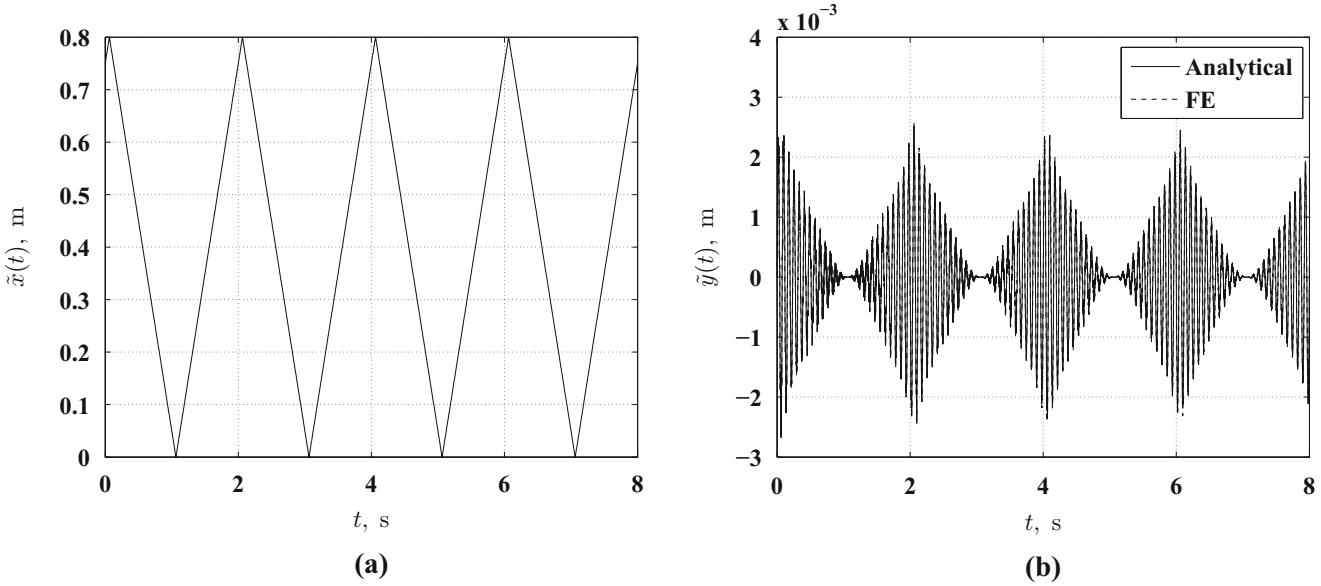

Fig. 7.2 (**a**) Position of the laser spot of a simulated CSLDV system on the beam structure and (**b**) response from its analytical and FE models measured by the simulated CSLDV system

7.3.2 Damage Identification Using FRDIs

Since fidelity of the FE model of the undamaged cantilever beam structure has been verified in Sect. 7.3.1, the FE model can be adapted to model such a beam structure with damage in the form of thickness reduction to numerically investigate the proposed damage identification methodology. The thickness of the section of the structure between $x = \frac{6}{16}L$ and $x = \frac{7}{16}L$ is reduced by 10%, while its E and volume mass density remain unchanged. Response of the damaged structure from its FE model is measured by the simulated CSLDV system with the same settings as those in Sect. 7.3.1, and it is used to obtain FRSs of the damaged structure associated with the first four modes in the first three half-scan periods, as shown in Fig. 7.5.

FRDIs associated with the first through fourth modes are shown in Fig. 7.6a–d, respectively. Note that numbers of FRSs included in the FRDIs associated with the first through fourth modes are 3, 3, 3 and 1, respectively. The damage can be clearly identified near neighborhoods with consistently high values of the FRDIs.

7.4 Conclusion

A new type of vibration shapes called a FRS is introduced in this work. A FRS can be obtained by use of a CSLDV system, and it can be obtained from the demodulation method using free response of a structure. An analytical expression of a FRS is derived for a beam structure with damping that can be modeled by Kelvin-Voigt viscoelastic model. FRSs from the analytical expression compare well with those from a FE model. A FRDI that uses differences between curvatures of FRSs associated with a mode and those from polynomial fits is proposed, and damage regions can be accurately identified near neighborhoods with consistently high values of FRDIs associated with different modes. It is numerically shown that amplitudes of FRSs decrease from one half-scan period to the next. The proposed methodology was numerically applied to a damaged beam structure with thickness reductions along their lengths. The damage region is successfully identified near neighborhoods with consistently high values of FRDIs associated with different modes.

Acknowledgements The authors are grateful for the financial support from the National Science Foundation under Grant Numbers CMMI-1229532 and CMMI-1335024.

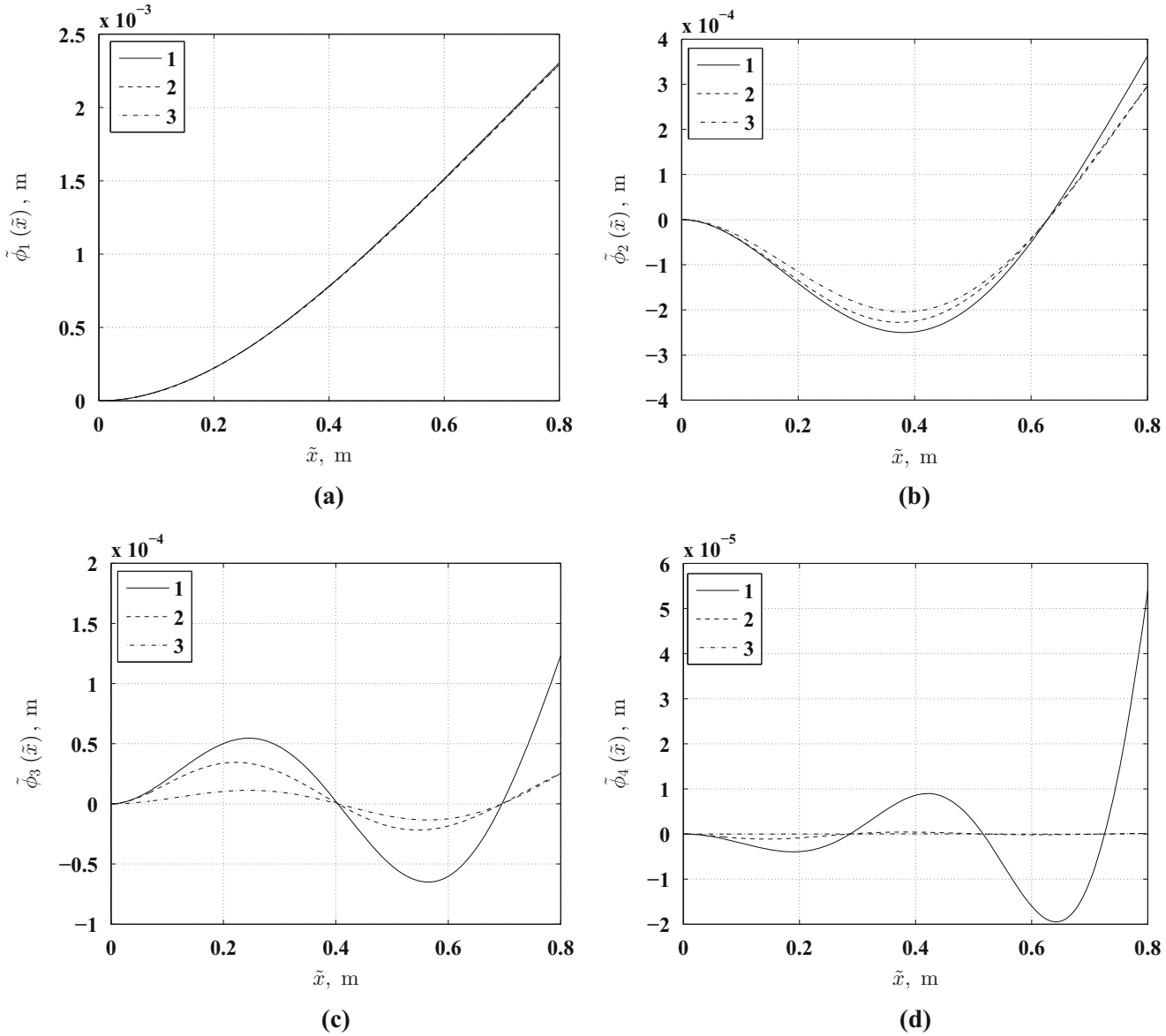

Fig. 7.3 FRSs of the beam structure from its analytical model associated with its (**a**) first, (**b**) second, (**c**) third and (**d**) fourth modes in the first three half-scan periods of the simulated CSLDV system

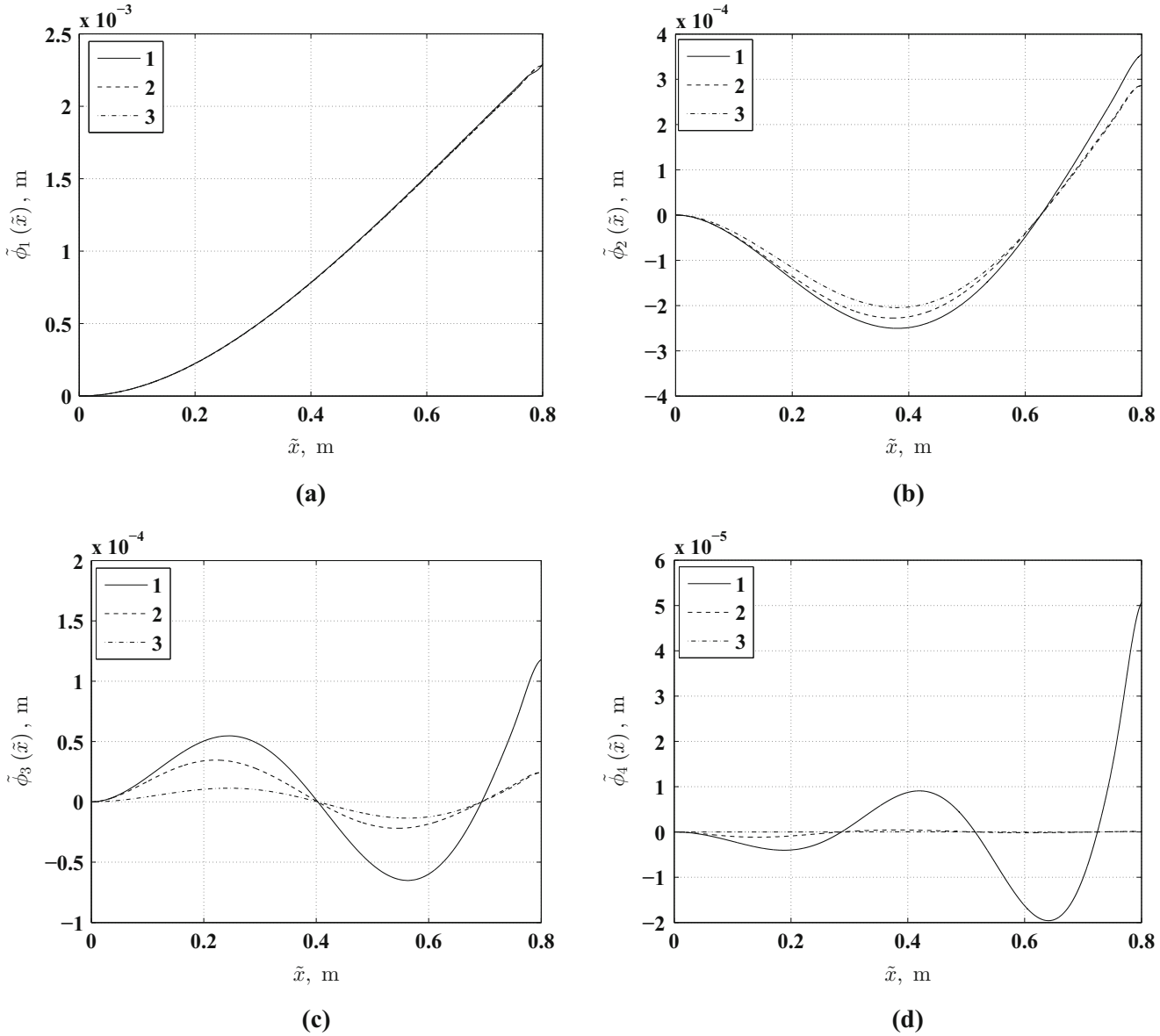

Fig. 7.4 FRSs of the beam structure from its FE model associated with its (**a**) first, (**b**) second, (**c**) third and (**d**) fourth modes obtained by use of the simulated CSLDV system in the first three half-scan periods

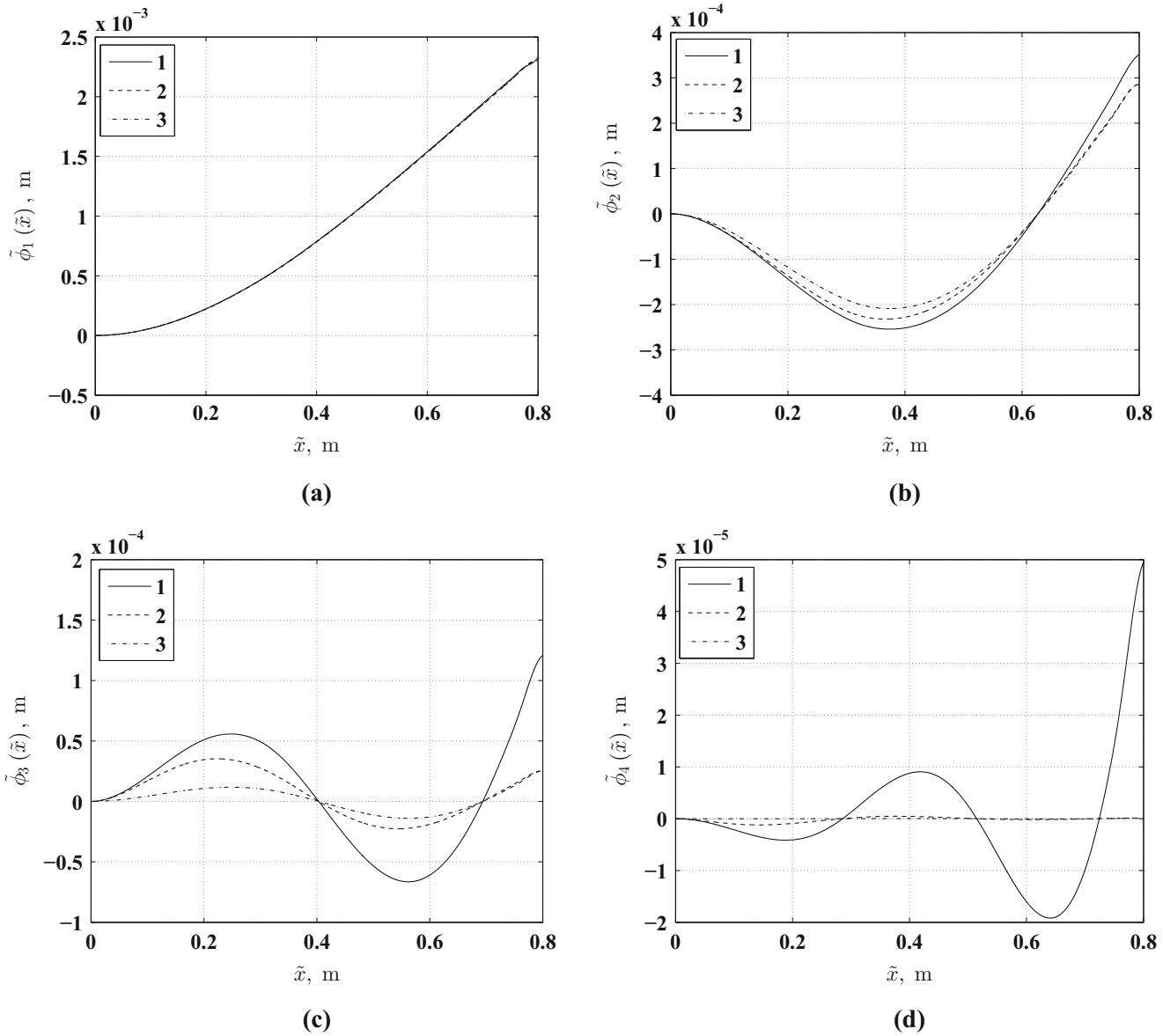

Fig. 7.5 FRSs from the FE model of the damaged beam structure obtained by use of the simulated CSLDV system associated with the (**a**) first, (**b**) second, (**c**) third and (**d**) fourth modes in the first three half-scan periods

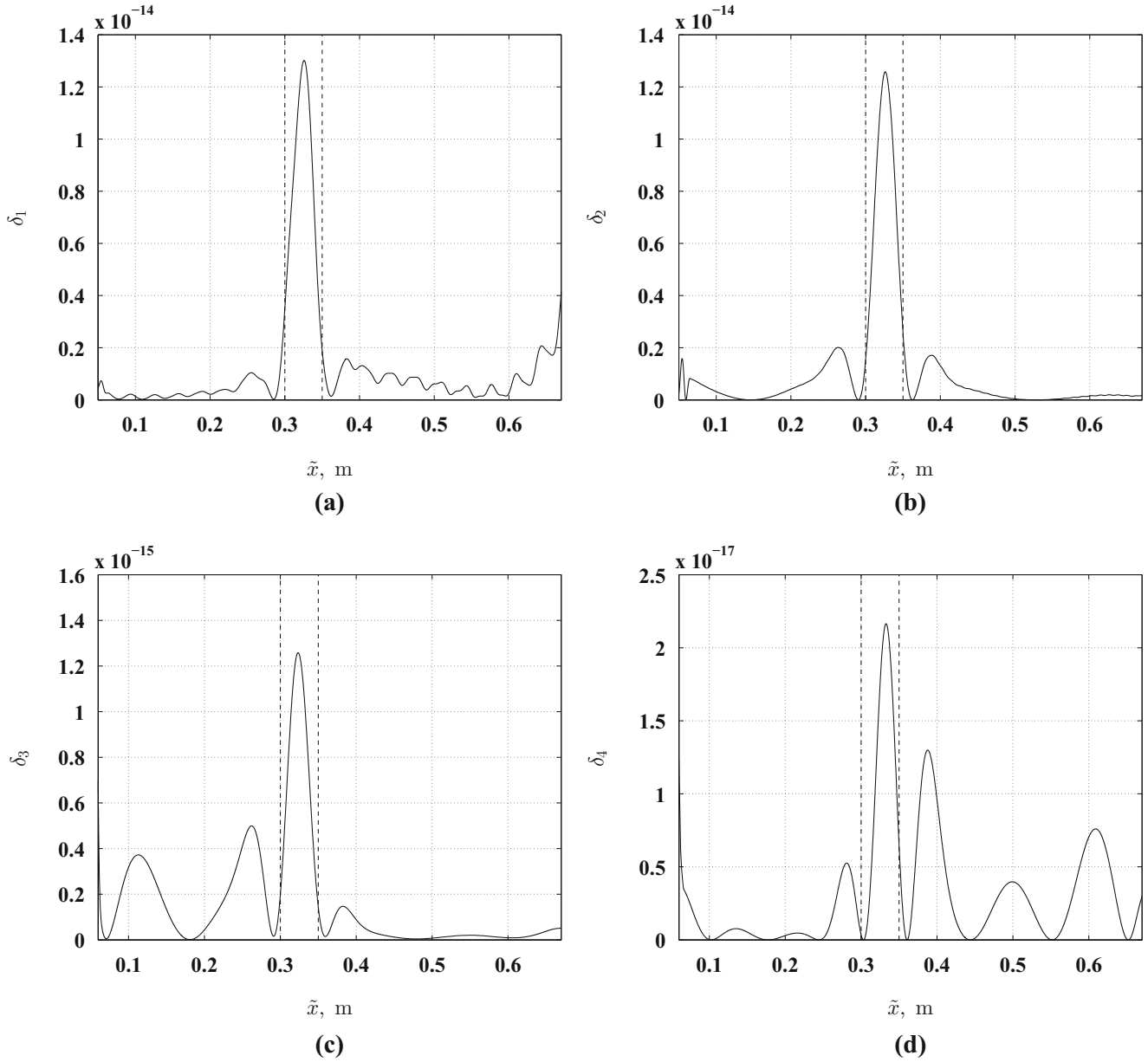

Fig. 7.6 FRDIs associated with the (**a**) first, (**b**) second, (**c**) third and (**d**) fourth modes of the damaged beam structure. Locations of damage ends are indicated by two *vertical dashed lines*

References

1. Fan, W., Qiao, P.: Vibration-based damage identification methods: a review and comparative study. Struct. Health Monit. **10**(1), 83–111 (2011)
2. Ewins, D.J.: Modal Testing: Theory, Practice and Application, 2nd edn. Research Studies Press, Hertfordshire (2000)
3. Wong, C.N., Zhu, W.D., Xu, G.Y.: On an iterative general-order perturbation method for multiple structural damage detection. J. Sound Vib. **273**(1), 363–386 (2004)
4. Xu, G.Y., Zhu, W.D., Emory, B.H.: Experimental and numerical investigation of structural damage detection using changes in natural frequencies. J. Vib. Acoust. **129**(6), 686–700 (2007)
5. He, K., Zhu, W.D.: Detection of damage and loosening of bolted connections in structures using changes in natural frequencies. ASNT Mater. Eval. **68**(6), 721–732 (2010)
6. He, K., Zhu, W.D.: Vibration-based structural damage detection method and its applications to engineering structures. Int. J. Smart Nano Mater. **2**(3), 194–218 (2011)
7. Zhu, W.D., He, K.: Detection of damage in space frame structures with l-shaped beams and bolted joints using changes in natural frequencies. J. Vib. Acoust. **135**(5), 051001 (2013)
8. He, K., Zhu, W.D.: Detecting loosening of bolted connections in a pipeline using changes in natural frequencies. J. Vib. Acoust. **136**(3), 034503 (2014)
9. Surace, C., Archibald, R., Saxena, R.: On the use of the polynomial annihilation edge detection for locating cracks in beam-like structures. Comput. Struct. **114**, 72–83 (2013)
10. Pandey, A.K., Biswas, M., Samman, M.M.: Damage detection from changes in curvature mode shapes. J. Sound Vib. **145**(2), 321–332 (1991)
11. Xu, Y.F., Zhu, W.D., Liu, J., Shao, Y.M.: Identification of embedded horizontal cracks in beams using measured mode shapes. J. Sound Vib. **333**(23), 6273–6294 (2014)
12. Rothberg, S., Baker, J., Halliwell, N.A.: Laser vibrometry: pseudo-vibrations. J. Sound Vib. **135**(3), 516–522 (1989)
13. Sriram, P., Hanagud, S., Craig, J., Komerath, N.: Scanning laser doppler technique for velocity profile sensing on a moving surface. Appl. Opt. **29**(16), 2409–2417 (1990)
14. Sriram, P., Hanagud, S., Craig, J.: Mode shape measurement using a scanning laser doppler vibrometer. J. Anal. Exp. Modal. Anal. **7**(3), 169–178 (1992)
15. Stanbridge, A., Ewins, D.: Using a continuously-scanning laser doppler vibrometer for modal testing. In: Proceedings of the International Modal Analysis Conference, pp. 816–822 (1996)
16. Stanbridge, A., Ewins, D.: Modal testing using a scanning laser doppler vibrometer. Mech. Syst. Signal Process. **13**(2), 255–270 (1999)
17. Allen, M.S., Sracic, M.W.: A new method for processing impact excited continuous-scan laser doppler vibrometer measurements. Mech. Syst. Signal Process. **24**(3), 721–735 (2010)
18. Khan, A., Stanbridge, A.B., Ewins, D.J.: Detecting damage in vibrating structures with a scanning LDV. Opt. Lasers Eng. **32**(6), 583–592 (1999)
19. Chen, D.-M., Xu, Y.F., Zhu, W.D.: Damage identification of beams using a continuous scanning laser doppler vibrometer system. J. Vib. Acoust. **138**(5), 051011 (2016)
20. Meirovitch, L.: Principles and Techniques of Vibrations. Prentice Hall, Englewood Cliffs (1997)
21. Caughey, T.K., O'kelly, M.E.J..: Classical normal modes in damped linear dynamic systems. J. Appl. Mech. **32**(3), 583–588 (1965)
22. Rao, S.S.: Mechanical Vibrations, 4th edn. Pearson Prentice Hall, Upper Saddle River (2004)

Chapter 8
Mitigation of Structural-Acoustic Mode Coupling in a Modal Test of a Hollow Structure

Ryan Schultz and Ben Pacini

Abstract A phenomenon in which structural and internal acoustic modes couple is occasionally observed during modal testing. If the structural and acoustic modes are compatible (similar frequencies and shapes), the structural mode can split into two separate modes with the same shape but different frequencies; where one mode is expected, two are observed in the structural response. For a modal test that will inform updates to an analytical model (e.g. finite element), the test and model conditions should closely match. This implies that a system exhibiting strongly coupled structural-acoustic modes in test should have a corresponding analytical model that captures that coupling. However, developing and running a coupled structural-acoustic finite element model can be challenging and may not be necessary for the end use of the model. In this scenario, it may be advantageous to alter the test conditions to match the in-vacuo structural model by de-coupling the structural and acoustic modes. Here, acoustic absorption material was used to decouple the modes and attempt to measure the in-vacuo structural response. It was found that the split peak could be eliminated by applying sufficient acoustic absorbing material to the air cavity. However, it was also observed that the amount of acoustic absorbing material had an effect on the apparent structural damping of a second, separate mode. Analytical and numerical methods were used to demonstrate how coupled systems interact with changes to damping and mode frequency proximity while drawing parallels to the phenomena observed during modal tests.

Keywords Acoustic modes • Coupled modes • Structural-acoustic interaction • Acoustic absorption • Modal testing

Abbreviations

CMIF	Complex mode indicator function
CPB	Cylinder-plate-beam
DOF	Degree of freedom
FEM	Finite element model
FRF	Frequency response function
MAC	Modal assurance criterion
SMAC	Synthesize modes and correlate

8.1 Introduction

A typical practice in the analysis of component or system dynamics is to use a linear modal test for calibration of a finite-element model (FEM). This process is well understood for a linear test article that exhibits a purely structural response. However, for test articles that do not meet these criteria, FEM calibration can become more challenging. An example of such

Sandia National Laboratories is a multi-program laboratory managed and operated by Sandia Corporation, a wholly owned subsidiary of Lockheed Martin Corporation, for the U.S. Department of Energy National Nuclear Security Administration under Contract DE-AC04-94AL85000.

R. Schultz (✉)
Analytical Structural Dynamics Department, Sandia National Laboratories, P.O. Box 5800 – MS0840, Albuquerque, NM 87185, USA
e-mail: rschult@sandia.gov

B. Pacini
Structural Dynamics Department, Sandia National Laboratories, P.O. Box 5800 – MS0840, Albuquerque, NM 87185, USA

D. Di Maio, P. Castellini (eds.), *Rotating Machinery, Hybrid Test Methods, Vibro-Acoustics & Laser Vibrometry, Volume 8*,
Conference Proceedings of the Society for Experimental Mechanics Series, DOI 10.1007/978-3-319-54648-3_8

a structure is one that contains an internal acoustic volume which interacts with the structural response; one such structure is the focus of this work. Calibration of a coupled structure involves performing coupled structural-acoustic simulations which are significantly more computationally expensive than a purely structural simulation. Additionally, eigen solutions of acoustic and structural-acoustic finite element models with absorbing boundary conditions remains an area of research [1]. However, if in the experiment the structure and acoustic responses could be decoupled, the FEM calibration would devolve into the simpler process of calibrating a purely structural model. This work demonstrates how changes can be made to increase the air damping and decouple the structure from the acoustic cavity. Models, both numerical and analytical, were developed to explain phenomena observed in testing.

Section 8.2 describes the physical hardware tested in this work and its associated instrumentation. This structure was selected for this work because it exhibits structural-acoustic interactions. Section 8.3 shows the effects of this coupling on modal parameter extraction (natural frequencies, damping estimates, and mode shapes) from experimental data. Additionally, structural and acoustic modes of the coupled system are shown using FE simulations. Results of an initial decoupling attempt are also shown in this section. Behavior observed in testing is explained by analogy to a two degree of freedom (DOF) system in Sect. 8.4. Section 8.5 shows a series of tests using two methods for applying absorbing material to the air cavity and the influence of the amount of absorbing material on two different sets of ovaling modes.

8.2 Description of Hardware and Test Setup

A solid model cross-section of the test hardware (named the Cylinder-Plate-Beam assembly (CPB)) under study in this work is shown in Fig. 8.1 and the physical hardware is shown in Fig. 8.2. The Beam is bolted and epoxied to the Plate. The Plate-Beam is then mounted on the forward face of the hollow Cylinder using eight bolts. All three components are 6061-T6 aluminum. Note that the right end of the Cylinder is open, meaning the interior acoustic cavity is only partially contained.

For the experiments discussed in Sects. 8.3 and 8.5, the CPB was softly suspended using two bungee cords to approximate a free-free boundary condition and instrumented with 10 and 100 mV/g accelerometers. Twenty-six triaxial and four uniaxial accelerometers were mounted at locations that were selected as a subset of the FEM nodes to capture the Beam bending, axial extension, and Cylinder ovaling modes below 1600 Hz.

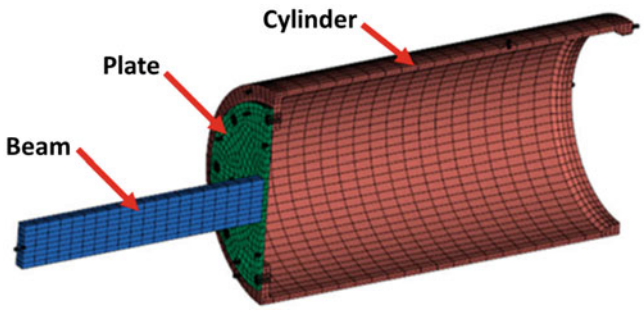

Fig. 8.1 Cylinder plate beam assembly full system solid model

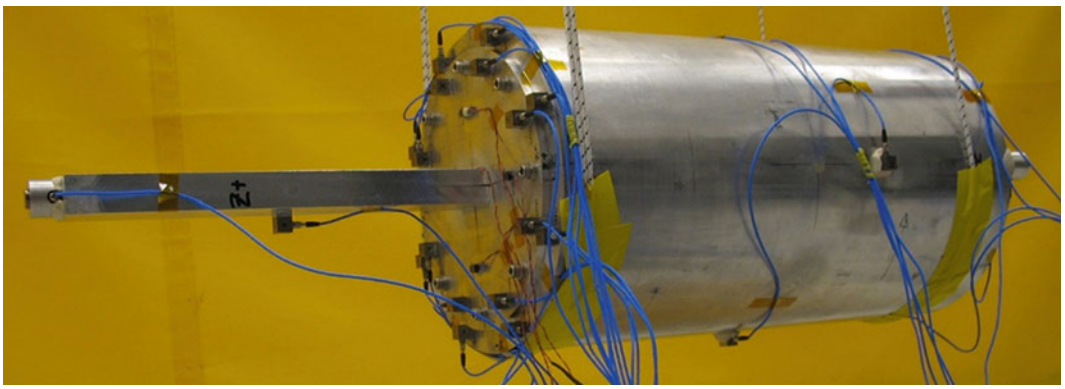

Fig. 8.2 Physical test hardware

8.3 Modal Hammer Test Results Indicate Acoustic Coupling

During a standard impact modal test conducted on the CPB, there appeared to be evidence of structural-acoustic interactions. The following subsections describe the processes and methodologies that led to this determination. First, the standard modal test is discussed where an unexpected trend in the measured frequency response functions (FRFs) was observed. Subsequently, the results from a coupled structural-acoustic FEM are shown which confirm the potential for the air cavity within the Cylinder to interact with the structure. This section concludes with the results of an experiment where an initial decoupling method was successfully employed which appeared to mitigate the influence of the acoustic response on the structural response.

8.3.1 Initial Modal Test Results

A standard hammer impact modal test was initially conducted on the CPB in order to calibrate the FEM for the structure shown in Fig. 8.2. In order to extract the natural frequencies, damping values, and mode shapes of the ovaling modes, the data from impacts at two different radial DOFs on the Cylinder were analyzed together using the multi-reference fit functionality in Synthesize Modes And Correlate (SMAC) developed by Mayes and Hensley [2] using a real modes approximation. The extracted modal parameters were used to synthesize the FRF matrix and the multi-reference complex mode indicator function (CMIF) was subsequently calculated from these synthesized FRFs. Figure 8.3 overlays the measured and synthesized multi-reference CMIFs.

An unexpected trend in the data was observed in the vicinity of the (3,1) ovaling mode pair (see Fig. 8.3b): the CMIF shows the presence of more than two modes. This trend is also observed in the measured FRFs, see Fig. 8.4. The extra peak in the data was difficult to fit and reduced the confidence in the extracted modal parameters for the (3,1) ovaling modes. Upon further investigation, it was determined that this extra peak was not due to modes of the other components of the CPB (e.g. a higher order bending of the Beam or Plate) even though SMAC fit three modes in this region. It was then hypothesized that the superfluous peak was the result of an interaction between the structure and the acoustics of the air contained within the Cylinder, similar to that seen in [3]. In order to help confirm this, a coupled structural-acoustic FEM was developed as discussed in the next subsection.

8.3.2 Coupled Structural-Acoustic Finite Element Model

A coupled structural-acoustic FEM was created in order to determine if the superfluous peaks seen in the measured data were due to structural-acoustic interactions. Each subsection below describes in detail the structural model, acoustic-only model, and the coupled model. The meshes associated with each component of the structure and the air cavity are shown in Fig. 8.5. These models were run in Sandia National Laboratories in-house structural dynamics finite element code, Sierra Mechanics [1].

8.3.2.1 Structural Model

The structural portion of the FE model had been previously developed for other research efforts [4] and contains all solid elements, approximate size of 1 [cm], with springs and tied connections at the bolted joint interfaces. Modes of the purely structural system, the in-vacuo modes, were calculated with an eigen solution of this model. Predicted mode frequencies were generally similar to those measured in the test, with the exception of the additional peak near 1400 Hz.

8.3.2.2 Acoustic Model

The acoustic model was built using the structural model as a basis to ensure a tight fit between structural and acoustic meshes. The open face of the acoustic domain was given an absorbing (impedance-matching) boundary condition. Quadratic, Hex-20, elements of approximately 1 [cm] were used in the acoustic mesh, which has 90k DOF. This element size is acceptable to approximately 3 kHz using a heuristic of 10 elements per wavelength.

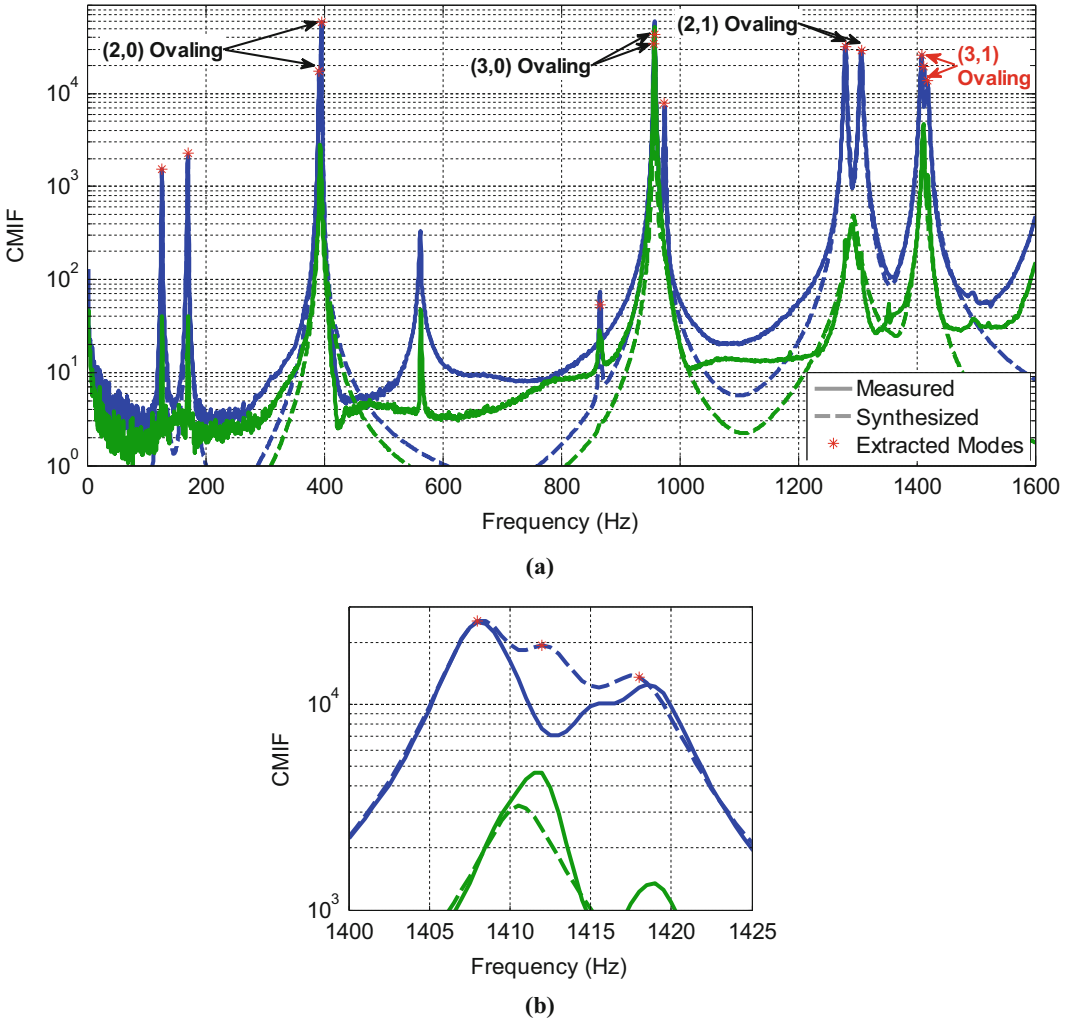

Fig. 8.3 Measured (*solid*) and synthesized (*dashed*) multi-reference CMIFs for the empty CPB showing (**a**) full measurement bandwidth and (**b**) detailed view of (3,1) ovaling mode. *Blue*: primary singular value. *Green*: secondary singular value

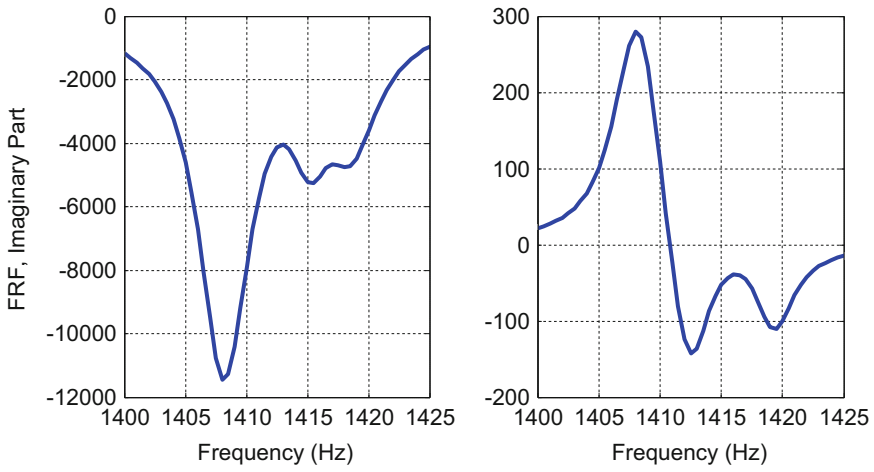

Fig. 8.4 Examples of measured FRFs which show the presence of more than two modes near 1410 Hz

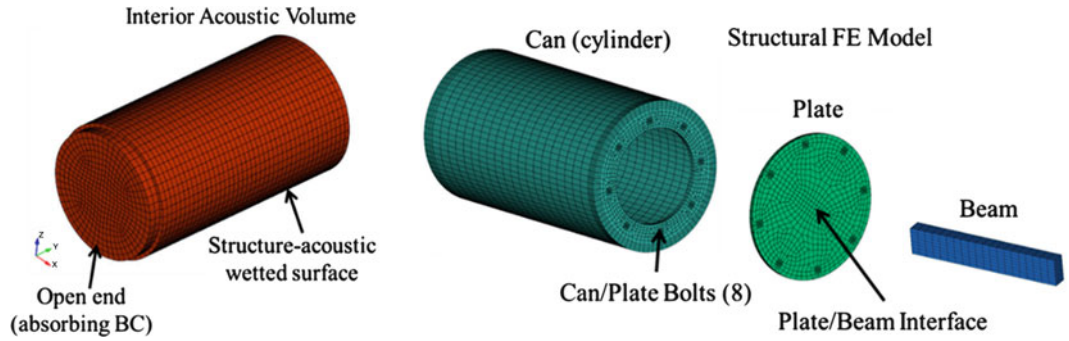

Fig. 8.5 Finite element model meshes of the acoustic internal cavity (*left*) and the structure assembly (*right*)

Modes of the acoustic cavity were computed using a quadratic eigenvalue simulation due to the absorbing boundary condition, resulting in complex modes [5]. The solution method employed here projects the problem onto a subspace of real-valued modes and as such the solution accuracy is affected by modal truncation [1]. The number of requested modes was increased until convergence in the modes of interest was obtained. There were several acoustic modes in the frequency range of interest, but particularly of interest was the acoustic (2,0) mode at 1408 Hz which is similar to the structural modes in both frequency and shape.

8.3.2.3 Coupled Finite Element Model

The structure and acoustic models were combined and run with a quadratic eigen solution method using a component modes approach. Similar to the projection method used in the purely acoustic simulation, this method is also subject to modal truncation errors and as such multiple simulations were run to assess and obtain a converged result [1, 6]. It was determined that using a basis of 150 modes was sufficient. A subset of results of the coupled-system quadratic eigen simulation are shown in Table 8.1. One output from the coupled simulation is a ratio indicating the contribution of the structure and air cavity to the overall mode shape. This value ranges from zero to one for both the structure and air cavity, but the sum of the two ratios must be equal to one. For this system, there were no modes where the mode ratio was nearly even between the structure and acoustic portions (i.e. no mode had the mode ratio near 0.5 for the structure and air cavity). However, the modes most similar to the (2,1) structural mode and (2,0) acoustic mode show contributions of the lesser component that are orders of magnitude larger than the other modes, which indicates there is some structural acoustic coupling for these modes. Also, the mode similar to the (3,1) structural mode shows larger than typical contribution by the acoustic component, though not as significant as the two previously mentioned modes.

The (2,0) acoustic mode at 1408 Hz is close in frequency to the (3,1) structural mode at 1416 Hz. This suggests that the superfluous peaks seen in the measured data at the (3,1) ovaling modes (Figs. 8.3 and 8.4) are due to coupling between the structure and air cavity within the Cylinder. The next subsection discusses a second impact modal test where an initial attempt is made at decoupling the structural response from the acoustic response.

8.3.3 Initial Decoupling Attempt

As an initial attempt to decouple the structure from the acoustic response, a foam covered rod was inserted into the empty cavity of the Cylinder, see Fig. 8.6. Adding this device to the air cavity possibly changes the acoustic modes in two ways. First, there is significant damping of the air mode from the absorption properties of open-cell foam. Second, the foam rod occupies volume, which changes the boundary conditions in the air cavity and could shift the acoustic mode frequency or alter the shape. Note that the rod is held away from the Cylinder walls to avoid adding unwanted structural damping to the system.

The two impacts from the first modal test described in Sect. 8.3 were repeated and the modal parameters were again extracted. These natural frequencies, damping values, and mode shapes were again used to synthesize the multi-reference CMIF which is overlaid with the corresponding measured multi-reference CMIF in Fig. 8.7. Additionally, the FRFs from Fig. 8.8 are overlaid with the corresponding FRFs from this latter experiment. These plots show that the foam covered rod performed as desired and the peaks from the acoustic-structure interaction were removed.

Table 8.1 Coupled FE structure + acoustic eigen results

Description	Mode Type	In-vacuo Freq. (Hz)	Coupled Freq. (Hz)	% Structure	% Acoustic	Mode Shape: Left-Structure, Right-Acoustic
(2,1) Ovaling Pair	Structure	1321.0	1321.0	99.960	0.040	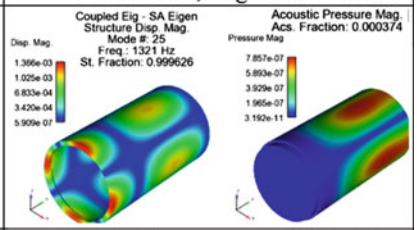
(2,0) Ovaling Pair	Acoustic	1408	1407.0	0.040	99.960	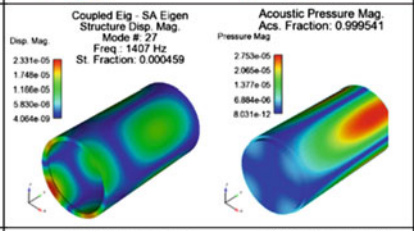
(3,1) Ovaling Pair	Structure	1416.0	1416	99.998	0.002	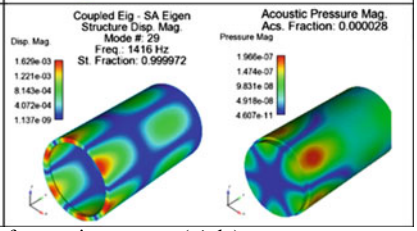

Mode shape visualizations are magnitude of radial displacement of structure (*left*) and magnitude of acoustic pressure (*right*)

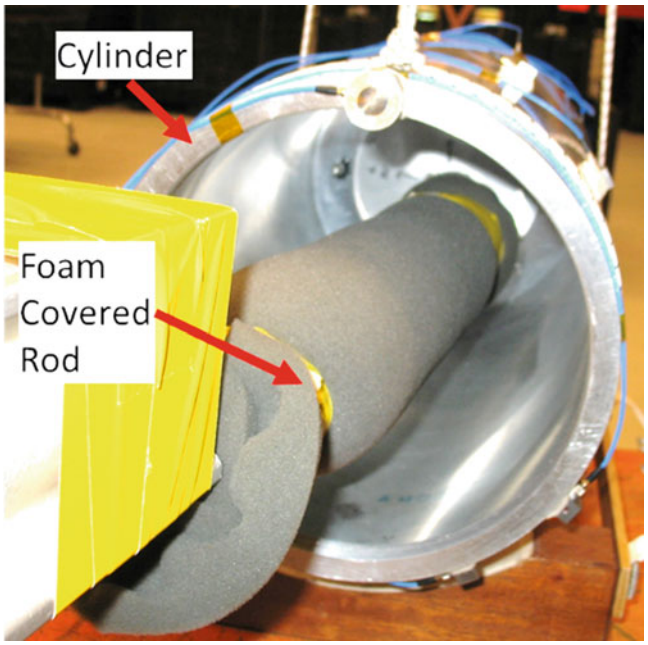

Fig. 8.6 Initial attempt at acoustic-structure decoupling with foam-covered rod inserted in the air cavity

8.4 Coupling Effects Demonstrated with a Simple Two Degree of Freedom Model

The previous section showed the successful implementation of an initial decoupling strategy in which the test setup was altered to sufficiently add damping to the acoustic response such that the superfluous peaks in the experimental data were removed and structural modal parameters could be extracted. In order to better understand the relationship between particular test setup changes and their corresponding influence on the acoustic modal properties (natural frequency and damping),

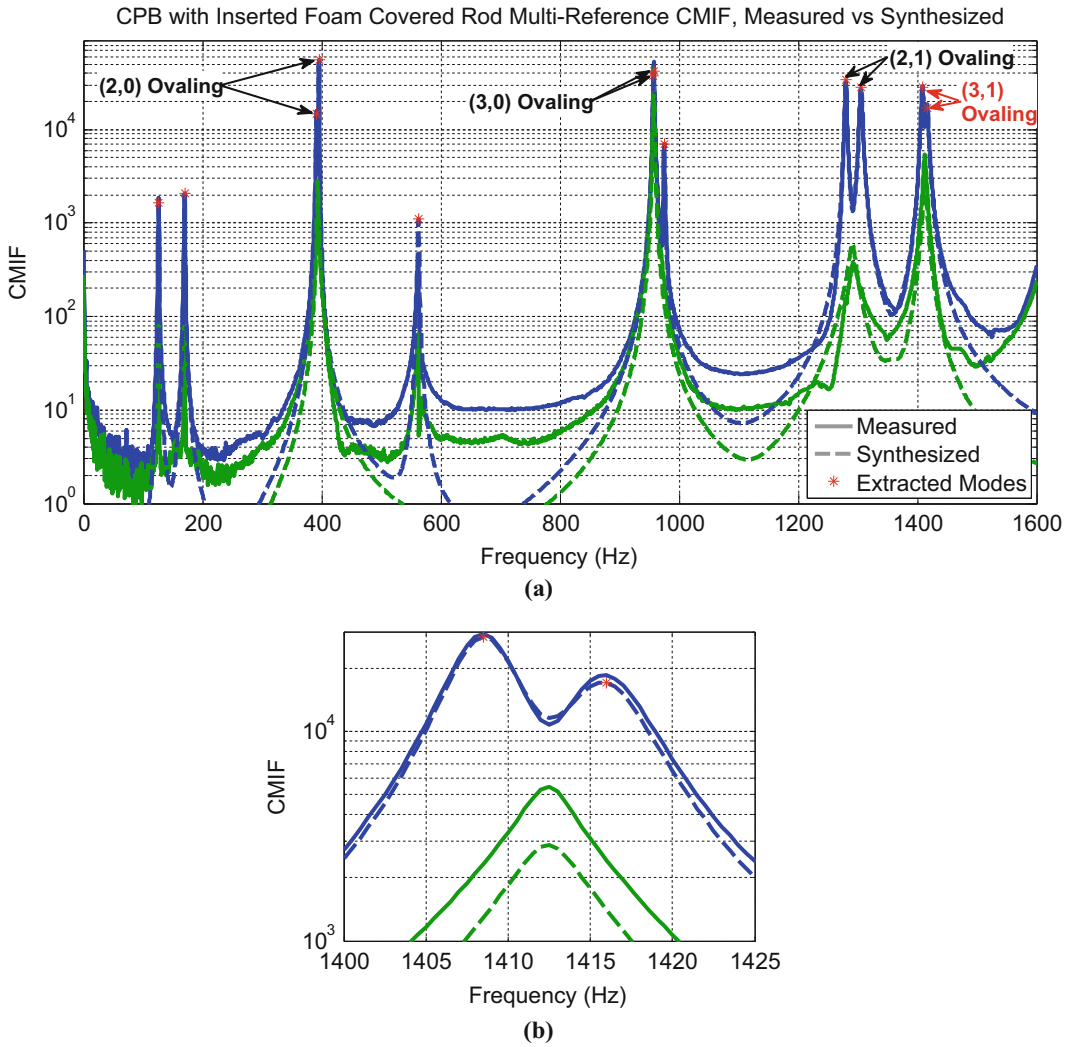

Fig. 8.7 Measured (*solid*) and synthesized (*dashed*) multi-reference CMIFs for the CPB with the inserted foam covered rod showing (**a**) full measurement bandwidth and (**b**) the detailed view of the (3,1) ovaling mode pair

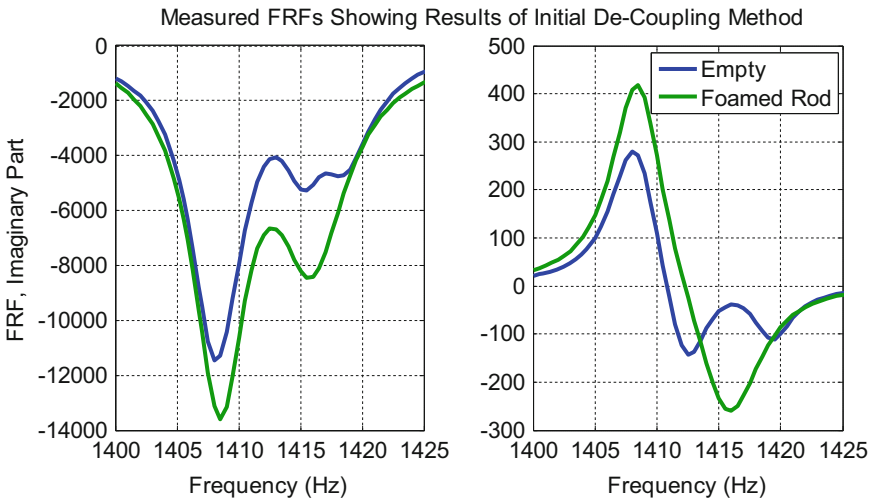

Fig. 8.8 A sample of measured FRFs from two experiments: empty cylinder (*blue line*) and foam covered rod inserted (*green line*)

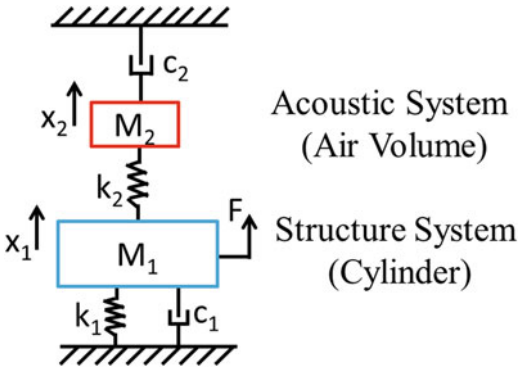

Fig. 8.9 Two DOF system representing a coupled structural-acoustic system, the structure is mass $\boldsymbol{M}_1$ and the acoustic volume is mass $\boldsymbol{M}_2$. The connecting spring, $\boldsymbol{k}_2$, is the stiffness of the air and is driven by motion of the structure

a simple analytic model was employed, shown in Fig. 8.9. Coupled structural-acoustic modes act like a two DOF system and are akin to a classic tuned absorber system [7]. The first DOF (M_1) is the structure component, grounded by its stiffness and damping. The second DOF (M_2) is the acoustic component and is connected to M_1 by a spring, k_2, which determines the acoustic mode frequency. This configuration where the acoustic volume is connected to the structure (as opposed to ground) was selected because the motion of the air is driven solely by the structure. Damping, however, is different in that the acoustic damping due to some absorptive material is only dependent on the motion of the air, x_2, and not the relative motion of $x_2 - x_1$. As such, the air damping, c_2, is connected to ground.

The k_2 spring couples the structure and acoustic components. This coupling affects the response of both components, and if the modes of each component are similar in frequency, the response will be very different from the response of the components individually. This is the desired behavior of a vibration absorber, where the presence of mass M_2 causes a split in the resonant peak of mass 1 [8]. This two DOF system is a special case in that the mode shapes of each component are identical. However, for most systems, even if the component modes are the same frequency, they can have different shapes and the coupled system behavior will be different from the two DOF vibration absorber. In the extreme case where one component is very light relative to the other, as in the interaction of most structures with air, the structure response is generally not affected by the air if the modes of the structure and air are different in frequency and/or shape; air simply provides trivial mass loading to the structure [9]. However, if the modes of the air and structure are similar in frequency and shape, the structure response is affected.

The simple model in Fig. 8.9 can be used to study the structural response under various coupling scenarios by simply altering the acoustic spring (k_2) and damper (c_2). Of particular interest for this work is investigating the influence of modifying c_2 since that is main approach utilized in the experimental mitigation strategies discussed later in this report (see Sect. 8.5). Note that since the analytic model from Fig. 8.9 is just a coupling of two single degree of freedom systems, the mode shapes of each system are inherently compatible (the same shape), an important distinction between this simple model and the full FE coupled model.

The values for the parameters from Fig. 8.9 were selected to match the structural modes studied in the mitigation strategies discussed in Sect. 8.5. As seen from Sect. 8.1, the (3,1) ovaling modes exhibit structural-acoustic coupling. However, as discussed later, the (2,1) ovaling modes near 1300 Hz also show this coupling (see Sect. 8.5.3). Therefore, the parameters for this model were chosen to reflect the test item near the 1320 Hz ovaling mode (note that this is frequency from the FEM for this mode). Mass M_1 is the mass of the test structure, M_2 is set to the weight of the air volume, k_1 is set to put the structure mode at 1320 Hz, and c_1 set to give 0.50% damping in the structure. In the following sections, the parameters of the air, k_2 and c_2 are varied to observe the effects on the structure response. Section 8.4.1 demonstrates the structural FRF influences from various proximities of the structural and acoustic modal frequencies. Section 8.4.2 sets the structural and acoustic modal frequencies equal and shows how the structural response changes when the damping of the air is altered. Section 8.4.3 presents a similar analysis as 8.4.2 where the air damping is varied except the modal frequencies of the two components are no longer set equal. Note that the FRF for the purely structural response is plotted in each section for comparison.

8.4.1 Effects of Modal Frequency Proximity

By adjusting the stiffness of the air component, the effect on the structural response of the proximity of the structure and acoustic modes can be observed in the acceleration over force FRF for mass M_1 in Fig. 8.10. When the modes are near in frequency (in-tune), there is a large change in the structure response, with a split peak as in a typical tuned absorber system.

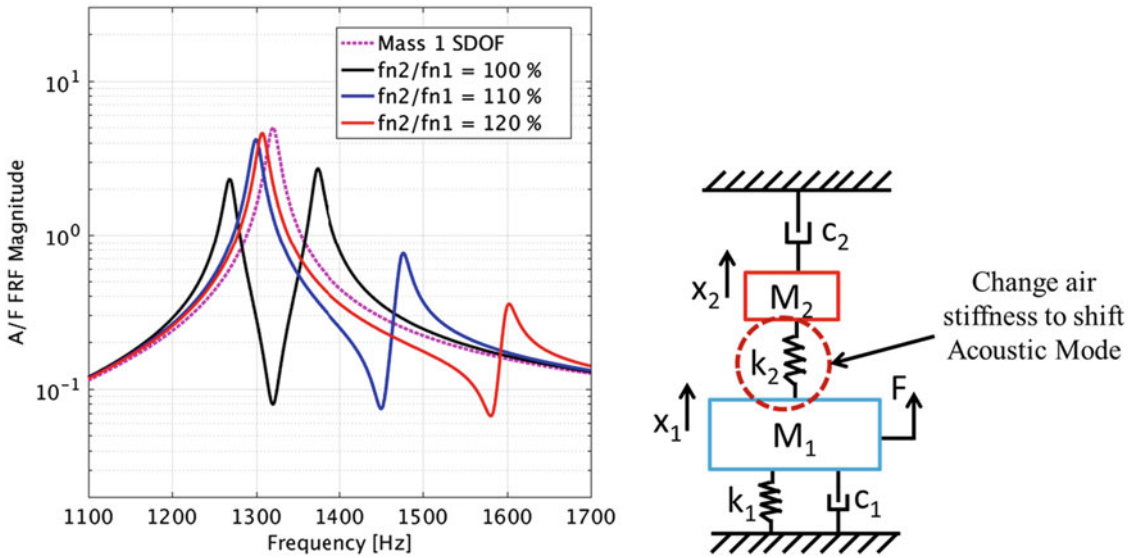

Fig. 8.10 Effect of acoustic mode to structural mode frequency ratio (mistuning) on the acceleration/force FRF for the structure

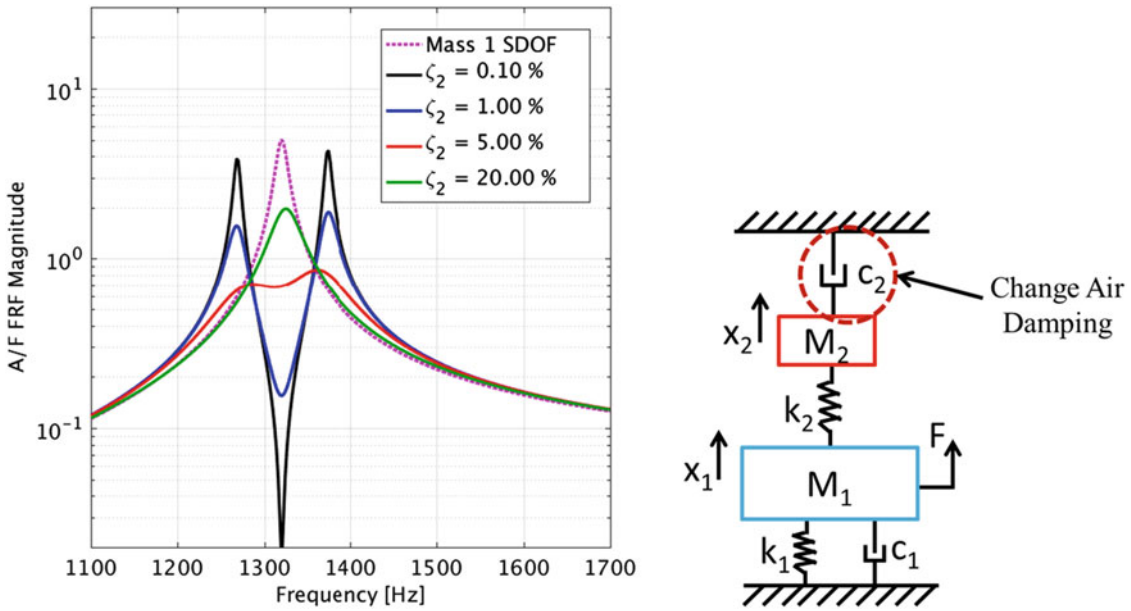

Fig. 8.11 Effect of acoustic damping for the case when acoustic and structure modes are close in frequency

When the frequencies are different (mistuned), there is some small shift in the structure mode's frequency and amplitude, but mostly the effect is observed away from the resonance, where an anti-resonance and secondary resonance is observed near the mistuned acoustic mode frequency. This is the expected behavior of a tuned absorber [8].

8.4.2 Effect of Air Damping When Structural and Acoustic Frequencies Are In-Tune

Figure 8.11 shows the effect of air damping for the case when the structure and acoustic modes are well aligned. The pink dotted line shows the structure-only single DOF FRF. Interestingly, with small air damping, the split peak response is seen, but as air damping is increased, the response looks more like the original, structure-only response. With progressively more air damping, the structure response actually increases.

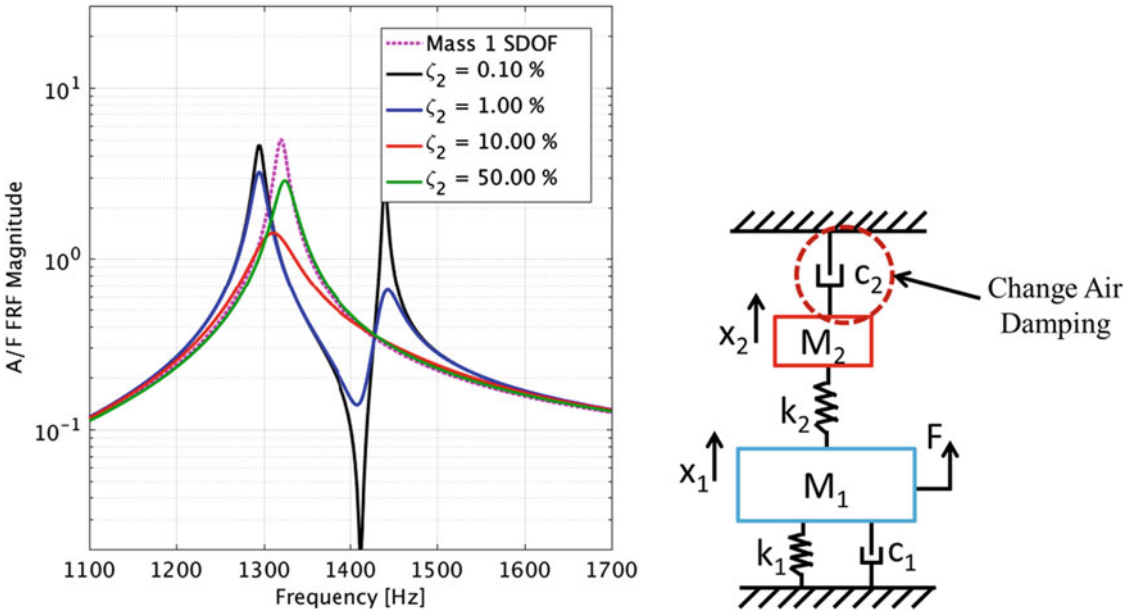

Fig. 8.12 Effect of acoustic damping for the case when acoustic and structure modes are not close in frequency

8.4.3 Effect of Air Damping When Frequencies Are Well Separated

This scenario is the most relevant as it relates to the phenomena observed in testing in Sect. 8.5.3 where greatly increased air damping modified the damping of a structural mode ((2,1) ovaling at 1305 Hz) when the acoustic mode of similar shape had a much different frequency ((2,0) ovaling at 1408 Hz). As seen in Fig. 8.12, when the air damping is small, there is a shift in the structure mode peak and the amplitude decreases with increasing damping. However, when damping becomes very large, the structure peak amplitude actually increases and approaches the structure-only FRF.

8.5 Experimental Study of the Effect of Added Air Damping

This section details the experimental efforts to replicate the structural-acoustic coupling effects analytically observed with the two-DOF model in the previous section. Since altering the air damping is most conveniently implemented in experiment, it was selected as the main decoupling method for this work (i.e. the experiments discussed in this section correlate to the results from Sects. 8.4.2 and 8.4.3).

In the following subsections, two series of experiments were performed to show the influence of test setup modifications on the coupling effects observed by measured accelerometer data. The first modification was an extension of the foam covered rod method utilized in Sect. 8.3.3. Several iterations were conducted where more foam was sequentially added and its effect on the structural response was observed. The second modification explored adding progressively larger blocks of foam set directly in contact with the Cylinder inner walls. This approach is easy to implement, though has the potential downside of adding unwanted structural damping due to some contact with the Cylinder walls.

Note that the original intent was to observe the changes in the (3,1) ovaling modes near 1400 Hz. However, as testing progressed and upon further inspection of the FRFs, it was found that the responses of the (2,1) ovaling modes near 1300 Hz were also being modified. This trend is consistent with the FEM results from Table 8.1 which show very similar structure and acoustic mode shapes at 1321 Hz and 1408 Hz, respectively. It would be expected that these modes couple in ways similar to the two-DOF system shown in Sect. 8.4.3.

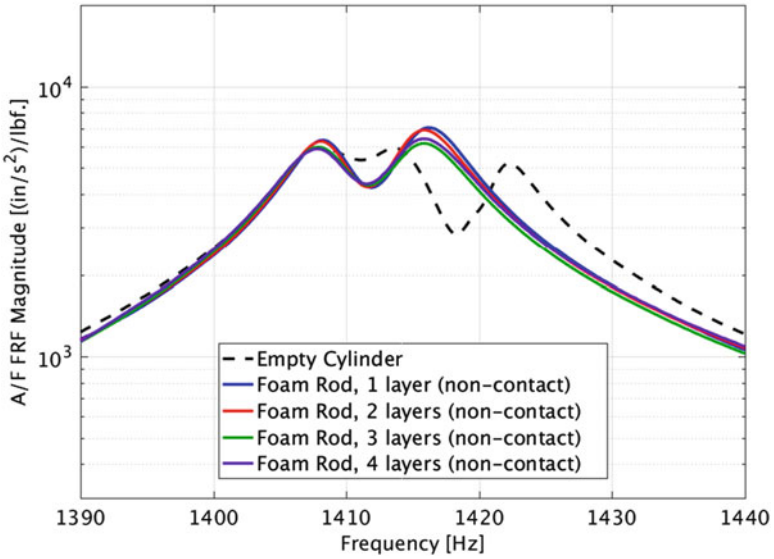

Fig. 8.13 Measured drive point acceleration/force FRFs of the CPB near the (3,1) ovaling mode for test runs with a non-contacting foam rod with progressive added foam layers

8.5.1 Decoupling Strategy 1: Non-Contact Foam Covered Rod

This strategy is a continuation of that employed in Sect. 8.3.3 and involved progressively adding absorptive material (foam) to the air cavity without contacting the CPB structure. This was accomplished by holding a foam-wrapped rod in the middle of the air cavity, Fig. 8.6. The rod was located off-center and not aligned parallel with the central axis of the Cylinder. The rod was wrapped with one layer of open cell foam, then progressively more layers of foam were added to observe the effect of increasing the amount absorptive material (increase in air damping) on the structural response. Care was taken to ensure the foam did not contact the Cylinder walls.

The results of this test series are shown in Fig. 8.13 which shows the drive point FRF for the different number of foam layers added to the rod. This coupling mitigation strategy removed the split-peak in the drive point FRF, but significant differences are not observed after the insertion of the foam rod with one layer of foam (blue line in Fig. 8.13); there appears to be sufficient acoustic absorption in all cases and the results at this mode are converged.

8.5.2 Decoupling Strategy 2: Foam Blocks Set Directly on Inner Wall of Cylinder

The second decoupling strategy also involved adding acoustic absorption material (foam) into the Cylinder. However, instead of a non-contacting, foam-covered rod, small foam blocks ranging in size from a 2.5 cm cube to a $5 \times 5 \times 25$ cm brick were placed inside and in direct contact with the Cylinder, see Fig. 8.14. This would be the most practical mitigation method for a modal test engineer as it simply involves putting some volume of acoustic absorption material in the cavity, without the need for special hardware to suspend the absorbing material away from the structure. As such, it is important to understand (1) how much foam is needed to decouple the structure and remove the split peak at the (3,1) mode and (2) if there is any noticeable added structural damping.

The results of the test runs of the various sizes of foam blocks are shown in Fig. 8.15. A clear progression is observed as the volume of the foam blocks increases from the empty Cylinder configuration to the response where the split peak is completely removed. It appears that even a modestly-sized piece of foam ($5 \times 5 \times 12$ cm) provides sufficient absorption to remove the split peak at this mode. This added air damping affects this system in a similar manner to the two-DOF system in Sect. 8.4.2. In terms of adding unwanted structural damping to the system, the addition of these foam blocks did change the peak FRF for other modes, though the effects were not quantified.

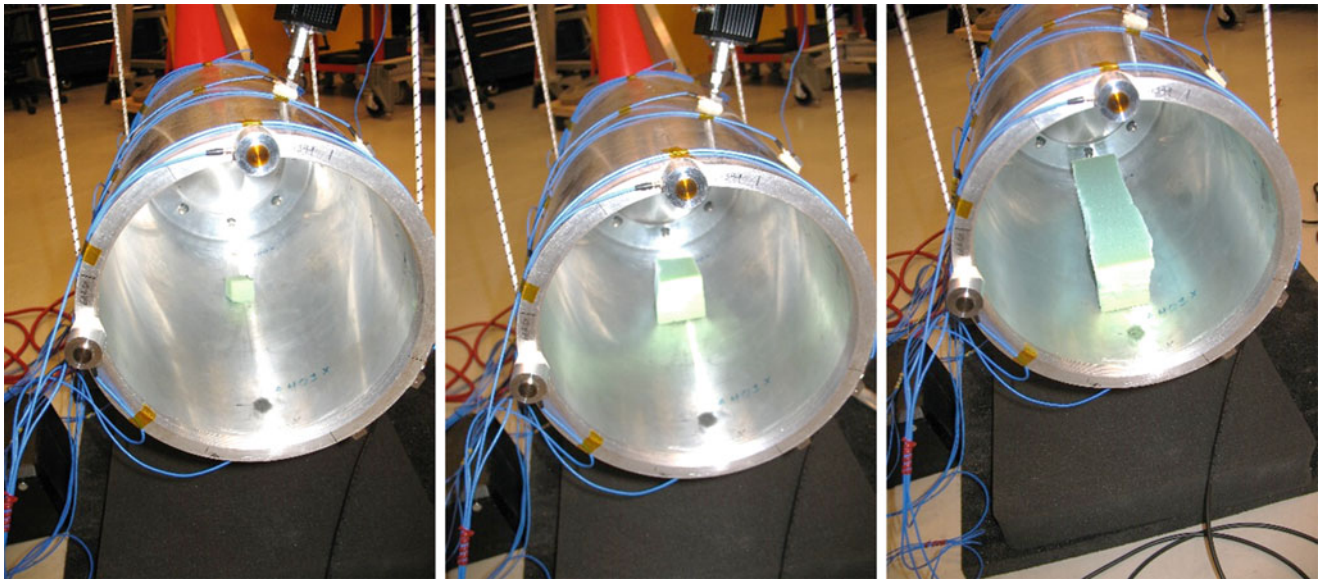

Fig. 8.14 Open-cell foam set on Cylinder wall for acoustic absorption, varying from small cube (*left*) to larger block (*right*)

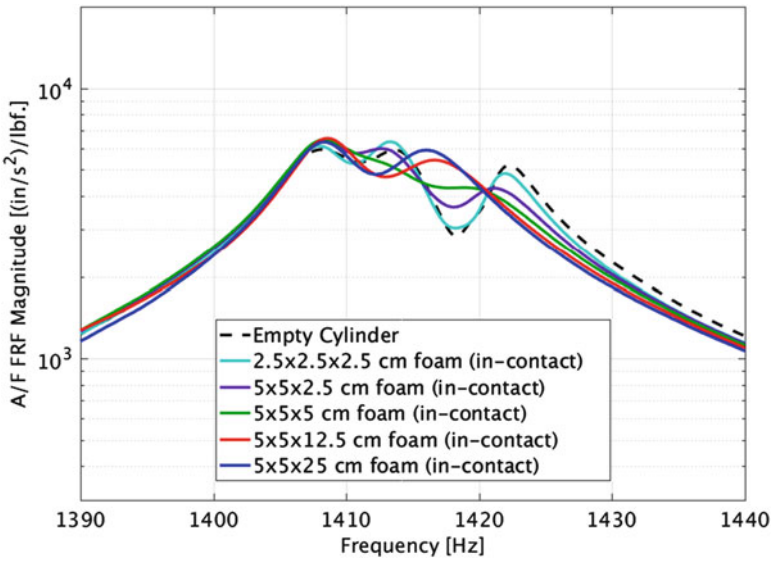

Fig. 8.15 Experimental drive point FRFs near the (3,1) ovaling mode, for runs with progressively larger foam blocks set on the cylinder inner wall

8.5.3 Effect of Added Absorptive Material on the (2,1) Ovaling Mode

Adding foam to the air cavity, either with the non-contact or in-contact methods, was effective in removing the superfluous peak near the (3,1) structural mode pair. However, during testing it was observed that the response well away from this mode, near the 1300 Hz (2,1) ovaling mode, was being noticeably altered by adding foam to the interior cavity. While adding more absorbing material to the air cavity did change the peak response somewhat at all resonances, the effect was most significant at the (2,1) ovaling mode pair, and this is the mode most similar in both shape and frequency to an acoustic mode of the cavity.

Figure 8.16 shows the effect of the added damping on the (2,1) structural mode drive point FRF for the two decoupling strategies mentioned above. In both cases, the structural damping is affected by the presence of the acoustic absorption material. Note that there is much more acoustic absorption material wrapped around the rod (strategy 1) than the inserted foam blocks (strategy 2). One interesting observation from the foam rod results is that initially the added damping decreases the structural response, but as more foam is added, the response actually increases slightly. This phenomenon is observed in

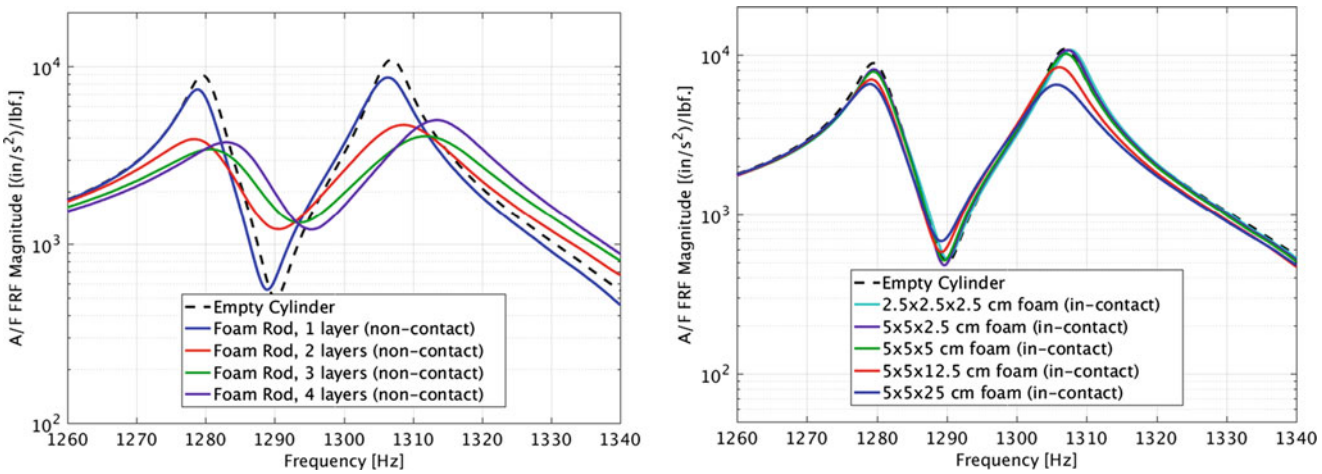

Fig. 8.16 Test FRF near the (2,1) ovaling mode, with non-contact foam rod (*left*) and in-contact foam blocks (*right*)

the two-DOF model shown Sect. 8.4.2. What appears to happen is the structure is driving the air which is being absorbed by the foam. When the absorption in the foam is very high, however, the air is no longer being driven by the structure and the damping from the air goes away, leaving something more like the in-vacuo structure response.

The results for strategy 2 (foam blocks placed on the inner wall) again show some change in structural damping. Note that for both mitigation strategies, adding air damping appears to increase structural damping and as such it is difficult to say that the foam blocks on the inner wall are adding structural damping due to being in contact with the structure. Instead, it could be that the structure is simply interacting with a heavily-damped air cavity which appears to increase structural damping, as evidenced by the foam rod results.

8.6 Conclusions and Future Work

The objective of this work was to explore methods for obtaining the structure-only response from a system which exhibits structural-acoustic interactions. These phenomena can manifest in measured FRFs as superfluous resonant peaks. Modes predicted with a coupled FEM indicated that there is an acoustic mode of similar shape in the vicinity of the superfluous peak measured in preliminary testing. It was found via experimentation that these peaks can be eliminated by adding acoustic absorption material (various amounts open-cell foam in this case) to the air cavity. Unfortunately, simply adding an arbitrary amount of foam does not immediately yield the in-vacuo structural response. Rather, the structure begins to act more uncoupled as more absorbing material is added to the air cavity. In addition to the removal of the superfluous coupled peak, the increased amount of absorbing material also affected the apparent structural damping. Interestingly, while it was observed that structural damping is affected at multiple modes, it most significantly affected at the (2,1) ovaling mode. This is the structural mode which is most compatible to an acoustic mode, as evidenced by the coupled FEM simulations and observation of the structure and acoustic mode shapes and frequencies. Coupled system response as a function of air damping was also explored using a simple two-DOF system with the component modes both in and out of tune, which reflects the structure-acoustic mode proximity observed in the test article. The effects of air damping on the two-DOF system response were very similar to those seen in the experiments, including a case where the structural response began to increase when the acoustic damping became very high.

It remains an open question if the in-vacuo response was achieved by any of the acoustic damping approaches—in part because the in-vacuo response is not known. Future work will focus on performing frequency response simulations of this coupled FE model to replicate the damping-dependent trends observed in test and compare to the purely structural response. This will provide some method for assessing if mitigation approaches employed experimentally sufficiently decouple the system. It would also be useful to investigate a metric for assessing structure and acoustic modes to determine if they are likely to couple. Additionally, further testing is needed to better understand the change in apparent structural damping observed in the (2,1) mode when the amount of air damping is changed.

References

1. Sierra Structural Dyanmics Development Team: Sierra Structural Dynamics - User's Notes. Sandia National Laboratories SAND Report, 2015
2. Hensley, D.P., Mayes, R.L.: Extending SMAC to multiple references. In: Proceedings of the 24th International Modal Analysis Conference, 2006
3. Pacini, B.R., Tipton, G.: Structural-acoustic mode coupling in a bolted aluminum cylinder. In: Proceedings of the 34th International Modal Analysis Conference, Orlando, FL, 2016
4. Owens, B., Schultz, R., Mayes, R., Pacini, B.: Nonlinear identification for improved modeling of nonlinear damping in structural dynamics analysis. In: International Modal Analysis Conference 2017 (IMAC 35), Garden Grove, CA, 2016
5. Day, D.M., Walsh, T.F.: Quadratic Eigenvalue Problems. SAND Report, Sandia National Laboratories, Albuquerque, NM, 2007
6. Tisseur, F., Meerbergen, K.: The quadratic eigenvalue problem. SIAM Rev. **43**(3), 235–286 (2001)
7. Hambrick, S.A., Sung, S.H., Nefske, D.J.: Engineering Vibroacoustic Analysis: Methods and Applications. Wiley, Hoboken (2016)
8. Rao, S.: Mechanical Vibrations. Prentice Hall, Upper Saddle River (2003)
9. Junger, M., Feit, D.: Sound, Structures, and Their Interaction. Acoustical Society of America, Melville (1993)

Chapter 9
Applications of 3D Scanning Laser Doppler Vibrometry to an Article with Internal Features

Bryan Witt, Brandon Zwink, and Ron Hopkins

Abstract 3D scanning laser Doppler vibrometry (LDV) systems continue to gain popularity for use in experimental modal analysis as the systems become more widespread. LDV is, by its nature, limited to measurements with line-of-sight visibility. This work presents an application of 3D scanning LDV to a test article with un-instrumented internal features that were not accessible to the lasers. The internal features, while not directly measurable, were known to contribute strongly to the modal characteristics of the test article. Initially, a traditional roving hammer test was conducted and modal parameters were extracted. The limited degrees of freedom inherent to this test method proved to be inadequate to correctly identify key mode shapes. It was found that by increasing the measurement point density and including all three translational degrees of freedom at each point, the key modal characteristics of the full system were able to be inferred from purely external measurements. These characteristics were essential in updating the mechanical behavior and material properties of the corresponding finite element model. The response measurements required for system identification were only practically achievable using the 3D LDV system. Comparisons of key experimental results to those of the calibrated analytical model are demonstrated.

Keywords 3D • Laser • Vibrometer • Experimental • Modal

9.1 Introduction

A cylindrical test article was constructed with internal features that significantly contributed to the lower frequency elastic modes of vibration. These internal features were un-instrumented and could not be measured directly. A finite element model (FEM) was constructed of the test article to predict its dynamic characteristics, however experimental modal data were necessary to update the FEM to provide appropriate results.

The first attempt to extract modal parameters from the test article involved performing a roving hammer modal test. Results from this test, where impacts can only be made perpendicular to surfaces, were difficult to decipher and correlate to the finite element model. It was decided that adding measurement degrees of freedom (DOF) at locations tangential to the surface of the test article would help improve the ability to discern and match mode shapes between the experimental results and the analytical model.

To that end, a second test set was performed on the same test article using a 3D scanning laser Doppler vibrometer (LDV) which allowed three degrees of freedom to be measured at each measurement location without mass loading the surface of the test article with instrumentation. The LDV testing also employed impact excitation at selected DOF. The LDV results were then analyzed and used to update the FEM as the laser results were viewed as an improvement over the original roving hammer results.

Sandia National Laboratories is a multi-program laboratory managed and operated by Sandia Corporation, a wholly owned subsidiary of Lockheed Martin Corporation, for the U.S. Department of Energy's National Nuclear Security Administration under contract DE-AC04-94AL85000.

B. Witt (✉) • B. Zwink • R. Hopkins
Sandia National Laboratories, P.O. Box 5800 - MS0557, Albuquerque, NM 87185, USA
e-mail: blwitt@sandia.gov; bzwink@sandia.gov; rnhopki@sandia.gov

D. Di Maio, P. Castellini (eds.), *Rotating Machinery, Hybrid Test Methods, Vibro-Acoustics & Laser Vibrometry, Volume 8*,
Conference Proceedings of the Society for Experimental Mechanics Series, DOI 10.1007/978-3-319-54648-3_9

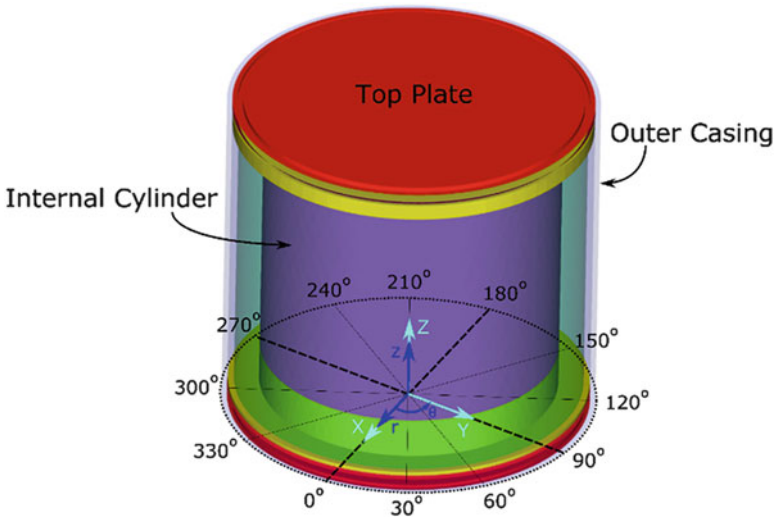

Fig. 9.1 Test article representation

9.2 Test Article

The test article can be characterized as a sealed outer cylindrical casing with a solid cylindrical internal feature. The outer casing is metallic and the top and bottom plates are welded to the outer casing. The internal cylindrical feature is supported within the casing by a non-homogeneous layer which contacts all internal surfaces. A pictorial representation of this generalized characterization is provided in Fig. 9.1. The effective stiffness of the internal support layer is assumed to be different in each of the six DOF.

A global Cartesian coordinate system, denoted [*X*, *Y*, *Z*] was defined at the center of the outer casing bottom plate. A cylindrical coordinate system, denoted [r, θ, z], used to locate the measurement nodes, was defined at [0, 0, 0] in the global Cartesian system. The 0° azimuth was aligned directly the global *X* axis (see Fig. 9.1).

9.2.1 Preliminary Model Predictions

The primary modes of interest for FEM updating were the shear (translation) and axial modes of the internal cylinder. The test article is a preloaded assembly; the preload effects on the stiffness of the members which support the internal cylinder are very difficult to determine analytically. Therefore, it was necessary in the development of a predictive FEM to experimentally determine the natural frequencies and shapes of the modes in which the internal cylinder participates heavily. The analytically generated shapes for the internal cylinder shear (one of two orthogonal modes) and the axial mode are shown in Fig. 9.2.

9.3 Initial Roving Hammer Testing

9.3.1 Test Setup

Initially, a traditional roving hammer test was performed to extract modal parameters (natural frequencies, damping ratios, and mode shapes) of the test article in an approximated free-free boundary condition by placing the test article on soft foam. The roving hammer method was used to increase measurement point density without severely mass loading the test article with accelerometers. In order to capture all modes of potential interest, testing was conducted in two configurations: (1) axial/radial and (2) torsional.

In the axial/radial configuration, columns of five measurement nodes were spaced along the *Z* axis at 30° intervals around the outer casing, resulting in 60 nodes. Nine nodes were placed on the bottom plate along the [0°, 90°, 180°, 270°] azimuths. Finally, five nodes were placed on the top plate along the [0°, 90°, 180°, 270°] azimuths. A total of 74 measurement locations

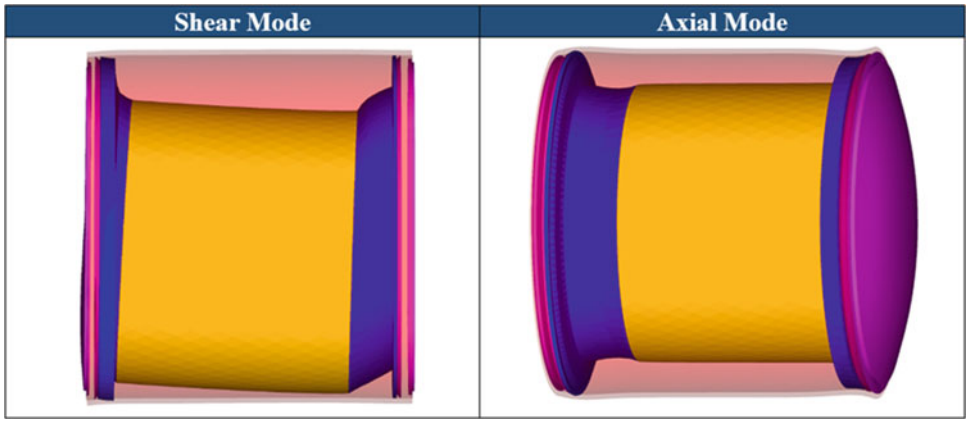

Fig. 9.2 Preliminary internal cylinder shear and axial modes

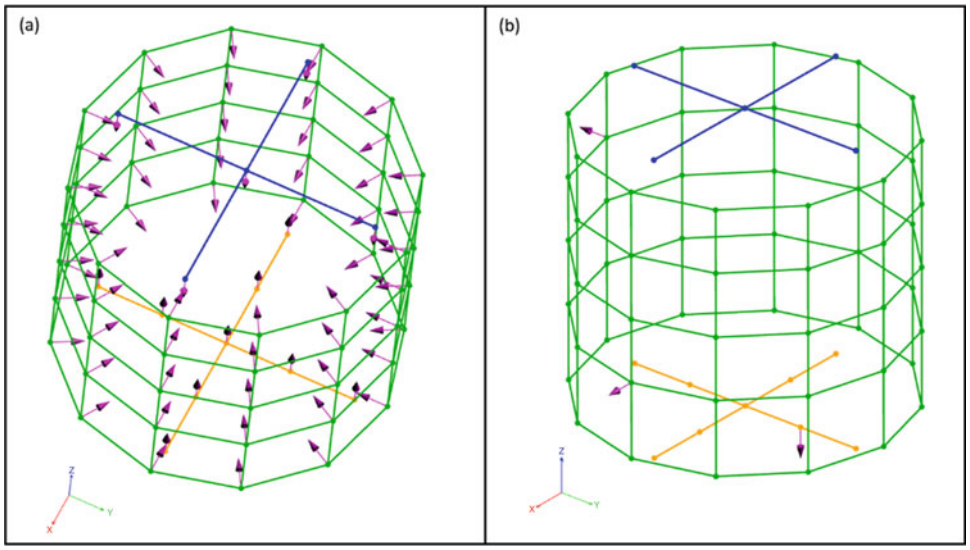

Fig. 9.3 Roving hammer axial/radial configuration (**a**) axial/radial impact locations, (**b**) accelerometer locations

were used for the axial/radial test configuration; impacts were made at each of these nodes, perpendicular to the surface as shown in Fig. 9.3a. Three reference accelerometers were affixed to the test article at the locations and directions shown in Fig. 9.3b.

In the torsional configuration, eight additional lightweight instrumentation blocks were affixed to the test article with cyanoacrylate at the locations denoted with arrows in Fig. 9.4a. These were necessary in order to provide surface locations for torsional excitation impacts and mounting a reference accelerometer to measure their corresponding responses. In this configuration, impacts were only made at each of the eight instrumentation blocks as shown in Fig. 9.4a; no axial impacts were performed. The limited number of impact locations in the torsional configuration was thought to be adequate, as this configuration was intended only for extraction of the internal cylinder's first torsional mode. One reference accelerometer was located as shown in Fig. 9.4b.

The weights and locations of all accelerometers and instrumentation blocks were provided to the analyst for inclusion during model updating. The total weight of all eight instrumentation blocks amounted to 1.25% of the test article's weight. These effects were not expected to substantially change the final results.

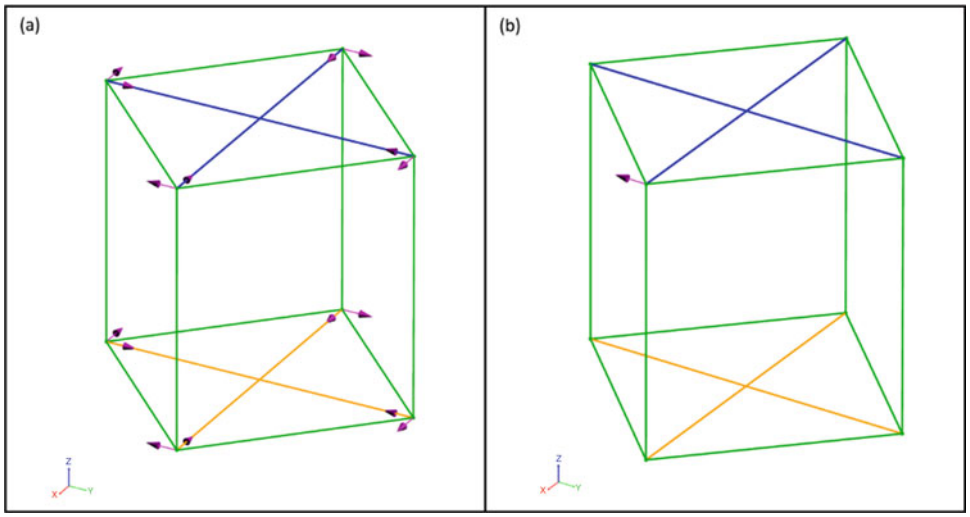

Fig. 9.4 Roving hammer instrumentation for (**a**) torsional impacts, (**b**) torsional reference accelerometer

Table 9.1 Modal parameters extracted from roving hammer test

Mode #	Description
1	Internal cylinder shear in X
2	Internal cylinder shear in Y
3	Internal cylinder torsion
4	Top & bottom plate drumming together 1
5	Top & bottom plate drumming together 2

9.3.2 Results

Modal parameters were extracted using the Synthesize Modes and Correlate (SMAC) algorithm developed by Hensley and Mayes [1]. Results for the two configurations (axial/radial and torsional) were extracted separately and then combined into a final set. The final set of extracted modes for roving hammer testing is given in Table 9.1, and corresponding mode shapes are shown in Fig. 9.5. The modal properties were used to resynthesize the FRF and subsequently the complex mode indicator function (CMIF) to evaluate how well the extracted results represented the overall system dynamic characteristics (see Fig. 9.6).

The first two modes appear to exhibit "rigid body" type motions of the external casing, although at frequencies much too high to be actual rigid body modes of the test article. These two modes were inferred as the internal cylinder translating, or shearing, in a direction opposite to that of the external casing.

Initial review of the experimental CMIF indicated that there were likely three modes in the area near Modes 4 and 5 highlighted in Fig. 9.6a with a dashed box. Modes 4 and 5 could not be visually distinguished, as can be seen in Fig. 9.5, and exhibited high off-diagonal modal assurance criterion terms. Not surprisingly, a good fit could not be achieved in this frequency range. Further, the small CMIF local maximum between Modes 2 and 4 in Fig. 9.6a was originally thought to be the internal cylinder torsion mode; it was poorly excited by axial/radial hits and no acceptable fit could be made. However, the internal cylinder first torsion (Mode 3) was extracted from the second configuration at a *higher* frequency, which was curious since the added mass of the instrumentation blocks would be expected to lower the frequency. This led to speculation that perhaps Mode 3 (observed as pure torsion) was the manifestation of either Mode 4 or 5, lowered in frequency (due to added instrumentation mass), and this mode itself had a torsional component not observed in the axial/radial data. Based on these results, it was determined that the roving hammer testing, as conducted, was not adequate to provide the necessary modal information for model updating.

9.4 3D LDV Testing

Based on the difficulties in fitting modal data and distinguishing the resulting shapes, it was decided that supplemental testing would be needed. Preferably, the new test set would provide all directional information (radial, axial and torsional) in

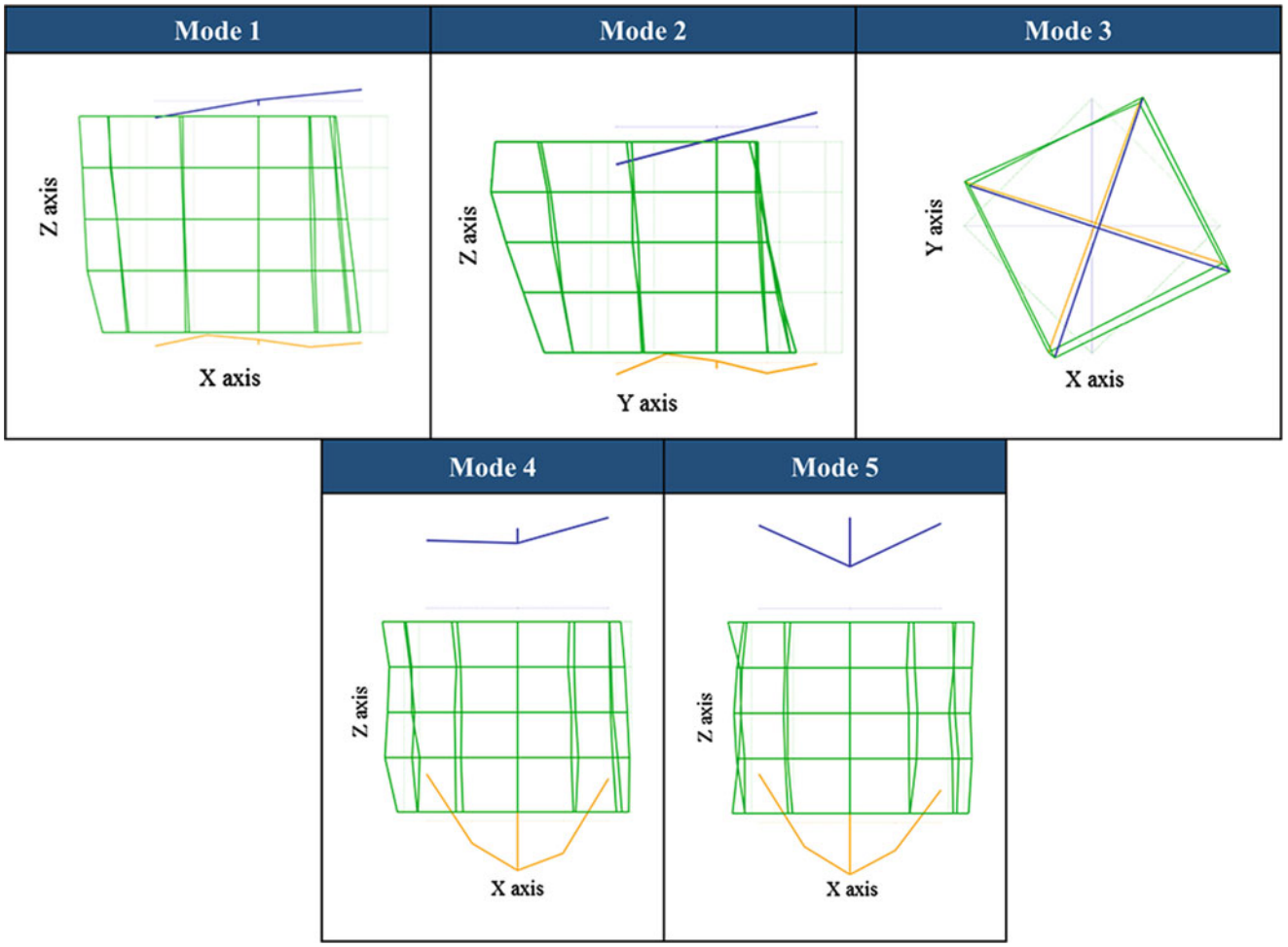

Fig. 9.5 Mode shapes from roving hammer test

a single test configuration, eliminating the addition of instrumentation blocks and their inherent changes to the test article's dynamic characteristics. These testing requirements led to the use of the 3D scanning LDV system, which is able to provide non-contact response measurements in all three translational DOF.

9.4.1 Test Setup

The test article was again tested under approximated free-free boundary conditions. As mentioned above, only one configuration of the test article was required since the 3D measurements at each node would allow visualization of radial, axial and torsional motions; additional instrumentation blocks were not needed. Although only one test article configuration was necessary, a total of five scan orientations were necessary to have line-of-sight visibility to all sides of the test article. For each scan orientation, the LDV heads were held in a fixed position using a custom stand constructed from 95 mm optical railing (see Fig. 9.7) and the test article was repositioned.

The same instrumented modal hammer used in the initial roving hammer testing was used to excite the test article for LDV testing. Rather than roving the hammer to each measurement point, the scanning LDV was used to sequentially measure responses at each node. Five nodes were selected as references where impacts were made. Measured response and impact reference locations are shown in Fig. 9.8. All five references were collected for each of the five scan orientations, resulting in a total of 25 scans performed. Node locations were similar to those of the initial roving hammer test, though all three translational DOF are measured at each node, resulting in a substantially greater number of measured DOF.

It was highly desirable to automate the hammer excitation for LDV testing due to the large number of impacts that were required, as well as to minimize inconsistencies in impact amplitudes, orientations and locations. A linear actuator attached to

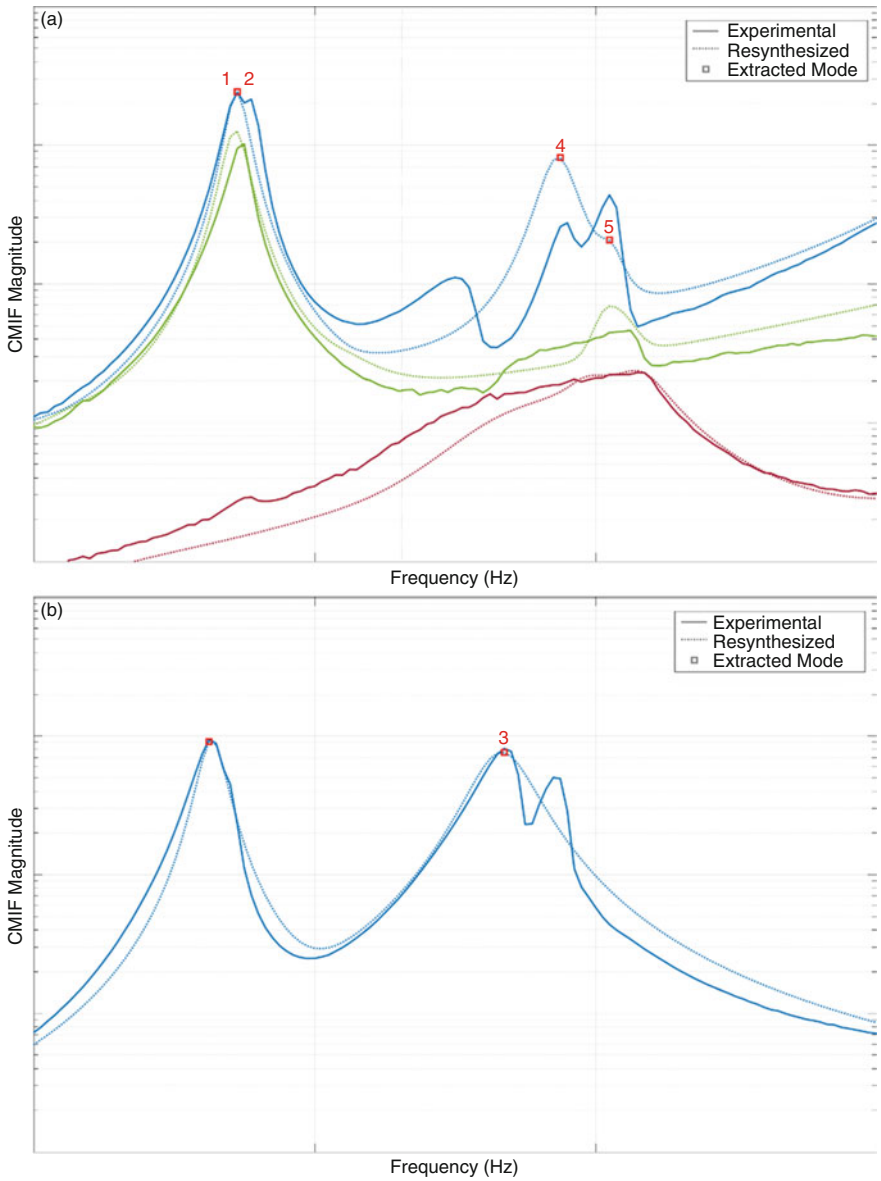

Fig. 9.6 CMIF for (**a**) axial/radial configuration (**b**) torsional configuration

a flexible positioning arm was used to "hold and swing" the modal hammer, which greatly sped up test time and repeatability. A signal generator was used to send a square wave function to the linear actuator controller. The control unit had an adjustable gain which allowed for changing the stroke of the actuator arm, and subsequently the impulse force amplitude imparted to the test article. The auto hammer was positioned to impact each of the five reference nodes individually, for each of the five scan orientations.

This test article exhibited highly nonlinear response characteristics, particularly in the frequency range including the axial and torsional modes. Even though the automated modal hammer was employed to help with the large number of impacts necessary for the hammer testing, its most useful contribution was in minimizing impact force variations and allowing consistent low-level excitation impulses. This effectively prevented the corresponding deviations in the measured FRF which accompany nonlinear systems subjected to varying excitation levels. In the roving hammer test method where the automated hammer was not used, it was difficult and time consuming to achieve a tight tolerance on impact amplitudes and angles. Some nonlinear behavior was likely induced causing difficulty in fitting the roving hammer data.

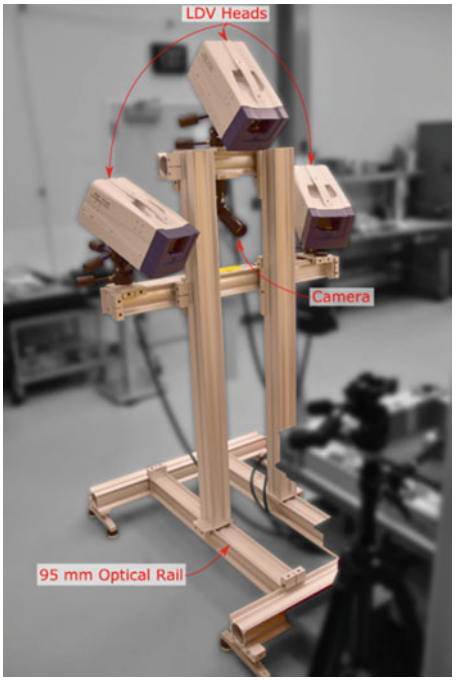

Fig. 9.7 3D LDV test stand

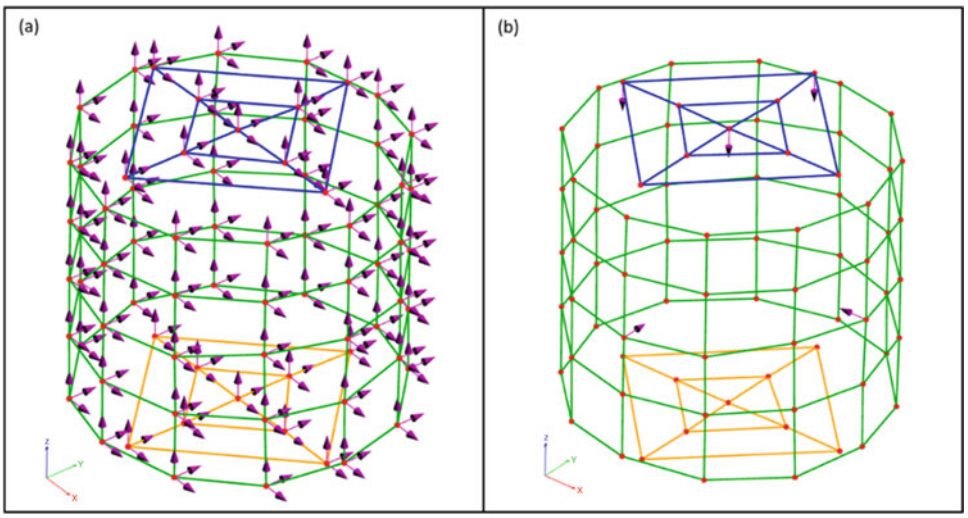

Fig. 9.8 3D LDV instrumentation (**a**) velocity measurement locations (**b**) impact reference locations

9.4.2 Results

Modal parameters were extracted using the SMAC algorithm [1] and are listed in Table 9.2. The corresponding mode shapes are provided in Fig. 9.9. Again, the modal parameters are based purely on external observations of the test article and internal cylinder motions must be inferred when possible.

Modal parameters were extracted from each of the five references separately (see Sect. 9.4.1), then combined and reduced to the final set of modes listed in Table 9.2. This final set of modes was used to resynthesize all FRF and CMIF, the latter of which is shown in Fig. 9.10. Overall, these plots indicated the extracted modal parameters adequately captured the test article dynamic characteristics.

Table 9.2 Modal parameters extracted from 3D LDV test

Mode #	Description
1	Internal cylinder shear in Y with rocking
2	Internal cylinder shear in X with rocking
3	Headers drumming opposite directions
4	Internal cylinder axial & torsion (clockwise)
5	Internal cylinder axial & torsion (counterclockwise)

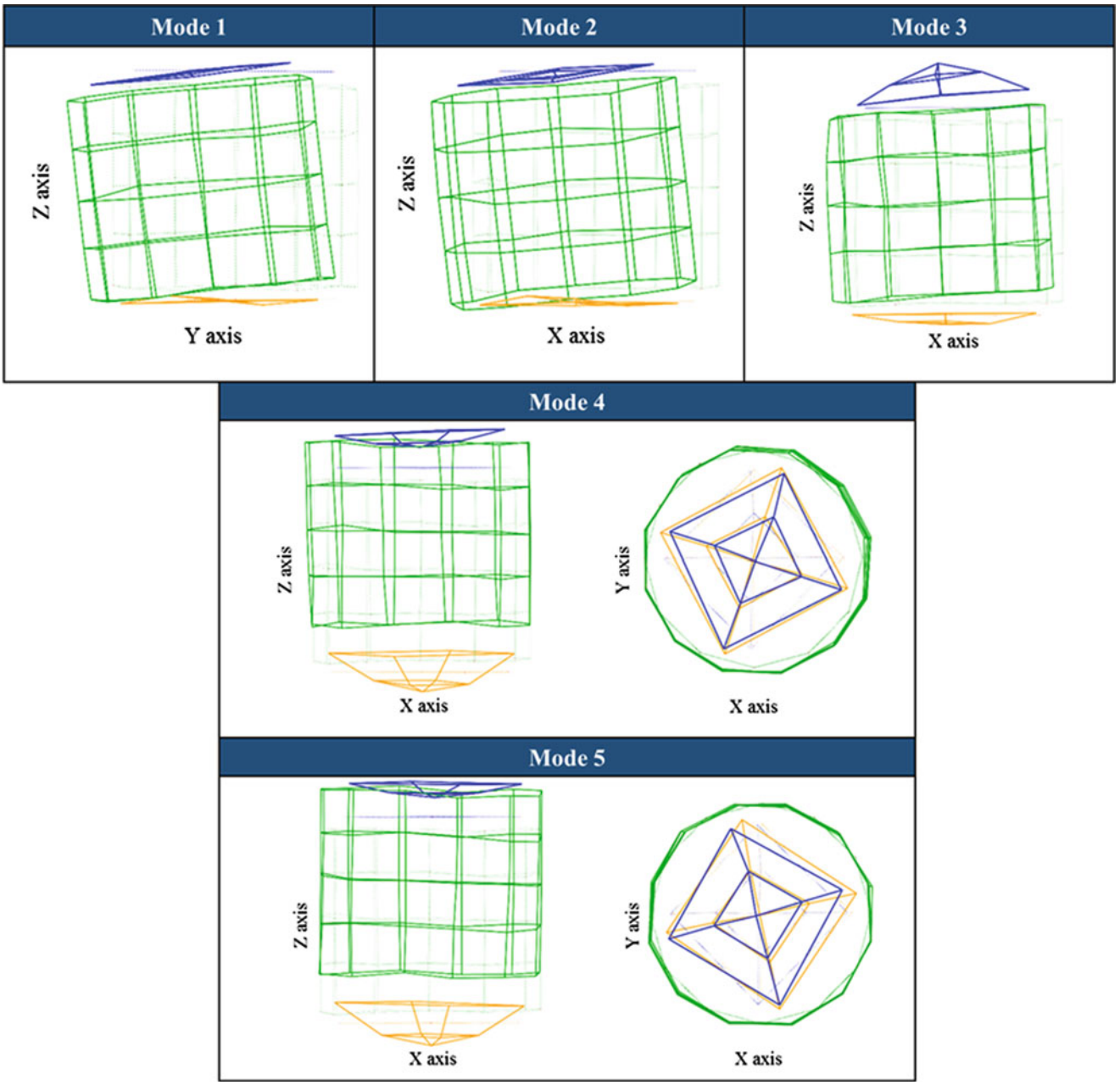

Fig. 9.9 Mode shapes from 3D LDV test

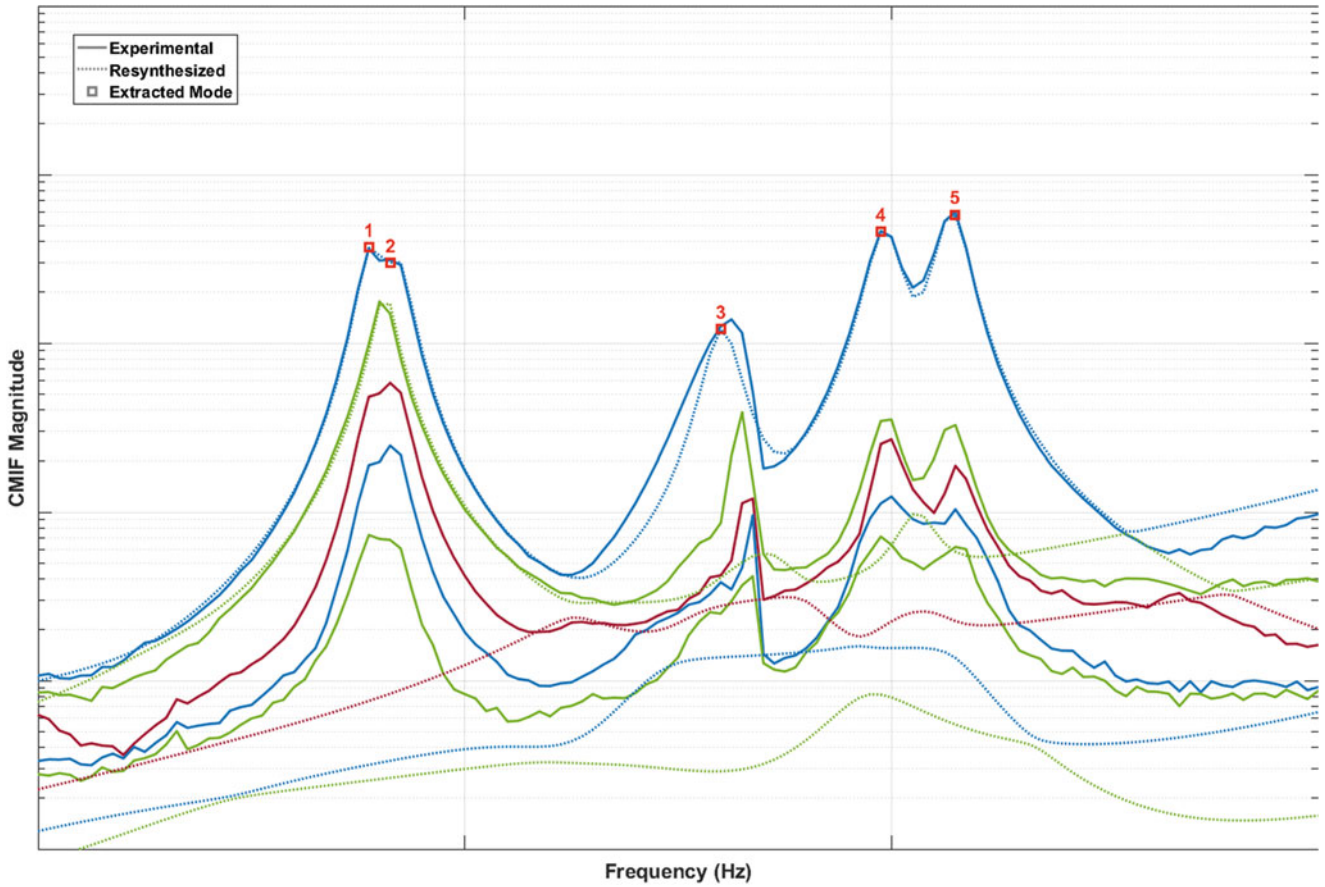

Fig. 9.10 CMIF for 3D LDV test

Table 9.3 Modal parameters comparisons for roving hammer and 3D LDV tests

Roving hammer		LDV		Natural frequency difference (%)
Mode #	Description	Mode #	Description	
1	Internal cylinder shear in X	2	Internal cylinder shear in X with rocking	−0.84
2	Internal cylinder shear in Y	1	Internal cylinder shear in Y with rocking	−0.96
3	Internal cylinder torsion	3	Headers drumming opposite directions	–
4	Top & bottom plate drumming 1	4	Internal cylinder axial & torsion (clockwise)	−2.48
5	Top & bottom plate drumming 2	5	Internal cylinder axial & torsion (counterclockwise)	−4.26

9.5 Comparison of Roving Hammer and LDV Results

The 3D scanning LDV results immediately shed light on issues encountered during roving hammer testing. Table 9.3 demonstrates a direct comparison, where possible, of the extracted modal parameters for both test methods.

The closely spaced internal cylinder shear modes were extracted in different orders between the two methods, most likely due to the differences in excitation locations, although both were within one percent difference in natural frequency. A comparison of the shear mode shapes from either test method are shown in Fig. 9.11. Again, the higher frequency "rigid body" type motion exhibited by the external features are inferred as the internal features moving in the opposite direction. Due to the presence of the additional DOFs on the outer casing, the LDV test shapes more clearly illustrate that the internal cylinder exhibits a high degree of rocking coupled with the shear translational motion. Although the rocking motion may have been inferred in the roving hammer data from the top and bottom plates, the lack of axial DOF on the casing would have made this judgement call more difficult in the model updating process. The FEM results also exhibited some rocking characteristics in the shear modes as seen in Fig. 9.2.

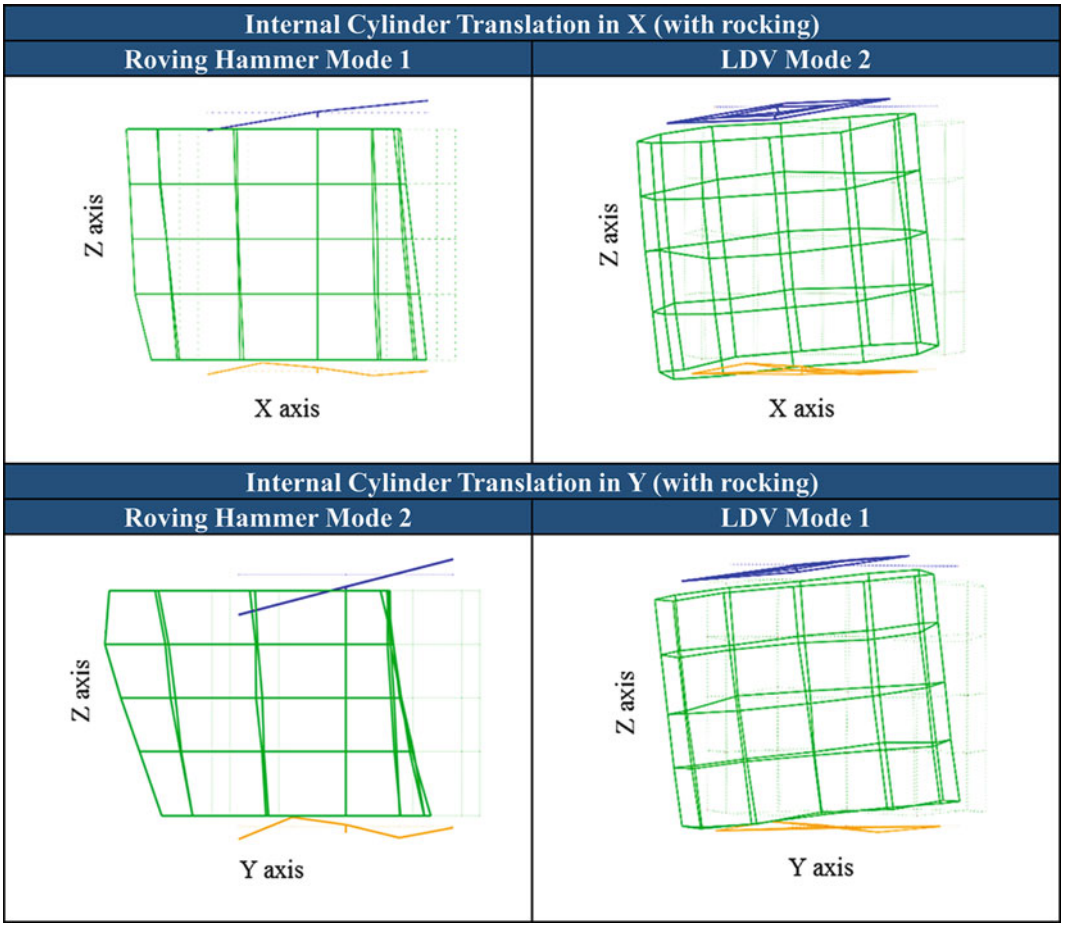

Fig. 9.11 Internal cylinder shear mode shape comparisons from Roving Hammer and 3D LDV tests

The torsion and axial modes of vibration appeared to manifest themselves differently when comparing the roving hammer and LDV data. Initially, roving hammer Modes 3, 4 and 5 were extracted and thought to be unique. However, in light of the LDV results, it is believed that roving hammer Modes 3 (torsion) and 4 (axial drumming) are actually the same mode. The measured difference in frequency is thought to have been induced by the added mass of the instrumentation blocks added in the torsional configuration. Further, the axial motion of the test article was not captured in the torsional configuration test, explaining why Mode 3 was observed as pure torsion. The reverse is true as well, explaining the lack of torsional motion in roving hammer Modes 4 and 5. A comparison of the modes from both the test methods is shown in Fig. 9.12. Without the additional DOF gained in the 3D LDV testing, determining that the internal cylinder's axial and torsional motions are highly coupled for these two distinct modes would have been difficult.

The LDV testing also resulted in the extraction of an additional mode of vibration, Mode 3 (plates drumming opposite), that was not extracted in the roving hammer data. In retrospect, this is thought to be the mode observed in Fig. 9.6a between Modes 2 and 4 which could not be extracted from the roving hammer data.

9.6 Model Updating and Correlation

Once the experimental mode shapes and frequencies were identified, it was a very straight forward process to update the FEM to agree with the modal test results. The error between the predicted and the measured frequency for the shear mode was reduced from 6.4% to 0.2% and the error between the predicted and the measured frequency for the axial mode was reduced from 4.9% to 1.0%. The development of such a predictive FEM would not have been possible without the experimental modal data acquired with the LDV system. Further, the LDV data very clearly captured the coupled internal cylinder rotational and shear (translation) motion which also predicted by the FEM, giving more confidence in the accuracy of analytical predictions.

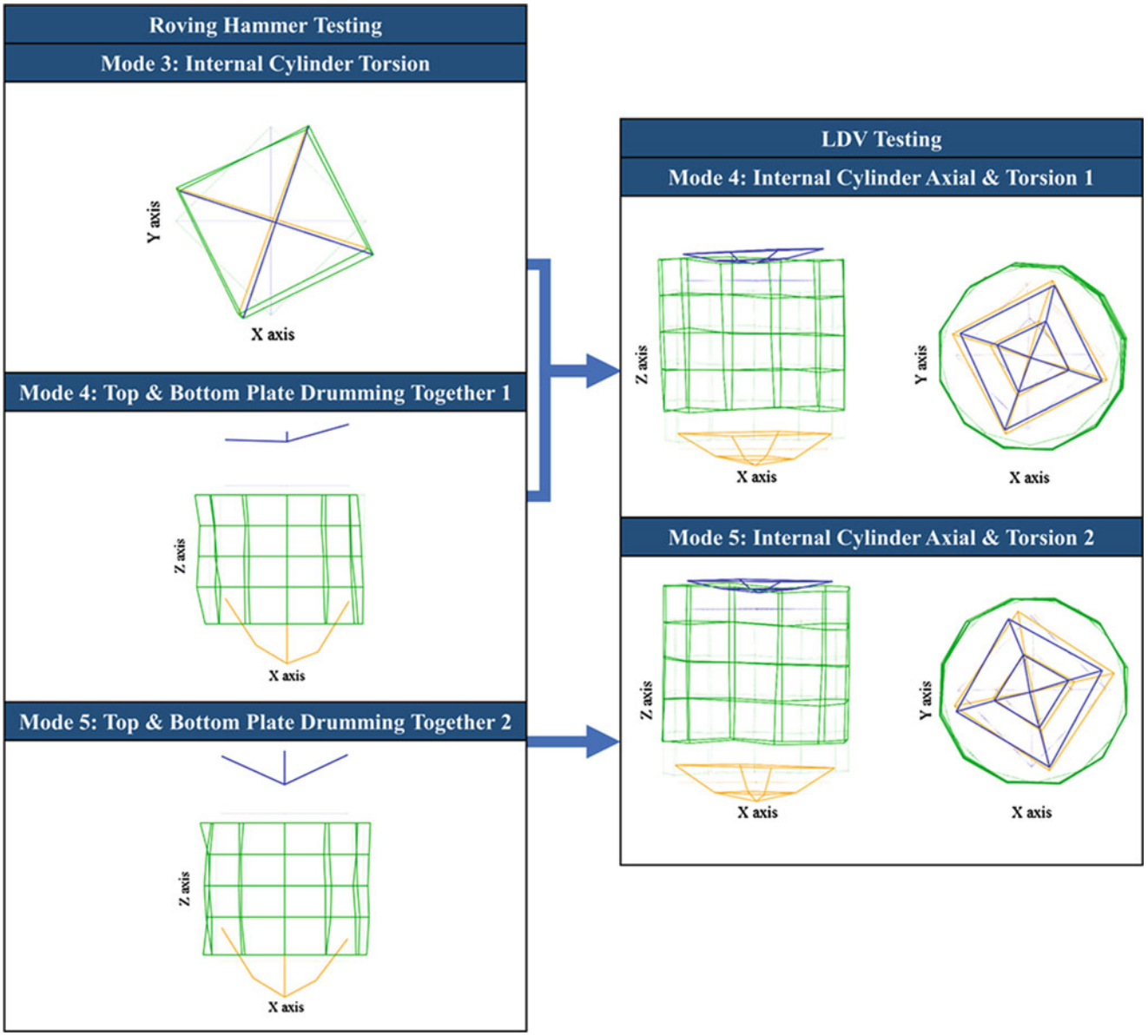

Fig. 9.12 Axial and torsion mode shape comparison from roving hammer and 3D LDV tests

9.7 Conclusions

Traditional roving hammer impact testing can be useful by minimizing mass loading of test articles when compared with the alternative of fully instrumenting a test article with accelerometers. However, it was found that a far better alternative for some applications is to utilize 3D scanning LDV measurements with impact excitation to practically eliminate mass loading all together. Addition of non-contact 3D measurements allowed for internal feature motion inferences, correct shape interpretations, and eliminated need for multiple test article configurations which, in this case, resulted in erroneous initial results.

Reference

1. Hensley, D.P., Mayes, R.L.: Extending SMAC to multiple references. In: Proceedings of the 24th International Modal Analysis Conference, pp. 220–230, February 2006

Chapter 10
The Measurement of a Nonlinear Resonant Decay Using Continuous-Scan Laser Doppler Vibrometry

David A. Ehrhardt, Matthew S. Allen, and Timothy J. Beberniss

Abstract The nonlinear resonant decay of a structure offers much insight into the frequency-amplitude behavior of a structure's dynamic response. The spatial deformation during this decay is especially important since nonlinear responses can cause unexpected stress concentrations necessitating full-field measurements for comparison with a model. In this context, full-field measurement techniques, such as continuous scan laser Doppler vibrometry (CSLDV) and high speed three dimensional digital image correlation (3D-DIC) provide tools to obtain the full-field dynamic response experimentally. While CSLDV has been used to measure the steady state response of linear and nonlinear structures as well as transient responses of linear structures, it is unclear whether the approach can be successful for transient nonlinear measurements where the frequency of the dynamic response is amplitude dependent. In this investigation, the capabilities of CSLDV will be utilized to measure the nonlinear resonant decay of a clamped-clamped flat beam. The response measured using CSLDV will then be compared with the decay response measured with 3D-DIC to validate the CSLDV method and to understand the advantages and disadvantages of each.

Keywords Continuous-scan laser Doppler vibrometry • 3D digital image correlation • Resonant decay

10.1 Introduction

The measurement of a structure operating in a dynamic environment requires special considerations, especially when the structure of interest is lightweight. In this context, noncontact sensors are needed so the dynamic measurements are not corrupted by mass loading. Since light weight structures can also be prone to nonlinear behavior, the concept of a roving sensor and averaging cannot be directly applied to a point-by-point measurement of the structure. Therefore, non-contact, full-field measurement techniques are ideal when measuring light-weight structures prone to nonlinear behavior in dynamic environments. In this work Continuous-Scan Laser Doppler Vibrometry (CSLDV) and high-speed Three Dimensional Digital Image Correlation (high-speed 3D-DIC) have been employed to measure the full-field dynamic response of a clamped-clamped flat beam.

Previous works have shown the capability of CSLDV to measure full-field deformations of a structure oscillating in linear response regimes when subjected to sinusoidal [1], random [2, 3], and impulse excitation [4, 5]. The work by Yang et al. [6] which used the demodulation of the CSLDV signal coupled with linear time periodic system identification was extended to examine the dynamic response of a structure oscillating in nonlinear response regimes, but was limited to purely sinusoidal excitation [7]. On the other hand, the capability of high-speed 3D-DIC has been explored on structures operating in linear and nonlinear environments when subjected to sinusoidal [7], random [8, 9], and impulse excitation [10, 11], with no major difference in the application of the method.

In this investigation, CSLDV and high-speed 3D-DIC are used to measure the nonlinear resonant decay of a 228.6 mm steel clamped-camped beam. At large amplitudes of vibration, the fundamental frequency of vibration for this setup increases due to the geometric nonlinear stiffness. In this work, the fundamental frequency of vibration is 176% higher than the linear

D.A. Ehrhardt (✉)
UES/Air Force Research Laboratory, Wright-Patterson AFB, OH, 45433, USA
e-mail: david.ehrhardt@bristol.ac.uk

M.S. Allen
Department of Engineering Physics, University of Wisconsin-Madison, 1500 Engineering Drive, Madison, WI 53706, USA

T.J. Beberniss
Structural Sciences Centers, Aerospace Systems Directorate, Air Force Research Laboratory, Wright-Patterson AFB, OH 45433, USA

D. Di Maio, P. Castellini (eds.), *Rotating Machinery, Hybrid Test Methods, Vibro-Acoustics & Laser Vibrometry, Volume 8*,
Conference Proceedings of the Society for Experimental Mechanics Series, DOI 10.1007/978-3-319-54648-3_10

natural frequency of the first bending mode at the start of the decay. Displacements measured using the high-speed 3D-DIC setup are post-processed using a commercial software Aramis [12] and its Real Time Sensor program [13], and velocities measured with CSLDV are post-processed using linear-time periodic algorithms developed in [4].

10.2 Background

10.2.1 High-Speed 3D-DIC Processing

Accurate 3D displacements can be obtained with digital image correlation using two cameras in a stereo configuration as described in [14]. As shown in Fig. 10.1, the two cameras (Photron SAZ's) are placed at a specific distance from the test article to allow the surface to be captured simultaneously and an LED panel light is used to illuminate the surface. A frame rate of 7000 Hz is used to image the structure over 15 s resulting in 105,000 images requiring 15.2 GB of memory.

Once the stereo camera setup is assembled and fixed, principles of triangulation are used to establish each camera's position in reference to the global experimental coordinate system. Additionally, lens distortion and variations between the sensor of the camera and the final images can be corrected through a bundle adjustment [14]. The coordinate system transformation matrix is established through the use of images of a known pattern or calibration panel. With this calibration, the accuracy of the coordinate transformation matrix is not limited to the pixel size of the imaged surface of the test specimen, but instead can be interpolated on the sub pixel level (i.e. calibration deviation for this setup is 0.018 pixels). Once the calibration of the 3D-DIC system is established, images of the fully deformable structure can be analyzed to obtain displacements. Prior to testing, a high-contrast random pattern is applied to the measurement surface so the defined subsets can be uniquely and accurately fit. Triangulation is used to determine the coordinate value of each subset using the Real Time Sensor mode in IVIEW [12]. In this work, the subset size is 15 pixels × 15 pixels laid out manually as shown in Sect. 10.2.3. The final displacements are processed with the Hilbert Transform so the instantaneous frequency and amplitude is determined.

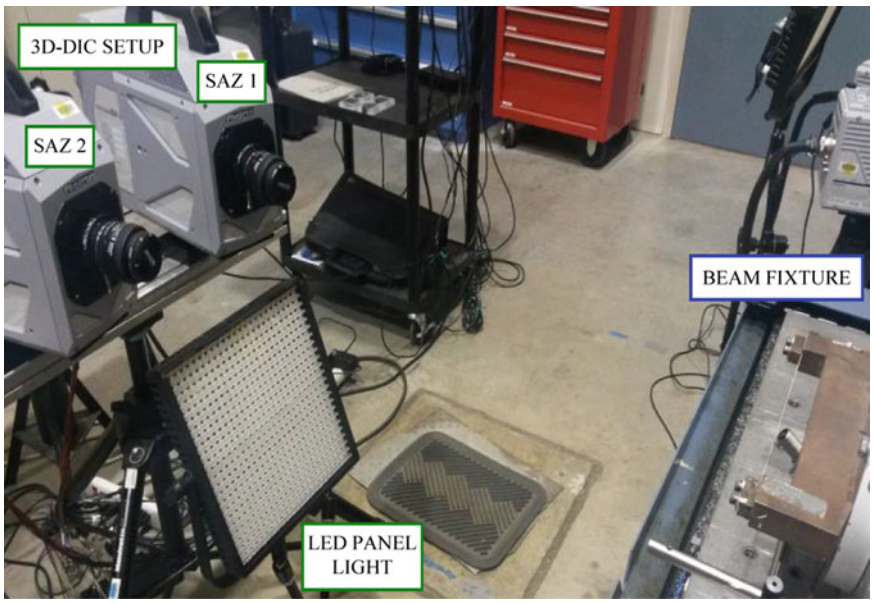

Fig. 10.1 3D-DIC system

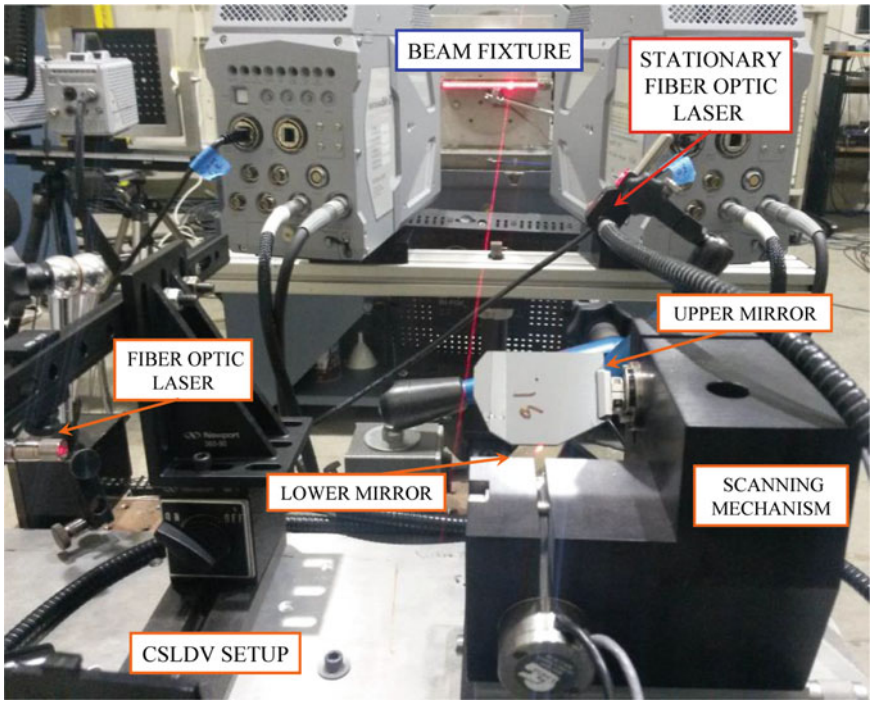

Fig. 10.2 CSLDV System Diagram. The laser beam was redirect by a pair of rotating mirrors

10.2.2 CSLDV Processing

A laser Doppler vibrometer (LDV) is a non-contact measurement technique that detects the Doppler frequency shift in a beam of laser light and converts it to the velocity component of the measurement point along the direction of the incident laser [15]. Continuous-scan laser Doppler vibrometry (CSLDV) extends the LDV measurement by moving the laser beam across the surface of a structure with a pre-defined pattern [16, 17]. In this work, a periodic line pattern is used so that the observed deformation becomes a periodic function of time [2, 18] and hence the deformation shape doesn't need to be approximated with a polynomial in the spatial coordinates as done in [16, 17, 19–21].

The laser beam of a fiber optic LDV is scanned across the beam's surface in a periodic line pattern at 145 Hz using external mirrors, as seen in Fig. 10.2. The laser beam of a second fiber optic LDV is also set on the beam's surface for comparison to CSLDV measurements. Both lasers are sampled at 20 kHz.

The implementation of a time-periodic CSLDV scan pattern couples the motion of the measurement point with the deformation of the structure, so the measured velocity appears as an amplitude modulated signal. Therefore, post-processing is required to separate the laser motion from the structural deformation as previously discussed in [22]. In this work, the free decay measured with CSLDV is divided into blocks of 8000 samples so the average frequency and deformation is examined instead of the instantaneous decay. However, results show a favorable comparison.

10.2.3 Structure of Interest

The structure for this investigation is a precision-machined feeler gauge made from high-carbon, spring-steel with clamped boundary conditions. The final clamped-clamped beam configuration has an effective length of 228.6 mm, a nominal width of 12.7 mm, and a thickness of 0.76 mm. Prior to clamping, the beam was painted with a white basecoat and a speckle

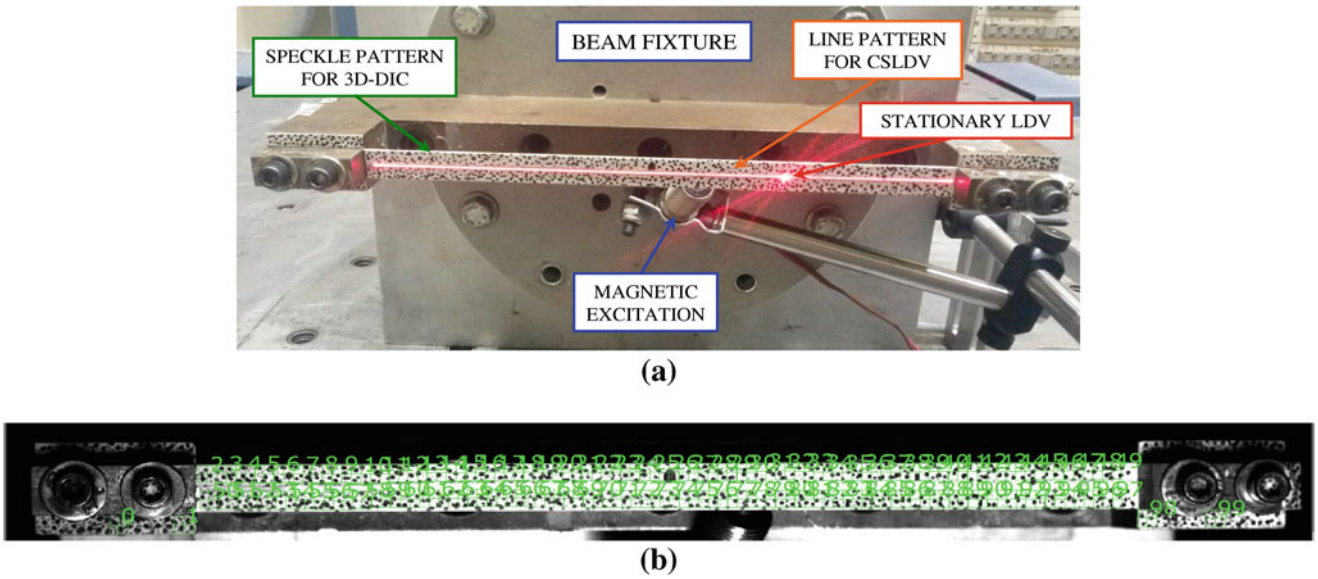

Fig. 10.3 Clamped-clamped beam configuration. (**a**) Physical setup, (**b**) 3D-DIC measurement points

pattern was applied using a marker to allow for tracking positions with the 3D-DIC system. Once the beam had dried, a strip of retro-reflective tape was added to increase feedback for the CSLDV. The final prepared beam is shown in the clamping fixture in Fig. 10.3.

10.3 Results

The structure of interest is subjected to a nonlinear resonant decay of the first mode using nonlinear force appropriation as described in [23]. The initial excitation is supplied using a magnetic field generated by a fluctuating voltage through an inductance coil. This method of excitation is beneficial in the measurement of a free decay since the magnetic field can be cut off abruptly and has no lasting effect on the structure.

The magnetic forcing induces an asymmetry in the deformation of the beam, which can be seen in Fig. 10.4 The asymmetry is most notable in the displacement measurements (Fig. 10.4a, b), but is also visible in the harmonic distortion observed in the LDV shown in Fig. 10.4d. Figure 10.4d also displays the amplitude modulation of the scanning LDV when compared with the stationary LDV. Since the structure is lightly damped, when the force is removed the structure will decay near the fundamental nonlinear normal mode [24]. For this structure, the observable decay occurs in approximately 10 s.

A fast-Fourier Transform (FFT) of the measured time domain signals presented in Fig. 10.4 provides insight to the frequency content of each signal. The FFT of the displacement measurements (Fig. 10.5a) shows the fundamental frequency of vibration of the decay starts near 139.7 Hz and ends near 79.3 Hz. Although higher frequencies appear in the response, the focus of this work is on the fundamental frequency. Due to this large shift in the fundamental frequency of vibration, care must be taken in the selection of the scanning frequency used in CSLDV so no overlap of the sideband harmonics of interest occurs. In this investigation 145 Hz is used so the 0th, $\pm$2nd, and $\pm$4th sideband are visible. All odd and higher sideband harmonics are below the noise floor for this setup. Figure 10.5b shows the FFT of the LDV signals where the 0th and $\pm$2nd sideband harmonics are visible.

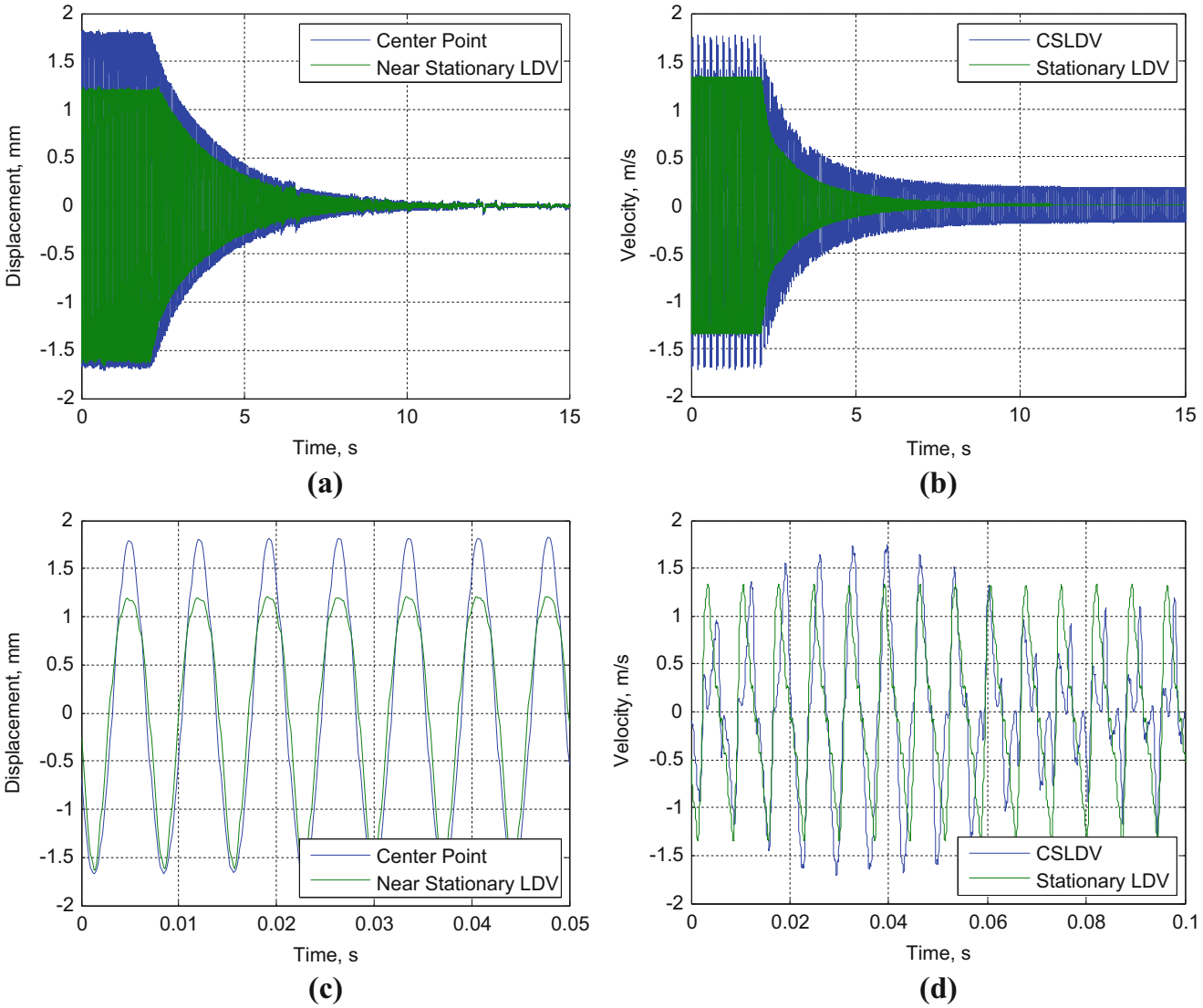

Fig. 10.4 Measured data. (**a**) Displacement measured with 3D-DIC, (**b**) Velocity measured with CSLDV. The first 0.05 s of the 3D-DIC (**c**) and 0.1 s of the CSLDV signal (**d**)

The instantaneous frequency can be approximated for both 3D-DIC and CSLDV measurements using several methods. The displacements measured with 3D-DIC are first filtered around the fundamental frequency of vibration and the Hilbert transform applied to calculate complex amplitude of the signal and approximate the instantaneous frequency. The resulting time vs. frequency plot for 3D-DIC is shown in Fig. 10.6a. The LDV measurements are split into 8000 sample blocks with 50% overlap and a least-squares sinusoid fit applied to each block. The resulting time vs. frequency plot for CSLDV is shown in Fig. 10.6b. The stationary LDV point follows the instantaneous frequency with similar accuracy to the 3D-DIC measurements; however, the estimated instantaneous frequency from the CSLDV measurement is corrupted by the noise from scanning the laser.

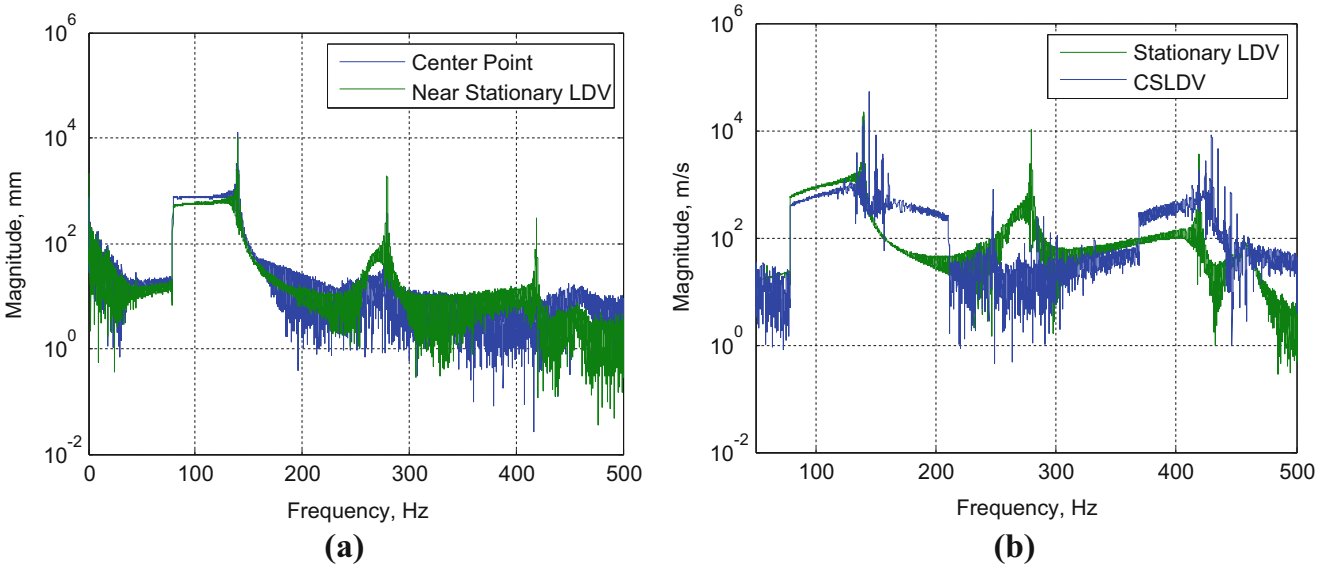

Fig. 10.5 Fourier transform of the (**a**) 3D-DIC and (**b**) CSLDV measurements

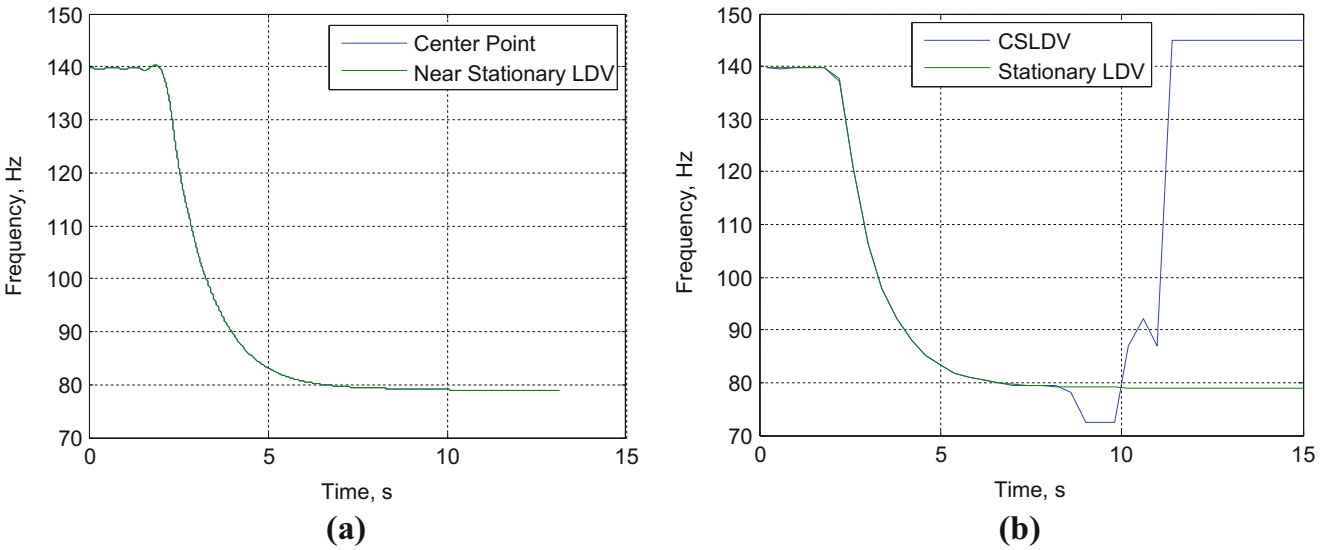

Fig. 10.6 Instantaneous frequency estimated from: (**a**) 3D-DIC and (**b**) CSLDV measurements

Although the instantaneous frequency predicted with CSLDV is corrupted by noise the full-field displacements from each measurement technique agree well as shown in Fig. 10.7. At the initial decay, the CSLDV is shown to slightly under predict the displacement experienced by the beam when compared with 3D-DIC. This is difference is likely from the 'averaged' displacement measurement taken in the blocked CSLDV data as opposed to the predicted instantaneous deformation calculated with the Hilbert transform of the 3D-DIC displacements.

10.4 Conclusions

In this investigation, a nonlinear resonant decay is measured with 3D-DIC and CSLDV. It is shown that the 3D-DIC can capture the frequency and amplitude of the decay as the structure's response decays into the linear realm; however, 3D-DIC will be subject to more noise at lower response amplitudes. It is discussed that care must be taken when selecting the scanning frequency of the CSLDV so there is no overlap in the desired signal and the sidebands of the response.This

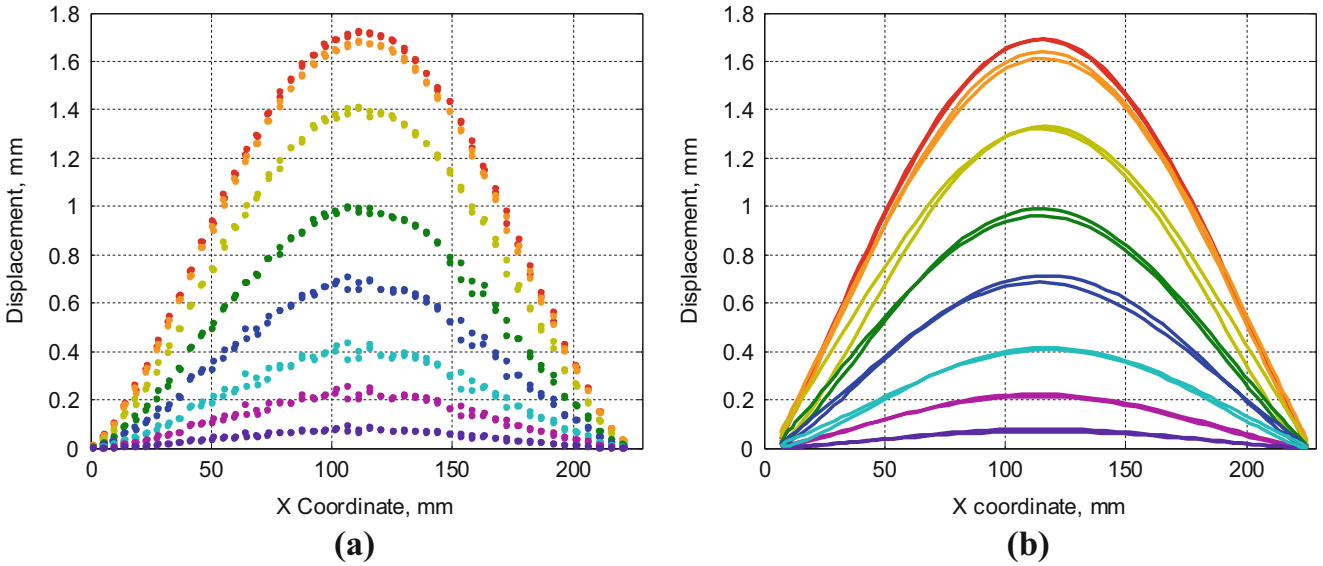

Fig. 10.7 Full-field deformation using (**a**) 3D-DIC and (**b**) CSLDV near 139.7 Hz (*red*), 136.8 Hz (*orange*), 121.0 Hz (*light green*), 102.6 Hz (*dark green*), 91.2 Hz (*dark blue*), 83.6 Hz (*light blue*), 80.6 Hz (*pink*), and 79.34 Hz (*violet*)

work focused on the fundamental frequency of vibration since higher frequencies observed in the response of the beam overlapped the sidebands due to the scanning laser in the CSLDV measurement corrupting the velocity signal. It was shown that CSLDV was able to provide similar amplitude measurements for the range shown; however, the predicted frequency became corrupted by the noise from scanning the laser at lower amplitudes.

References

1. Di Maio, D., Ewins, D.J.: Continuous scan, a method for performing modal testing using meaningful measurement parameters Part I. Mech. Syst. Signal Process. **25**, 3024–3042 (2011)
2. Yang, S., Allen, M.S.: Output-only modal analysis using continuous-scan laser doppler vibrometry and application to a 20 kW wind turbine. Mech. Syst. Signal Process. **31** (2011)
3. Maio, D.D., Carloni, G., Ewins, D.J.: Simulation and validation of ODS measurements made using continuous SLDV method on a beam excited by a pseudo random signal. In: XVIII International Modal Analysis Conference, Jacksonville, FL, 2010
4. Yang, S., Sracic, M.W., Allen, M.S.: Two algorithms for mass normalizing mode shapes from impact excited continuous-scan laser Doppler vibrometry. J. Vib. Acoust. **134**(2), 021004 (2012)
5. Stanbridge, A.B., Ewins, D.J., Khan, A.Z.: Modal testing using impact excitation and a scanning LDV. Shock Vib. **7**(2), 91 (2000)
6. Yang, S.: Modal identification of linear time periodic systems with applications to continuous-scan laser doppler vibrometry. In: Engineering Physics, University of Wisconsin-Madison, 2013
7. Ehrhardt, D.A., Allen, M.S., Yang. S., Beberniss, T.J.: Full-field linear and nonlinear measurements using continuous-scan laser Doppler vibrometry and high speed three-dimensional digital image correlation. Mech. Syst. Signal. Process. **86**, 82–97 (2017)
8. Beberniss, T.J., Spottswood, S.M., Eason, T.: High-speed 3D digital image correlation measurement of long duration random vibration: recent advancements and noted limitations. In: ISMA Biennial Conference, Lueven, Belgium, 2012
9. Niezrecki, C., et al.: A review of digital image correlation applied to structural dynamics. AIP Conf. Proc. **1253**(1), 219–232 (2010)
10. Schmidt, T.E., et al.: Full-field dynamic deformation and strain measurements using high-speed digital cameras. In: 26th International Congress on High-Speed Photography and Photonics, Bellingham, WA, 2005
11. Tiwari, V., Sutton, M.A., Shultis, G., McNeill, S.R., Xu, S., Deng, X., Fourney, W.L., Bretall, D.: Measuring full-field transient plate deformation using high speed imaging systems and 3D-DIC. In: Proceedings of the Society for Experimental Mechanics Annual Conference, Albuquerque, 2009
12. mbH, G.: Aramis, Braunschweig, Germany, 2011
13. mbH, G.: IVIEW Real Time Sensor, Braunschweig, Germany, 2011
14. Sutton, M.A., Orteu, J.J., Schreier, H.: Image Correlation for Shape, Motion, and Deformation Measurements: Basic Concepts, Theory, and Applications. Springer, New York (2009)
15. Bell, J.R., Rothberg, S.J.: Laser vibrometers and contacting transducers. Target rotation and six degree-of-freedom vibration: what do we really measure? J. Sound Vib. **237**, 245–261 (2000)
16. Stanbridge, A.B., Ewins, D.J.: Modal testing using a scanning laser Doppler vibrometer. Mech. Syst. Signal Process. **13**(2), 255–270 (1999)
17. Stanbridge, A.B., Khan, A.Z., Ewins, D.J.: Modal testing using impact excitation and a scanning LDV. Shock Vib. **7**(2), 91–100 (2000)

18. Allen, M.S.: Frequency-domain identification of linear time-periodic systems using LTI techniques. J. Comput. Nonlinear Dyn. **4**(4), 041004 (2009)
19. Martarelli, M.: Exploiting the laser scanning facility for vibration measurements. In: Technology & Medicine. Imperial College, London (2001)
20. Stanbridge, A.B., Martarelli, M., Ewins, D.J.: Measuring area vibration mode shapes with a continuous-scan LDV. Measurement. **35**(2), 181–189 (2004)
21. Schwingshackl, C.W., et al.: Full-field vibration measurement of cylindrical structures using a continuous scanning LDV technique. In: 25th International Modal Analysis Confernce (IMAC XXV), Orlando, Florida, 2007
22. Ehrhardt, D.A., Allen, M.S., Yang, S., Beberniss, T.J.: Full-field linear and nonlinear measurements using continuous-scan laser Doppler vibrometry and high speed three-dimensional digital image correlation. Mech. Syst. Signal Process. (2016), in press
23. Ehrhardt, D.A., Allen, M.S.: Measurement of nonlinear normal modes using multi-harmonic stepped force appropriation and free decay. Mech. Syst. Signal Process. **76–77**, 612–633 (2016)
24. Peeters, M., Kerschen, G., Golinval, J.C.: Modal testing of nonlinear vibrating structures based on nonlinear normal modes: experimental demonstration. Mech. Syst. Signal Process. **25**(4), 1227–1247 (2011)

Chapter 11
Vibro-Acoustic Modulation of a Spinning Apparatus for Nondestructive Evaluation

Martin J. Ward, Wesley E. Scott, Nicholas M. Diskerud, Alessandro Cattaneo, John D. Heit, and John D. Bernardin

Abstract As the cost and complexity of equipment used in fields such as aerospace and defense has increased, so has the value of methods known as nondestructive evaluation (NDE), which can detect faults without damaging or disassembling the equipment. Air bearing spin-down testing is a form of NDE that detects minute amounts of damage by rotating the entire assembly and measuring energy dissipation as it decelerates. While this method is highly sensitive to determining the existence of damage, it cannot determine the location or type of the damage. The proposed method merges spin-down testing with vibro-acoustic modulation (VAM) to locate simulated damage in a test piece mounted on a test bed featuring conventional rolling bearings and an electric motor to control the spin-down rate. VAM utilizes a high-frequency probing signal modulated by a low-frequency pumping signal to excite non-linearities caused by damage. In this case, the pumping signal is provided by the rotation of the sample and the resulting gravitational and inertial forces. A piezoelectric actuator provides the probing signal and an acoustic emission sensor detects variations in the signal response. This work explores combining acoustic, angular velocity and position signal analysis to locate the source of the damage.

Keywords Nondestructive evaluation • Ultrasonics • Vibro-acoustic modulation • Spin-down testing • Damage detection

11.1 Introduction

For some systems or components, it is undesirable to damage or disassemble the test article due to the associated cost of funds and time. This problem of assessing damage in an article with complex geometry or inaccessible components has been simplified through nondestructive evaluation (NDE) techniques, which perform examinations without degrading the test subject. A wide variety of NDE techniques and structural health monitoring (SHM) approaches exist [1–3], and the choice of method depends largely on the type of damage and region of the test article that are of interest.

In this study, an additional NDE method is researched and used in tandem with a pre-existing form of NDE in order to augment its performance. This established method—namely conventional spin-down testing—uses the angular deceleration of the test article to assess its structural health [4]. A healthy specimen is spun to an angular velocity set by what interval will contain the angular velocity that excites the damage, and then is allowed to decelerate to rest. The test performed on the healthy specimen provides a benchmark to which future samples can be compared. If any subsequent sample decelerates at a higher rate than the healthy specimen, it is assumed that dissipation in angular momentum is due to some damage or structural defect. In order to achieve a system with minimal physical interference, the test article needs to be spun in a very low friction environment. A practical means to implement a low friction environment is, for instance, through the use of

M.J. Ward
Department of Mechanical Engineering, University of Texas, 204 E Dean Keeton St, Austin, TX 78712, USA

W.E. Scott
Department of Engineering Physics, University of Wisconsin – Madison, 324 Sommers Street, Stevens Point, WI 54481, USA

N.M. Diskerud
Department of Mechanical Engineering, Rose-Hulman Institute of Technology, 5500 Wabash Avenue, Terre Haute, IN 47803, USA

A. Cattaneo (✉) • J.D. Bernardin
Applied Engineering Technologies, Los Alamos National Laboratory, AET-1, MS J576, PO BOX 1663, Bikini Atoll Rd., Los Alamos, NM 87545, USA
e-mail: cattaneo@lanl.gov

J.D. Heit
Los Alamos National Laboratory, Q-15, PO BOX 1663, Bikini Atoll Rd., Los Alamos, NM 87545, USA

D. Di Maio, P. Castellini (eds.), *Rotating Machinery, Hybrid Test Methods, Vibro-Acoustics & Laser Vibrometry, Volume 8*,
Conference Proceedings of the Society for Experimental Mechanics Series, DOI 10.1007/978-3-319-54648-3_11

an air bearing. Air bearing spin-down testing provides very good resolution in determining whether or not damage exists, even in complex, multi-component systems. However, this method alone cannot locate or characterize the damage after it is identified.

In order to answer the question of where in the test object the damage is located, an additional method of NDE is necessary. It can be observed that two possible forms of NDE—either ultrasonic techniques, or the use of propagating waves—could serve as an investigative tool.

The first method uses the time delay of arrival of the signal caused by the damage to locate its position [5, 6]. This method, known as triangulation, is a previously established and well known tool for damage detection, but has a few limiting constraints. The accuracy of the triangulation methods depends on an intimate knowledge of the test article. Material properties as well as geometry must be known in order to determine how the waves will travel from the damage source to the sensor.

The second method involves utilizing the relationship between two different signals inputted into the test article. If the system is in an undamaged state, the frequency response of the system will show the two superimposed signals. These two signals consist of a lower frequency pumping signal, and a higher frequency probing signal. The pumping signal is traditionally chosen as the fundamental frequency of the test specimen. This is done to best excite the damage present in the system [7]. If damage exists in the system, the non-linearity caused by that damage will cause the pumping signal to modulate the probing signal, alerting the user to the damage. This method is known as vibro-acoustic modulation (VAM) [7, 8].

This paper focuses on the results obtained by applying VAM. In the case of this study, the pumping signal will be supplied by the rotation of the test article. At the Los Alamos National Laboratory, the rotation in conventional spin-down testing has been done on an air bearing in order to minimize friction and maximize output resolution. However, a major objective of this study is to determine if damage can be located by spinning the test article on a less ideal system, so an air bearing will not be used. The rotation will be monitored and used to find the instance in the angular direction when the damage becomes apparent, effectively providing the damage's angular position. To locate the damage in the radial direction, the balance of gravitational and inertial forces will be computed to find the specific radius at which the gravitational force overcomes inertial force and cause the source to be detectable. In the case of the current study, the simplest model relating gravitational body forces to angular forces will be assumed. In future reproductions of this work, a more complex damage model can be implemented.

The paper is organized as follows. Section 11.2 outlines the experimental procedures adopted in the current work. Section 11.3 describes the analysis methods used to process VAM data. Results and conclusions are respectively presented in Sects. 11.4 and 11.5.

11.2 Experimental Procedures

As aforementioned, the test article for this investigation was not spun on an air bearing, but rather turned using motor and conventional bearing, as will be explained below. This was done so that readers interested in incorporating what has been done here for their own purposes need not have overly expensive or sensitive equipment to get meaningful results.

The entire basis for the prediction of damage is a constitutive model of how the damage will behave in the spin-down process. Figure 11.1 provides a graphical representation of the constitutive model.

In this system, angular velocity which would excite the damage was found with the Eq. (11.1) [9]:

$$r\omega^2 = g \tag{11.1}$$

The data acquisition was done with a Physical Acoustic's Pocket Acoustic Emission system using acoustic emission sensors (see Fig. 11.2). The collected data were then analyzed with Physical Acoustic's AEwin Replay software before being transferred to MATLAB for further post processing.

11.2.1 Experimental Setup for Vibro-Acoustic Modulation

In order to properly test the feasibility of the chosen constitutive method, it was necessary to precisely control the angular velocity. This control accurately identified the velocity that resulted in an equilibrium between the gravitational and inertial forces. To ensure that mass could only move in the radial direction, it was securely fastened to the spinning test plate as shown in Fig. 11.3a, b.

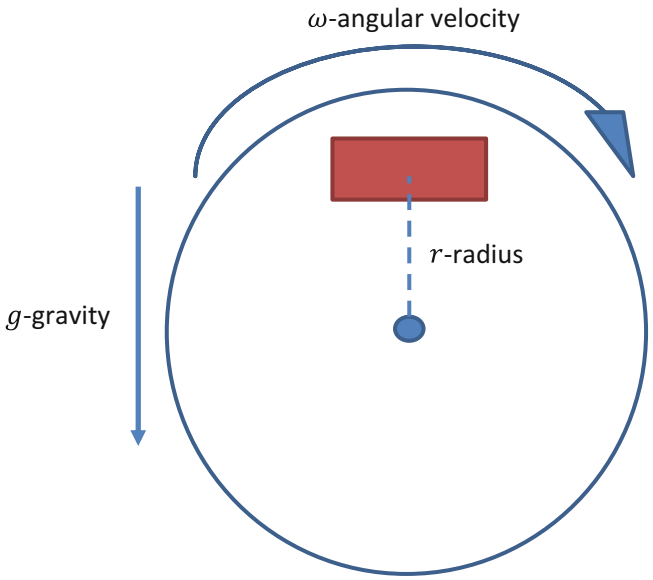

Fig. 11.1 Improvised damage model

Fig. 11.2 Pocket AE acquisition systems

Also shown in Fig. 11.3a are the acoustic sensor Physical Acoustic's PK15I and the PZT crystal that provide the sensing and probing signals for the vibro-acoustic modulation respectively. A slip ring manufactured by SparkFun Electronics (part number ROB-13063) was used to route the signal to the PZT crystal. The acoustic sensor was conditioned and sampled using the Physical Acoustic's Pocket Acoustic Emission system. Thanks to its small size and ability to be battery operated, the Physical Acoustic's Pocket Acoustic Emission system was attached to the spinning plate of the testing apparatus (see Fig. 11.3b). The acoustic sensor was sampled at a rate of 200 kHz. The sample rate was chosen because it was the lowest frequency above the Nyquist value for the PZT input frequency of 83 kHz, being this frequency the resonant frequency of the crystal. Maximizing the time resolution of each measurement meant to keep the upper bound of the frequency domain as small as possible. This PZT crystal was chosen for due to its low resonant frequency, which aided in that objective. Data acquisition was set to record 15,000 samples per event, the maximum allowed by the data acquisition unit being used. This resulted in 78 ms of data per event. It is worth noting that Pocket AE system is unable to continuously record waveform information, so all data was collected as discrete sample, with a test consisting of thousands of samples. This will affect the analysis methods of the data, which will be discussed in later section.

In order to ensure fine control of the rotation, a dual DC motor system was used to provide power to rotate the test fixture. These motors, shown in Fig. 11.4 were controlled with a speed control system, coordinated through an Arduino™ microcontroller. This system elements will also be expanded upon below.

The motors spun up the system to 1.6 Hz and then decelerated it to 1 Hz over the course of 5 min to simulate a test that the article would experience if an air bearing had been used. In order to measure the angular velocity, an angular encoder was mounted concentrically to the drive shaft at the rear of the test setup, as shown in Fig. 11.5.

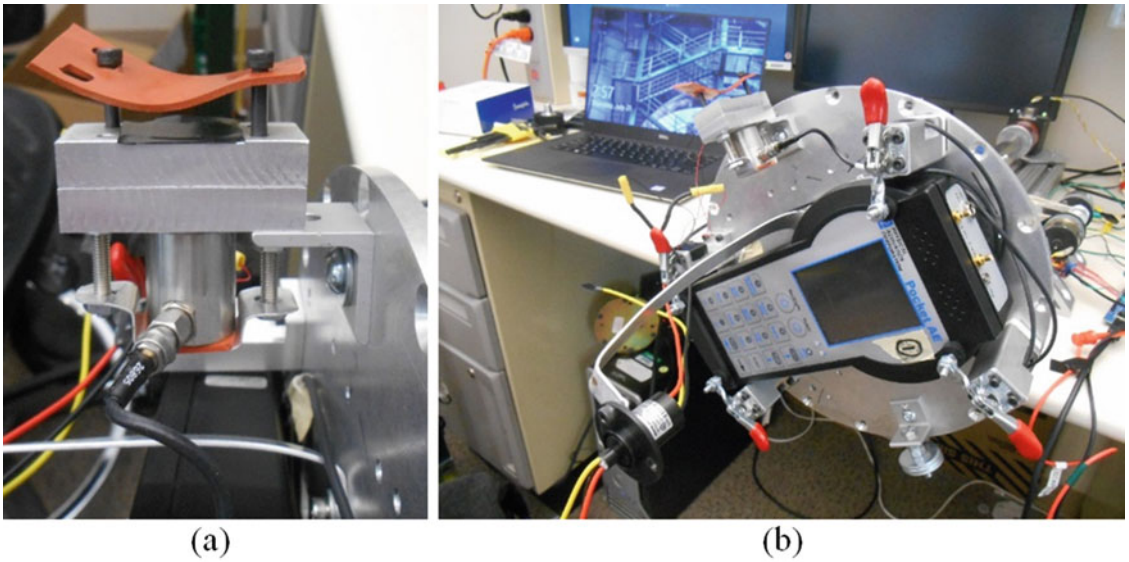

Fig. 11.3 Depiction of the improvised damage source (**a**) and the spinning plate with Pocket AE acquisition system (**b**)

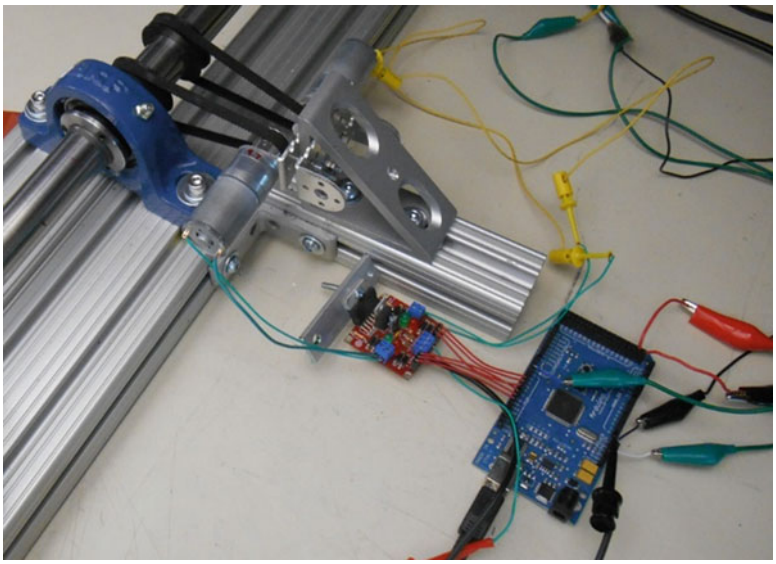

Fig. 11.4 Drive train system consisting of DC motors and Arduino™ speed controller

The angular encoder used had a capability of recording 1200 counts per revolution, which resulted in a 0.3° resolution. This information was fed into a computer running a proportional-integral-differential (PID) control algorithm to control the motor speed. In order to synchronize the collection of angular position and acoustic emission, the crystal was triggered in tandem with the reading received from the angular encoder. This was accomplished with having the Arduino™ trigger the bench-top power source for the PZT crystal in equivalent increments that corresponded to the collection rate of the angular encoder. After each test, the acoustic data was saved and the angular position information with respect to time was exported.

11.3 Analysis

This section outlines the analysis methods used to implement the VAM technique. The proposed analysis methods has enabled to successfully implement the VAM technique notwithstanding the limitations in the acquisition system. In this regard, it is worth noticing that the Pocket AE system (see Sect. 11.2.1) was unable to continuously record waveform information and the length of each recorded event was limited to 78 ms (corresponding to a frequency resolution of about 12.82 Hz).

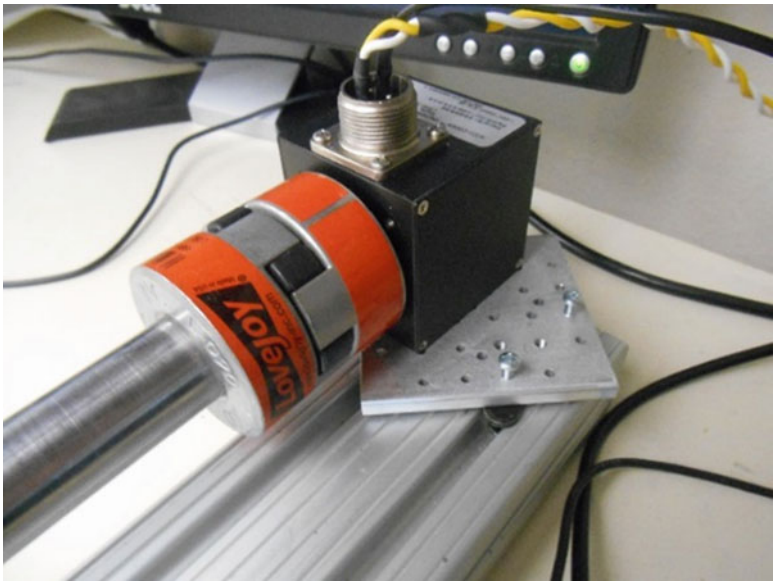

Fig. 11.5 Angular encoder mounting position on the drive shaft

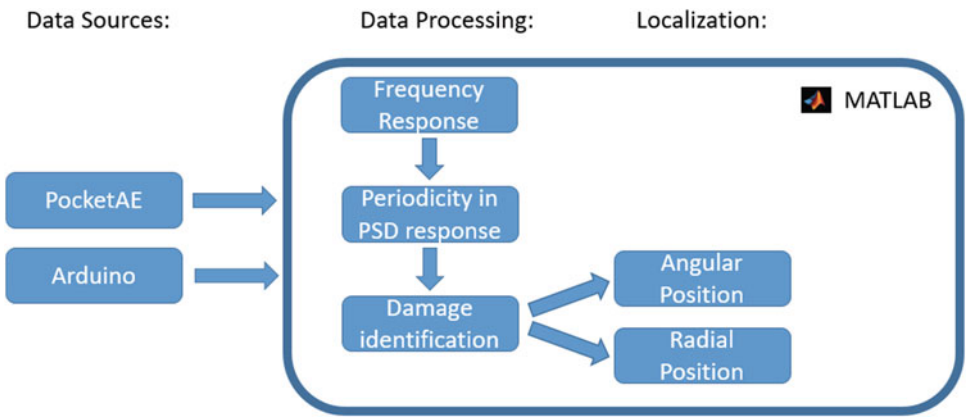

Fig. 11.6 Spin-down VAM post processing steps used in experiment

11.3.1 Analysis Methods for VAM

Waveform data from the AE sensors was transformed to the frequency domain and the periodicity of the power spectral density (PSD) response was analyzed, at the frequency of the probing signal, for the onset of damage in the experiment. Then, coupling with data from the Arduino system, statistical techniques were utilized to locate the source of damage in the experiment. This process can be seen graphically in Fig. 11.6 and will be discussed in depth in this section.

As previously described, data came from the experimental setup in two primary formats: Arduino output to serial port, and AE waveform data recorded at discrete points throughout the experiment. The primary purpose of the waveform data was to record the spectra of the emissions coming from the system and track if and how that spectra changed throughout the experiment. The Arduino data kept track of additional information vital to the ultimate goal of localization: time, angular position, and angular velocity data.

The PSD of each waveform was acquired with a Hanning window applied to remove end effects. These frequency domain responses were then plotted over time to acquire a spectrogram of the response and monitor changes to frequency content throughout the experiment. A periodicity exhibits itself in the PSD after the damage source becomes active.

Instead of analyzing the spectrogram as a whole, a single frequency can be picked off and changes to its amplitude can be monitored throughout the length of the experiment. As can be seen in the Fig. 11.7, the amplitude of the acoustic emission varies periodically. The frequency content of this variation shows important information which can be used to

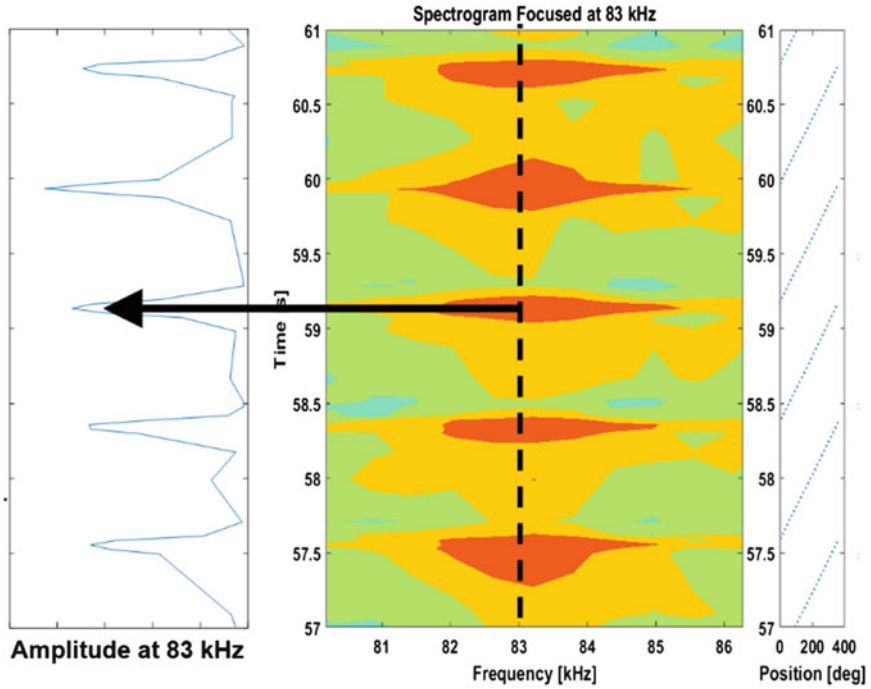

Fig. 11.7 A single frequency line of the spectrogram (*middle*) is tracked throughout the experiment to monitor the amplitude modulation (*left*) caused by non-linearity of the damage. When comparing to the angular position (*right*), it can be seen that the occurrence is periodic with the rotation of the apparatus

identify the location of the damage in the system. However, the sample points acquired from the PocketAE system do not change uniformly with time. Therefore, an interpolation was performed to create a uniformly spaced time vector with which to perform the Discrete Fourier Transform (DFT).

This new DFT was performed on the amplitude response of a single, constant frequency of the waveform data. The probing frequency input through the piezoelectric crystal was chosen so that the modulation by the pumping frequency might become apparent. A sliding window was employed to perform the DFT at sample intervals of 10 s for the 5 min tests. The result of this method was a new spectrogram with a resolution of approximately 0.05 Hz in the range of 0–75 Hz. This allowed viewing the pumping frequency modulation as the rotation rate of the experimental apparatus. These traits will be further described in the following results section.

As previously mentioned, the constitutive model related to the damage behavior in this experiment was $\omega^2 r = g$, see Eq. (11.1). Therefore, as ω was varied through the experiment, there reached an angular rate at which the damage became excited. Recording this angular velocity, a value r could be calculated which corresponded to the radial location of the damage. The angular position could also be computed using a statistical binning method which recorded a count for each peak in the PSD amplitude at the excitation frequency. As will be seen in the upcoming results section, this resulted in a normally distributed histogram for angular position.

11.4 Results

11.4.1 Localization Using VAM

Spin-down VAM analysis was applied to accumulated acoustic emission data to create a spectrogram. This raw spectrogram, seen in Fig. 11.8, clearly shows a consistent amplitude peak over the course of the test at the probing frequency of 83 kHz. It also shows peaks at harmonics of this frequency. A shift in the data is clearly visible at around 45 s and can be attributed to the non-linearity caused by the damage beginning to react in the rotating gravitational field.

A magnified view (highlighted by red box in Fig. 11.8a) of the probing frequency shows a periodicity in the amplitude of the probing signal that can be directly correlated to the angular position of the apparatus. As described in the previous section, extracting the probing line frequency data and performing a sliding window DFT results in a new spectrogram shown in Fig. 11.9.

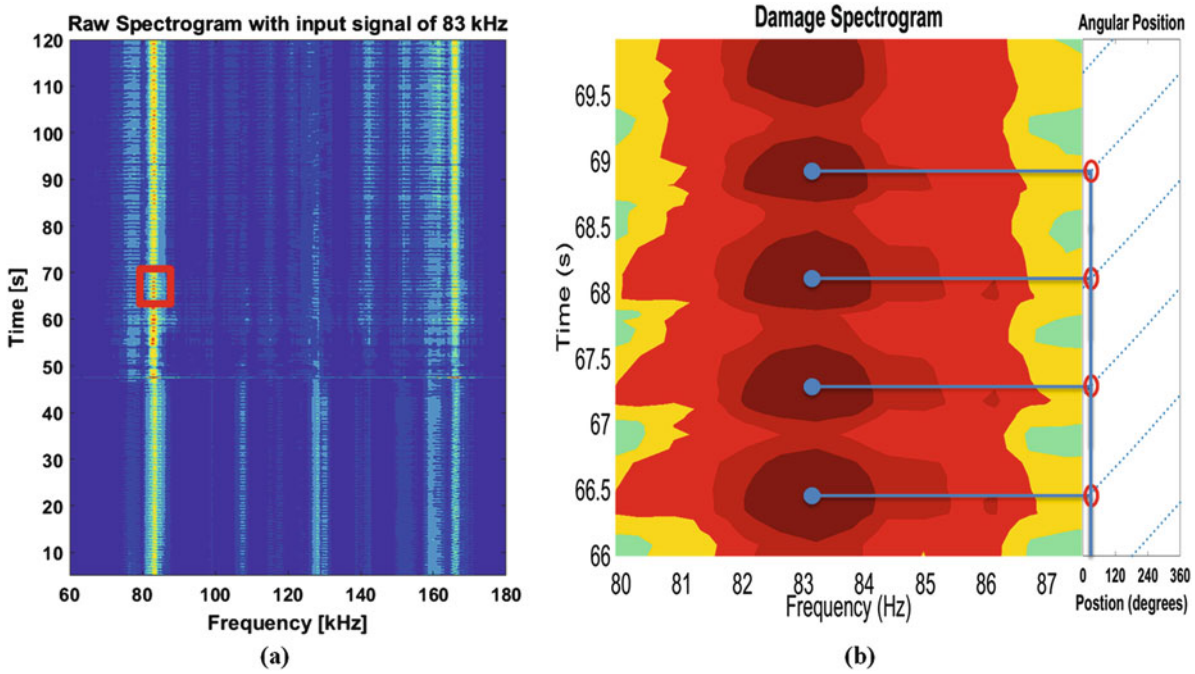

Fig. 11.8 Raw spectrogram (**a**) and magnified view (**b**) to show periodicity

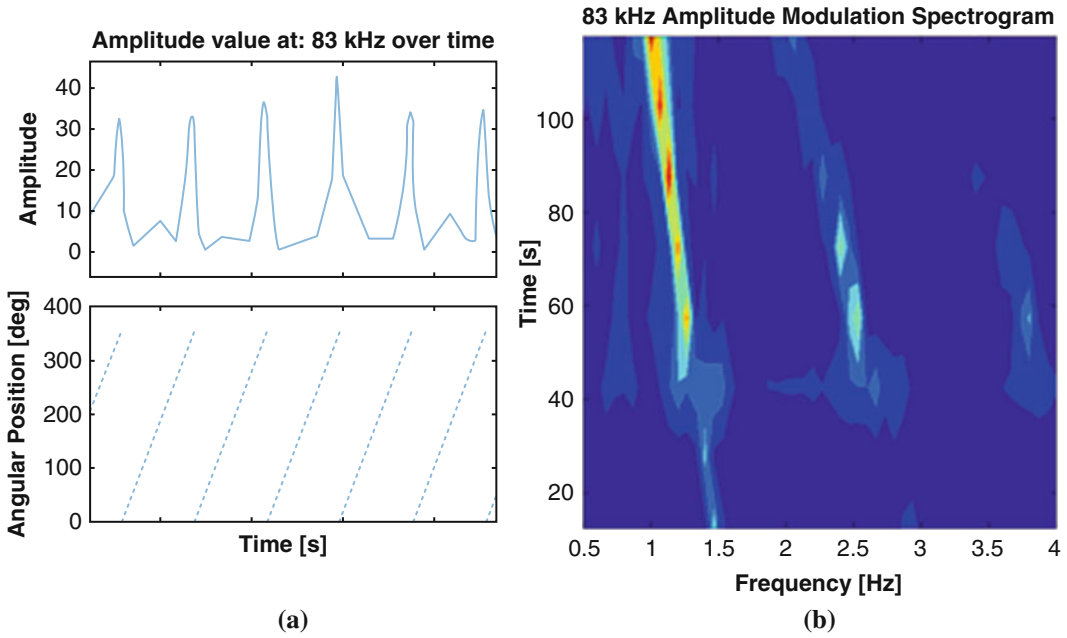

Fig. 11.9 Probing frequency amplitude (**a**) and new spectrogram showing pumping frequency modulation (**b**)

The slope of the apparent lines in this spectrogram (see Fig. 11.9b) represent the changing angular velocity input (pumping frequency) to the system and the amplitude indicates its modulation of the probing frequency. Again an event is evident at around 45 s. The key result visible in this spectrogram is that the probing frequency only begins to be modulated by the pumping frequency after the damage begins to actuate. In order to determine the radial position of the damage, the time actuation began needed to be quantified.

Going back to the extracted probing line frequency data, shown in Fig. 11.10, the beginning of actuation was taken to be the inflection point in the data as determined by the intersection of two linear trends (see Fig. 11.10a). Comparing this point in time to the input angular velocity, the constitutive model was used to compute the radial position of the damage source.

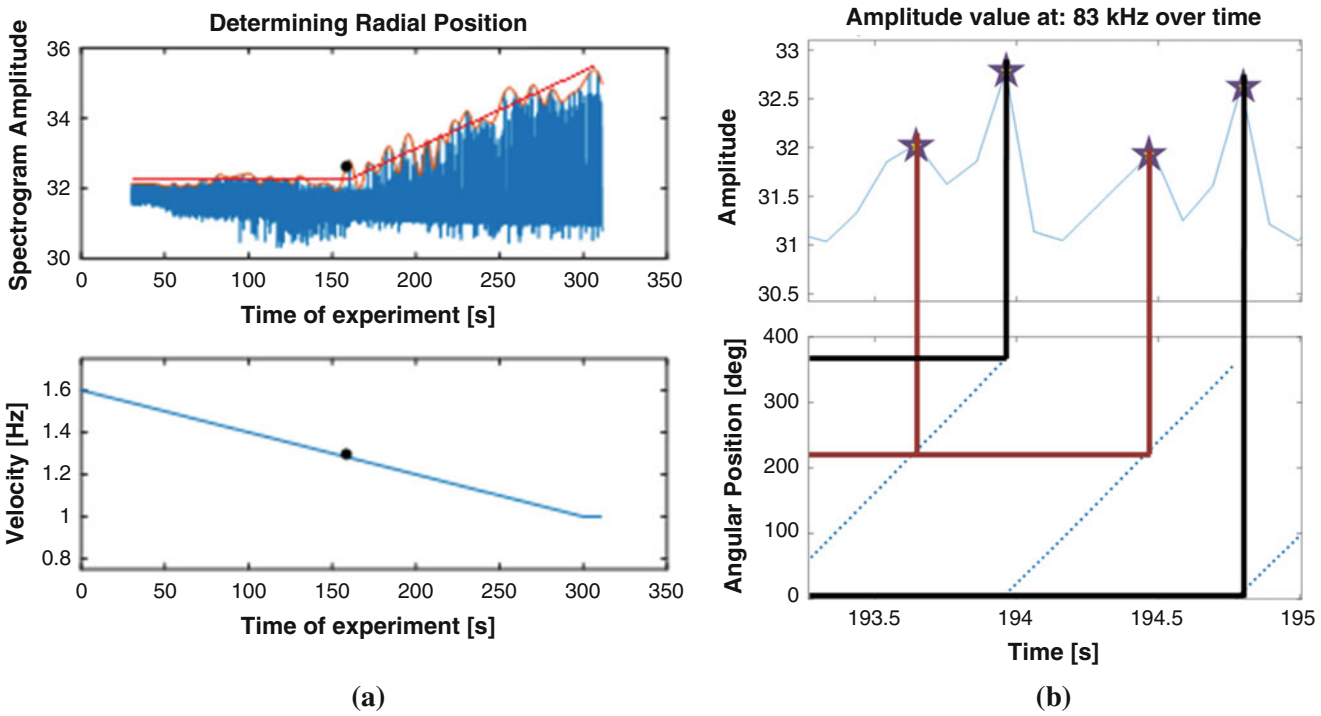

Fig. 11.10 Probing frequency amplitude with time-synced angular velocity data (**a**) and a magnified view with time synced angular position data (**b**)

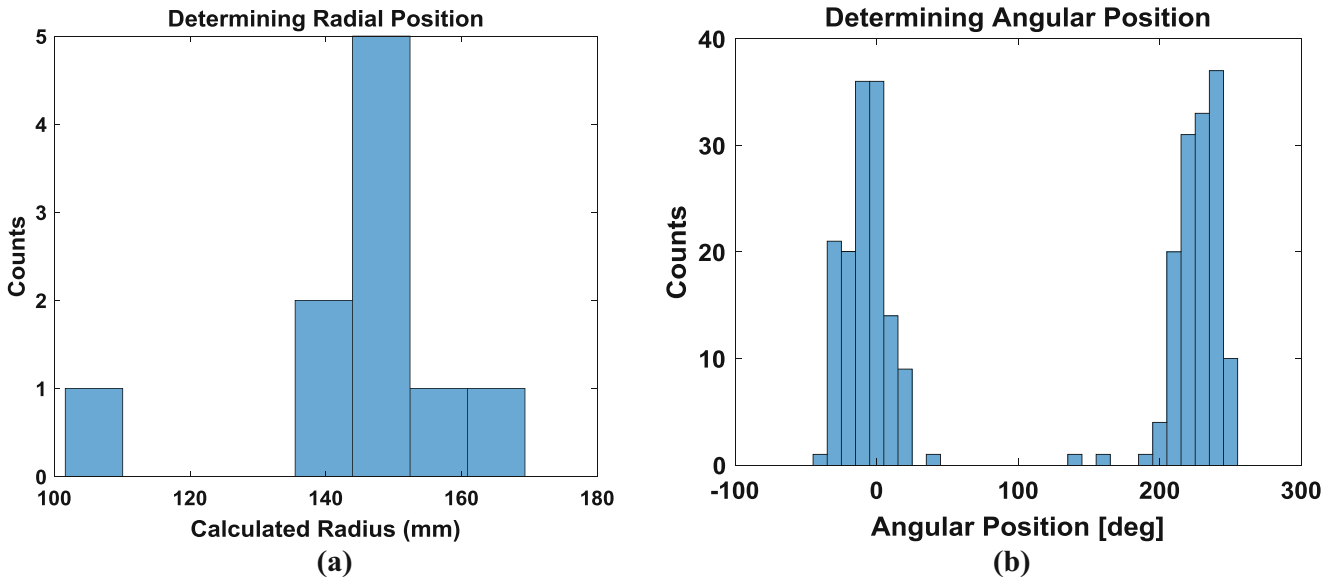

Fig. 11.11 Binned statistical data for radial (**a**) and angular position (**b**)

Angular position was determined by matching peak amplitudes in the probing line frequency data with specific times and their associated angular positions. The primary peak amplitude appeared where expected, but there was also an unexpected secondary peak around 245°. Further investigation revealed this secondary peak to be a small extra motion in the damage mechanism due to mechanical limitations in the construction of the damage. This extra signal in a simple test piece emphasizes the need for an accurate constitutive model of the test article.

The test described above was repeated 10 times to gain some statistical information about the method with the results complied in Fig. 11.11.

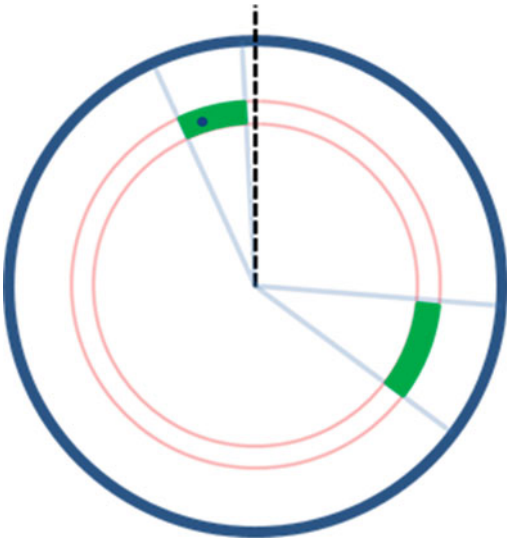

Graphic not to scale

(a)

	Mean	Est. Standard Deviation	Actual
Radial Position	144.8mm	15.5mm	142.9
Angular Position	18°	12°	20°
Secondary Angular Position	243°	16°	-

(b)

Fig. 11.12 Spin-down VAM results representation (**a**) and tabulated results (**b**)

Radial data count was too small for a full statistical characterization, but the data appears centered, minus one outlier. The angular position data presents a bimodal, approximately Gaussian distribution, with a mean matching each the primary and secondary damage types.

The obtained results (see Fig. 11.12) represent a successful radial and angular location of a simulated damage source despite using a noisy surrogate air-bearing. The secondary damage source—due to extra motion in the damage mechanism—complicates the location, but a more complete constitutive model would eliminate this.

11.5 Conclusions

This study was conducted to investigate whether it was possible to detect damage non-destructively using a novel method of VAM. The new method entailed spinning the test article to provide the low frequency pumping signal, rather than excitation with a piezoelectric device or shaker table as in conventional methods. The damage was detectable in this testing paradigm due to the nonlinearity it caused, which resulted in a visible modulation of the high frequency probing signal on an acoustic emission spectrogram, occurring at frequency off-bands equivalent to the pumping frequency at the time of modulation. This method yielded an angular and radial position with corresponding uncertainties that formed a statistical area that correctly encapsulated the improvised damage source added to the system.

This method relies on the use of a constitutive model of how the damage will behave as a way to categorize and predict how certain types of damage will appear in the acoustic emission response. For example, in the case of this study, the damage was modeled as a mass free to move in the radial direction, encumbered by friction, so that gravitation and inertial forces acting upon it could reach an easily computable equilibrium angular velocity. This velocity was used as an estimate of at what speed the damage would become visible, and pumping frequency interval was set based off of that prediction.

Also, it is important to mention that this study was conducted to augment a pre-existing NDE method using spin-down on an air bearing to determine the presence of damage. However, it was shown in this study that an air bearing is not expressly necessary to perform spin-down NDE. This information could be value for a reader interested in reproducing this method for other NDE needs. All that is required to test an article with this method is a valid constitutive model of how the damage will behave, and an apparatus that can accelerate and decelerate the test article with acceptable precision and accuracy.

Acknowledgments This work is approved for public release and distribution is unlimited under LA-UR-16-28176. This project was funded through the Los Alamos Dynamics Summer School program of the Los Alamos National Laboratory under the direction of Charles Farrar.

References

1. Farrar, C.R., Doebling, S.W., Nix, D.A.: Vibration-based structural damage identification. Philos. Transact. A. **359**(1778), 131–149 (2001)
2. Masmoudi, S., El Mahi, A., Turki, S.: Use of piezoelectric as acoustic emission sensor for in-situ monitoring of composite structures. Comp. Part B Eng. **80**, 307–320 (2015)
3. Gyekenyesi, A., Sawicki, J.T., Haase, W.C.: Modeling disk cracks in rotors by utilizing speed dependent eccentricity. J. Mater. Eng. Perform. **19**(2), 207–212 (2010)
4. Sehloff, D., Shurtleff C., Pribe, J., Haynes, C., Heit, J.: Enhanced spin-down diagnostics for nondestructive evaluation of high-value systems, rotating machinery, hybrid test methods, vibro-acoustics and laser vibrometry. In: Proceedings of the 34th IMAC, A Conference and Exposition on Structural Dynamics 2016, vol. 8, pp. 255–265, 2017
5. Kundu, T.: Acoustic source localization. Ultrasonics. **54**(1), 25–38 (2012)
6. Coverley, P.T., Staszewski, W.J.: Impact damage location in composite structures using optimized sensor triangulation procedure. Smart Mater. Struct. **12**(5), 795–803 (2003)
7. Duffour, P., Morbidini, M., Cawley, P.: A study of the vibro-acoustic modulation technique for the detection of cracks in metals. J. Acoust. Soc. Am. **119**(3), 1463–1475 (2006)
8. Yoder, N., Adams, C., Douglas, E.: Vibro-acoustic modulation utilizing a swept probing signal for robust crack detection. Struct. Health Monit. **9**(3), 257–267 (2010)
9. Gray, G., Costanzo, F., Plesha, M.: Engineering Mechanics: Dynamics, 2nd edn. McGraw-Hill Education (2012)

Chapter 12
Nonlinear Phase Separation Testing of an Experimental Wing-Engine Structure

L. Renson, J.P. Noël, D.A.W. Barton, S.A. Neild, and G. Kerschen

Abstract Modal testing of nonlinear engineering structures is currently a research area that attracts substantial attention. Recently, a nonlinear generalisation of phase separation testing has been proposed for identifying nonlinear normal modes (NNMs) based on input and output measurements. The nonlinear phase separation (NPS) method integrates identification and continuation tools to calculate multiple NNMs from broadband data. The present contribution reports the first experimental application of the NPS method. The structure of interest is a model inspired by a wing with two engines connected by means of nonlinear pylons with softening-hardening stiffness characteristics. The frequency-energy dependences of four NNMs in the 0–100 Hz range are estimated, including modal interactions. NNMs identified using the NPS method are also compared to free-decay testing results.

Keywords Nonlinear normal modes • Experimental identification • Broadband excitation • Experimental model • Discrete-time continuation

Experimental linear modal analysis (EMA) is routinely practiced in industry and plays an important role in the development and certification of aerospace structures. For instance, the resonance frequencies, vibration modes and damping ratios identified from experimental tests are used to update and validate mathematical models that can be used for flutter predictions. However, the increasing presence of nonlinearity arising, for example, from large displacements, joints or complex material properties, poses a number of issues leading to erroneous identification results [1].

Nonlinear normal modes (NNMs) offer a theoretical framework to extend the concept of modal analysis to nonlinear systems. NNMs can explain important nonlinear phenomena such as mode bifurcations and interactions between modes with well-separated, non-commensurate natural frequencies. The most popular definition defines NNMs as periodic solutions of the unforced, undamped equations of motion of the system in question. The experimental identification of such periodic motions can be performed by applying an excitation, multi-harmonic and distributed across the structure as appropriate, in phase quadrature with the response of the structure. At quadrature, the applied excitation counterbalances exactly the damping forces present in the system and the dynamics of the unforced, undamped system is recovered [2]. Such an approach follows the philosophy of linear phase resonance (force appropriation) techniques to extract each NNM individually.

A nonlinear phase separation (NPS) technique where multiple NNMs are extracted from broadband data collected during a single experiment was proposed and demonstrated on a nonlinear beam using simulated data [3]. The present paper improves this NPS methodology and reports its first experimental demonstration.

The structure of interest for this study is shown in Fig. 12.1a. It consists of a continuous 1m-long, 5mm-thick aluminum plate (the wing) to which two masses of 1.38 kg (the engines) are suspended. The suspension of each mass is made of two vertical thin beams, one at the front and one at the back of each mass. The beams are bolted to the mass at one end and clamped to the wing at the other end. The surface of the clamps is curved such that the effective length of the suspension beams is a function of the deflection amplitude, hence providing nonlinearity. The whole structure is suspended on soft springs such that rigid-body-like modes are restrained below 5 Hz. The reader is referred to Londoño et al. [4] for further details about the experimental setup.

L. Renson (✉) • D.A.W. Barton • S.A. Neild
Faculty of Engineering, University of Bristol, Bristol, UK
e-mail: l.renson@bristol.ac.uk

J.P. Noël • G. Kerschen
Department of Aerospace and Mechanical Engineering, University of Liège, Liège, Belgium
e-mail: jp.noel@ulg.ac.be

D. Di Maio, P. Castellini (eds.), *Rotating Machinery, Hybrid Test Methods, Vibro-Acoustics & Laser Vibrometry, Volume 8*,
Conference Proceedings of the Society for Experimental Mechanics Series, DOI 10.1007/978-3-319-54648-3_12

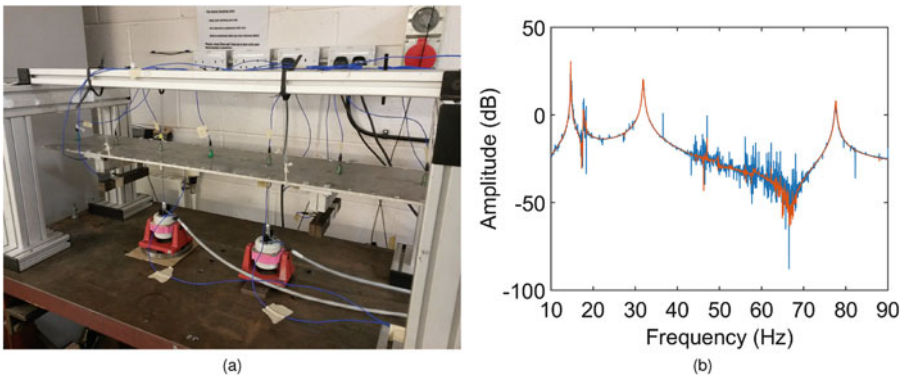

Fig. 12.1 (**a**) Picture of the Wing-Engine structure. (**b**) FRF of the structure at 0.25 V (—) and 1.25 V (—)

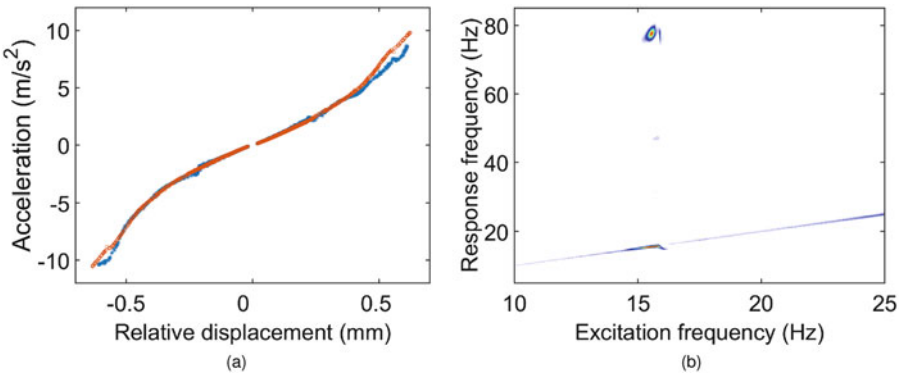

Fig. 12.2 (**a**) Qualitative restoring force measured at the right (—) and left (—) nonlinear connections. (**b**) Wavelet transform analysis of the sine-sweep data collected at a high level of excitation

Figure 12.1b presents the frequency response functions (FRFs) of the system collected at 0.25 V (—) and 1.25 V (—). The structure presents four modes between 10 and 90 Hz. The FRF measured at high level shows clear signs of nonlinear distortions. The peaks corresponding to the first two modes shift towards higher frequencies and the whole FRF is altered by nonlinear stochastic distortions.

The first and second modes have mode shapes in which the two masses move out-of- and in-phase respectively and are the most affected by nonlinearity. As such, sine-sweep data were also collected at different excitation levels around these two modes. The sweeps were performed at a linear rate of 5 Hz per minute between 10 and 25 Hz. The restoring force surface (RFS) method was applied to the time series around the first mode in order to characterise the form of the nonlinearity. The nonlinear stiffness curve obtained for each connection is smooth as shown in Fig. 12.2a. The time-frequency content of the high-level sine sweep data were also analyzed using the wavelet transform, revealing the presence of a 5:1 modal interaction between the first and fourth modes of the structure (see Fig. 12.2b).

The NPS method comprises two main steps. The first one consists of processing the acquired broadband input and output data to derive an experimental model of the structure. To this end, a frequency-domain subspace identification (FNSI) method is used [5], although any method applicable to broadband data can be employed. The second step of the identification methodology is to extract the NNMs from the identified model using numerical continuation techniques [6].

The broadband input is a pseudo-random signal (multisine with random phases) defined between 10 and 90 Hz in order to encompass the four modes of interest and the fundamental harmonics of the first two modes. The random signal is repeated 15 times and the last ten periods are considered for averaging. The structure response is recorded through 11 accelerometers. The model provided by FNSI is a discrete-time state-space model of the form

$$\begin{cases} \mathbf{x}_{k+1} = \mathbf{A}\mathbf{x}_k + \mathbf{B}\mathbf{e}(\mathbf{y}_k, \mathbf{u}_k) \\ \mathbf{y}_k \quad\;\; = \mathbf{C}\mathbf{x}_k + \mathbf{D}\mathbf{e}(\mathbf{y}_k, \mathbf{u}_k) \end{cases} \tag{12.1}$$

where the matrices $(\mathbf{A}, \mathbf{B}, \mathbf{C}, \mathbf{D})$ are the state, extended input, output and direct feedthrough matrices, respectively. The vectors $\mathbf{x}$, $\mathbf{y}$, and $\mathbf{u}$ are the states, outputs, and external inputs of the system, respectively. The vector $\mathbf{e}$, termed the extended

input vector, concatenates the external forces and the nonlinear basis functions used to model the nonlinearities. Considering the smoothness of the stiffness curves observed in Fig. 12.2a, smooth basis functions such as polynomials (cubic) and splines are considered to model the nonlinearity.

Noël et al. [3] considered the transformation of Eq. (12.1) into continuous time and its projection onto the linear modal basis in order to easily remove damping terms and carry out the computation of the NNMs in a conservative setting. In the present paper, the original discrete-time model (12.1) provided by FNSI is kept. An single-point external harmonic excitation is applied to the damped system. The excitation is of the form $u_k = F\cos(2\pi kh/T)$ where F and T are the amplitude and period of forcing, and h is the sampling time used to collect experimental data. Numerical continuation is used to track the forced response of the system. To extract the NNMs, an additional quadrature condition between the phase of the response and the excitation is imposed and a two-parameter continuation in (F, T) is carried out.

The NNMs extracted using the NPS method are analyzed and compared to resonant decay results [4]. The reproduction by the first NNM of the modal interaction observed in the sine sweep data is discussed. Additional comparisons between the nonlinear forced responses calculated from Eq. (12.1) and the sine sweep data are also carried out.

References

1. Peeters, B., Van der Auweraer, H.: Application of multisine excitation to aircraft ground vibration testing. In: Proceedings of the 16th IFAC Symposium on System Identification, Brussels (2012)
2. Peeters, M., Kerschen, G., Golinval, J.C.: Modal testing of nonlinear vibrating structures based on nonlinear normal modes: experimental demonstration. Mech. Syst. Signal Process. **25**(4), 1227–1247 (2011)
3. Noël, J.P., L. Renson, C. Grappasonni, G. Kerschen, Identification of nonlinear normal modes of engineering structures under broadband forcing. Mech. Syst. Signal Process. **74**, 95–110 (2016)
4. Londoño, J.M., Neild, S.A., Cooper, J.E.: Identification of backbone curves of nonlinear systems from resonance decay responses. J. Sound Vib. **348**, 224–238 (2015)
5. Noël, J.P., Kerschen, G.: Frequency-domain subspace identification for nonlinear mechanical systems. Mech. Syst. Signal Process. **40**, 701–717 (2013)
6. Renson, L., Kerschen, G., Cochelin, B.: Numerical computation of nonlinear normal modes in mechanical engineering. J. Sound Vib. **364**, 177–206 (2016)

Chapter 13
Wind Turbine Health Monitoring: Current and Future Trends with an Active Learning Twist

N. Dervilis, A.E. Maguire, E. Papatheou, and K. Worden

Abstract The use of offshore wind farms has been geometrically growing in recent years. Offshore power plants move into deeper waters as European water sites offer impressive wind conditions. However, the cost of an offshore wind farm is relatively high, and therefore, their reliability is crucial if they ever need to be fully integrated into the energy arena. This paper presents an investigation of current monitoring trends for wind turbines (WTs) and will try to address the motivation and the effectiveness of Structural Health Monitoring (SHM) machine learning applications for the different components of a WTs, as well as, the novel idea of intelligent WT in terms of data knowledge transfer and learning.

Keywords Environmental and operational variations • Manifold learning • Pattern recognition • Gaussian processes

13.1 The Past, the Present, the Laboratory and the Reality

It is very evident within the wind energy industry that there is a thirst for an efficient, online, continuous and as accurate monitoring tool for whole wind turbines (WTs) and especially the blades (the most expensive part of a WT), foundations and permanent magnet generators. Condition monitoring (CM), due to the long and established history for rotating machinery (e.g. gearboxes or bearings) is already a major part of the services that are provided by WT manufactures. However, the market is starving for an SHM system that can monitor other components that could cause catastrophic failures, such as offshore WT blades or the massively expensive PM generators or the complicated foundations.

Failure of any WT can cause massive financial losses, especially for structures that are operating in offshore sites. SHM of WTs is essential in order to ensure not only structural safety, but also to avoid component overdesign that could lead to economic and structural inefficiency. Automatic mechanisms for damage detection of the blades, foundations, tower and generators are still at an embryonic stage. In particular, WT blades are susceptible to multiple modes of failure. In addition, the continuous nature of their operation under variable loading and environmental conditions makes the employment of a damage detection or prognosis system challenging.

If one keeps searching in the literature, one will find hundreds (or thousands probably) of papers, technical reports and laboratory experiments that all deal with some sort of health monitoring, from non-destructive evaluation techniques (NDE) to vibration-based health monitoring. A major portion of this research follows the path to apply damage detection technologies, and these studies were mainly in a laboratory environment [1]. Briefly, both passive and active sensing technologies have been applied in the context of WT SHM [2]. Most of the SHM techniques and sensor systems that are discussed in the literature and available to industry have been considered for application to WT blade fatigue tests.

However, there is not much progress on robust, successful and on-line application of these techniques in the SHM of in-service WTs. The methods [2–10] that have been applied to WT SHM [2] include vibration monitoring based methods (accelerometers, piezo or microelectromechanical systems (MEMSs), strain (strain gauge or fibre optic cables), ultrasonic waves which are popular with composite structures (piezoelectric transducers), smart paint (piezoelectric or fluorescent particles), acoustic emissions (usually barrel sensors), impedance techniques (piezoelectric transducers), laser vibrometry (scanning laser Doppler), impedance tomography (carbon nanotubes), thermography (infrared cameras), laser ultrasound (laser devices), nanosensors (electronic nano-particles) and buckling health monitoring (piezoelectric transducers) [2–10].

N. Dervilis (✉) • E. Papatheou • K. Worden
Dynamics Research Group, Department of Mechanical Engineering, University of Sheffield, Mappin Street, Sheffield S1 3JD, UK
e-mail: n.dervilis@sheffield.ac.uk

A.E. Maguire
Vattenfall Research & Development, New Renewables, The Tun Building, Holyrood Road, Edinburgh EH8 8AE, UK

D. Di Maio, P. Castellini (eds.), *Rotating Machinery, Hybrid Test Methods, Vibro-Acoustics & Laser Vibrometry, Volume 8*,
Conference Proceedings of the Society for Experimental Mechanics Series, DOI 10.1007/978-3-319-54648-3_13

Other techniques include using digital image correlation snapshots taken along the length of the blade that allow observations of the shape and curvature of the entire blade, as well as techniques such as image correlation, shearography, acoustic emission, fiber-optic strain sensing, thermal imaging [11, 12]. Finally, wireless systems are a potential replacement for wired systems in the case that structures are in remote areas such as offshore WTs. The main disadvantage of wireless sensors for SHM are power supply of the sensors and data telemetry, with energy harvesting being a field that presents an interesting increase for powering such sensors. Some very recent research can be found in [13, 14]. Last but not least, the new implementation of hardware and sensors could be subject to lighting issues.

13.2 Intelligent WT and the Future

The future is different, and everyone is searching for clever approaches which offer a robust implementation of SHM systems that can deal both with the current hardware/software of WTs and the continuous stream of big data and complicated data bases. The challenges are:

- The use of the sensors that are already placed on the WTs to create a robust, holistic SHM system that will detect failures and performance issues of the whole WT structure as efficiently as possible, while taking advantage of the current hardware, and improving the current software.
- Introduce and evolve the idea of intelligent WTs that communicate with each other by exchanging information and implement adaptive learning as new data arrives by correcting and replacing unknown sources of outliers [15]. A totally new paradigm-Population-Based SHM-can be created [16]. This will ultimately lead to the need for less data storage-evaluation, quicker maintenance response, and less hardware/sensors on the system. This research is currently carried out by making inferences between WTs of the same and different farms and by introducing advanced machine learning techniques like extreme function theory [17]. Power curves from an actual wind turbine, are assessed as whole functions, and not individual datapoints, with the help of Gaussian process regression and extreme value distributions, with the ultimate aim of the performance monitoring of the wind turbine in a weekly resolution, and has been shown to be superior in terms of the number of false identifications, with a significantly lower number of false-positives.
- Develop new technology that will address the challenges of future WTs and propose novel methods for WT failure inspection, location and evaluation. This should include UAV remote sensing technology [18], as well as laser technology, evolution of vibration-based and ultrasonic SHM/CM techniques for blades, foundation and tower.
- There is a need for better control of uncertainty in load prediction and thus to open the path to improved prognosis.
- New design evaluations for new generation WTs in terms of validation and verification by, taking advantage of the concept of the digital twin.

13.3 An Active Learning Twist

The central idea behind active learning is that a pattern recognition algorithm can obtain computational performance and accuracy efficiencies by utilising fewer training labels, if it is allowed to find the most informative data from which it learns. In many SHM applications, there is a significant supply of unlabelled data but an important undersupply of labelled data, which are usually difficult, time-consuming or expensive to extract. In this case an active learner will arise queries, in the form of unlabelled data to be labelled by a predictor [19–31]. This semi-supervised learning tool will use only very few data points from the WT data as labelled data and will try to classify all the rest of the incoming data with no prior knowledge exchange. Because the engineering knowledge is very informative regarding the SCADA labelled data, one can check accurately if the active learning technique performs as well as it should by clustering correctly the unlabelled data to the labelled clusters coming from very few measured observations.

Active learning (commonly called “query learning”) is a machine learning approach with one purpose: to learn with less data. When supervised learning is utilised especially in an SHM context, then often a large number of labelled observations is needed. Active learning tools seek to bypass the labelling curse by generating queries for unlabelled data points that can potentially provide optimal information, that have to be labelled online and automatically by a learner [19, 19–23, 25, 27–30].

In a nutshell, the active learning method seeks to find data which contains the most informative points and as a result, to identify those data points that will give the trained classifier the best performance in terms of reduced labelled observations. Some popular methods in the machine learning community are active support vector machines, probabilistic

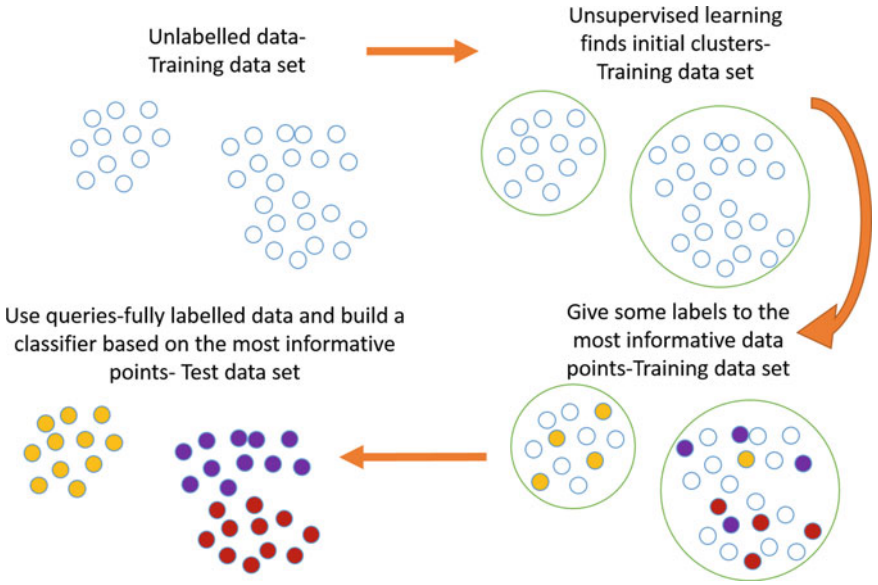

Fig. 13.1 Active learning graphical steps

decision boundary algorithms, query-by-committee or error reduction methods [28]. The algorithm that will be used here is called the Manifold Adaptive Experimental Design Algorithm or (MAED) [28]. MAED is a combination of Optimal Experimental Design (OED), Transductive Experimental Design (TED) and Manifold Adaptive Kernel (MAC) methods [19, 19–23, 25, 27–30].

The basic tasks the active learning algorithm has to perform, so that the readers can easily follow the concept behind active learning tools, are (see Fig. 13.1):

- Find an initial clustering of the data.
- Sample a few chosen points in each cluster that contain the most information.
- Assign each cluster a label (of course, based on engineering knowledge, Step 2 can be enhanced by assigning more labelled points).
- One can use this labelled data set to build a classifier (the nature of the classifier at this point is not critical as the main job was performed by the active learning clustering. So, one can use support vector machines, neural networks, radial basis networks or Gaussian processes).

13.4 An Illustrative Toy Example

One can demonstrate active learning classification, using three partially overlapping Gaussian sources of data in two dimensions, as in Fig. 13.2. The procedure in Figs. 13.3, 13.4, and 13.5 follows exactly the methodology described before: find an initial clustering of the data, sample a few chosen points in each cluster that contain the most information, assign each cluster a label (of course based on engineering knowledge, second Step can be enhanced by assigning more labelled points) and use this labelled data set to build a classifier (in this case the classifier is a relevance vector machine (RVM) [32–34]). RVM is a machine learning tool that uses Bayesian inference to obtain probabilistic classification (or regression). In essence the RVM has a very close functional form to the support vector machine, but provides probabilistic framework. One could say it is actually equivalent to a Gaussian Process machine with a specified covariance function (kernel). Due to the benefits of probabilistic predictions, confidence intervals on this prediction can be calculated from the predictive distribution.

As one can notice in Fig. 13.5 the decision boundary that separates the clusters is shown as a solid line and the predictions confidence intervals as dashed lines. In the demonstrated example 40 random points that were chosen form the active learning algorithm were used as training set. Last but not least, RVM in combination with active learning offers accurate prediction models which typically use significantly fewer basis functions compared to SVM while offering additional advantage of probabilistic predictions.

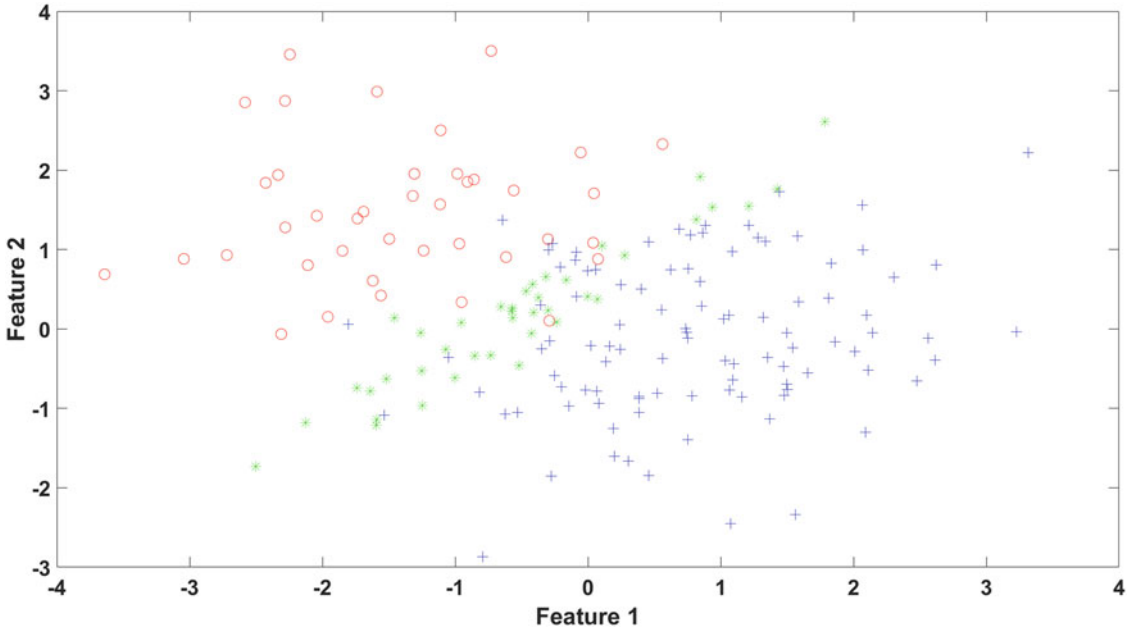

Fig. 13.2 Gaussian sources of data in two dimensions with three partially-overlapping clusters

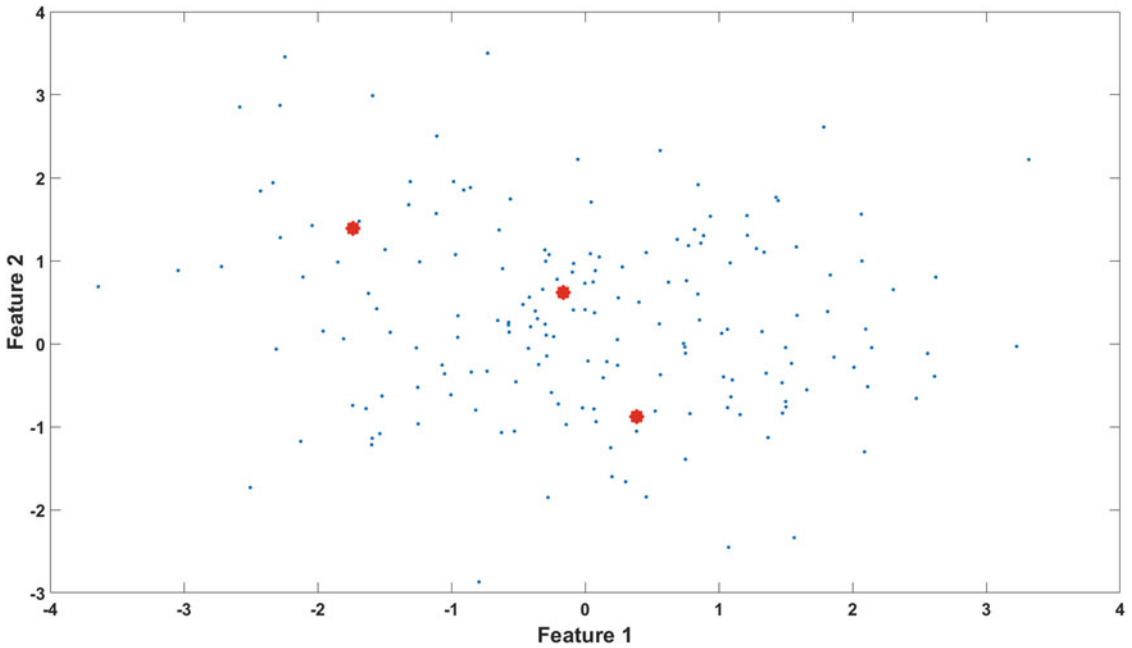

Fig. 13.3 Data selection by the active learning algorithm MAED during training of a randomly-selected few points. The selected data points are marked as *red stars* and, in this example, the number of labelled samples to select is 3. Note that the algorithm has basically selected the cluster centres

13.5 Offshore Wind Farm Active Learning Approach

Here an analysis of supervisory control and data acquisition (SCADA) extracts from the Lillgrund offshore wind farm (see Fig. 13.6) for the purposes of monitoring is used [16, 35].

Data mining and machine learning are promising approaches for modelling wind energy aspects such as power prediction or wind load forecasting. Gaussian processes [36] were used to build a reference power curve (wind speed versus power produced) for each of the 48 turbines existing in the farm. Then, each reference model was used to predict the power produced in the rest of the turbines available, thus creating a confusion matrix of the regression model errors (MSEs) for all combinations.

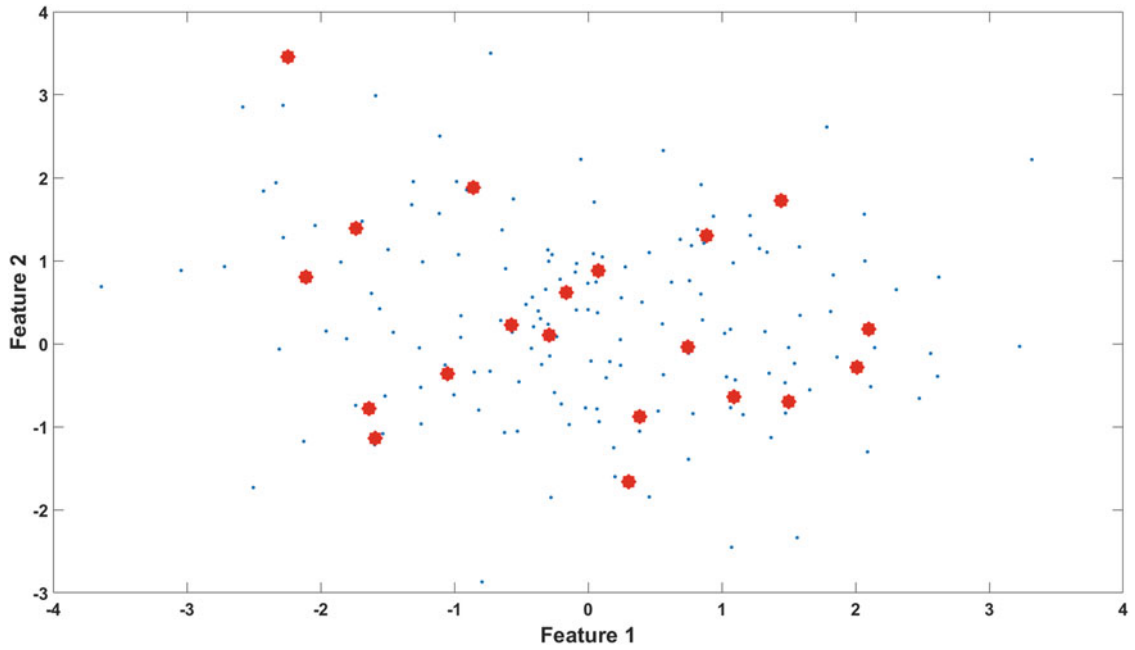

Fig. 13.4 Data selection by the active learning algorithm MAED during training of a randomly-selected few points. The selected data points are marked as *red stars* and, in this example, the number of labelled samples to select is 20

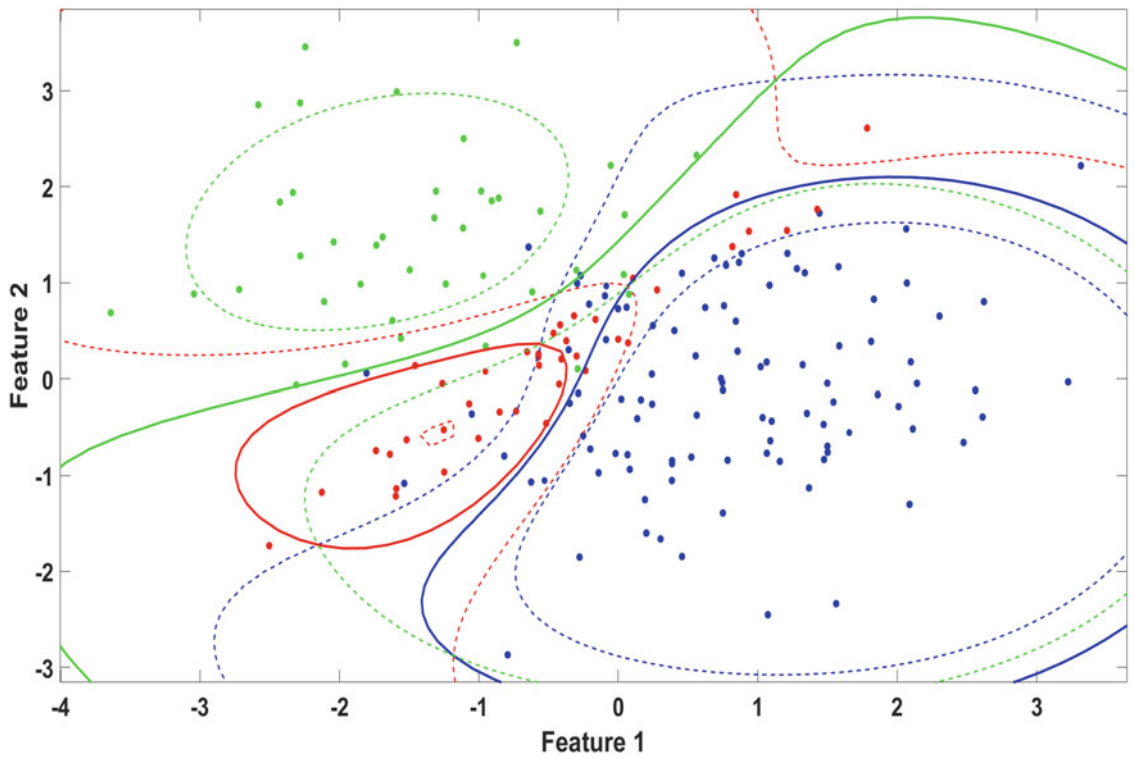

Fig. 13.5 RVM classification based on active learning information

The reference power curve is a healthy power curve, i.e. built only using data corresponding to time instances with a status code equal to '0' ('no error' in the turbines). The results showed that nearly all the models fitted were very robust with sensibly low MSE errors.

Each axis of the confusion matrix shown corresponds to one up to 48 turbines, where on the y-axis is the number of the trained turbine and on the x-axis the number of the tested turbine.

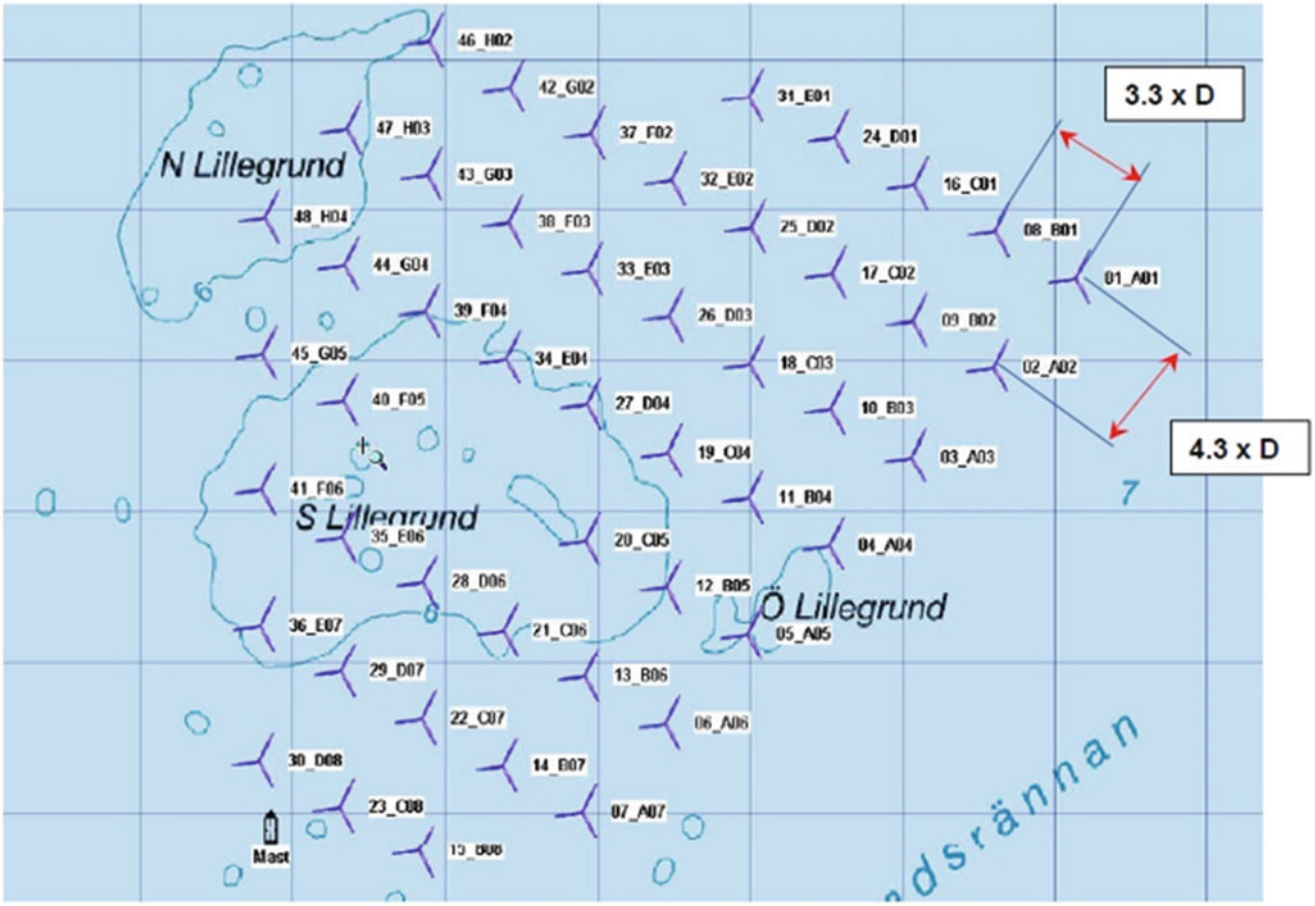

Fig. 13.6 Lillgrund wind farm 48 Siemens turbines

Low MSE errors show that the power curves have the potential for being used as a feature for the monitoring of the whole farm, as they were shown to be generally robust to the individual differences that the turbines inevitably present. So, it can be seen how well the power produced in each turbine is predicted by the rest of the trained curves (corresponding to the rest of the turbines). Such analysis is a necessary first step in establishing novelty detection between individual machines.

GPs are computationally demanding. The GP algorithm has a computational cost of order N^3 where N is the number of training points. Simply halving N produces a speed up factor of 8 and this is the main advantage of active learning in regression analysis, as it learns with less data that carry most of the information, as can be seen in Figs. 13.7 and 13.8. The active learning method is given a number k of training examples and is let free to find these labelled points that carry the most information. As can be seen from Figs. 13.7 and 13.8 the active learning algorithm selected data points that carry the most information by utilising only a few points without giving any a priori knowledge of the exact labels (this follows the schematic of Fig. 13.1). In reality, engineering judgement can be utilised and a certain number of training data points can be used in addition to the active learning job. After implementing active learning one can create computationally more efficient and fast GPs to compute the confusion matrix as can be seen in Fig. 13.9.

Furthermore, apart from using active learning for regression analysis, one can also use any sort of classifier that is trained on these active learning points with their labels. The trained classifier can then be used in order to predict the class labels of the unlabelled remaining observations (this follows the schematic of Fig.13.1). So, if data with error codes (different than zero) are flowing into the monitoring system, one can run an active learning algorithm and let free the pattern recognition tool to find labelled points that carry the most information as well as the clusters of the assigned data (see Fig. 13.10).

After each cluster is assigned with a label, one can use this labelled data set to build a classifier. In this case one asks: is the new data coming from the normal condition of the wind turbine (no error) or from a specific error code. To present things in as simplified manner as possible, here there is a two-class problem, error or no error, but the active learning semi-supervised learning can assign more labels depending on how many labels are arising. In Fig. 13.11, one can see the results of this binary classification (http://covartech.github.io/) with the cluster boundary lines on a power curve that assigns the data very efficiently into one of two classes.

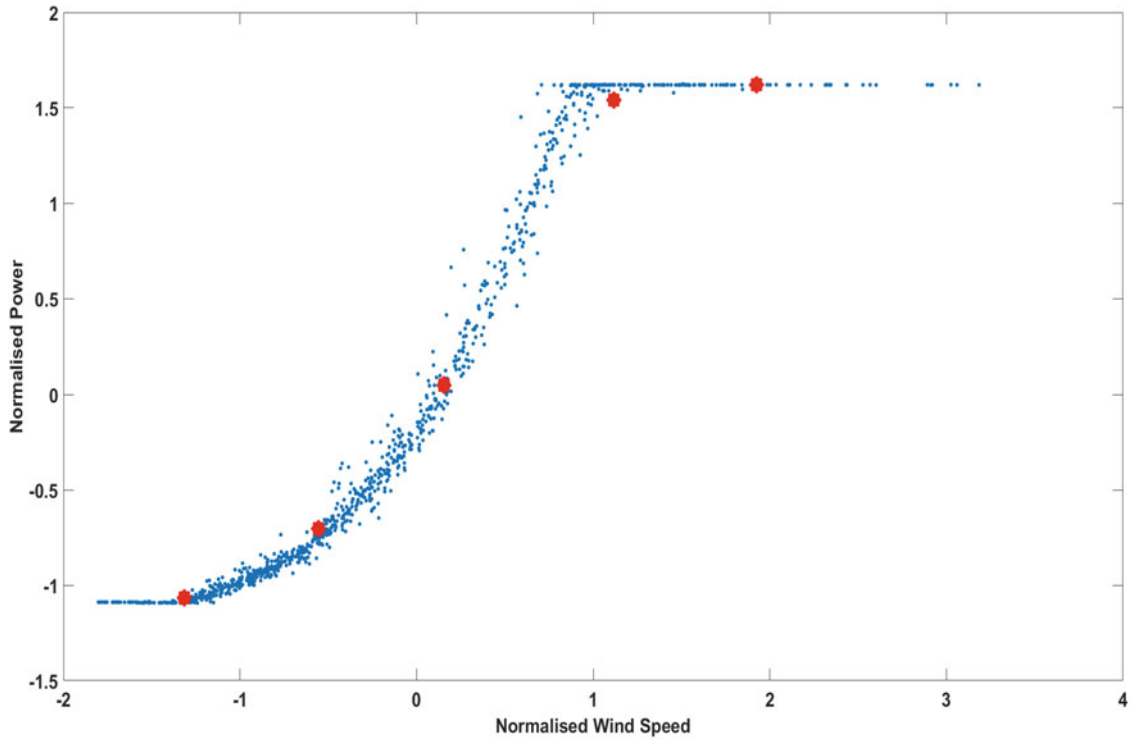

Fig. 13.7 Data selection by active learning algorithm MAED during training of randomly selected few points. The selected data points are marked as *red stars* and in this example the number of labelled samples to select is 5

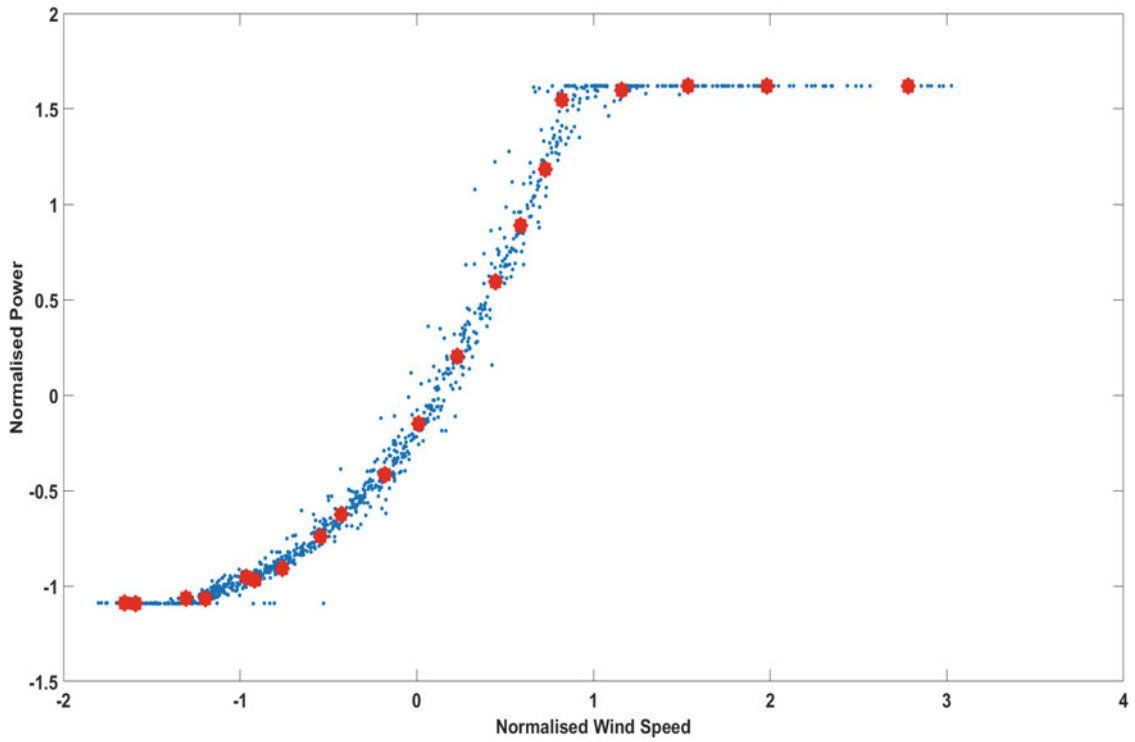

Fig. 13.8 Data selection by active learning algorithm MAED during training of randomly selected points. The selected data points are marked as *red stars* and in this example the number of labelled samples to select is 20

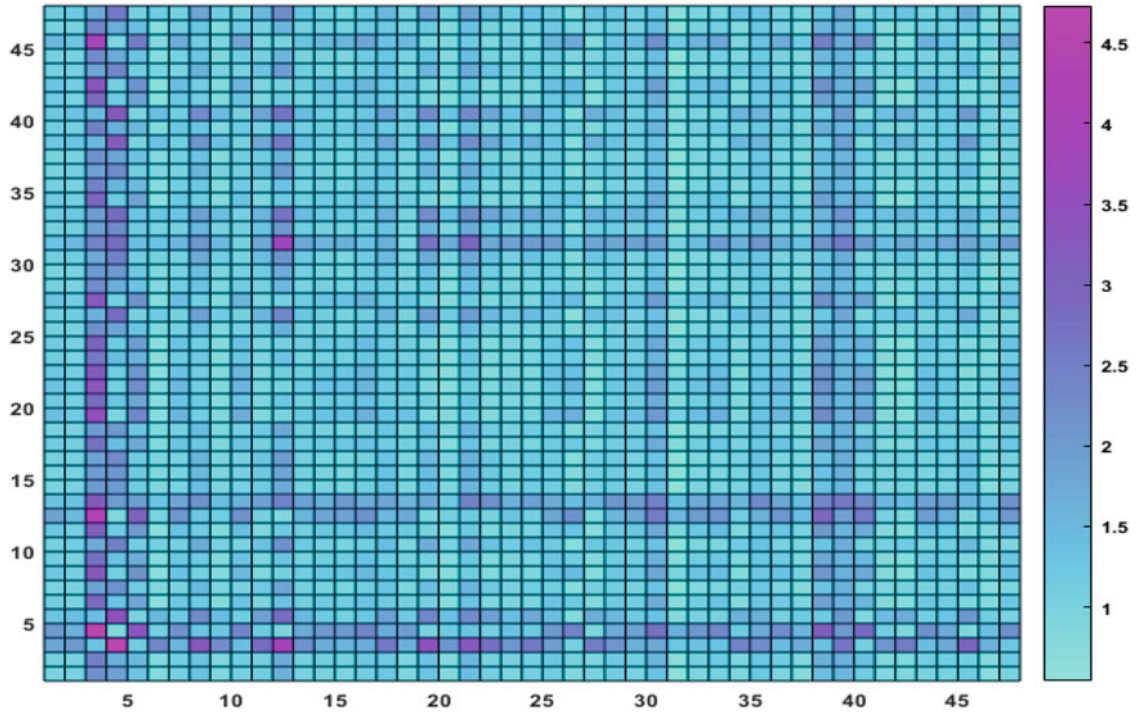

Fig. 13.9 Confusion matrix with MSE errors created from the GPs: testing set by using active learning

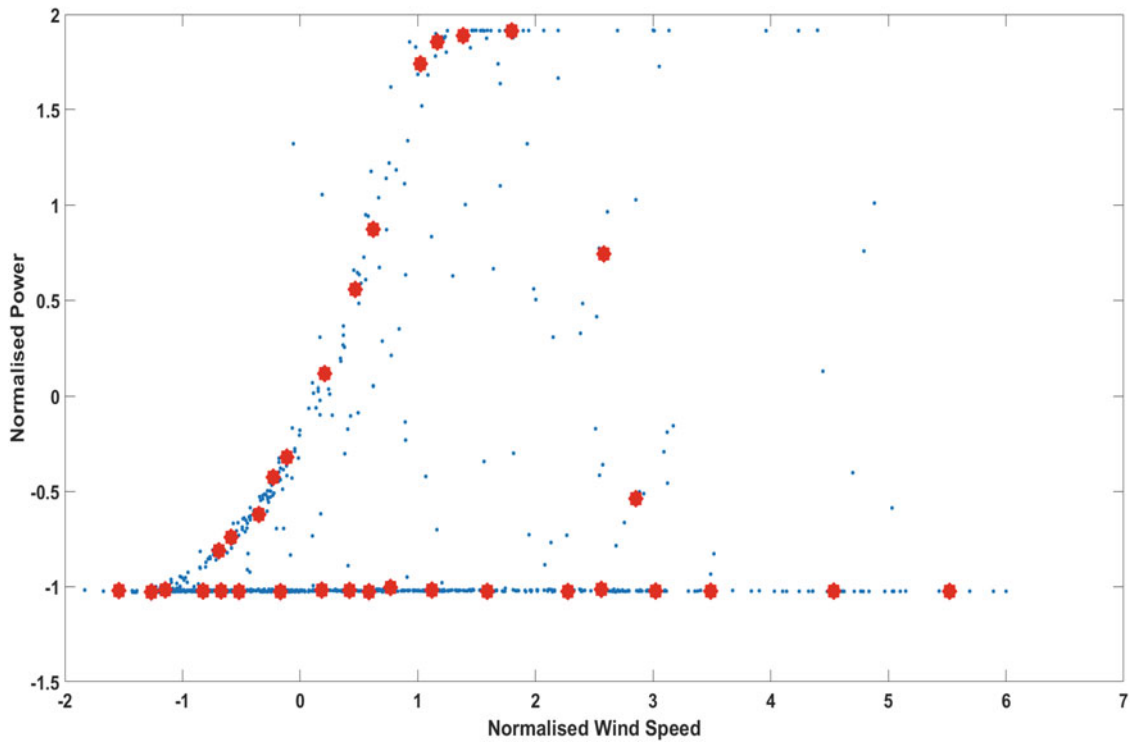

Fig. 13.10 Data selection by active learning algorithm MAED during training of randomly selected points including error flagged data

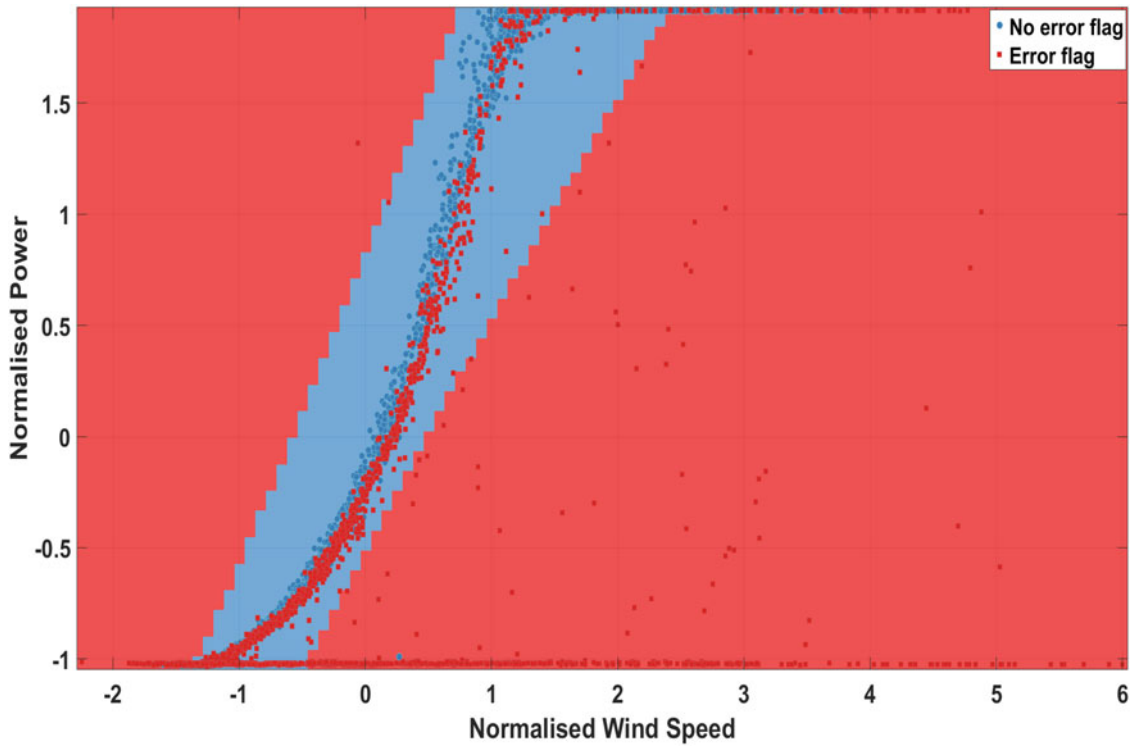

Fig. 13.11 Binary data clustering based on active learning information

In Fig. 13.12, relevance vector machines (RVM) [32–34] are utilised when three labelled classes are identified via active learning. One can see the decision boundaries for the three classes and can noticeable see that the blue data (no error flag) and the green data (error flag) overlap, as the green data indicates error flags that are insignificant for the WT structural health compared to red ones. As can be seen from Fig. 13.12, the classification accuracy will definitely increase with more training examples, as more labelled points are automatically selected. It is very encouraging that the learning method performs noticeably well even when there is a limited number of training data points and goes under a very restrictive binary selection between data that have no error flag and data with an error flag. In reality of course, when only a limited number of data points are selected, then it would be possible that some categories are not represented at all, and this could lead to misclassification of certain categories. Therefore, labelling resources during active learning can critically affect the performance in terms of classification results.

13.6 Conclusion

This paper discusses some of the latest advances in the SHM of wind turbines. In order to achieve an effective damage detection strategy, the use of different kinds of data is needed, depending on the approach. Data-driven analysis methods are essential in order to provide such solutions, although difficulties exist related to the operational conditions of wind turbine systems. Pattern recognition and machine learning approaches are not only useful for the feature extraction of the SHM procedure, but also for the manipulation of data and will lead in the very near future in SHM of WT.

Acknowledgements The support of the UK Engineering and Physical Sciences Research Council (EPSRC) through grant reference number EP/J016942/1 and EP/K003836/2 is gratefully acknowledged.

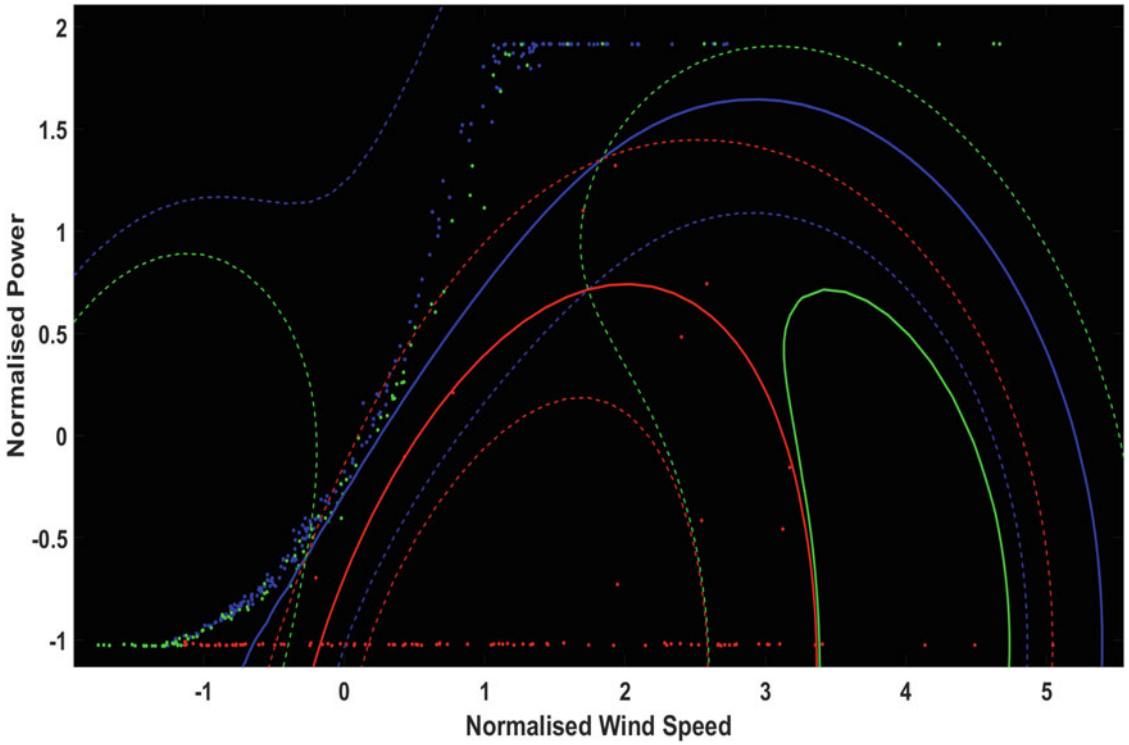

Fig. 13.12 RVM classification based on active learning information

References

1. Dervilis, N., Choi, M., Taylor, S.G., Barthorpe, R.J., Park, G., Farrar, C.R., Worden, K.: On damage diagnosis for a wind turbine blade using pattern recognition. J. Sound Vib. **333**(6), 1833–1850 (2014)
2. Kirikera, G.R., Sundaresan, M., Nkrumah, F., Grandhi, G., Ali, B., Mullapudi, S.L., Shanov, V., Schulz, M.: Wind turbines. Encyclopedia of Structural Health Monitoring.
3. Adams, D., White, J., Rumsey, M., Farrar, C.: Structural health monitoring of wind turbines: method and application to a HAWT. Wind Energy **14**(4), 603–623 (2011)
4. Jørgensen, E.R., Borum, K.K., McGugan, M., Thomsen, C.L., Jensen, F., Debel, C.P., Sørensen, B.F.: Full scale testing of wind turbine blade to failure-flapwise loading. Report Risø (2004)
5. Kristensen, O.J.D., McGugan, M., Sendrup, P., Rheinländer, J., Rusborg, J., Hansen, A.M., Debel, C.P., Sørensen, B.F.: Fundamentals for Remote Structural Health Monitoring of Wind Turbine Blades-a Preproject, Annex E: Full-scale Test of Wind Turbine Blade, Using Sensors and NDT. Risø National Laboratory (2002)
6. Overgaard, L.C.T., Lund, E.: Structural collapse of a wind turbine blade. part b: progressive interlaminar failure models. Compos. A: Appl. Sci. Manuf. **41**(2), 271–283 (2010)
7. Overgaard, L.C.T., Lund, E., Thomsen, O.T.: Structural collapse of a wind turbine blade. part a: Static test and equivalent single layered models. Compos. A: Appl. Sci. Manuf. **41**(2), 257–270 (2010)
8. Sørensen, B.F., Jørgensen, E., Debel, C.P., Jensen, F.M., Jensen, H.M., Jacobsen, T.K., Halling, K.M.: Improved design of large wind turbine blade of fibre composites based on studies of scale effects. Technical Report, Danmarks Tekniske Universitet, Risø Nationallaboratoriet for Bæredygtig Energi (2004)
9. White, J.R., Adams, D.E., Rumsey, M.A.: Modal analysis of cx-100 rotor blade and micon 65/13 wind turbine. Struct. Dyn. Renew. Energy **1**, 15–27 (2011)
10. Zhou, H.F., Dou, H.Y., Qin, L.Z., Chen, Y., Ni, Y.Q., Ko, J.M.: A review of full-scale structural testing of wind turbine blades. Renew. Sustain. Energy Rev. **33**, 177–187 (2014)
11. LeBlanc, B., Niezrecki, C., Avitabile, P., Chen, J., Sherwood, J.: Damage detection and full surface characterization of a wind turbine blade using three-dimensional digital image correlation. Struct. Health Monit. **12**(5–6), 430–439 (2013)
12. Niezrecki, C., Avitabile, P., Chen, J., Sherwood, J., Lundstrom, T., LeBlanc, B., Hughes, S., Desmond, M., Beattie, A., Rumsey, M., et al.: Inspection and monitoring of wind turbine blade-embedded wave defects during fatigue testing. Struct. Health Monit. (2014). doi:10.1177/1475921714532995
13. Joyce, B.S., Farmer, J., Inman, D.J.: Electromagnetic energy harvester for monitoring wind turbine blades. Wind Energy (2013)
14. Song, G., Li, H., Gajic, B., Zhou, W., Chen, P., Gu, H.: Wind turbine blade health monitoring with piezoceramic-based wireless sensor network. Int. J. Smart Nano Mater. **4**(3), 150–166 (2013)
15. Dervilis, N., Papatheou, E., Antoniadou, I., Cross, E.J., Worden, K.: On the usage of active learning for SHM. In: Proceedings of ISMA (2016)

16. Papatheou, E., Dervilis, N., Maguire, A.E., Antoniadou, I., Worden, K.: A performance monitoring approach for the novel Lillgrund offshore wind farm. IEEE Trans. Ind. Electron. **62**(10), 6636–6644 (2015)
17. Papatheou, E., Dervilis, N., Maguire, E.A., Campos, C., Antoniadou, I., Worden, K.: Extreme function theory for SHM: a case study for wind turbines. Struct. Health Monit. (2015)
18. Yang, Y., Dorn, C., Mancini, T., Talken, Z., Kenyon, G., Farrar, C., Mascareñas, D.: Blind identification of full-field vibration modes from video measurements with phase-based video motion magnification. Mech. Syst. Signal Process. **85**, 567–590 (2017)
19. Tong, S., Koller, D.: Support vector machine active learning with applications to text classification. J. Mach. Learn. Res. **2**(Nov), 45–66 (2001)
20. Prince, M.: Does active learning work? a review of the research. J. Eng. Educ. **93**(3), 223–231 (2004)
21. Zhu, X.: Semi-supervised learning literature survey (2005)
22. Sindhwani, V., Niyogi, P., Belkin, M.: Beyond the point cloud: from transductive to semi-supervised learning. In: Proceedings of the 22nd International Conference on Machine Learning, pp. 824–831. ACM, New York (2005)
23. Yu, K., Bi, J., Tresp, V.: Active learning via transductive experimental design. In: Proceedings of the 23rd International Conference on Machine Learning, pp. 1081–1088. ACM, New York (2006)
24. Frey, B.J., Dueck, D.: Clustering by passing messages between data points. Science **315**(5814), 972–976 (2007)
25. Dasgupta, S., Hsu, D.: Hierarchical sampling for active learning. In: Proceedings of the 25th International Conference on Machine Learning, pp. 208–215. ACM, New York (2008)
26. Givoni, I.E., Frey, B.J.: A binary variable model for affinity propagation. Neural Comput. **21**(6), 1589–1600 (2009)
27. Settles, B.: Active learning literature survey. Univ. Wis. Madison **52**(55–66), 11 (2010)
28. Cai, D., He, X.: Manifold adaptive experimental design for text categorization. IEEE Trans. Knowl. Data Eng. **24**(4), 707–719 (2012)
29. Shahraiyni, H., Ghafouri, M., Shouraki, S., Saghafian, B., Nasseri, M.: Comparison between active learning method and support vector machine for runoff modeling. J. Hydrosci. Hydraul. Eng. **60**(1), 16–32 (2012)
30. Hospedales, T.M., Gong, S., Xiang, T.: Finding rare classes: Active learning with generative and discriminative models. IEEE Trans. Knowl. Data Eng. **25**(2), 374–386 (2013)
31. Zheng, W., Yu, W.: Probabilistic approach to assessing scoured bridge performance and associated uncertainties based on vibration measurements. J. Bridge Eng. (2014)
32. Thayananthan, A., Navaratnam, R., Stenger, B., Torr, P.H.S., Cipolla, R.: Multivariate relevance vector machines for tracking. In: European Conference on Computer Vision, pp. 124–138. Springer, Heidelberg (2006)
33. Thayananthan, A.: Relevance Vector Machine Based Mixture of Experts. Department of Engineering, University of Cambridge, Cambridge (2005)
34. Tipping, M.E.: Sparse bayesian learning and the relevance vector machine. J. Mach. Learn. Res. **1**(Jun), 211–244 (2001)
35. Dahlberg, J-A.: Assessment of the Lillgrund wind farm: power performance wake effects. Vattenfall Vindkraft AB, 6_1 LG Pilot Report, http://www.vattenfall.se/sv/file/15_Assessment_of_the_Lillgrund_W.pdf_16596737.pdf(citedMarch30,2012) (2009)
36. Rasmussen, C.E., Williams, C.K.I.: Gaussian Processes for Machine Learning. MIT, Cambridge (2006)

Chapter 14
Nonlinear 3D Dynamic Model of an Automotive Dual Mass Flywheel

G. Quattromani, A. Palermo, F. Pulvirenti, E. Sabbioni, and F. Cheli

Abstract Internal combustion engines produce a fluctuating torque due to discrete pistons combustion, as well as induced inertial imbalance of the reciprocating pistons. In standard operating conditions, the resulting torsional oscillations of the crankshaft are transferred to the gearbox, leading to a number of comfort problems. Rattle noise is one of these problems and it is caused by impulsive forces caused by clearances across the driveline and especially in the gearbox. In order to prevent rattle, dual mass flywheels may be used to reduce torsional oscillations in automotive powertrains.

The present paper presents a 3D nonlinear dynamic model of an automotive dual mass flywheel. The model is made of primary and secondary masses and the arc springs between them. Centrifugal effects and redirection forces acting on the springs as well as nonlinear contact forces due to stoppers and flanges bounding spring motion are accounted for. Moreover, friction occurring in seals and friction resulting from the spring radial forces are included. The developed dual mass flywheel model is included into a multi-body model of the vehicle powertrain to assess the effect of its main parameters on the driveline behaviour (e.g. modes of vibration, radial forces).

Keywords Dual mass flywheel • 3D nonlinear multibody model • Powertrain • Modal analysis

Nomenclature

J_p , J_s	Inertia of Primary and Secondary mass of DMF
$J_{OUT,i,j}$	Inertia of the i-th lumped mass of the j-th outer arc springs
$J_{IN,i,j}$	Inertia of the i-th luped mass of the j-th inner arc springs
r_{out} , r_{in} , r	External radius of outer arc springs, external radius of internal arc springs, mean radius of arc springs
μ_{out} , μ_{in}	Friction coefficient of outer and inner arc springs
ϕ_p , ϕ_s	Absolute angular displacement of primary and secondary mass
$\phi_{OUT,i,j}$	Absolute angular displacement of the i-th lumped mass of the j-th outer arc spring
$\phi_{IN,i,j}$	Absolute angular displacement of the i-th lumped mass of the j-th inner arc spring
$T_{FRout,i,j}$	Friction torque acting on the i-th lumped mass of the j-th outer arc spring
$T_{FRin,i,j}$	Friction torque acting on the i-th lumped mass of the j-th inner arc spring
$T_{CONout-p,i,j}$	Contact torque acting on the i-th lumped mass of the j-th outer arc spring with primary mass of the DMF
$T_{CONin-p,i,j}$	Contact torque acting on the i-th lumped mass of the j-th inner arc spring with primary mass of the DMF
$T_{CONout-s,i,j}$	Contact torque acting on the i-th lumped mass of the j-th outer arc spring with secondary mass of the DMF
$T_{CONin-s,i,j}$	Contact torque acting on the i-th lumped mass of the j-th inner arc spring with secondary mass of the DMF
T_{DAMPER}	Friction torque of the damper
$T_{ELout,i,j}$	Elastic torque acting on the i-th lumped spring of the j-th outer arc spring
$T_{ELin,i,j}$	Elastic torque acting on the i-th lumped spring of the j-th inner arc spring
T_{FC}	Extra elastic torque of full compressed arc springs
$F_{OUT,i,j}$	Force acting on the i-th lumped spring of the j-th outer arc spring
$F_{IN,,i,j}$	Force acting on the i-th lumped spring of the j-th inner arc spring
$F_{TAN_{OUT,i,j}}$	Tangential force acting on the i-th lumped spring of the j-th outer arc spring

G. Quattromani • E. Sabbioni (✉) • F. Cheli
Department of Mechanical Engineering, Politecnico di Milano, Via La Masa 1, Milan (MI), Italy
e-mail: edoardo.sabbioni@polimi.it

A. Palermo • F. Pulvirenti
Ferrari S.p.A., Via Abetone Inferiore 4, Maranello (MO), Italy

D. Di Maio, P. Castellini (eds.), *Rotating Machinery, Hybrid Test Methods, Vibro-Acoustics & Laser Vibrometry, Volume 8*,
Conference Proceedings of the Society for Experimental Mechanics Series, DOI 10.1007/978-3-319-54648-3_14

$F_{TAN_{IN,i,j}}$	Tangential force acting on the i-th lumped spring of the j-th inner arc spring
$F_{RAD_{OUT,i,j}}$	Radial force acting on the i-th lumped spring of the j-th outer arc spring
$F_{RAD_{IN,i,j}}$	Radial force acting on the i-th lumped spring of the j-th inner arc spring
$F_{CF_{OUT,i,j}}$	Centrifugal force acting on the i-th lumped mass of the j-th outer arc spring
$F_{CF_{IN,i,j}}$	Centrifugal force acting on the i-th lumped mass of the j-th inner arc spring
$N_{OUT,i,j}$	Total radial force acting on the i-th lumped mass of the j-th outer arc spring
$N_{IN,i,j}$	Total radial force acting on the i-th lumped mass of the j-th inner arc spring
$R_{OUT,i,j}$	External torque acting on the i-th lumped mass of the j-th outer arc spring
$R_{IN,i,j}$	External torque acting on the i-th lumped mass of the j-th inner arc spring
$M_{OUT,i,j}$	Mass of the i-th lumped mass of the j-th outer arc spring
$M_{IN,i,j}$	Mass of the i-th lumped mass of the j-th inner arc spring
$\dot{\phi}_{ref}$	Reference angular velocity for friction model
T_{ENG}, T_{CLU}	Torque transmitted by the engine and by the clutch
k_{out}, k_{in}	Stiffness of outer and inner arc springs elastic element only
k_{imp}, e	Stiffness, stiffness exponential and max damping coefficient for contact forces
c_{max}, d	max damping coefficient and saturation displacement threshold in contact forces

14.1 Introduction

Most of nowadays vehicles are equipped with alternative internal combustion engines, which produce a fluctuating torque. Torque variations are mainly due to piston combustion, which is a non-continuous event. In fact, piston combustion is a cyclical event which occurs every 2 crankshaft rotations in 4T engines and every rotation for 2T engine. In multi-cylinder engines, torque variation order is directly linked to pistons number. Moreover piston combustion itself may be a source of irregularity, because the instantaneous pressure generated during combustion slightly changes from cycle to cycle.

Torque variations transmitted from the engine generate torsional vibration along all the driveline. These vibrations involve a number of NVH (Noise Vibration and Harshness) problems, among which one of the most relevant is driveline rattle.

Rattle noise is generally generated by the sudden impacts between parts of the driveline with clearance/backlash (e.g. meshing gears of the gearbox) and it is particularly audible at low speed regimes of the engine.

One of the most effective solutions to reduce torsional vibrations (and so driveline rattle) is the introduction of a Dual Mass Flywheel (DMF, see Fig. 14.1) between the engine and the driveline.

Although DMFs vary a lot depending on the application, the basic mechanical layout is the one shown in Fig. 14.1. As it can be seen it consists of a primary mass connected to the engine, a secondary mass connected to the transmission shaft and two or more sets of arc springs placed between the two rotary inertias. The desired damping can be obtained by combining friction devices to the friction existing between arc springs and primary mass.

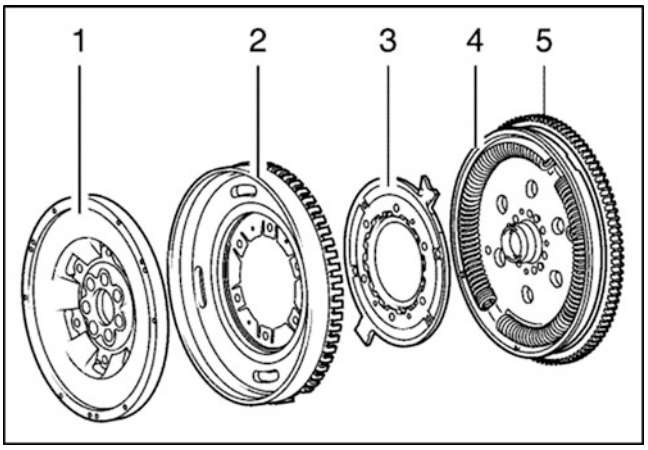

Fig. 14.1 Main mechanical components composing the DMF. From *left* to *right*: (*1*) Secondary mass, (*2*) Addition mass, (*3*) Flange, (*4*) Arc springs, (*5*) Primary mass

Modelling the dynamic behaviour of DMF is of utter importance to accurately reproduce and study torsional vibrations and rattle phenomenon affecting vehicle driveline and consequently several models were proposed in the technical literature.

A simplified 2 degrees of freedom (dofs) dynamic model of DMF is presented by Walter et al. [1, 2] and by Lei et al. in [3]. The model consists of two rotating inertias connected by a linear spring-damper element.

In [4], a 1D lumped-parameters nonlinear dynamic model of DMF is proposed, describing friction phenomena occurring between arc springs and primary mass due to centrifugal and redirection forces, which provide a physical explanation of hysteresis and springs hardening.

In [5], Lei et al. updated the previously developed 2-dofs model introducing a nonlinear spring connecting the two rotatory inertias and a Bouc–Wen model to introduce the hysteretic frictional behaviour of DMF.

Beside the great effort spent to investigate and reproduce the torsional behaviour of DMF, a model capable of studying its 3D dynamics and especially able of estimating the radial forces transmitted by DMF to vehicle powertrain has still to be developed.

The present paper proposes a 3D nonlinear model of DMF based on MultyBody (MB) approach. Great attention is given to modelling contacts between arc springs and DMF stages so to evaluate radial forces transmitted to the powertrain. First, capability of the developed model to reproduce DMF behaviour was assessed by means of static and dynamic experimental tests. Then the DMF model was introduced into a complete MB model of the vehicle powertrain to evaluate its influence on powertrain modes of vibration.

14.2 DMF Torsional Model

In this section, the multibody model of DMF is presented. In the following subsections, DMF is modelled allowing only rotations of primary and secondary masses around DMF axis (torsional model). This model allows to investigate the torsional behaviour of DMF and the comparison with the experimental data.

In Sect. 14.4, constrains of primary and secondary masses will be removed so to allow relative rotations and translations of primary and secondary masses (3D model). In this way, the effects of 3D dynamics of DMF on vehicle powertrain will be evaluated.

The model of the DMF is implemented using a commercial MB code.

14.2.1 Description of Bodies, Constraints and Number of d.o.f.

In the developed MB model of DMF primary mass and secondary mass are considered as rigid bodies. The shape of these bodies is carved in order to create two or more (three in the present application) sections where the arc springs are housed.

Sections hosting arc springs are bounded by stoppers equally spaced along the primitive circumference of primary and secondary masses (Fig. 14.2a). Generally speaking, stopper profiles are the same for every sector but they can also be slightly different due to manufacturing tolerance or design choice.

Concerning arc springs, we consider the most generic case with two concentric arc springs for each sector. Inner and outer arc springs have different angular extension, in this way it is possible to obtain a different DMF torsional stiffness at different relative angular displacement between primary and secondary masses.

Note that the centrifugal force pushes the arc springs against the inner surface of the primary mass as angular speed increases. To include centrifugal force effects into the model, each arc spring is modelled as a series of lumped springs and masses [6, 7], as shown in Fig. 14.2b.

In the case of the torsional model, primary and secondary masses are constrained to the ground with revolute joints. Outer arc spring lumped masses are constrained to the primary DMF mass with revolute joints. Inner arc spring lumped masses are constrained to the outer arc spring elements with a revolute joint. Assuming to divide each of the three arc springs in 6 elements (Fig. 14.2b), the torsional model has thus 44 dofs: rotations of primary and secondary masses and 42 dofs related to the lumped masses schematizing the arc springs.

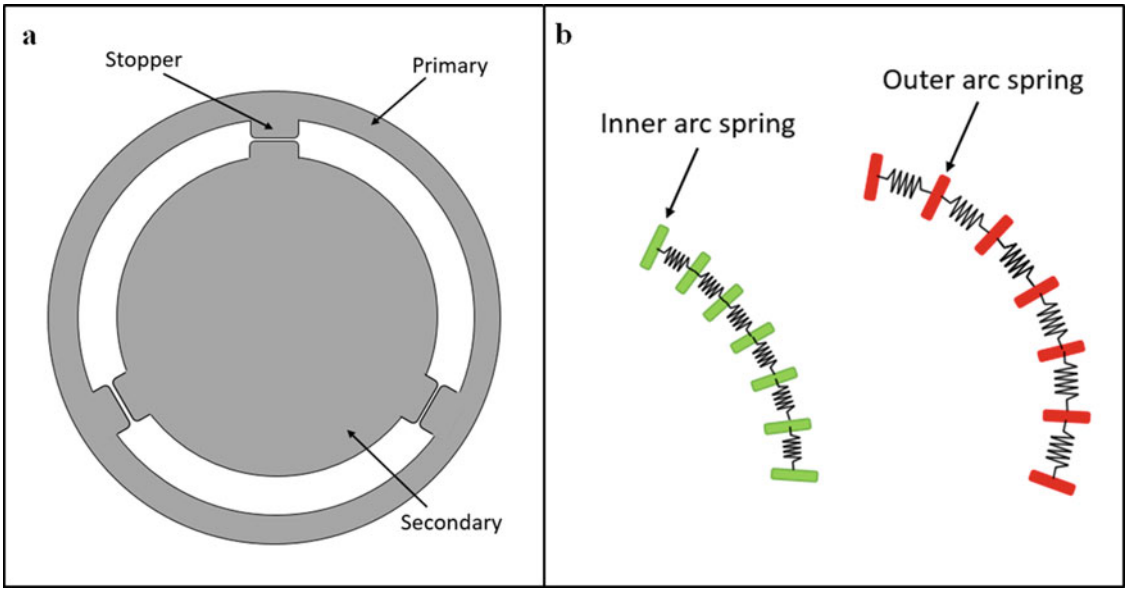

Fig. 14.2 (**a**) Simplified sketch of the primary and secondary mass of the DMF. (**b**) Sketch of the schematization of inner and outer arc springs. Inner and outer arc spring are repeated for each circular sector of DMF

14.2.2 Equations of Motion

To write the equations of motion of the lumped masses included into the DMF model, the minimal set approach is used [6]. The adopted reference frame is centred in the COG (centre of gravity) of the DMF, with z-axis oriented along the rotation axis. Rotations are positive with counter clockwise angular displacement.

Let's start considering the equations of motion of primary and secondary masses:

$$J_p\ddot{\phi}_p = T_{ENG} + \sum_{J=1}^{3}\sum_{i=1}^{7} T_{FRout,i,j} + \sum_{J=1}^{3}\sum_{i=1}^{2} T_{CONout-p,i,j} + \sum_{J=1}^{3}\sum_{i=1}^{2} T_{CONin-p,i,j} - T_{DAMP} - T_{FC} \tag{14.1}$$

$$J_s\ddot{\phi}_s = T_{CLU} + \sum_{J=1}^{3}\sum_{i=1}^{2} T_{CONout-s,i,j} + \sum_{J=1}^{3}\sum_{i=1}^{2} T_{CONin-s,i,j} + T_{DAMP} + T_{FC} \tag{14.2}$$

As described in Eq. (14.1), on the primary mass of DMF is applied the engine torque, T_{ENG}, which balances the friction torque of the outer arc springs, T_{FRout}, the contact torque of inner and outer arc springs, T_{CONout}, and the moment of inertia, $J_p\ddot{\phi}_p$. Torque T_{FC} accounts for arc springs nonlinearity when they are fully compressed, while torque T_{DAMP} accounts for friction between primary and secondary masses [8].

Similar terms appear in the equation of motion of the secondary mass (Eq. (14.2)) to balance the torque transmitted by the clutch, T_{CLU}. Friction torque due to arc springs is neglected for the secondary mass since during NVH analyses angular speeds are always different from zero and so arc springs are pushed against the DMF primary mass due to centrifugal forces.

To write the equations of motion of the lumped masses schematizing the arc springs, let's consider the simplified scheme shown in Fig. 14.3. On each lumped mass of outer arc springs (except the ones which get in contact with the stoppers) are applied the elastic torques due to adjacent elements and friction torques due to normal loads acting on both outer and inner lumped masses (Eq. (14.3)). Similar terms appear in the equations of motion of the lumped masses of inner arc springs (Eq. (14.4)).

$$J_{OUT,i,j}\ddot{\phi}_{OUT,i,j} = T_{ELout,i,j} - T_{ELout,i-1,j} - T_{FRout,i,j} + T_{FRin,i,j} \quad \forall \boldsymbol{j} = 1,2,3 \;\; \forall \boldsymbol{i} = 2,3,\ldots,6 \tag{14.3}$$

$$J_{IN,i,j}\ddot{\phi}_{IN,i,j} = T_{ELin,i,j} - T_{ELin,i-1,j} - T_{FRin,i,j} \quad \forall \boldsymbol{j} = 1,2,3 \;\; \forall \boldsymbol{i} = 2,3,\ldots,6 \tag{14.4}$$

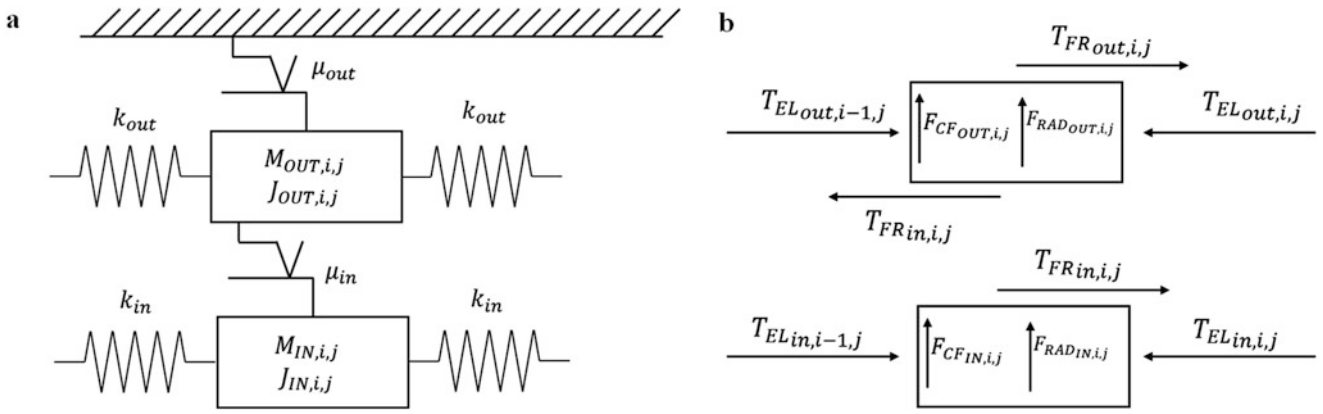

Fig. 14.3 (**a**) Planar representation of lumped mass elements and lumped elastic elements of inner and outer arc springs. (**b**) Force and torques acting on inner and outer arc springs elements

Fig. 14.4 Tangential and radial forces transmitted from elastic element only of DMF

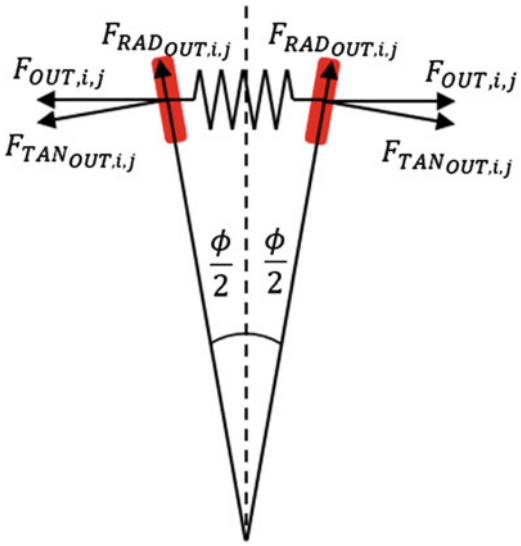

Elastic torques acting on the lumped masses can be simply obtained through some geometrical considerations. Making reference to Fig. 14.4, the forces, F_{OUT}, transmitted by the elastic elements can be divided into tangential, F_{TAN}, and radial forces, F_{RAD}, according to:

$$F_{OUT,i,j} = 2k_{out}r\left[\sin\left(\frac{\phi_{OUT,i,j}}{2}\right) - \sin\left(\frac{\phi_{OUT,i,j}\big|_{t=0}}{2}\right)\right]$$

$$F_{TAN_{OUT,i,j}} = F_{OUT,i,j}\left[\cos\left(\frac{\phi_{OUT,i,j}}{2}\right)\right]$$

$$T_{ELout,i,j} = rF_{TAN_{OUT,i,j}} \tag{14.5}$$

$$F_{RAD_{OUT,i,j}} = F_{OUT,i,j}\left[\sin\left(\frac{\phi_{OUT,i,j}}{2}\right)\right] + F_{(OUT,i,j-1)}\left[sin\left(\frac{\phi_{(OUT,i,j-1)}}{2}\right)\right] \tag{14.6}$$

Centrifugal forces can instead be computed as:

$$F_{CF_{OUT,i,j}} = M_{OUT,i,j}\left(\dot{\phi}_{OUT,i,j}\right)^2 r \tag{14.7}$$

Elastic torques, radial forces and centrifugal forces for inner arc spring elements can be obtain in a similar way.

For what friction torque is concerned, it is to point out that this is mainly due to normal forces generated by high angular speeds (which generate significant centrifugal forces) and radial forces caused by the curvature of arc springs.

Note that friction in DMF is of fundamental importance for two main reasons: first of all, friction is the main cause of energy dissipation in DMF (hysteresis of spring coils is in fact negligible); moreover stiction of arc spring coils generate a phenomenon known as *coil deactivation* [4]. Some coils during small angular oscillations around an equilibrium position get stuck on the primary mass. This leads to a stiffer response of the DMF when forced to oscillate with small angles.

To account for stiction effects during DMF motion, Karnopp friction model is used to calculate friction torque acting on the outer arc springs [8, 9]:

$$\begin{aligned} N_{OUT,i,j} &= F_{RAD_{OUT,i,j}} + F_{CF_{OUT,i,j}} + F_{RAD_{IN,i,j}} + F_{CF_{IN,i,j}} \\ R_{OUT,i,j} &= T_{ELout,i,j} - T_{ELout,i-1,j} + T_{FRin,i,j} \\ \dot{\phi}_{OUT_{rel,i,j}} &= \dot{\phi}_{OUT,i,j} - \dot{\phi}_p \end{aligned} \tag{14.8}$$

$$T_{FRout,i,j} = \begin{cases} \mu_{out} r_{out} \left| N_{OUT,i,j} \right| \bullet sign\left(\dot{\phi}_{OUT_{rel,i,j}}\right) & \left|\dot{\phi}_{OUT_{rel,i,j}}\right| > \left|\dot{\phi}_{ref}\right| \\ R_{OUT,i,j} & \left|\dot{\phi}_{OUT_{rel,i,j}}\right| \le \left|\dot{\phi}_{ref}\right| \ \bigwedge \ R_{OUT,i,j} \le \mu_{out} r_{out} \left| N_{OUT,i,j} \right| \\ \mu_{out} r_{out} \left| N_{OUT,i,j} \right| \bullet sign\left(\dot{\phi}_{OUT_{rel,i,j}}\right) & \left|\dot{\phi}_{OUT_{rel,i,j}}\right| \le \left|\dot{\phi}_{ref}\right| \ \bigwedge \ R_{OUT,i,j} > \mu_{out} r_{out} \left| N_{OUT,i,j} \right| \end{cases} \tag{14.9}$$

Similarly, for the inner arc springs, we have:

$$\begin{aligned} N_{IN,i,j} &= F_{RAD_{IN,i,j}} + F_{CF_{IN,i,j}} \\ R_{IN,i,j} &= T_{ELin,i,j} - T_{ELin,i-1,j} \\ \phi_{IN_{rel,i,j}} &= \dot{\phi}_{IN,i,j} - \dot{\phi}_{OUT,i,j} \end{aligned} \tag{14.10}$$

Note that DMFs always account a certain amount of clearance between arc springs, primary and secondary masses. Thus taking backlash into account is a key point to obtain a descriptive model for NVH analysis. On purpose, the equations of motion of the lamped masses getting in contact with primary and secondary masses of DMF can be written as follows:

$$J_{OUT,i,j}\ddot{\phi}_{OUT,i,j} = T_{ELout,i,j} - T_{CONout-p,i,j} - T_{CONout-s,i,j} - T_{FRout,i,j} + T_{FRin,i,j} \quad \forall \boldsymbol{j} = 1,2,3 \ \ \boldsymbol{i} = 1 \tag{14.11}$$

$$J_{IN,i,j}\ddot{\phi}_{IN,i,j} = T_{ELin,i,j} - T_{CONin-p,i,j} - T_{CONin-s,i,j} - T_{FRin,i,j} \quad \forall \boldsymbol{j} = 1,2,3 \ \ \boldsymbol{i} = 1 \tag{14.12}$$

$$J_{OUT,i,j}\ddot{\phi}_{OUT,i,j} = T_{CONout-p,i,j} + T_{CONout-s,i,j} - T_{ELout,i-1,j} - T_{FRout,i,j} + T_{FRin,i,j} \quad \forall \boldsymbol{j} = 1,2,3 \ \ \boldsymbol{i} = 7 \tag{14.13}$$

$$J_{IN,i,j}\ddot{\phi}_{IN,i,j} = T_{CONin-p,i,j} + T_{CONin-s,i,j} - T_{ELin,i-1,j} - T_{FRin,i,j} \quad \forall \boldsymbol{j} = 1,2,3 \ \ \boldsymbol{i} = 7 \tag{14.14}$$

Contact torques, T_{CON}, in Eqs. (14.11)–(14.14) are obtained through penalty approach [10, 11]. The penalty model returns a nonlinear elastic force and damping in function of penetration of the two bodies in contact. In particular, the damping coefficient starts from zero and rises up to a saturation value to ensure a contact force which always start from zero when contact begins (independently from approaching velocity). The penalty contact approach formulation [10, 11] for two generic i, j components is thus given by:

$$T_{CON} = r \begin{cases} k_{imp}\left[r\left(\phi_i - \phi_j\right)\right]^e + c_{max} smooth\left[\frac{r\left(\phi_i - \phi_j\right)}{d}\right]\left(r\left(\dot{\phi}_i - \dot{\phi}_j\right)\right) & \left|\phi_i - \phi_j\right| > 0 \\ 0 & \left|\phi_i - \phi_j\right| \le 0 \end{cases} \tag{14.15}$$

$$smooth(x) = 3x^2 - 2x^3 \tag{14.16}$$

14.3 Numerical-Experimental Comparison

To assess the capability of the developed model to reproduce the DMF dynamic behaviour, two experimental tests were carried out:

1) torsion test at standstill;
2) small displacement cycles at different rotating speeds.

Experimental setup is composed by two electric motor, feedback controlled. The first motor transmits torque to the primary mass of the DMF, the second one imposes the load on the secondary mass of the DMF. Loads imposed on the DMF is achieved by dynamometer. The torque transferred by the DMF and torsional displacements of the primary and the secondary flywheels are detected by torque sensors and encoders, respectively.

14.3.1 Torsion Test at Standstill

The first torsion test is carried out at standstill. This implies that the primary mass is fixed, while the secondary mass is slowing rotating.

Figure 14.5a shows the transmitted torque over the relative angle (wind-up angle). Numerical (solid line) and experimental data (dashed line) are compared.[1] As it can be noticed, the developed model is able to capture the quasi-static behaviour of the DMF. Specifically the following phenomena are reproduced:

- since the primary mass compresses at first outer arc springs and then both outer and inner arc springs, a double-stage linear behaviour of the transmitted torque over the wind-up angle can be observed;
- at small wind-up angles, when the secondary mass is rotating inside the clearance between arc springs and stoppers, only ground friction torque is transmitted;
- transmitted torque is different depending on compression or decompression phase. This is due to friction torque which is always opposite to wind-up angular speed;
- friction torque generates hysteresis during the test, which is represented by the area enclosed by the curve of Fig. 14.5a (i.e. the dissipated energy). Hysteresis tends to increase with the wind-up angle. This is due to radial elastic forces (Eq. (14.6)), which change with the wind-up angle;
- finally, at high wind-up angles, stiffness increases abruptly since arc springs get fully compressed.

14.3.2 Small Displacement Cycles at Different Rotating Speeds

During the test, the secondary mass of the flywheel is forced to rotate at constant speed, while the primary mass of the flywheel is rotating at the same mean speed plus an harmonic component:

$$\dot{\phi}_p = \dot{\phi}_0 + A_1 \sin(\omega_1 t + \theta_1) \tag{14.17}$$

$$\dot{\phi}_s = \dot{\phi}_0 \tag{14.18}$$

In Eq. (14.17) $\dot{\phi}_0$ is the mean velocity, ω_1 the frequency of the harmonic, A_1 the amplitude and θ_1 the phase.

Figure 14.5b shows the transmitted torque over the wind-up angle at three different speeds. As it can be seen, even in this test, there is a reasonable agreement between the numerical (solid line) and the experimental data (dashed line).

Note that in this test, the mean stiffness of the hysteresis cycle is higher than in the standstill test. This is due to the *coil deactivation* phenomenon: for small rotations around the equilibrium position, some coils of the arc springs get stuck on primary mass of the DMF. This implies that only some coils take part to the motion, stiffening the DMF response.

[1] Scales of x and y axes are not shown in all figures due to industrial privacy reasons.

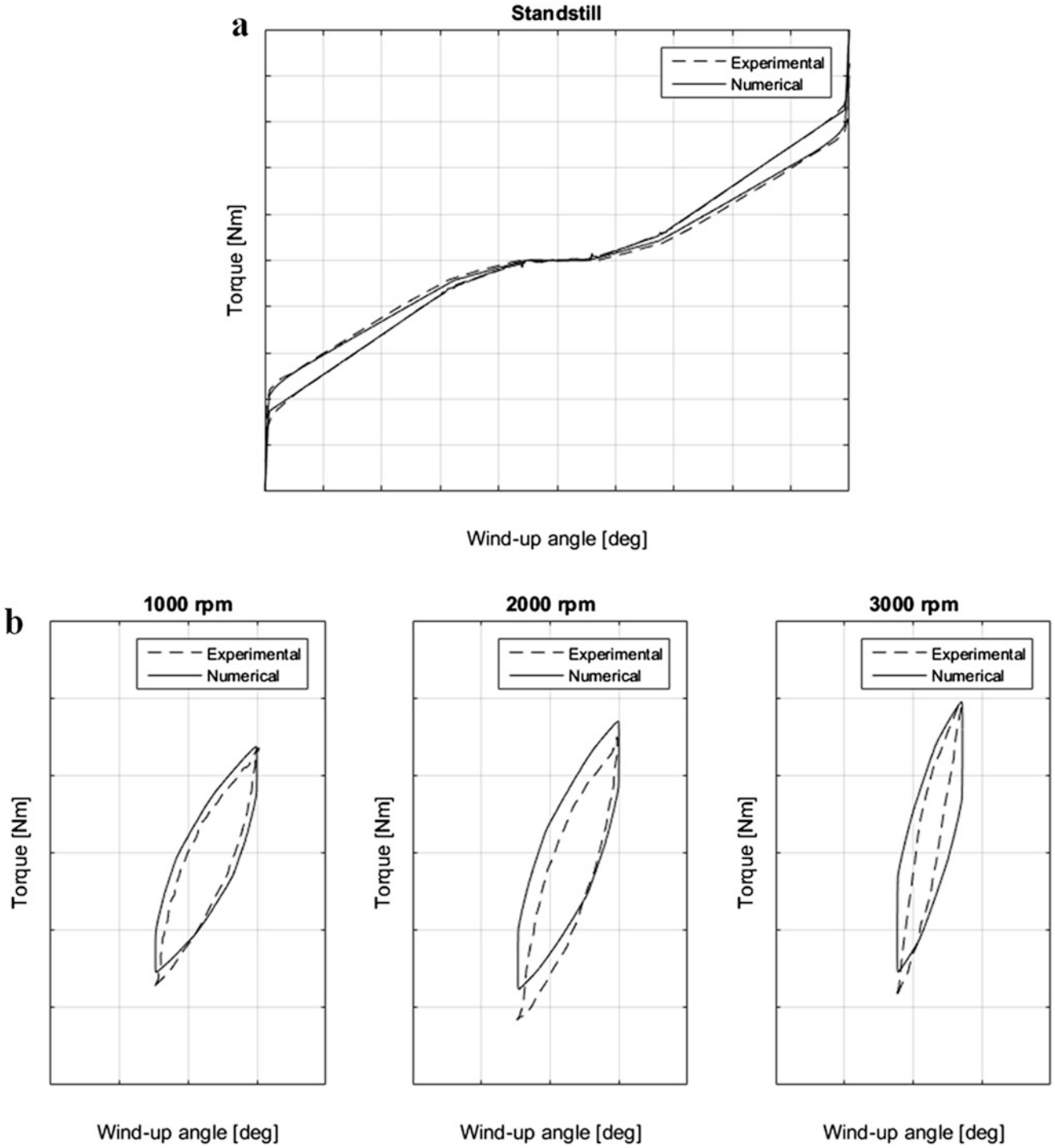

Fig. 14.5 (**a**) Comparison between experimental and numerical results during standstill test. (**b**) Comparison between experimental and numerical results during hysteresis loop test. From *left* to *right* the mean velocity of DMF is: (*1*) 1000 rpm, (*2*) 2000 rpm, (*3*) 3000 rpm

As it can be seen, the developed model is able to capture this phenomenon. Moreover the developed model is able to capture the stiffening trend of DMF behaviour with increasing mean angular speed: hysteresis cycles become steeper as the mean angular speed increases.

14.4 DMF 3D Model

A complete 3D multibody model of DMF allows to evaluate not only torsional dynamics, but also lateral and vertical dynamics. From a mechanical point of view, it is extremely important to understand if secondary mass of DMF can transmit radial forces to the driveline due to torsional vibrations. In fact, these forces may lead to noise and vibration problems all along the driveline.

On the purpose of introducing 3D effects into the DMF torsional model, revolute joints constraining primary and secondary masses are removed so to allow relative motions/rotations. Thus radial forces and bending moments acting on the components of the DMF can be evaluated. Specifically, radial forces and bending moments are mainly due to:

- presence of misalignment between crankshaft and transmission shaft;
- flexural deflections of the driveline shafts;
- misalignment between stopper and arc spring profiles, which may cause not perfectly tangential reaction forces;
- differences/asymmetry between stopper profiles. If for example stoppers have different angular extension, backlash between primary/secondary mass and arc springs are recovered for different angular displacements between primary and secondary masses, this leading to unbalanced contact forces, as shown in Fig. 14.6a.

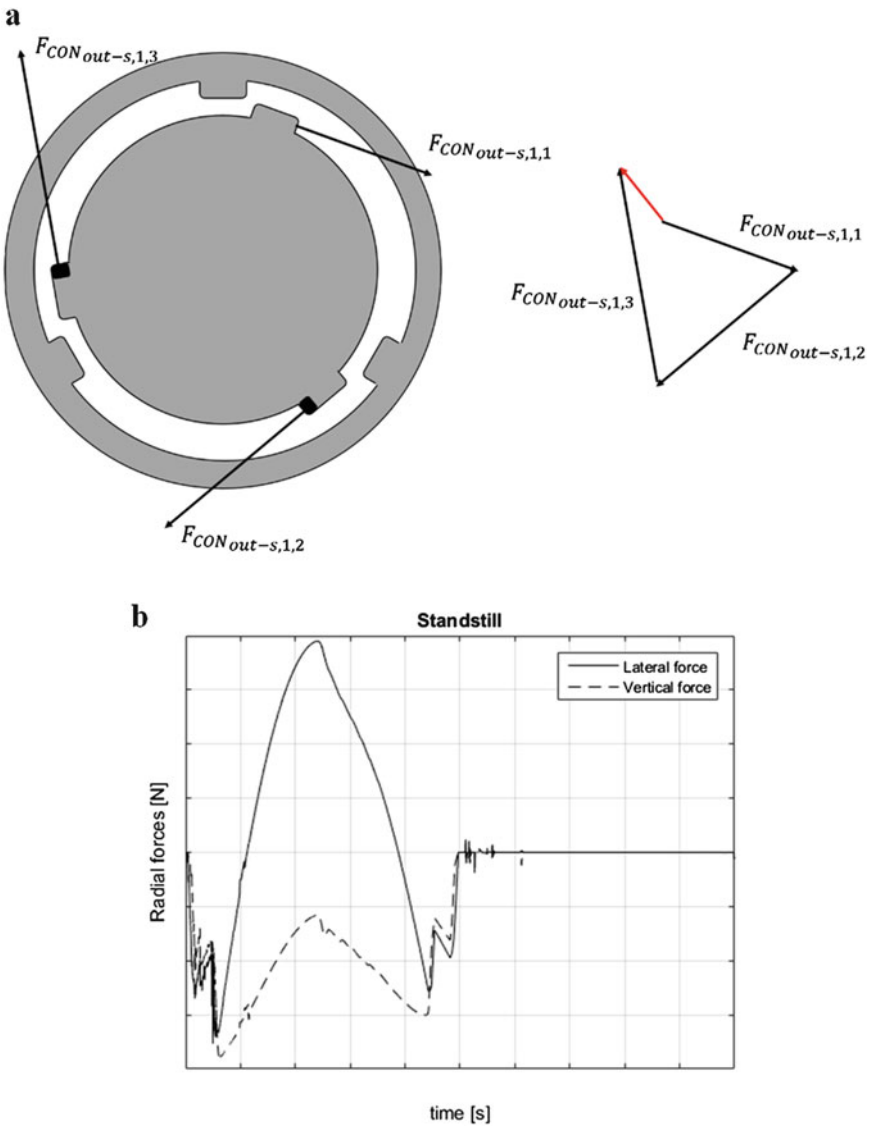

Fig. 14.6 (**a**) Not balanced contact forces due to stoppers asymmetry, (**b**) Lateral and vertical force transmitted by secondary mass of the DMF to driveline shaft during standstill simulation. Axes are scaled in respect to maximum value of time and maximum value of radial force magnitude

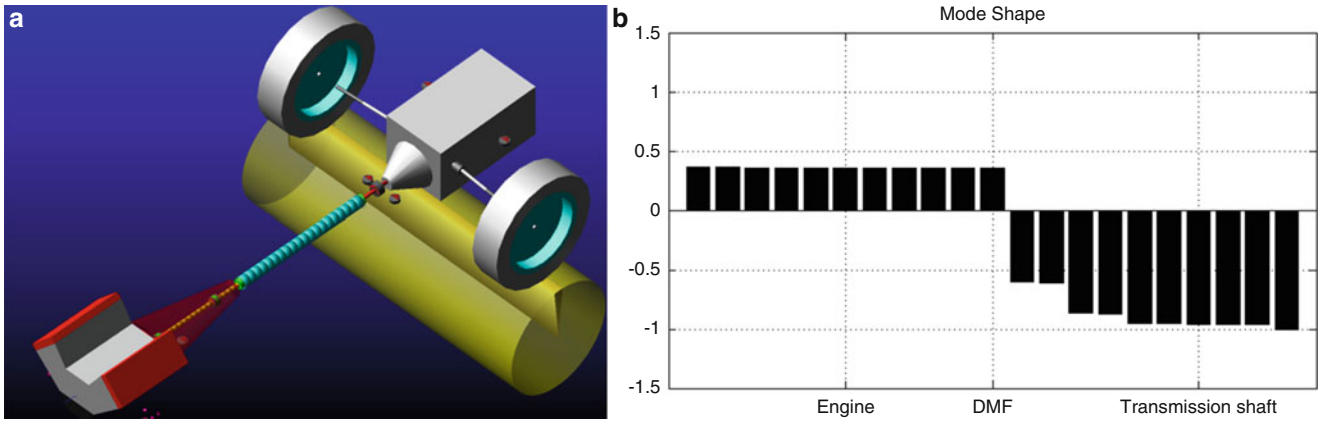

Fig. 14.7 (**a**) Picture of the complete powertrain multibody model. (**b**) First torsional model shape of the powertrain

In the developed 3D MB model of DMF, a contact detection algorithm [11] coupled with the previously described penalty contact force approach allows the estimation of amplitude and direction of contact forces, independently from geometry and orientation of the bodies. In Fig. 14.6b, an example of radial forces exchanged between secondary mass of DMF and driveline shafts during a torsion test at standstill is reported.

14.5 Analysis on the Complete Driveline Multibody Model

The previously described 3D model of DMF has been included into a complete MB model of the vehicle powertrain, as shown in Fig. 14.7a.

The powertrain layout of the considered vehicle is the classical front engine, rear-wheel drive with transaxle gearbox.

The MB model of the vehicle powertrain was used to evaluate the influence of DMF *coil deactivation* phenomenon on the powertrain dynamics. On purpose, the MB model of the powertrain was linearized in the neighbourhood of three different steady-state conditions: 1000, 2000, 3000 rpm. Selected angular speeds correspond to the conditions previously analysed during small displacement cycles (Sect. 14.3.2).

As an example, Fig. 14.7b shows the first torsional mode shape of the powertrain at 2000 rpm. As it can be seen, the crankshaft and transmission shaft motions are in counter-phase and there is a node between first and second stage of DMF. Due to *coil deactivation* phenomenon, a frequency shift of the eigenvalue corresponding to this mode shape is expected as angular speed varies.

To evaluate the frequency shift, Fig. 14.8 compares the DMF stiffness variation estimated from the hysteresis loops reported in Fig. 14.5b at the three considered angular speeds (Fig. 14.8a) with the variation of undamped FRF (Frequency Response Function), angular acceleration at clutch versus torque at the crankshaft, of the linearized powertrain model (Fig. 14.8b).

As it can be seen, the frequency shift of the FRF is directly correlated with the stiffness variation of DMF.

14.6 Conclusion

In this work a 3D nonlinear MB model of DMF was presented. It takes into account 3D dynamics of primary and secondary masses of DMF. Contact forces between primary and secondary masses of DMF with arc springs were modelled with a penalty approach and a contact detection algorithm. The developed 3D MB model was compared with experimental data to assess its capability to reproduce DMF dynamics. A good correlation was found between numerical and experimental data during torsion tests at standstill and small displacement cycles at different angular speeds. Complex stick and slip phenomena are correctly captured, furthermore radial forces exchanged between DMF stages and transmission shafts can be evaluated to simulate driveline rattle phenomena.

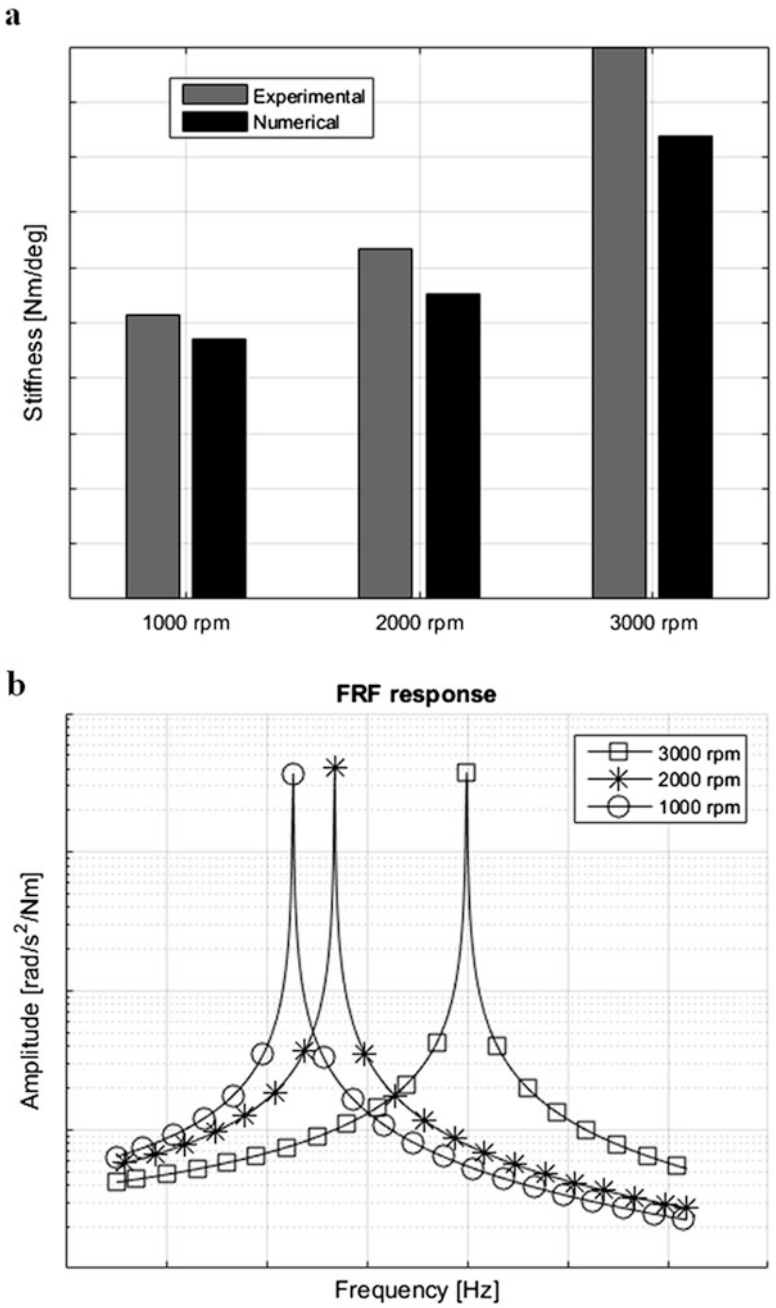

Fig. 14.8 (**a**) Mean stiffness value of the DMF during hysteresis compared with the mean angular velocity variation of the DMF assumed during hysteresis cycle. Stiffness values are scaled with respect the maximum stiffness reached in experimental tests at 3000 rpm. (**b**) Undamped FRF response (Clutch angular acceleration vs Torque at First DMF stage) in correspondence of the first torsional mode shape. Frequency are scaled with respect the maximum natural frequency of the mode shape at 3000 rpm

Acknowledgements Authors Gianluca Quattromani, Edoardo Sabbioni and Federico Cheli would like to acknowledged Ferrari S.p.A. for the financial support and for their kind backing of this work. The authors Antonio Palermo and Francesco Pulvirenti are research partners of Ferrari S.p.A.

References

1. Walter, A., Kiencke, U., Jones, S., Winkler, T.: Anti-jerk & idle speed control with integrated sub-harmonic vibration compensation for vehicles with dual mass flywheels. SAE Int. J. Fuels Lubr. **1**, 1267–1276 (2009)
2. Walter, A., Kiencke, U., Jones, S., Winkler, T.: Misfire detection for vehicles with Dual Mass Flywheel (DMF) based on reconstructed engine torque. SAE Technical Paper (2007)
3. Lei, C., Ming-Ran, D., Zhengfeng, J.: Optimization method of performance parameters of dual mass flywheel. Trans. CSICE (30), 277–283 (2012)
4. Albers, A.: Advanced development of Dual Mass Flywheel (DMFW) design. In: 5th Luk Symposium, Bühl, 1994
5. C. Lei, Z. Rong, Z Jiang. Nonlinear dynamical model of an automotive dual mass flywheel. Adv. Mech. Eng., vol. VII, n. 6, pp. 1–11, 2015.
6. Cheli, F., Pennestrì, E.: Cinematica e dinamica dei sistemi multibody 1-2, Casa Editrice Ambrosiana, 2006
7. Cheli, F., Diana, G.: Advanced Dynamics of Mechanical Systems. Springer, Berlin (2015)
8. Schaper, U., Sawodny, O., Mahl, T., Blessing, U.: Modeling and torque estimation of an automotive dual mass flywheel. In: American Control Conference, St. Louis, 2009
9. D. Karnopp, Computer simulation of stick-slip friction in mechanical dynamic systems, J. Dyn. Syst. Meas. Control., vol. CVII, n. 1, pp. 100–103, 1985.
10. Flores, P., Pimenta Claro, J., Lankarani, H.: A comparative study on continuous force models for constrained multibody systems. In: Multibody Dynamics ECCOMAS, Brussels, 2011
11. Wriggers, P.: Computational Contact Mechanics. Springer, Berlin (2006)

Chapter 15
Investigation of Notch-Type Damage Identification by Using a Continuously Scanning Laser Doppler Vibrometer System

Da-Ming Chen, Y.F. Xu, and W.D. Zhu

Abstract This paper experimentally investigates a notch-type damage identification methodology for beams by using a continuously scanning laser Doppler vibrometer (CSLDV) system. The velocity response of a beam along a scan line under sinusoidal excitation is measured by the CSLDV system and a corresponding operating deflection shape (ODS) of the beam is obtained by the demodulation method. The ODS of the associated undamaged beam is obtained by using a polynomial with a proper order to fit the corresponding ODS from the demodulation method. The curvature of an ODS (CODS) can be calculated with a high quality due to a dense measurement grid of the ODS. A curvature damage index (CDI) is proposed to identify a notch with a length of 1 mm along a beam and a depth of 0.9 mm under different sinusoidal excitation frequencies. The CDI uses the difference between CODSs associated with ODSs that are obtained by the demodulation method and the polynomial fit. The notch is successfully identified near regions with high values of CDIs at different excitation frequencies.

Keywords Continuously scanning laser Doppler vibrometer system • Notch • Damage identification • Operating deflection shape • Curvature

15.1 Introduction

A scanning laser Doppler vibrometer (SLDV) system is widely used in the vibration community because it provides a non-contact and spatially dense measurement. In a conventional measurement method, the laser spot from a SLDV system stays at one point long enough to acquire sufficient vibration data of that point and then moves to the next one. This point-by-point measurement method usually takes a long acquisition time, especially when the measurement grid is large and dense. An alternative method is that the laser spot continuously sweeps over the surface of a structure. Since the laser spot continuously moves instead of staying at one point, the velocity response measured by a continuously SLDV (CSLDV) system is modulated by an operating deflection shape (ODS) along the scan trajectory. Several methods to extract ODSs and modal characteristics from the velocity response have been investigated [1–4]. Stanbridge and Ewins [1] developed two CSLDV measurement methods to obtain ODSs of a structure under sinusoidal excitation. One measurement method is the demodulation method, where the velocity response is multiplied by sinusoidal signals at the excitation frequency and a low-pass filter is applied to obtain an ODS. The other one is the polynomial method, where an ODS is represented by a polynomial whose coefficients are obtained by processing the discrete Fourier transform of the velocity response. Allen and Sracic [4] proposed a "lifting" method to treat the velocity response of a structure as the free response of a linear time-periodic system and decompose it into a set of frequency response functions (FRFs), from which mode shapes and modal damping ratios of the structure can be obtained using conventional curve fitting methods.

Vibration-based methods are widely used for damage detection. Since modal characteristics of a structure, i.e., natural frequencies, mode shapes, and modal damping ratios, are directly related to physical properties of the structure, such as mass, stiffness, and damping, measured modal characteristics can be processed to detect, locate, and characterize damage in the structure [5]. Methods that use changes of natural frequencies due to the existence of damage have been investigated by many researchers. Natural frequencies are global characteristics of a structure and relatively easy to measure from just a few accessible points on the structure [6–9]. However, changes of natural frequencies caused by damage are usually small and may be buried in changes caused by environmental and operational conditions [10]. Natural frequencies also do not directly provide spatial information of structural changes due to damage, and accurate and physics-based models are needed to apply the methods, which can be difficult for real complex structures. Unlike natural frequencies, mode shapes contain

D.-M. Chen • Y.F. Xu • W.D. Zhu (✉)
Department of Mechanical Engineering, University of Maryland, Baltimore County, 1000 Hilltop Circle, Baltimore, MD 21250, USA
e-mail: wzhu@umbc.edu

D. Di Maio, P. Castellini (eds.), *Rotating Machinery, Hybrid Test Methods, Vibro-Acoustics & Laser Vibrometry, Volume 8*,
Conference Proceedings of the Society for Experimental Mechanics Series, DOI 10.1007/978-3-319-54648-3_15

local information of a structure and are more sensitive to local damage than natural frequencies. However, mode shapes are not sensitive to small damage, even with a dense measurement grid of mode shapes [10, 11]. Pandy et al. [12] proposed that curvature mode shapes, i.e., second derivatives of mode shapes, are highly sensitive to damage and can be used to localize it. Differences between curvature mode shapes of damaged and undamaged beams mainly exist in damage regions and increase as the damage extent increases. Wahab and Roeck [13] computed curvature mode shapes of a finite element model (FEM) of a beam and a real bridge. They suggested that a dense measurement grid is required to get a good estimation of higher order curvature mode shapes. Sampaio et al. [14] applied a FRF curvature method to a lumped-mass system and a real bridge. They found that higher order curvature mode shapes can indicate better results of damage. Ratcliffe [15] used broadband curvatures from a set of FRFs to identify damage in beams and proposed a gapped-smoothing method to fit curvatures of associated undamaged beams, where a gapped cubic polynomial is applied to every measurement point using its neighboring points. The gapped-smoothing method eliminates the need for baseline information from undamaged beams. However, the technique can be computationally inefficient for a large-sized dense measurement grid. Yoon et al. [16] extended the gapped-smoothing method to a global fitting method by using generic mode shape forms to globally fit mode shapes obtained from FEMs or experiment. Xu et al. [17] proposed a curvature-mode-shape-based method to identify embedded horizontal cracks in beams, where curvature mode shapes of associated undamaged beams are obtained from polynomials with proper orders that fit mode shapes of damaged beams.

Since a CODS is more sensitive to small damage than an ODS, it is used to identify a notch in this work. In order to obtain a CODS with a high quality, a dense measurement grid is required. In a CSLDV system, an ODS along a scan trajectory can be obtained from the velocity response measured by the system using the demodulation method or the polynomial method. The measurement grid is ideally infinitesimal. In reality, the grid resolution is determined by scan and sampling frequencies used during the acquisition of the velocity response. With a low scan frequency and a current commercially available data acquisition board with a sampling rate of over 50,000 samples per second, a dense ODS can be obtained and a CODS can be calculated with a high quality. Chen et al. [18] proposed a damage identification methodology for beams by using a CSLDV system. They used the demodulation method and the polynomial method to obtain ODSs and CODSs, and investigated effects of scan and sampling frequencies on qualities of ODSs and CODSs. The aim of this work is to further exploit the potential of a CSLDV system on small damage identification, such as a notch on a beam. An improved time-saving experimental procedure is presented here, where only the demodulation method is used to obtain an ODS of a beam and the corresponding ODS of the associated undamaged beam is obtained by using a polynomial with a proper order to fit the ODS from the demodulation method. A curvature damage index (CDI) is proposed to identify a notch with a length of 1 mm along a beam and a depth of 0.9 mm under different sinusoidal excitation frequencies. The CDI uses the difference between CODSs associated with ODSs that are obtained by the demodulation method and the polynomial fit. The notch is successfully identified near regions with high values of CDIs at different excitation frequencies.

15.2 Methodology

15.2.1 CSLDV System

A laser spot in a CSLDV system continuously sweeps over a vibrating structure surface by continuously rotating its pair of orthogonal scan mirrors, called X and Y mirrors, which are connected to two independent stepper motors. Input signals to the stepper motors directly control rotation angles and speeds of the mirrors, and create different scan trajectories of the laser spot for different structures. A constant scan speed is required for the demodulation method [1]. For a horizontally placed beam in this work, a straight scan line with a constant scan speed along the length of the beam can be achieved by giving a triangular input signal to the X mirror and a constant signal to the Y mirror. When a triangular signal is given to the X mirror, the rotation speed of the mirror is constant. It can be assumed that the resultant velocity of the laser spot on the beam is constant along the scan line when the rotation angle is sufficiently small. The CSLDV system developed in this work consists of a Cambridge 6240H scanner and a Polytec OFV-353 single-point vibrometer, as shown in Fig. 15.1; the CSLDV system is controlled by the dSPACE MicroLabBox instead of the dSPACE DS1103 control board in [18].

An experiment is set up to obtain ODSs of an aluminum beam with a notch that is across the beam width using the CSLDV system. The notch location with respect to a scan line with a length of 555 mm is shown in Fig. 15.2a. The length of the notch is 1 mm along the beam and the depth is 0.90 mm, as shown in Fig. 15.2b. A bench vice is used to clamp the left end of the beam to simulate a fixed boundary. A straight scan line is assigned on the opposite side of the notch along the length of the beam. A piece of retroreflective tape is attached on the beam to enhance laser reflection. The experimental setup is shown in Fig. 15.2c: an MB Dynamics MODAL-50 shaker is connected to the right end of the beam with a shaker screw, and the

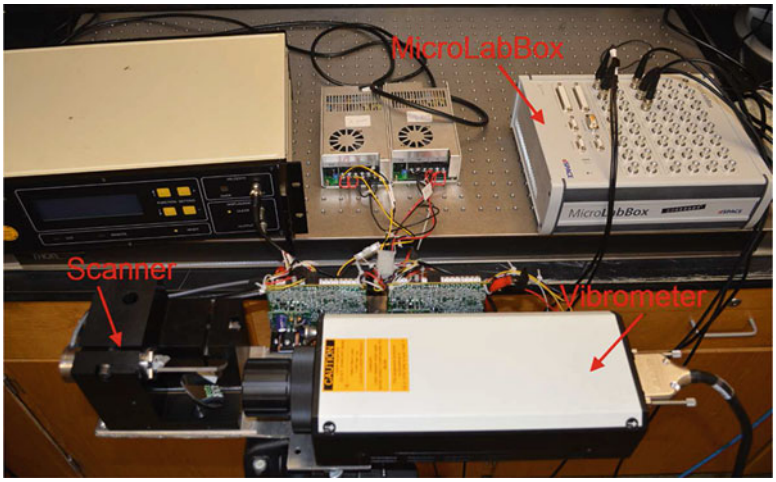

Fig. 15.1 CSLDV system developed in this work

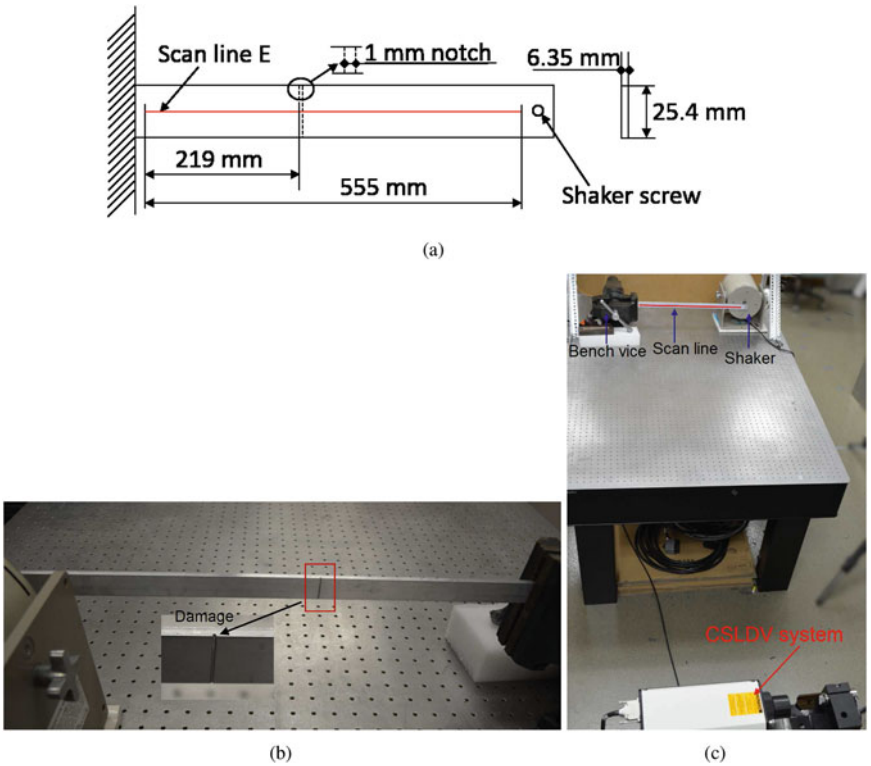

Fig. 15.2 (**a**) Dimensions of a damaged aluminum beam and the notch location with respect to a scan line, (**b**) details of the notch, and (**c**) the experimental setup to obtain ODSs of the beam by the CSLDV system

CSLDV system is used to measure the velocity response of the beam along the scan line. The sampling frequency of the CSLDV system is 50,000 Hz in this work. In the following description, a scan line is nondimensionalized to range from 0% to 100%, where 0% and 100% represent left and right ends of the scan line, respectively.

15.2.1.1 Demodulation Method

The steady-state response frequency of a linear time-invariant structure that results from sinusoidal excitation is equal to the excitation frequency. When using the CSLDV system to measure the velocity response of the beam in Fig. 15.2c, the laser

spot from the system continuously sweeps over the surface of the beam along a scan line instead of staying at one point. Hence, the velocity response is modulated by an ODS along the scan line and can be expressed as

$$v_d(x,\, t) = V_d(x)\cos(\omega t - \alpha - \theta) = V_{I,d}(x)\cos(\omega t) + V_{Q,d}(x)\sin(\omega t) \tag{15.1}$$

where x is the location of the laser spot on the beam along the scan line, ω is the excitation frequency, $V_d(x)$ is the ODS of the beam along the scan line at the excitation frequency, α is the phase difference between the excitation and the X mirror feedback signal, and $V_{I,d}(x) = V_d(x)\cos(\alpha + \theta)$ and $V_{Q,d}(x) = V_d(x)\sin(\alpha + \theta)$ are in-phase and quadrature ODS components, respectively, in which θ is a phase variable that controls amplitudes of $V_{I,d}(x)$ and $V_{Q,d}(x)$. In order to obtain $V_{I,d}(x)$ and $V_{Q,d}(x)$ from the velocity response, $v_d(x,\, t)$ in Eq. (15.1) is multiplied by $\cos(\omega t)$ and $\sin(\omega t)$, which gives

$$\begin{aligned} v_d(x,\, t)\cos\omega t &= V_{I,d}(x)\cos\omega t\cos\omega t + V_{Q,d}(x)\sin\omega t\cos\omega t \\ &= \frac{1}{2}V_{I,d}(x) + \frac{1}{2}V_{I,d}(x)\cos 2\omega t + \frac{1}{2}V_{Q,d}(x)\sin 2\omega t \end{aligned} \tag{15.2}$$

and

$$\begin{aligned} v_d(x,\, t)\sin\omega t &= V_{I,d}(x)\cos\omega t\sin\omega t + V_{Q,d}(x)\sin\omega t\sin\omega t \\ &= \frac{1}{2}V_{Q,d}(x) + \frac{1}{2}V_{I,d}(x)\sin 2\omega t - \frac{1}{2}V_{Q,d}(x)\cos 2\omega t \end{aligned} \tag{15.3}$$

respectively. Terms $\frac{1}{2}V_{I,d}(x)\cos 2\omega t$ and $\frac{1}{2}V_{Q,d}(x)\sin 2\omega t$ in Eq. (15.2) and terms $\frac{1}{2}V_{I,d}(x)\sin 2\omega t$ and $\frac{1}{2}V_{Q,d}(x)\cos 2\omega t$ in Eq. (15.3) can be eliminated by applying a low-pass filter to $v_d\cos\omega t$ and $v_d\sin\omega t$ to yield $\frac{1}{2}V_{I,d}(x)$ and $\frac{1}{2}V_{Q,d}(x)$, respectively. Further, $V_{I,d}(x)$ and $V_{Q,d}(x)$ can be obtained by multiplying corresponding filtered signals by two, which completes the demodulation method. The phase variable θ is optimized to be the one with which $V_{I,d}(x)$ and $V_{Q,d}(x)$ have their maximum and minimum amplitudes, respectively. In what follows, all ODSs are represented by their maximized in-phase components $V_{I,d}(x)$.

When the scan line shown in Fig. 15.2c is applied to the beam, the velocity response measured by the CSLDV system under sinusoidal excitation by the shaker at an excitation frequency of 67 Hz and the corresponding X mirror feedback signal are shown in Fig. 15.3a. Note that a triangular signal is given to the X mirror and the scan frequency is 0.1 Hz, which indicates that the scan time from one end of the scan line to the other is 5 s. The X mirror feedback signal is used to determine the location of the laser spot, based on which one can extract an end-to-end ODS of the beam along the scan line. The ODS obtained from the velocity response by the demodulation method is shown in Fig. 15.3b, which corresponds to boundary conditions of the beam. The number of total measurement points of an ODS along a scan line obtained by the demodulation method is determined by the scan and sampling frequencies. With frequency settings in this case, the ODS is made up by $50{,}000 \times (\frac{1}{0.1} \times 0.5) = 250{,}000$ measurement points along the scan line, which is a very dense measurement grid. With a lower scan frequency and a higher sampling frequency, the measurement grid of a resulting ODS from the demodulation method can be denser.

15.2.2 Curvature-Based Damage Identification Method

It has been shown that curvature mode shapes or CODSs are highly sensitive to small damage and can be used to localize it. CODSs are used for damage identification in this work. A CODS can be calculated using a finite difference scheme

$$y''(x) = \frac{y(x-h) - 2y(x) + y(x+h)}{h^2} \tag{15.4}$$

where $y(x)$ is an ODS and h is the distance between the point x and either end of a derivative interval; h determines the resolution of the resulting curvature [19]. Adverse effects of measurement noise on calculation of a CODS can be alleviated by increasing the value of h, and a suitable value of h can be obtained by increasing it from a small one until a CODS with a low noise level is obtained. Identification of damage can be achieved by quantifying the effect of damage on the CODS

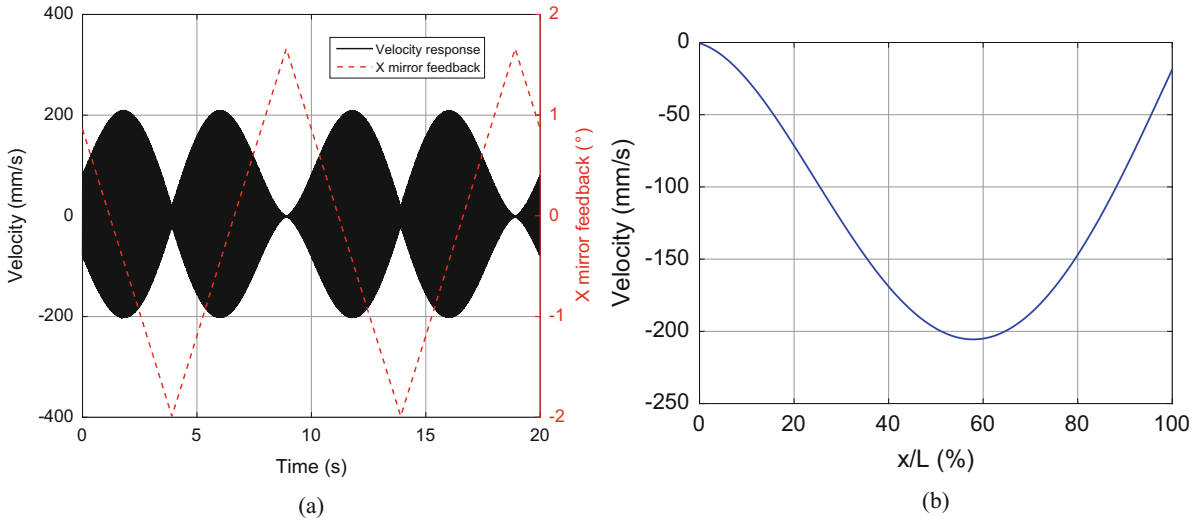

Fig. 15.3 (**a**) Velocity response of the beam at a sinusoidal excitation frequency of 67 Hz and the corresponding X mirror feedback signal with a triangular input signal, and (**b**) the corresponding ODS obtained by the demodulation method

using a curvature damage index (CDI), which can be expressed as

$$\delta(x) = \left[y_d''(x) - y_p''(x)\right]^2 \tag{15.5}$$

where $y_d(x)$ is an ODS from a damaged beam obtained by the demodulation method, $y_p(x)$ is obtained by using a polynomial with order m to fit $y_d(x)$ and is considered as the ODS of the associated undamaged beam, and $y_d''(x)$ and $y_p''(x)$ are CODSs of $y_d(x)$ and $y_p(x)$, respectively. In order to determine the proper order m, the modal assurance criterion (MAC) is used to obtain the least value of m when the $MAC(y_d, y_p)$ value, which is expressed as [Ewins textbook]

$$MAC\left(y_d, y_p\right) = \frac{\left|\{y_p\}^T\{y_d\}\right|^2}{\left(\{y_p\}^T\{y_p\}\right)\left(\{y_d\}^T\{y_d\}\right)} \times 100\% \tag{15.6}$$

is above 90%. It is proposed in this work that the proper order m be two plus the least value of m with which $MAC(y_d, y_p)$ is above 90%. Two is added here in order to preserve the smoothness of the CODS from the polynomial fit, since the calculation of a curvature incurs second-order differentiation, which reduces the order of a polynomial by two. Damage can be identified near a region of high values of the CDI, which appears as a prominent peak.

A dense measurement grid of an ODS can be obtained by using a CSLDV system. Hence, CODSs of higher order modes can be obtained with high qualities, which can increase the possibility to identify small damage, such as a notch.

15.3 Experimental Investigation of Notch-Type Damage Identification

To experimentally investigate the proposed methodology in notch-type damage identification, the velocity response of the damaged beam in Fig. 15.2c under sinusoidal excitation by the shaker at different frequencies is measured by the CSLDV system. ODSs of the damaged beam are obtained by the demodulation method and ODSs of associated undamaged beams are obtained by the polynomial fit. CODSs are then calculated and CDIs are used to identify the notch location. An impact test is first conducted on the damaged beam in Fig. 15.2c to measure its first five natural frequencies; a PCB 086C03 impact hammer and the single-point vibrometer in Fig. 15.1 are used to excite the beam at an impact point and measure its velocity response at a measurement point, respectively. Both the impact and measurement points on the beam are arbitrarily selected as long as they do not coincide with nodal points of its first five modes. The beam is then sinusoidally excited by the shaker at different frequencies of 67, 220, 450, 754, and 1133 Hz, which are obtained by rounding the first through fifth natural frequencies of the beam in the current experimental setup, respectively.

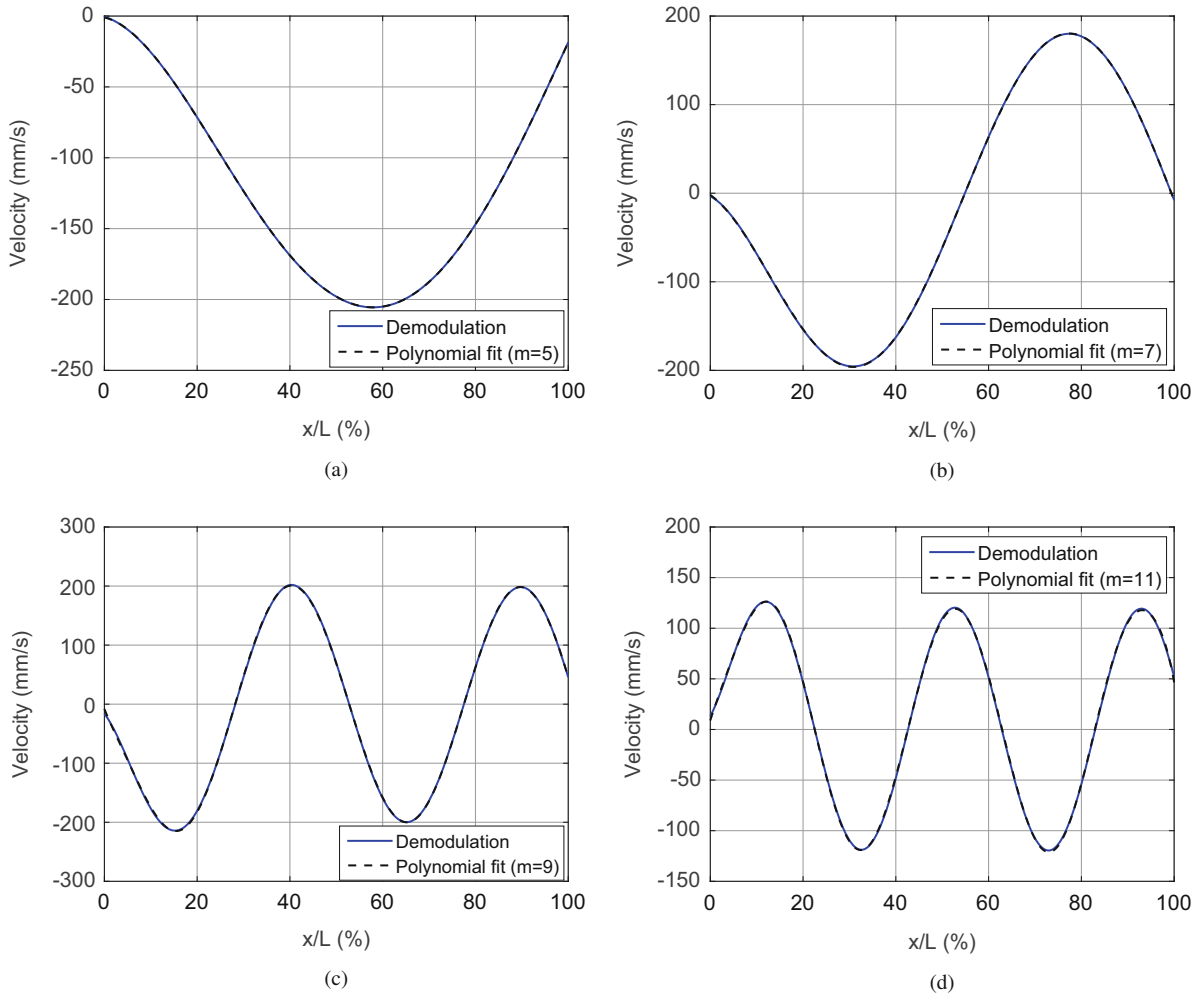

Fig. 15.4 ODSs from the demodulation method with the average number being 50 and those from the polynomial fit at sinusoidal excitation frequencies of (**a**) 67 Hz, (**b**) 220 Hz, (**c**) 754 Hz, and (**d**) 1133 Hz; all the ODSs are along the scan line E

15.3.1 Notch Identification Along the Whole Length of the Beam

A scan line E shown in Fig. 15.2c is applied to the whole beam and a low scan frequency of 0.1 Hz is used. The total scan time is 500 s at each sinusoidal excitation frequency and the average number is 50. The notch location is at [39.46, 39.64]% along the scan line E. It can be seen that the notch extent is only 0.18% along the scan line E. ODSs obtained by the demodulation method and the polynomial fit are shown in Fig. 15.4. No local abnormality can be seen in the ODSs. The ODSs obtained by the demodulation method are then smoothed with 5% of the total measurement points, and CODSs are calculated using Eq. (15.4), as shown in Fig. 15.5. Prominent peaks can be seen in the notch region in all the four modes. The peak in the fourth mode is most obvious, since the notch is near the location where the change of the curvature is the largest in the fourth mode. CDIs are calculated using Eq. (15.5) and are shown in Fig. 15.6. Prominent peaks in the CDIs can be seen in the notch region in all the four modes. Compared with the first mode, the second, fourth, and fifth modes yield better notch identification results, since the peaks in the notch region are more prominent than those in other regions.

While the notch extent is only 0.18% along the scan line E, the notch can still be identified with high values of CDIs near the notch region. The reason is that a very dense measurement grid of an ODS can be obtained by using the CSLDV system with a low scan frequency and a high sampling frequency. CODSs of higher order modes can then be calculated with high qualities and they are sensitive to the local abnormality caused by the notch. Meanwhile, measurement noise can be reduced by increasing the average number. In the practical application of the proposed methodology, a long scan line can be first applied to a beam to identify the existence and location of damage, a local scan line can then be applied to a neighboring region of damage to further verify the damage location.

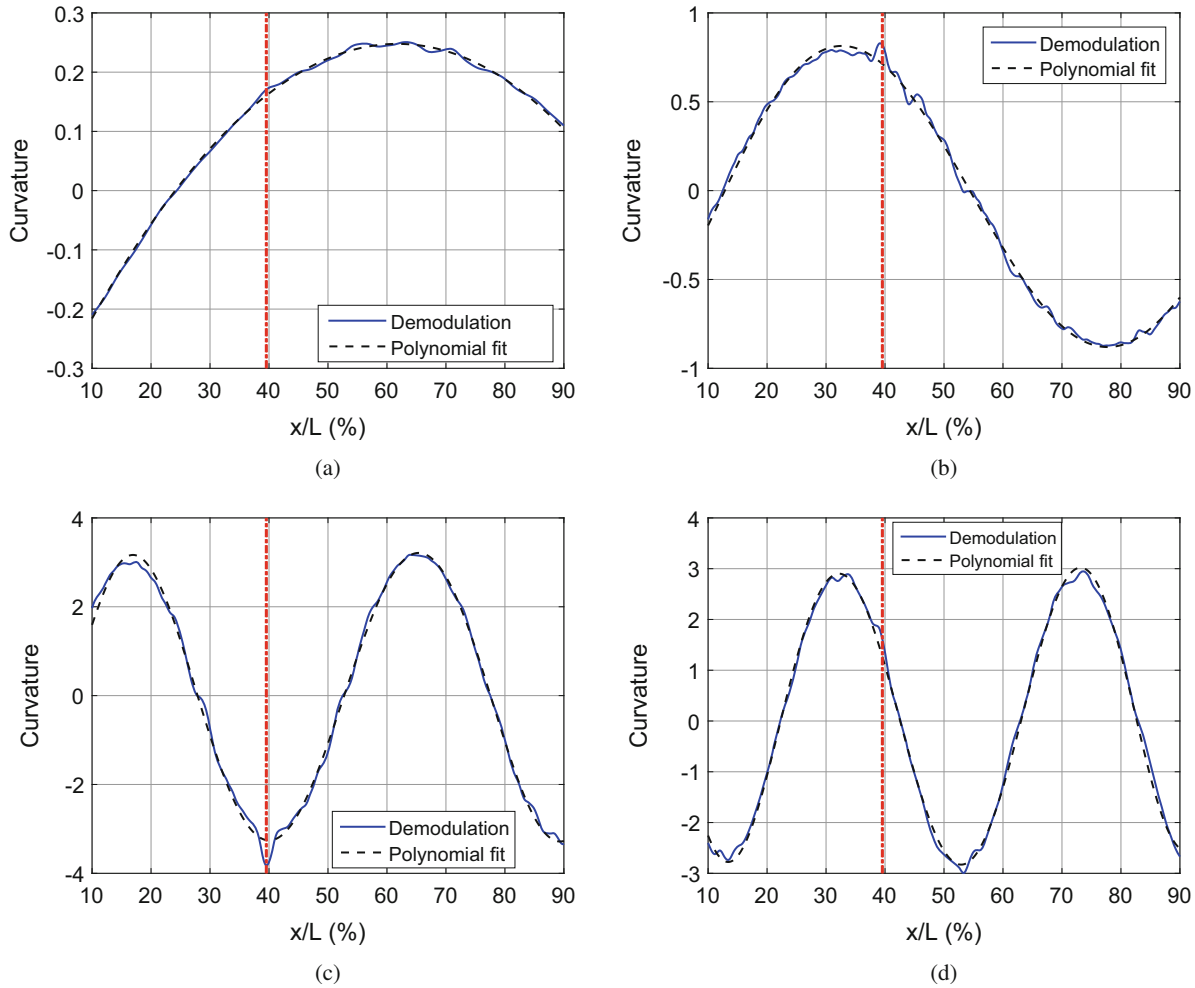

Fig. 15.5 CODSs associated with the ODSs from the demodulation method with the average number being 50 and those associated with the ODSs from the polynomial fit at sinusoidal excitation frequencies of (**a**) 67 Hz, (**b**) 220 Hz, (**c**) 754 Hz, and (**d**) 1133 Hz; all the CODSs are along the scan line E

15.4 Conclusion

A CSLDV system is used in this work to identify notch-type damage in a beam without use of any baseline information of the associated undamaged beam. An ODS with a dense measurement grid is obtained by the demodulation method from the velocity response measured by the CSLDV system. The corresponding ODS of the associated undamaged beam is obtained by using a polynomial with a proper order to fit the ODS from the demodulation method. A CODS with a high quality is calculated and used to localize a notch due to its sensitivity to damage. A CDI that uses the difference between CODSs from the demodulation method and the polynomial fit is proposed to identify a notch. An experimental investigation is conducted on a beam with a notch with a length of 1 mm along the beam and a depth of 0.9 mm. Two conclusions are obtained from the experimental investigation:

(1) CODSs of higher order modes can be obtained by the CSLDV system with high qualities and they can better identify a notch than the CODS of the first mode.
(2) The proposed methodology can provide reliable and correct results to identify the existence and location of a notch along a scan line.

Acknowledgements The authors are grateful for the financial support from the National Science Foundation under Grant numbers CMMI-1229532 and CMMI-1335024.

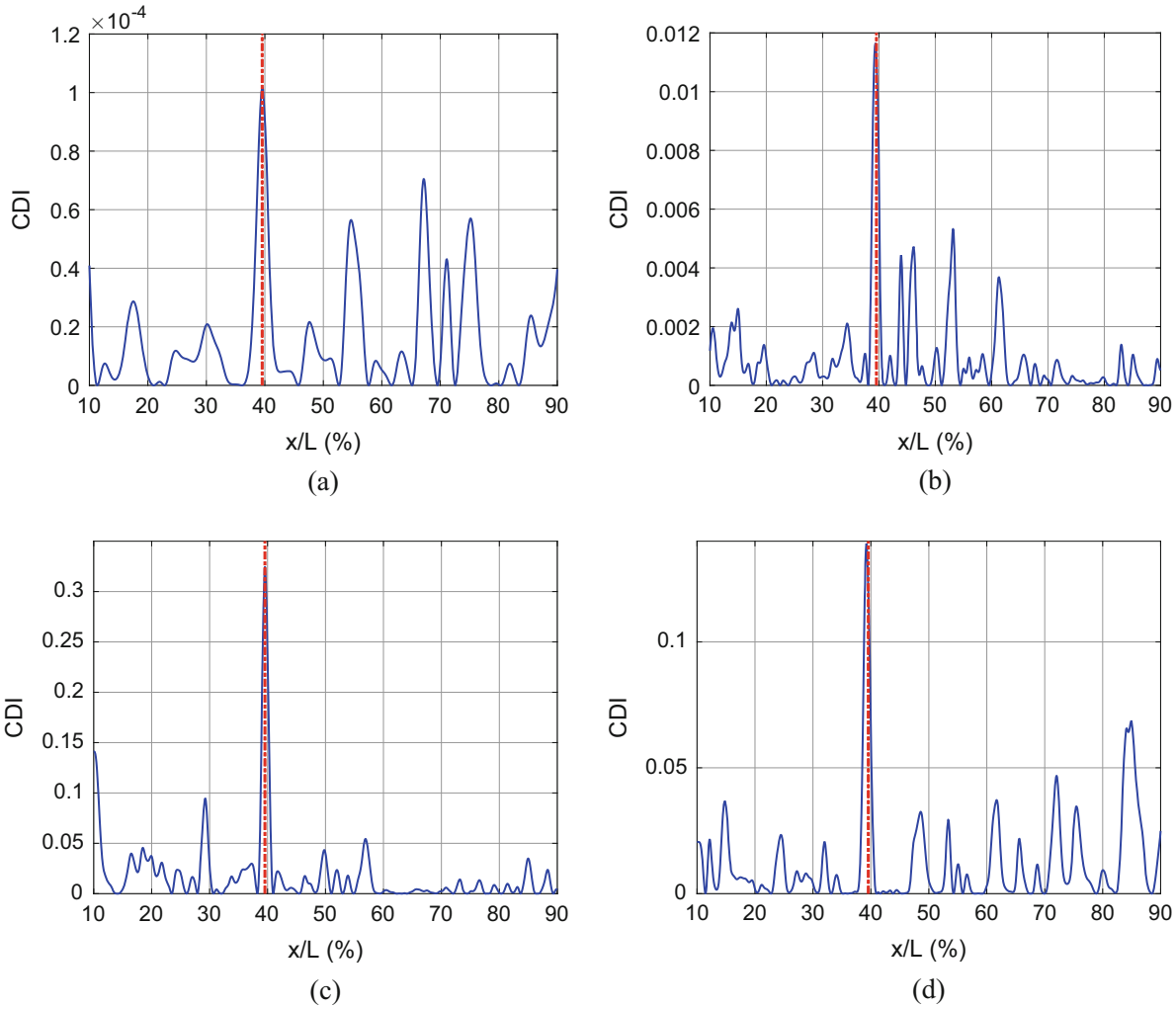

Fig. 15.6 CDIs along the scan line E at sinusoidal excitation frequencies of (**a**) 67 Hz, (**b**) 220 Hz, (**c**) 754 Hz, and (**d**) 1133 Hz

References

1. Stanbridge, A., Ewins, D.: Modal testing using a scanning laser doppler vibrometer. Mech. Syst. Signal Process. **13**(2), 255–270 (1999)
2. Stanbridge, A., Ewins, D., Khan, A.: Modal testing using impact excitation and a scanning LDV. Shock Vib. **7**(2), 91–100 (2000)
3. Di Maio, D., Ewins, D.: Continuous scan, a method for performing modal testing using meaningful measurement parameters; part i. Mech. Syst. Signal Process. **25**(8), 3027–3042 (2011)
4. Allen, M.S., Sracic, M.W.: A new method for processing impact excited continuous-scan laser doppler vibrometer measurements. Mech. Syst. Signal Process. **24**(3), 721–735 (2010)
5. Doebling, S.W., Farrar, C.R., Prime, M.B., et al.: A summary review of vibration-based damage identification methods. Shock Vib. Digest **30**(2), 91–105 (1998)
6. Fan, W., Qiao, P.: Vibration-based damage identification methods: a review and comparative study. Struct. Health Monit. **10**(1), 83–111 (2011)
7. Xu, G., Zhu, W., Emory, B.: Experimental and numerical investigation of structural damage detection using changes in natural frequencies. J. Vib. Acoust. **129**(6), 686–700 (2007)
8. Zhu, W., He, K.: Detection of damage in space frame structures with l-shaped beams and bolted joints using changes in natural frequencies. J. Vib. Acoust. **135**(5), 051001 (2013)
9. He, K., Zhu, W.: Detecting loosening of bolted connections in a pipeline using changes in natural frequencies. J. Vib. Acoust. **136**(3), 034503 (2014)
10. Farrar, C.R., Jauregui, D.A.: Comparative study of damage identification algorithms applied to a bridge: I. experiment. Smart Mater. Struct. **7**(5), 704–719 (1998)
11. Khan, A., Stanbridge, A.B., Ewins, D.J.: Detecting damage in vibrating structures with a scanning LDV. Opt. Lasers Eng. **32**(6), 583–592 (1999)
12. Pandey, A., Biswas, M., Samman, M.: Damage detection from changes in curvature mode shapes. J. Sound Vib. **145**(2), 321–332 (1991)

13. Wahab, M.A., De Roeck, G.: Damage detection in bridges using modal curvatures: application to a real damage scenario. J. Sound Vib. **226**(2), 217–235 (1999)
14. Sampaio, R., Maia, N., Silva, J.: Damage detection using the frequency-response-function curvature method. J. Sound Vib. **226**(5), 1029–1042 (1999)
15. Ratcliffe, C.P.: A frequency and curvature based experimental method for locating damage in structures. J. Vib. Acoust. **122**(3), 324–329 (2000)
16. Yoon, M.-K., Heider, D., Gillespie, Jr., J.W., Ratcliffe, C.P., Crane, R.M.: Local damage detection with the global fitting method using mode shape data in notched beams. J. Nondestruct. Eval. **28**(2), 63–74 (2009)
17. Xu, Y., Zhu, W., Liu, J., Shao, Y.: Identification of embedded horizontal cracks in beams using measured mode shapes. J. Sound Vib. **333**(23), 6273–6294 (2014)
18. Chen, D., Xu, Y., Zhu, W.: Damage identification of beams using a continuously scanning laser doppler vibrometer system. J. Vib. Acoust. **138**(5), 05011 (2016)
19. Sazonov, E., Klinkhachorn, P.: Optimal spatial sampling interval for damage detection by curvature or strain energy mode shapes. J. Sound Vib. **285**(4), 783–801 (2005)